MECHANICS AND MOTILITY OF EPITHELIAL CELLS: FROM SINGLE CELL BEHAVIOR TO COLLECTIVE MIGRATION

Dissertation
for the award of the degree
Doctor rerum naturalium
of the Georg-August-Universität Göttingen

within the doctoral program
"International Max Planck Research School
Physics of Biological and Complex Systems"
of the Georg-August University School of Science (GAUSS)

submitted by
Mark Skamrahl
from Peine, Germany

Göttingen, 2022

Thesis Committee

Prof. Dr. Andreas Janshoff
Institute of Physical Chemistry
University of Göttingen

Prof. Dr. Sarah Köster
Institute for X-ray Physics
University of Göttingen

Prof. Dr. Jörg Großhans
Department of Biology
University of Marburg

Examination Board

1st reviewer: Prof. Dr. Andreas Janshoff
Institute of Physical Chemistry
University of Göttingen

2nd reviewer: Prof. Dr. Sarah Köster
Institute for X-ray Physics
University of Göttingen

Prof. Dr. Jörg Großhans
Department of Biology
University of Marburg

Prof. Dr. Silvio Rizzoli
Department of Neuro- and Sensory Physiology
University Medical Center Göttingen

Prof. Dr. Holger Bastians
Institute of Molecular Oncology
University Medical Center Göttingen

Prof. Dr. Timo Betz
Third Institute of Physics – Biophysics
University of Göttingen

Date of oral examination: 05.07.2022

Meiner Familie

ABSTRACT

Mechanical behavior of cells plays a crucial role in a plethora of biological processes. Despite its importance, this aspect of life science has only more recently gained increasing interest. Yet, without mechanical force the most basic motion cannot be initiated at any length scale, ranging from single molecules to cells, organs, and the whole organism. Similar to human motion, cells employ mechanical force to move directedly, accomplishing diverse tasks. The interplay of motility and mechanics of single cells and force transmission between tightly connected neighbor cells shapes epithelial behavior, giving rise to collective phenomena. In this dissertation, three main aspects of epithelial cell mechanics and motility are discussed.

In the first project (Chapter 3), a simultaneous combination of atomic force microscopy (AFM) and fluorescence recovery after photobleaching (FRAP) was established, calibrated and then applied to cells. Here, AFM was used to provide a mechanical stimulus to single cells. In a simultaneous manner, FRAP was applied as the main readout tool, quantifying the turnover of actin in cellular stress fibers. Systematic application of forces ranging from 100 pN to 10 nN revealed a mechanical adaptation which scaled in an exponential manner: With increasing force application, actin turnover was downregulated to yield longer filaments, which could potentially withstand the external stress better. This novel combination of classic biophysical methods and its first application may enable promising insights into diverse mechanoadaptive processes, such as cell migration.

Chapter 4 discusses collective migration of epithelial cell layers. Wildtype (WT) cells and ones that lack tight junction (TJ) components (ZO1/2 double knockdown, dKD) were compared. dKD cell layers were found to be immobile and jammed. This was attributed to an extreme upregulation of actomyosin contractility upon dKD. However, not all cells were able to contract: In a tug-of-war mechanism, only some cells were able to contract, thereby pulling on their neighbors, which in turn were stretched laterally. The laterally contracted cells lacked directed motion and, thus, were particularly responsible for the jamming. In contrast, the larger, stretched cells remained more mobile. This mechanism was confirmed in co-cultures of WT and dKD cells, as the contractile dKD cells slowed down the whole layer. Overall, collective migration was abolished upon TJ disruption. Interestingly, single dKD cells remained motile, rendering the described mechanism a highly collective effect. This work demonstrates that TJs are vital for collective cell migration and tissue fluidity.

Building on results from Chapter 4, the third research project in Chapter 5 focused on co-cultures of dKD and WT cells. In initial migration measurements of these co-cultures a distinct demixing into clusters was observed but its origin remained unknown. Therefore, new mixing experiments were streamlined to specifically address the governing mechanism of this clustering. Here, dKD and WT cells demixed significantly compared with WT/WT controls. To explain this behavior, the tug-of-war from the previous project was examined further, this time with all dKD

cells able to contract, stretching out WT neighbors. The WT cells mainly responded by excess surface area dilatation. The tug-of-war resulted in tension increase at all junctions connected to dKD cells. In addition, the dKD cells exhibited weaker cell-cell adhesion. Finally, to assess the relative impact of differential adhesion and contractility on demixing, the latter was specifically decreased. This resulted in a slowing of the initial segregation but the final demixed state remained unchanged. Accordingly, differential contractility is needed for efficient early cell segregation but adhesion dominates on longer time scales. This well-controlled case of demixing provides novel insights into how physical forces govern cell sorting, which is crucial during development.

CONTENTS

Chapter 1
INTRODUCTION

How do single cells respond to mechanical force? How do epithelial cells mechanically connect to each other and organize in a tissue? How do intercellular connections influence the coordinated migration of cell collectives?

These are the main questions addressed in this dissertation. The processes underlying these questions rely on the correct function of the most fundamental unit of life, the biological cell. Each cell represents a highly dynamic, active system which operates autonomously but also in a sophistically orchestrated interaction with other cells. The relevant length and time scales of cellular functions and diseases are extremely broad. The human body is comprised of organs, which range from square meters of the skin to millimeter-sized glands, tissues that are only a few cells thick, micrometer-sized cells, protein aggregates, and single molecules.[1] Time scales range from years of aging to months and weeks, such as during the adaptation to exercise or wound healing, to one day cycles between cell divisions, to hours and minutes needed for cell motility and mechanical adaptation, down to seconds of protein turnover and fractions of a second observed for molecular conformation changes.[1,2] In addition, the stiffness of biological tissues ranges from several gigapascals of bones to a few hundred pascals of epithelia.[1] Epithelial cells, in particular, line the surface of organs, overall covering hundreds of square meters. This cell type establishes a tight barrier that prevents uncontrolled uptake of toxins and enables precise uptake of nutrients.

Biochemical aspects of cellular function have been extensively investigated, also regarding the three main questions addressed in the present dissertation. However, the picture is not complete without knowledge of the underlying physical laws. As such, cell mechanics has only more recently gained increasing attention. Yet, mechanical behavior is crucial to biological function because, ultimately, without mechanical force no motion and eventually no life exists. Not only is force exertion essential to generate motion, e.g., for cell motility, but external forces also need to commonly be resisted in nature, from a simple handshake to gravitation. Adaptation to mechanical cues even plays a central role in cell fate determination, e.g., of stem cells.[3,4]

– Ultimately, without mechanical force
no motion and eventually no life exists. –

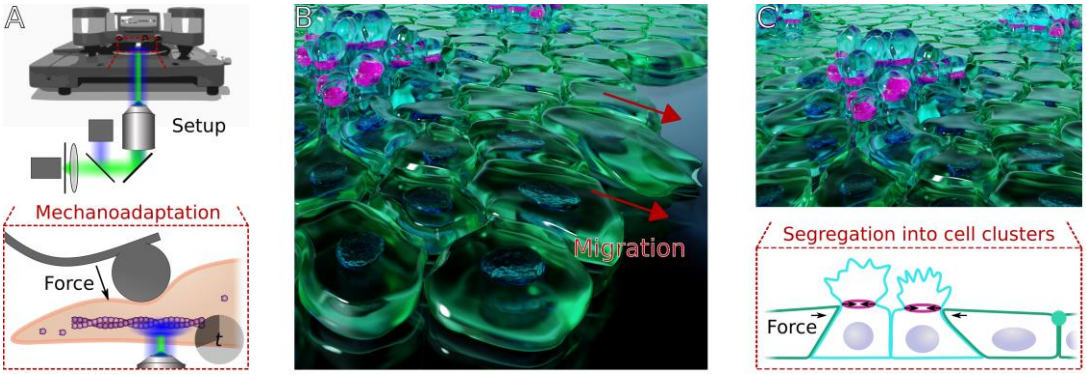

Figure 1.1: Overview of the projects in this dissertation. A) In Chapter 3, a methodological setup is established to quantify the mechanical adaptation of cells to external force. B) Migration of epithelial cells lacking junction components is examined in Chapter 4. C) Building on the findings about migrating cells that lack junction integrity, the segregation of these cells in co-culture with their wildtype counterparts is discussed in Chapter 5. The 3D image in B and C was adapted from our journal cover in *Advanced Science*, which was created by Alexey Chizhik.[6] The rest was adapted from the respective Chapter.

Despite the astounding range of complexity in biological systems, they share common characteristics. Force-sensing, -response and -exertion rely on the cytoskeleton of each cell, similar to the skeleton of a human.[5] Quantifying cytoskeletal responses to force was the first task in this thesis (Figure 1.1A). To this end, a novel combination of force and molecular measurements was introduced. By using precise physical tools such as atomic force microscopy, mechanical stimuli were controlled quantitatively. Upon varying the imposed stimuli systematically, adaptations in the cytoskeleton following an exponential behavior were identified.

In addition to force adaptation, cells also actively exert forces, for example, to move in space, commonly referred to as cell migration. This process relies on the interplay of the cytoskeleton and motor proteins which provide contractile forces.[7,8] Single cell migration has been studied intensely through the last decades. However, epithelial cells establish tight barriers and, thus, need to stay closely connected to each other. Therefore, much like birds fly in flocks and fish swim in swarms, these cells move in coordinated collectives. The relation between the behavior of single cells and collectives is not straightforward. Strikingly, collective behavior cannot simply be extrapolated from single cells but rather exceeds their capabilities, a phenomenon termed as emergent behavior.[9] Understanding collective migration is crucial in wound healing, cancer metastasis and many developmental processes.[10] The coordination within migrating epithelial cell collectives is facilitated by specialized junction complexes. These junctions establish a tight connection between adjacent cells and precisely interact with the cellular cytoskeleton. Hence, their disruption is implicated in several diseases.[11,12]

In this thesis, collective migration of epithelial cells lacking critical junction components was investigated (Figure 1.1B). While junction integrity loss barely affected single cell migration, cell layers were greatly impacted. Not only the barrier function was lost but also the cytoskeleton was

overly upregulated upon losing its connection to the junctions. In consequence, the cell layer lost its fluidity and ability to migrate efficiently.

Building on these results, the collective interaction of junction-inhibited cells mixed with their unchanged counterparts was studied next (Figure 1.1C). Sorting of cells with different properties is crucial in development to form organ boundaries.[13] Cell sorting into compartments can be driven by physical means. However, the impact of different physical driving forces has remained unclear. Physical theories, which rely on energy minimization, include forces that are governed by the cytoskeleton and the junctions. The main mechanical determinants of sorting are differential adhesion (provided by the junctions) and differential contractility (from the cytoskeleton).[14,15] However, it is not trivial to distinguish the relative impact of these factors, which was central in the final project of this dissertation. Essentially, a time-dependent role of contractility and adhesion was identified with differential contractility promoting fast segregation and differential adhesion determining the segregated state upon longer time scales.

Together, the importance of cell mechanics and motility is highlighted across a selection of biological settings, from single cells to collective interaction and migration, providing wide-ranging insights into mechanobiology.

1.1 THESIS OUTLINE

Chapter 2 of this dissertation provides an introduction to the cell- (mechano-) biological as well as the methodological background. Chapter 3 through Chapter 5 include the key findings and were written as separate manuscripts for publication in peer-reviewed research journals. While the topics are highly related, they are meant to be read individually and include a detailed and more specific introduction, methods section, and discussion.

Chapter 3 constitutes an independent research project, which aimed to establish a new method to simultaneously measure cell mechanics and molecular responses of the cytoskeleton. Chapter 5 builds on the findings from Chapter 4. In Chapter 4, the goal was to understand the impact of cell junction loss on collective migration. During this work, junction-inhibited cells were found to segregate into clusters of distinct properties. Understanding the fundamental physics of such segregation was the aim in Chapter 5. Finally, a general discussion in Chapter 6 concludes this thesis.

1.2 REFERENCES

1. Moeendarbary, E. & Harris, A. R. Cell mechanics: principles, practices, and prospects: Cell mechanics. *Wiley Interdiscip. Rev. Syst. Biol. Med.* **6**, 371–388 (2014).
2. Wyatt, T., Baum, B. & Charras, G. A question of time: tissue adaptation to mechanical forces. *Curr. Opin. Cell Biol.* **38**, 68–73 (2016).
3. Engler, A. J., Sen, S., Sweeney, H. L. & Discher, D. E. Matrix Elasticity Directs Stem Cell Lineage Specification. *Cell* **126**, 677–689 (2006).
4. De Belly, H., Paluch, E. K. & Chalut, K. J. Interplay between mechanics and signalling in regulating cell fate. *Nat. Rev. Mol. Cell Biol.* 1–16 (2022) doi:10.1038/s41580-022-00472-z.
5. Fletcher, D. A. & Mullins, R. D. Cell mechanics and the cytoskeleton. *Nature* **463**, 485–492 (2010).
6. Skamrahl, M. *et al.* Tight Junction ZO Proteins Maintain Tissue Fluidity, Ensuring Efficient Collective Cell Migration (Adv. Sci. 19/2021). *Adv. Sci.* **8**, 2170122 (2021).
7. Blanchoin, L., Boujemaa-Paterski, R., Sykes, C. & Plastino, J. Actin Dynamics, Architecture, and Mechanics in Cell Motility. *Physiol. Rev.* **94**, 235–263 (2014).
8. Vicente-Manzanares, M., Webb, D. J. & Horwitz, A. R. Cell migration at a glance. *J. Cell Sci.* **118**, 4917–4919 (2005).
9. Trepat, X. & Fredberg, J. J. Plithotaxis and emergent dynamics in collective cellular migration. *Trends Cell Biol.* **21**, 638–646 (2011).
10. Friedl, P. & Gilmour, D. Collective cell migration in morphogenesis, regeneration and cancer. *Nat. Rev. Mol. Cell Biol.* **10**, 445–457 (2009).
11. Förster, C. Tight junctions and the modulation of barrier function in disease. *Histochem. Cell Biol.* **130**, 55–70 (2008).
12. Cereijido, M. *et al.* New Diseases Derived or Associated with the Tight Junction. *Arch. Med. Res.* **38**, 465–478 (2007).
13. Fagotto, F. The cellular basis of tissue separation. *Development* **141**, 3303–3318 (2014).
14. Brodland, G. W. The Differential Interfacial Tension Hypothesis (DITH): A Comprehensive Theory for the Self-Rearrangement of Embryonic Cells and Tissues. *J. Biomech. Eng.* **124**, 188–197 (2002).
15. Harris, A. K. Is cell sorting caused by differences in the work of intercellular adhesion? A critique of the steinberg hypothesis. *J. Theor. Biol.* **61**, 267–285 (1976).

Chapter 2
Background and Theory

2.1 Biological Principles

2.1.1 Epithelial Cells

A biological cell is the essential unit of life. It is separated from the environment by a thin shell, the plasma membrane, and contains all components necessary for survival. While many different cell types exist, they share the same machinery for their basic functions. Hallmarks of living cells are metabolic activity and reproduction via cell division, also called proliferation. Cells are distinguished into two categories: prokaryotes and eukaryotes. While prokaryotic cells, e.g., bacteria, are more primitive and contain no nucleus or internal membranes, eukaryotes such as epithelial cells are more complex. They are composed of a variety of fundamental components as depicted in Figure 2.1.

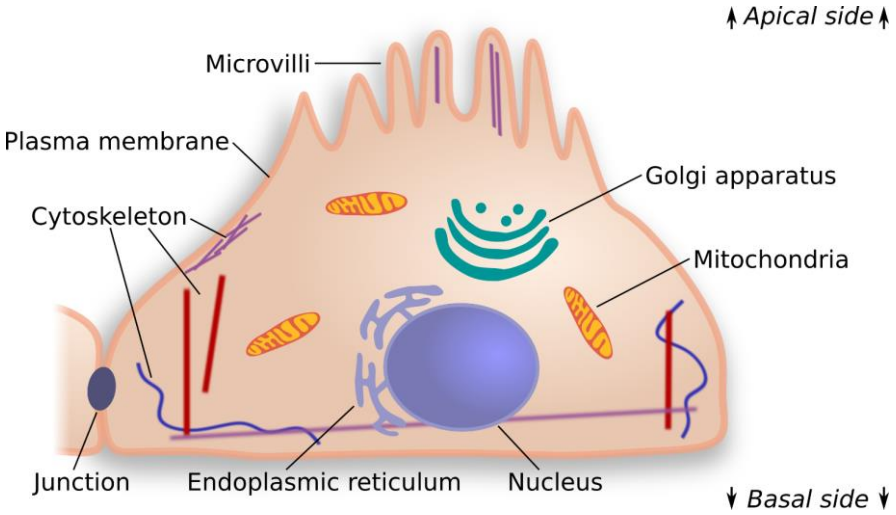

Figure 2.1: Cell composition. General and epithelial-specific cell components are labeled. In particular, epithelial cells are interconnected via junctions and have a pronounced apical-basal polarization with microvilli at the apical side.

Eukaryotic cells form organelles, internal compartments that are separated by membranes, and they have a nucleus, which stores genetic information as deoxyribonucleic acid. While mitochondria also contain certain genetic information, their main function is the cellular energy metabolism. The endoplasmic reticulum serves many functions including protein synthesis, calcium storage, and lipid metabolism. The Golgi apparatus is mainly responsible for lipid and

protein trafficking. An important cell component for the present thesis is the cytoskeleton. This complex network of filaments spans across the cell and is responsible for its stability, shape, and motion. It is helpful to remember that the cell's interior is extremely crowded and viscous forces dominate significantly over inertial ones.[1] Further information about the basic cell composition can be found in classic biology text books.[2]

Specific cell types, based on their particular functions, exhibit specialized structures. For instance, microvilli are thin, finger-like plasma membrane protrusions on the apical side of epithelial cells (Figure 2.1). Such protrusions, in conjunction with invaginations, provide tremendous surface area enlargement by a factor of about 6 to 8, enabling mechanical flexibility and nutrient uptake.[3–5] Several junctions establish the connection between epithelial cells. This connection is crucial because epithelia act as a critical selective barrier with very little intercellular space. In this way, they line the surface of organs, covering hundreds of square meters.[6] The epithelium is one of the main tissue types in animals amongst connective, muscle and nervous tissue.

In the present work, two cell lines were used: HeLa and Madin-Darby Canine Kidney (MDCKII) cells. The benign epithelial kidney cells MDCKII were isolated from a Cocker Spaniel and are widely used as a model system to understand epithelia.[7] These cells grow relatively fast and exhibit typical hallmarks of epithelia such as a prominent apical-basolateral polarity and a tight connection of neighboring cells with little intercellular space.[4,7] Therefore, this cell line is mainly used in this thesis to understand collective cell behavior as described in Chapter 4 and Chapter 5. HeLa cells are the first continuous cancer cell line and probably the most used human cell line in history.[8,9] These cervical carcinoma cells also exhibit epithelial-like character but this is much less pronounced. They are less tightly connected to their neighbors, stay more functional as single cells, and show less additional epithelial hallmarks such as apical-basolateral polarity. Thus, this cell line is better suited for the single cell studies described in Chapter 3.

2.1.2 THE CELLULAR PLASMA MEMBRANE

The plasma membrane separates the cellular content from the environment. It prevents random molecule diffusion, enables specific transport of diverse molecules, and serves as a basis for cell-cell connection and recognition. Phospholipids constitute the major component of this barrier, exhibiting a polar head group and a long non-polar hydrocarbon chain. Examples are phosphatidylethanolamin and phosphatidylinositol 4,5-bisphosphate (PIP_2). Additional important membrane components are glycolipids and cholesterol.[10] The lipids form a bilayer, in which hydrophilic head groups point to the out- and hydrophobic chains point to the inside. The arrangement of the bilayer is highly dynamic. Depending on the lipid type, molecules can quickly exchange their places with a lateral diffusion constant around 0.5 $\mu m^2\ s^{-1}$.[11,12] In contrast, diffusion from the out- to the inside and vice versa is rather rare. A distinct asymmetry between the inner

and outer membrane leaflet composition is important for many functions.[10] Lipids with glycosylated head groups are mainly directed towards the extracellular space, whereas anionic lipids such as PIP_2 point to the cytoplasm where they establish the connection to the cytoskeleton. The curvature of membranes depends on the length of the carbon chains, the size of the polar head group, the mixing ratio of the different lipids and sterols, and the associated proteins. A large number of proteins is directly embedded in or connected to the membrane. Transmembrane proteins traverse the membrane completely. At adhesion spots, transmembrane proteins connect a cell and its cytoskeleton to the surrounding. Integrins, on one hand, mainly establish cell-substrate adhesion while cadherins and other transmembrane proteins enable cell-cell adhesion.

Membrane tension is an important mechanical parameter, which is influenced by the lipid composition, the associated protein make-up, and excess membrane area reservoirs. Importantly, the plasma membrane is a largely inextensible liquid crystal and cannot bear strains of more than about 3%.[13] In consequence, surface area enlargement, in epithelial cells by a factor of 6 to 8, can contribute tremendously to membrane mechanics.[3–5] In addition, the membrane is mechanically supported by its adhesion to the cytoskeleton which significantly influences the overall tension.

2.1.3 THE CYTOSKELETON

Animal cells exhibit a complex and diverse network of filaments, the cytoskeleton. It generates forces that enable cellular motion, sets the foundation for intracellular transport, stabilizes cell-cell and cell-environment contacts, enables resistance against external stress, and it is responsible for stability and shape of cells.[14,15] Three main components constitute the cytoskeleton: actin, intermediate filaments, and microtubules. These different filament types hold distinct functions and form important cellular structures. Microtubules are most prominently known for their role in the separation of chromosomes during mitosis and meiosis but also as transport tracks inside cells.[16] Intermediate filaments are very diverse in nature and provide tremendous stretch resistance in a non-linear fashion.[17,18] The actin cytoskeleton is mainly known for its diverse mechanical roles. It is not only crucial for cellular stability but also the main driver of active forces in a plethora of biological processes, including mechanical adaptation, migration and intercellular interaction. Since these processes are extensively discussed in the experimental Chapter 3 through Chapter 5, we will focus on the actomyosin cytoskeleton in the following.

The Actomyosin Cytoskeleton

Actomyosin is a dynamic filamentous network consisting of actin and its motor protein myosin. Filamentous actin (F-actin) continuously undergoes turnover of its globular actin monomers (G-actin). The monomers polymerize to form long semi-flexible filaments with a persistence length of about 15 μm and a diameter of 8 nm.

G-actin is a polypeptide that forms a specific polarized structure. An actin protofilament is built by an ATP (Adenosine triphosphate)-hydrolysis-driven head-to-tail polymerization of the monomers, leading to an inherent polarity of the filaments (Figure 2.2A). The final actin filament consists of two protofilaments that form a helix. The reaction is reversible, resulting in a dynamic turnover between F- and G-actin with the presence of a certain amount of long and short filaments as well as a pool of monomers. G-actin is added or lost only at the two filament extremities, the predominantly growing barbed (+) end and the prevalently shrinking pointed (-) end. This dynamic behavior of actin allows for quick adaptation of cellular mechanics to external as well as internal stimuli.[15,19,20] It is possible that the net length of the filament remains constant if depolymerization at the minus end takes place at the same rate as polymerization at the plus end. This mechanism results in filament motion without net length variation and is called treadmilling. The polymerization of actin typically starts at the plasma membrane resulting in a preferred localization at the cell periphery.[20] Polymerization can induce a force that pushes the membrane outwards, resulting in protrusions.

Actin-based cell structures gain additional function from their interplay with the motor protein myosin in actomyosin networks. Different myosin isoforms exist that are important in diverse scenarios. Perhaps the most prominent function of myosin is muscle contraction but it is also crucial in non-muscle cells.[21] For instance, myosin-2 is most important in cell migration.[22,23] Myosins generate contractile forces under ATP consumption to induce motion or tension. Basically, myosin motors dynamically bind and pull on actin filaments. This results in a rearward motion of the filaments, called retrograde flow, or more static prestress in the network.

Nucleation as well as bundling and branching of actin networks can be controlled by several proteins and result in different functional cell structures. Important actomyosin-supported structures are shown in Figure 2.2B and will be briefly discussed in the following.

The cellular actin cortex is a submembranous, thin shell. This dense, cross-linked network is located directly underneath the plasma membrane and connects to the bilayer via specialized proteins such as ezrin. The cortex has been shown to be the main determinant of the shape and mechanical properties of cells.[24,25] It is mainly controlled by two associated proteins, the actin-related protein 2/3-complex (ARP2/3) and formins.[24,26,27] Formins are actin nucleators that promote polymerization at the plus end. ARP2/3 also controls nucleation and additionally induces branching at a characteristic angle of 70°.

Lamellipodia are thin (0.1 – 0.2 μm) sheet-like extensions of the cell periphery. Lamellipodia are supported by a branched actin network. Net-like cross-linked actomyosin structures are formed by ARP2/3-induced filament branching. Polymerization towards the plasma membrane induces a protrusion that expands the cell body. Lamellipodia are mainly formed at the leading edge, the side of the cell towards which it migrates.[19]

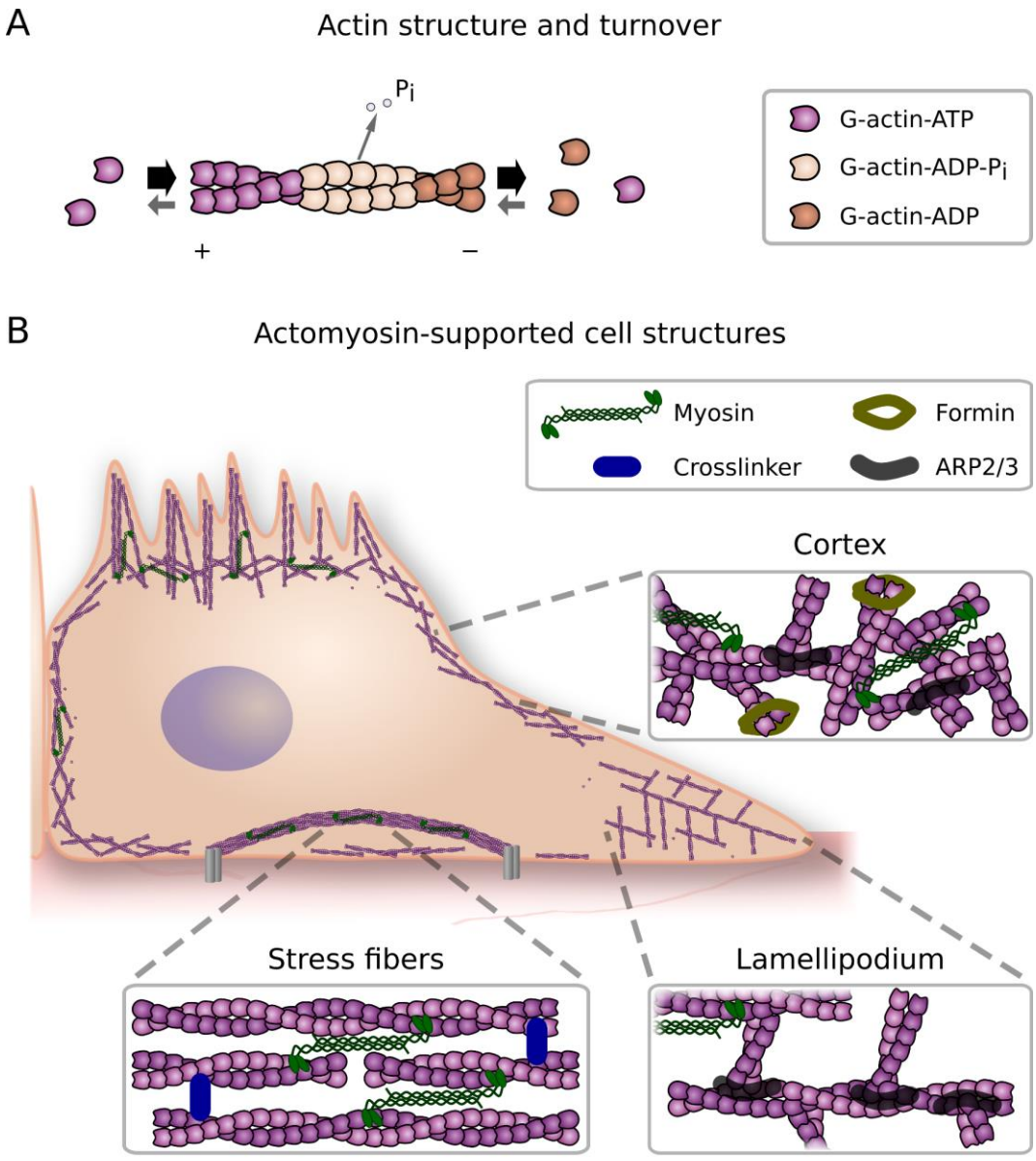

Figure 2.2: Actomyosin structure, turnover and structural architectures. A) Actin structure and turnover, indicating plus (+) and minus (-) end as well as phosphate (P_i) exchange. B) Actomyosin-supported structures in cells such as the cortex, lamellipodia and stress fibers, as well as the associated proteins.

Stress fibers are thick, cross-linked actomyosin bundles. Different types of stress fibers can be distinguished depending or their location and function. Two main classical types are ventral and dorsal stress fibers. The latter are located at the leading cell edge while ventral stress fibers are positioned closer to the cell center. Actin filaments in stress fibers are bundled by cross-linkers such as filamin and α-actinin into long arrangements. Both stress fiber types normally terminate at the cell-substrate interface where they bind to focal adhesions. The connection at focal adhesions is established by scaffolding proteins such as paxillin, talin, and viculin that connect actin to the transmembrane protein integrin. In turn, integrin binds to the extracellular substrate.

Herby, mechanical force from the extracellular matrix can be sensed and transmitted, and finally stress fibers can produce strong contractile force via myosin-2.[28,29]

Actomyosin action is mainly controlled by the interplay of the following signaling hubs: Rho and Rac GTPases.[30] While Rac typically promotes actin polymerization and protrusive behavior, Rho enhances contractility. Upon GTP binding, Rho activates the Rho-associated, coiled-coil containing protein kinase (ROCK). In turn, ROCK promotes myosin phosphorylation, i.e., activation, and blocks myosin phosphatases. In addition, ROCK upregulates kinases that phosphorylate and thereby deactivate cofilin, an actin-destabilizing protein. The interplay between Rac and Rho can be modulated externally, for example, by chemical treatment. To this end, the drug Y27632 was used to reduce actomyosin contractility by suppressing ROCK function in Chapter 4 and Chapter 5.

2.1.4 Mechanical Sensing and Adaptation of Single Cells

While sensing of biochemical signals is well documented, research on mechanosensation has only more recently gained increasing traction. On one hand, cells can apply force to their surrounding, on the other hand they can sense and adapt to mechanical cues from the outside. Mechanical sensing is accomplished by a variety of signal cascades that share general characteristics.[31] Typically, in a first step a receptor at the cell surface is triggered. A prominent example are mechanosensitive Piezo protein channels, who's discovery was awarded with the Nobel Prize in Physiology or Medicine in 2021. These proteins are crucial to sense temperature and touch.[32] Their opening and closing can be controlled by mechanical force: Basically, upon stretching of the membrane, the channel is opened. This first step can later be fine-tuned to different needs and cell types by translocation between different organelles, such as the plasma membrane or the endoplasmic reticulum.[33] Piezo1 has been shown to control proliferation, maintaining cell number homeostasis.[33,34] In addition to channel proteins, transmembrane receptors with an extracellular binding domain are able to sense forces by direct binding. Examples include the cell-substrate adhesion protein integrin, but also the cell-cell connectors cadherins, occludin and claudins as discussed in Chapter 2.1.5 below.

The second step can vary between different mechanisms. In the case of Piezo channels, it is the influx of calcium ions, inducing a biochemical signal that triggers downstream signaling cascades of several proteins. Alternatively, membrane-standing receptors can directly interact with intracellular proteins. This is true for integrins, cadherins, occludin as well as claudins. These adhesion proteins bind to intracellular scaffolding proteins. The resulting adhesion complexes can be modulated upon mechanical force. This can be accomplished via conformational changes of the scaffolding proteins and, as discovered more recently, of the transmembrane proteins.[35–38] Interestingly, pulling force at these structures can enhance their binding strength, a phenomenon known as catch bonds.[39]

In the next step, force is transmitted from the scaffolding proteins to the next binding partner, the actin cytoskeleton. At this point, the mechanical signal could be sensed virtually throughout the entire cell, because of actin's persistence length, which is roughly at the whole-cell length scale of several micrometers. The resulting actomyosin network tension can act as a template for cellular changes. For example, the described bond between membrane-standing, scaffolding, and actin proteins could be further enhanced by the acting forces. Force could also directly radiate through all components of a cell, for example, upon global compression or an osmotic shock.

Finally, the active adaptation to mechanical signals can take place by diverse means. Actin turnover can be modulated directly by several proteins, as described in Chapter 2.1.3. Here, formin and ARP2/3 are known as the main players in the cortex while formin is most important in stress fibers.[24,26] Additionally, a plethora of molecules and signal cascades can act in concert. For example, the Rho pathway can locally modulate myosin activity.[21] Lastly, expression of genes that encode specific proteins can be regulated. For instance, this is the case for the mechanosensitive YAP/TAZ cascade, which controls proliferation-modulating genes.[40] A classic example of considerable mechanical adaptation is stem cell lineage specification by substrate stiffness, with soft matrices inducing a brain-like phenotype and stiff matrices being osteogenic.[41]

Mechanosensing followed by mechanoadaptation are crucial not only for every cell to accommodate mechanical forces (which are an inevitable part of nature) as investigated in Chapter 3, but also for epithelial cells to properly interact with their neighbors as studied in Chapter 4 and Chapter 5.

2.1.5 INTERCELLULAR CONNECTIONS

Cells can bind to one another not only through unspecific electrostatic interactions but also via diverse and specialized intercellular connections. These connections can be homotypic or heterotypic, i.e., established in each binding partner by the same or different means, respectively. For instance, during immunological synapse formation an immune cell recognizes an antigen on a pathogen, e.g., a tumor cell, using specific surface receptors. Another example is found in development, where cell sorting can be achieved by different amounts of binding proteins in neighboring cells.[42] Intercellular connections are particularly crucial to tightly seal epithelial barriers. In this tissue type, three major intercellular connection complexes establish cell-cell adhesion: desmosomes, adherens junctions, and tight junctions (TJs). While desmosomes are connected to intermediate filaments, TJs and adherens junctions are mainly supported by actin but also bind to microtubules. Since adherens junctions and TJs were crucial in the experiments in Chapter 4 and Chapter 5, they will be further discussed next and are illustrated in Figure 2.3.

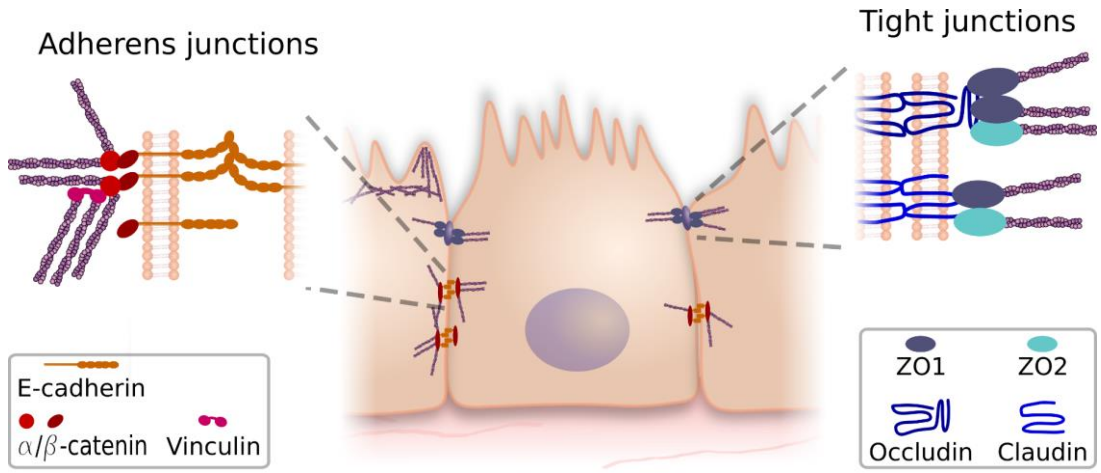

Figure 2.3: Epithelial cell-cell adhesion complexes. Tight junctions (right) are the most apical junction complex and located above the adherens junctions (left). The main junction proteins at the membranes of neighboring cells are indicated.

Adherens Junctions

The classical force transducer between epithelial cells is the adherens junction. This multi-molecular complex is located laterally at the plasma membrane of neighboring cells. Essentially, three components make up the adherens junctions: transmembrane proteins which connect neighboring cell membranes, scaffolding proteins inside the cell, and actin filaments (Figure 2.3, left). The transmembrane protein E-cadherin spans through the membrane and extends five repeating domains on the cell surface, which bind in a trans-interaction with E-cadherin of the neighboring cell.[43] Importantly in nature as well as many experimental protocols, this homophilic binding is calcium-dependent. Moreover, several E-cadherin proteins can cluster together (in a cis-interaction) to greatly enhance mechanical stability of the cell-cell connection.[44,45] Inside the cell, scaffolding proteins provide a mechanical connection to the actin cytoskeleton: ß-catenin binds to the intracellular domain of E-cadherin and to α-catenin, which attaches to the actin cytoskeleton. Importantly, α-catenin can change its conformation and be stretched into an open state. Vinculin can then bind and stabilize the complex, providing further binding sites and connecting to the cytoskeleton.[46,47] Another crucial feature of vinculin is that it can switch between focal adhesions, predominantly in single cells, and adherens junctions, mostly in interconnected epithelial layers.[48] p120 and many other proteins can also support this complex. In addition, adherens junction size and strength is enhanced by forces exerted by the cytoskeleton.[49,50] Depending on the circumstances, adherens junctions can be remodeled between different states.[51] On one hand, actin filaments can align in parallel with the junction complexes, building a ring around cells. On the other hand, the filaments can attach perpendicularly, allowing contractile force exertion perpendicular to the plasma membrane towards the cell center.

In collective migration as well as cell sorting during development, adherens junctions were determined to be the main player in force transduction. During migration, adhesion of these

junctions enables concerted action of cell collectives, ensuring efficient and directed migration.[52,53] Through the adherens junctions, force can be sensed as well as transmitted between neighboring cells. In cell sorting, segregation of cells was observed based on differential adherens junction strength. In general, these junctions were shown to provide greater adhesion than TJs.[54–56] However, more recent evidence also suggests a critical role in cell mechanics for TJs.

Tight Junctions

In epithelia, TJs are critical components with two main functions which are well characterized: The establishment of a paracellular diffusion barrier and of apical-basolateral cell polarity. They are the most apical junction type, located above the adherens junctions at the apical-lateral plasma membrane (Figure 2.3, right). Similar to adherens junctions, TJs consist of three main components: Membrane-spanning proteins that connect neighboring cell membranes, the actin cytoskeleton, and scaffolding proteins which connect the former two. The tetraspan proteins occludin and several claudins tightly seal the space between two cells. Importantly, this is calcium-dependent, similar to E-cadherin. ZO1 and 2 are the main scaffolding proteins, with ZO1 at about the tenfold concentration of ZO2.[57] Additional associated proteins comprise ZO3, MAGI proteins, and several others, together constituting large signaling hubs.[58]

By tightly sealing the space between cells, TJs prevent uncontrolled passing of molecules, such as toxins, through the epithelium. They also pose a diffusion barrier laterally within the plasma membrane. Here, they prevent the lateral diffusion of membrane components from the apical to the basal side and vice versa. Thereby, the apical-basolateral polarity is established with an apical and a basal side, which contain different lipid compositions, proteins, and membrane structures, such as the exclusively apical microvilli.

More recently, functions of TJs in cell mechanics emerged in the literature. Current developments were reviewed by S. Citi in 2019.[59] Similar to the adherens junctions, a dependence on cytoskeletal tension has been found. ZO1 was shown to be activated by unfolding under mechanical force, controlling its interacting proteins.[35] In addition, TJs were demonstrated to provide a negative mechanical feedback for cellular tension.[60,61] In particular, if ZO proteins are lost, cells begin to contract excessively, imposing tremendous tension at the adherens junctions. This is reflected in the upregulation of actomyosin-controlling signal pathways and affects the epithelial sheet morphology and cell-cell interactions.[62]

2.1.6 Cell-Cell Interactions and Sorting

Once intercellular connection is established, cell-cell interactions can be properly coordinated. Interestingly, cellular interactions are not always entirely reciprocal. When multiple cells with different properties bind, a distinct demixing of the cells can take place. This is employed in many

biological processes, including development, to enable deliberate sorting of cells.[63] Cellular sorting can be regulated by various biophysical factors.

An important physical idea is that the total free energy in a cell layer needs to be minimized in equilibrium. This energy can stem from different contributing driving forces. The most basic hypothesis assumes that demixing of unlike cell types is induced by differential adhesion, for example due to different adhesion protein levels.[64] Quite intuitively, contact is minimized between binding partners with low adhesion and maximized between ones with large adhesion. Considering the contractile behavior of actomyosin, differential cell contractility was additionally considered, resulting in a concept based on interfacial tension.[65,66] While adhesion increases interfacial contact, contractility induces cell rounding and minimizes the surface. Here, cells rearrange and sort in a way that minimizes the overall interfacial tension. More recently, this hypothesis has been extended by adding local cues. For example, cells of the Drosophila wing which are located at the anteroposterior compartment boundary show increased contractility.[67,68]

These hypotheses have in common that the Hamiltonian energy functional H needs to be minimized as mentioned above. A recently developed example of this function is the following form:[69]

$$H = \frac{K}{2}\sum_n^N (A_n - A_n^0)^2 + \sum_j^J \gamma_j l_j + \frac{k}{2}\sum_j^J (l_j - l_j^0)^2. \tag{2.1}$$

The first term describes that hydrostatic pressure drives a cell n to assume a preferred area A_n^0. The second term incorporates the line tension γ_j acting on a junction j of length l_j, however, in this model without adhesive contributions. Adhesion comes into play in the third term, which describes the tendency of a junction j to assume a preferred length l_j^0. K and k are elastic constants that can tune the relative impact of the terms. Many variations of this equation exist in so-called vertex models, which are appropriate to describe different scenarios.[70]

Similarly as in sorting, cells of the same type must still obey these energy laws. It has been shown that the interplay between cortical tension and intercellular adhesion gives rise to preferred cell shapes.[71] Strikingly, a snapshot of the 2D cell geometry alone can predict the degree of motility in the layer. In this regard, a distinct fluid-to-solid jamming transition threshold was determined: a cell shape index of 3.81 (calculated as the perimeter divided by the square root of the area).[71] Above this threshold a layer is motile and below it is jammed. These jamming transitions can be crucial in collective migration.[72,73]

2.1.7 Collective Cell Migration

Much like birds fly in flocks and fish swim in swarms, cells can move in coordinated collectives. Compared with single cell migration,[74,75] collective migration is less understood and poses interesting, yet complicated features and emergent phenomena.[76,77] On the cellular level, every

cell can move itself but it also interacts with its tightly connected neighbors, which, in turn, influence the next neighbors and so forth. Furthermore, collective cell migration relies on a sophisticated interplay of the mechanical interaction at different levels ranging from single molecules and protein complexes, to single cells, and finally to the collective behavior of an epithelial layer on a mesoscopic scale. This concerted interplay is based on the precise tuning of molecular action, cell contractility and motility, the degree of crowding, intercellular adhesion, cell-substrate dynamics, and even different cellular roles in the collective.

So-called leader cells emerge at the advancing migration front (Figure 2.4). These cells are positioned at the very front of a layer protrusion, they are usually larger than bulk cells, and have a large lamellipodium towards the migration direction. The actomyosin network in the lamellipodium pulls on the substrate (Figure 2.4A) and induces a directed forward motion (Figure 2.4B). The exerted forces are controlled by local Rho activity.[78] Leader cells then pull the following bulk cells along, using a thick, supracellular actin cable, also called purse string, which spans across the periphery of multiple cells (Figure 2.4B).[78] In this way, the purse string is under considerable tension. Additionally, stress can build up across even millimeters from the front into the bulk.[79] Interestingly, leader cells do not only exert tremendous force but are also initially elected as leaders by mechanical pull from their neighbors.[80] At the same time, to even add further complexity to the picture, the stress landscape in a whole epithelium was shown to be tremendously heterogeneous and dynamic.[81,82] Each bulk cell can also form a (cryptic) lamellipodium and interact with the next neighbors via the junction complexes (Figure 2.4A): When one cell contracts and pulls on the substrate, it evokes forces (and motions) that are transmitted via the junctions to the next cell. It has been shown that forces are sensed over a range of about 150 µm (called correlation length), i.e., across multiple cells.[80,83] In turn, this controls leader cell emergence and overall migration dynamics. The resulting motions in the bulk can be diverse (Figure 2.4B): well aligned and most efficient forward migration closest to the front, circular swirling motion (prominently observed within confinements) and uncoordinated movements.[23] The latter occur due to heterogenic stresses, at longer distances than the correlation length, or upon junction disruption.

Key progress has been made in understanding how mechanical force is transmitted through the junctions during collective migration.[53,77,81] In principle, transduction of intercellular forces guides neighboring cells in the layer. Here, adherens junctions are recognized as a main force transducer. However, there are inconsistent findings on the impact of particular TJ proteins during collective cell migration. Recently, several studies highlighted a strong influence of TJs on mechanobiology in general.[59–61] Yet, the consequences for collective behavior and migration remained elusive. Hence, this is addressed in Chapter 4.

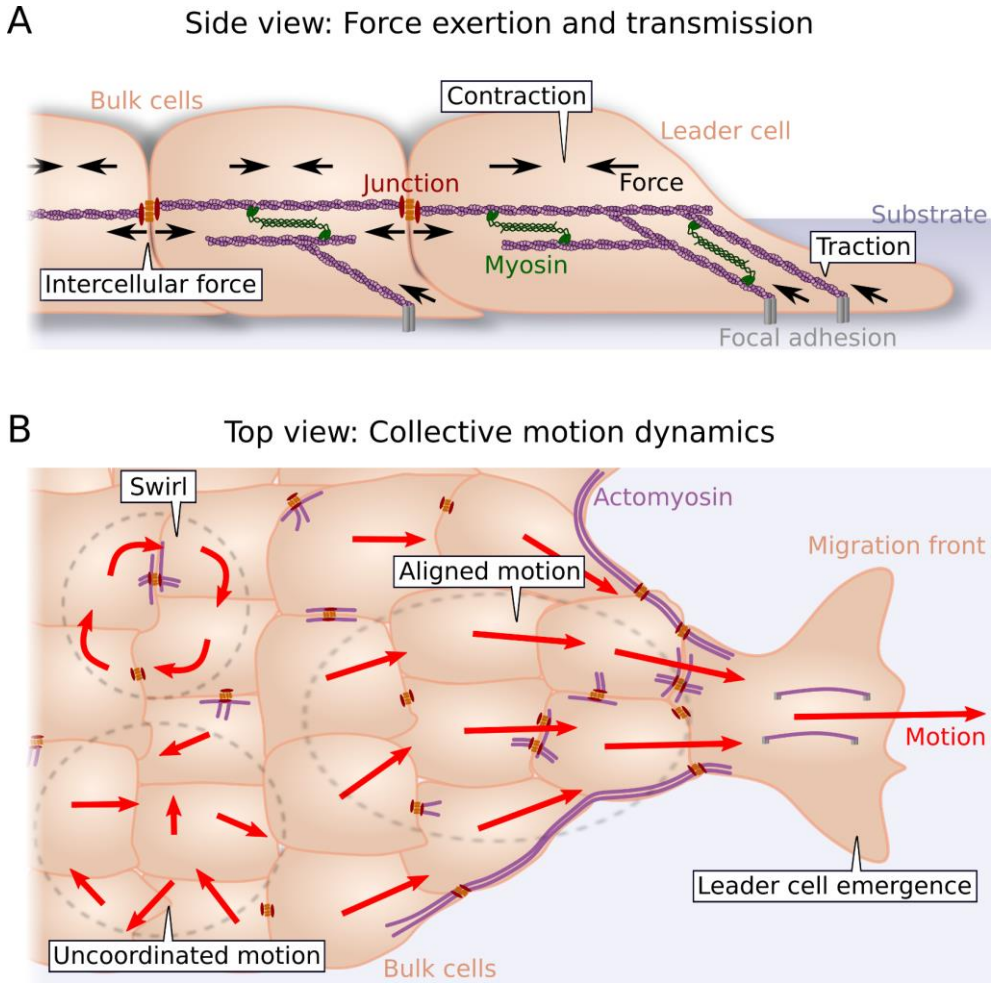

Figure 2.4: Principles of collective cell migration. A) Side view with a focus on force exertion and transmission. Leader cells at the front direct the collective by pulling on the substrate. Force exertion is performed by actomyosin contraction and transmitted via junction complexes. Bulk cells can also exert force and actively move. B) Top view with a focus on motion dynamics. Red velocity vectors indicate motion direction and magnitude. A leader cell emerges at the migration front and is connected to the following cells via an actin purse string and junction proteins. Motion is most efficient and best aligned closest to the migration front. Each bulk cell is also connected to its neighbors by junctions which are stabilized via actomyosin. Different motions can be observed, usually further in the bulk: mitosis (not shown), circular swirling motion (prominent in confined spaces) and uncoordinated motion. The latter occurs, for example, upon junction disruption (e.g., loss of TJ components in Chapter 4).

2.2 BIOPHYSICAL TECHNIQUES

In this Chapter, the methods used in this thesis will be discussed with a focus on general understanding and theory, while specific experimental procedures and conditions will be discussed in Chapter 3 through Chapter 5.

2.2.1 OPTICAL MICROSCOPY

Phase Contrast

Microscopic objects are magnified by optical microcopy based on the interaction of matter with light. Nowadays, phase contrast is ubiquitous and will therefore only be discussed briefly. In simple brightfield microscopy light is projected onto and partially absorbed by a sample. An objective lens captures the transmitted light and magnifies the object, which is finally projected onto a camera. Because biological cells absorb low amounts of light, they cannot be observed well.

Phase contrast was invented in 1934 to circumvent this problem.[84] This is accomplished by exploiting the wave character of light: While cells do not change the amplitude of the light waves, cellular structures do alter the phase of the waves due to slight differences in their refractive index. The refractive index differences induce a phase shift of the waves of about 90°. By the use of a phase plate inside the objective, another phase shift of 90° is introduced. The resulting overall phase shift of 180°, due to the wave character of light, introduces interference with the background light, which is influenced separately. To this end, a ring-shaped condenser annulus which restricts the light source to a circular ring is added in a conjugated plane to the phase plate. Thereby, background light and the object-passing light are affected differently: Background light only passes through the phase plate ring, while object-passing light is scattered and therefore passes the objective at all sites. By passing the phase plate the intensity of the background light is reduced so that it roughly matches the object light intensity. In the end, background and object-passing light beams are phase shifted by 180° relative to each other, inducing negative interference. Thus, the object appears dark in the image with enhanced contrast.

Fluorescence and Confocal Microscopy

Fluorescence and confocal microscopy are also commonly used standard techniques.[85,86] However, they lay the foundation for the methods described next (Chapter 2.2.2 and 2.2.3) and, thus, will be briefly discussed. Fluorescence microscopy provides tremendous specificity: Instead of observing light that passes through the whole sample, specifically labeled cell structures are examined while the rest remains dark. For this, myriads of fluorophores are available. Such molecules typically have many conjugated double bonds, so that they efficiently absorb light of certain wave lengths. Upon photon absorption, the molecules stay in an energetically excited state for a certain time - the fluorescence lifetime of a few nanoseconds - before falling back to the

ground state and emitting another photon. In this process some energy is dissipated, yielding emission light of longer wavelengths. This so-called Stokes shift is taken advantage of by the proper use of excitation and emission filters that only transmit light of the desired wavelengths.

In confocal microscopy, instead of illuminating the whole sample at once, a focused laser is used to excite the object in a scanning fashion. A pinhole in front of a point detector blocks out non-focused emission light, i.e., background light along the axial direction. Thereby, a better axial resolution can be achieved and three-dimensional views are created.[86]

In the present work, two main types of fluorophores, specified for different wavelengths, were used: Fluorescent proteins, e.g., green fluorescent protein (GFP), and organic labels such as AlexaFluor conjugates. The organic fluorophores were conjugated to antibodies and introduced after fixing the cells. In contrast, fluorescent proteins were genetically encoded in living cells, so that they were covalently bound to the protein of interest, i.e., actin monomers in Chapter 3 and myosin-2 or ZO1 in the other Chapters.

2.2.2 Fluorescence Recovery After Photobleaching

Fluorescence microscopy is not only restricted to recording images but also allows gaining quantitative information about molecular dynamics. Fluorescence recovery after photobleaching (FRAP) measures molecular dynamics by bleaching fluorophores attached to target molecules in a small region of interest (ROI) as depicted in Figure 2.5A. In the present work, a comprehensive protocol by Fritzsche et al. was followed.[87]

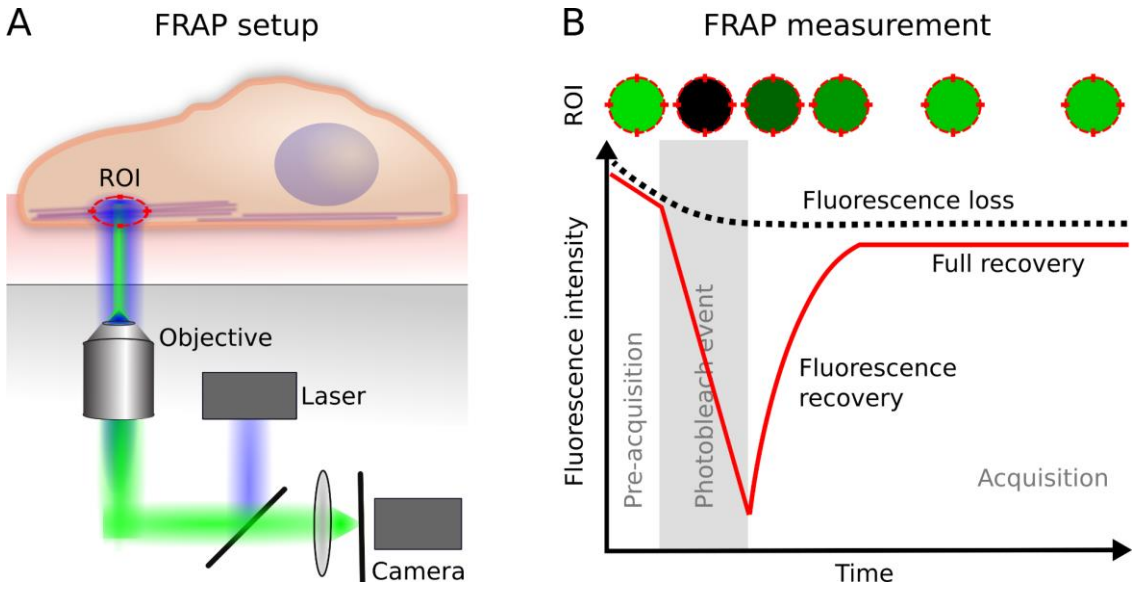

Figure 2.5: FRAP setup and measurement. A) FRAP laser and acquisition setup with an exemplary region of interest (ROI) located at cellular stress fibers. B) Fluorescence intensity during a FRAP measurement with characteristic events labeled. Figure modified from Figure 3.1 in Chapter 3.

After bleaching, recovery of the fluorescent signal is introduced when fluorophores from the surrounding enter the ROI (Figure 2.5B). A loss of fluorescence can be introduced by imaging-induced bleaching or an immobile fraction of molecules which essentially stay in the ROI. To account for this, frames before bleaching are recorded and used for normalization.

It is important to distinguish between different mechanisms how fluorescence is recovered. On one hand, molecules can passively diffusive into the ROI. On the other hand, reactions can take place that cause molecules to enter the ROI. The target in this work, actin, is an active filament network with dynamic turnover between bound and unbound monomers, as described in Chapter 2.1.3. However, monomers could also diffuse into the ROI. Fortunately, actin monomer diffusion takes places in a few seconds while reactive turnover occurs over tens of seconds to minutes in a ROI of 2 µm diameter.[26] Therefore, the reactive turnover can be quantified independently.

Here, a reaction is considered between two species, A (G-actin in my experiments) and B (free binding sites on filaments) that form a complex AB (F-actin):

$$A + B \underset{\omega_\mathrm{d}}{\overset{\omega_\mathrm{a}}{\rightleftarrows}} AB \tag{2.2}$$

with two rate constants ω_a and ω_d for the association and dissociation, respectively. The reaction-dominant case was described well by Sprague et al.[88] Three main assumptions are made: The component concentrations are in an equilibrium, i.e., the binding sites and monomer concentrations are constant. This is reasonable because genetic expression changes actin concentrations on much longer time scales than the tens of seconds examined by FRAP. Second, the actin network is large and immobile in comparison with the monomers on the experimental time and length scales. Finally, diffusion is much faster than reaction and, thus, does not contribute (vide supra). Therefore, the diffusion term from Fick's law can be omitted and the differential equation of the reaction reads

$$\frac{\partial[AB]}{\partial t} = \omega_\mathrm{a}[A][B] - \omega_\mathrm{d}[AB]. \tag{2.3}$$

Rectangular brackets indicate the respective concentration. Successful bleaching of all labeled molecules in the ROI means that at time $t = 0$, $[AB]$ is zero. In a cell, which is large compared with the ROI size, $[A]$ is assumed to be small in comparison with the total amount in the cell. Therefore, $[A]$ is readily replaced by diffusion from around and thus unaffected by bleaching. In addition, $[B]$ is also unchanged. With these assumptions equation (2.3) can be solved and recovery described by an exponential function with ω_d in the exponent:[89]

$$\frac{[AB]}{[AB]_{\mathrm{eq}}} = I(t) = 1 - e^{-\omega_{\mathrm{d}} t}. \tag{2.4}$$

$[AB]_{\mathrm{eq}}$ denotes the equilibrium concentration. Note, multiple reactive pathways with different off-rates could contribute to the observed recovery, e.g., formin- or ARP2/3-mediated polymerization.[26] To identify these contributors, strategies such as genetic or chemical perturbations can be employed. Alternatively, if the different reactions take place on sufficiently different time scales, they can be distinguished in the recovery kinetics. To this end, a sum of exponential functions $I(t)_i$ from equation 2.4 is used to describe all first-order reactions i that contribute to the total recovery. Finally, filament lengths can be inferred as described by Fritzsche et al. if the actin nucleator is known.[24] Note that it is crucial to carefully calibrate the laser power in order to prevent filament cuts. In sharp contrast, such cuts are desired in the laser ablation experiments discussed next.

2.2.3 LASER ABLATION

Laser ablation experiments were mainly performed by our collaborators, so that I will only briefly describe this technique. In mechanobiology, laser ablation is used to access mechanical properties by precisely cutting target structures in a sample.[90] Typically, a confocal microscope is used with a high-power laser, focused at the sample plane.[91] The energy density is adjusted, so that structures of interest are cut but excessive heat generation is prevented.

While it is possible to ablate even multiple cells at once, we focused on cutting single cell-cell junctions. After the laser ablation event, images are recorded to track the opposing cell vertices of the respective junction (i.e., the tricellular junction hubs).[91] The recoil of the vertices is a damped elastic response of exponential nature with a characteristic time interval that indicates the ratio of viscosity and elasticity.[90] However, not all material properties influencing the recoil curve are always known. Therefore, we used the whole curve mainly to validate successful and full ablation without any interference (e.g., disruptive influences by excessive laser powers). To estimate the apparent junction tension, we used the initial recoil velocity. On shorter time scales (here about 150 ms) elastic properties generally play a larger role than viscosity. Upon longer times, viscosity comes increasingly into play and proximal cell structures could influence the outcome.

Nevertheless, also on short time scales it is important to keep in mind that the absolute tension can only be derived if the viscosity is known. The tension-to-viscosity ratio determines the initial velocity.[91] Yet, if one assumes viscosity values to be constant or that their change can be neglected, relative line tension can be compared between different cells.[60,68,92] Indeed, in previous work comparing ZO1/2 dKD and WT MDCK cells viscous drag was assumed to be a minor factor.[60] Alternatively, if the viscosity at the junctions is known, absolute tension values could be obtained

from ablation. In any case, ablation experiments provide the advantage of accessing plane- and location-specific junction mechanics.

2.2.4 ATOMIC FORCE MICROSCOPY

Invented in 1986, following the development of the scanning tunneling microscope, atomic force microscopy (AFM) serves as a versatile tool from materials science to mechanobiological research. The main principle is that a small spring is brought into contact with a surface while the resulting spring deformation is recorded. AFM allows to assess mechanical properties and, alternatively, it can be used to scan surface topographies.

The basic setup of an AFM is shown in Figure 2.6A. The tip of a spring-like probe, the cantilever, is brought into contact with a surface. Upon contact, the cantilever will bend depending on the restoring (or attractive) force it experiences from the sample. A laser is directed onto the back of the cantilever tip and reflected onto a quadrant photo diode. Thereby, the bending motion of the tip is recorded as a change in the photo diode voltage. Axial and lateral motion is performed using a Piezo element, which expands or contracts precisely upon voltage application. By adjusting the voltage on the Piezo, a PID-based feedback loop keeps the desired deflection. To convert the recorded photo diode voltage signal to the bending distance, a force curve is recorded on an extremely rigid substrate yielding a linear bending response. Once the voltage-to-distance conversion factor is obtained, the spring constant can be derived by a calibration routine based on thermal fluctuations of the cantilever.[93] Here, the equipartition theorem and Hooke's law are considered.

Imaging

While AFM-based imaging is possible by intermittently tapping the surface, in this thesis it was performed only in contact mode. Here, a certain force is set as a constant setpoint while the tip is scanned laterally across the sample. Upon encountering changing surface topographies, the PID feedback system quickly adjusts the height of the probe to keep the set force. The surface topography can then be converted into a height image. In addition, the error signal of the feedback can be inspected, i.e., the small and short-lived differences between the setpoint and the actual value. Small tips are used to increase the obtainable resolution and imaging was performed on fixed cell layers. However, also on such stiffened samples it is advisable to choose small forces and low scanning speeds to avoid damaging any cell structures.

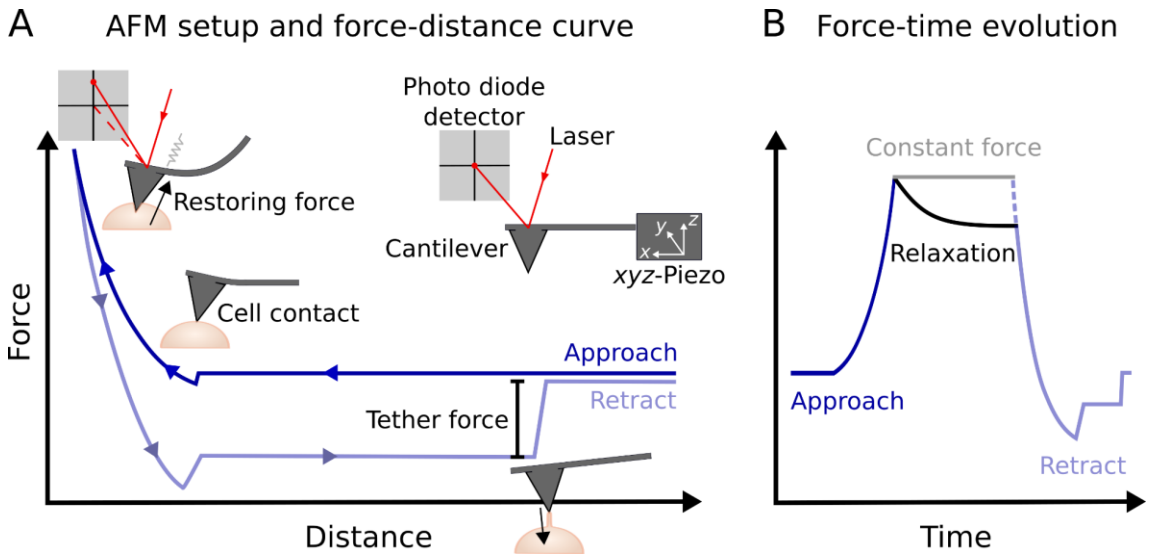

Figure 2.6: AFM setup and force-indentation cycle. A) Setup and a force-distance curve comprising characteristic events before and during contact. B) Indentation cycle from A against time, including a dwell time upon indentation at constant force (used in Chapter 3) and one at constant height with force relaxation of the cortex (as applied in the other Chapters). Figure adapted from Figure 3.1 in Chapter 3.

Force Spectroscopy

AFM-based force spectroscopy was performed in two ways. In Chapter 3, the cantilever was mainly used to apply a certain force as a mechanical stimulus to live cells. Here, the tip was lowered onto a cell until a constant restoring force was reached (Figure 2.6B). The force was kept constant for several minutes to allow the cell to actively adapt to the stimulus before the cantilever was retracted again. This stimulus was presented at different forces from 0.1 nN to 10 nN.

The second application is the more classical approach: The cantilever is indented into a cell to examine the force response, a certain height is shortly kept to monitor the force relaxation, and finally it is retracted and adhesion events are investigated (Figure 2.6). All three parts contain valuable information about the mechanical properties of the sample. When the cantilever has a bending stiffness on the order of the cell stiffness, which is a few kPa, both the lever and the cell deform upon indentation. The restoring force is non-linear and can be described by different models. The Hertz model is most commonly used but only assumes indentation of an infinite, isotropic, and fully elastic half space, which is not realistic for cells, as viscoelastic properties need to be considered. This is also reflected in the viscosity-induced force relaxation after indentation when the height is kept constant. Upon retraction, negative forces can be observed that result from adhesion events. Adhesion can stem from specific receptor-ligand binding or unspecific interaction. In the present experiments, membrane tethers were pulled based on broad-scale binding to the glycocalyx.

In this dissertation, the mechanics was described by the recently developed Evans model.[94] This viscoelastic model treats the apical cell cap as a liquid-filled composite shell of constant

volume, composed of plasma membrane and the attached actomyosin cortex underneath. The shell is considered as a thin, continuous and isotropic 2D material. Since the cortex is only 200-400 nm thin, bending stiffness as well as area shear modulus are neglected. Therefore, it resists deformation solely via its area compressibility modulus K_A, a measure of the ability to withstand lateral area change, and prestress T_0. Prestress mainly reflects the cortex network and contractility but also includes membrane tension. In contrast to earlier models, the area compressibility modulus is time-dependent and viscosity is considered. Viscoelasticity of K_A is assumed to follow a power law. Importantly for this thesis, the cell cap area and contact angle can be adjusted in this model.

Similar to the curvature of a fluid interface, the static equilibrium can be described by the Young-Laplace equation, $\Delta P/T = 2H$, with the pressure difference ΔP, tension T and mean curvature H. Upon indentation, the shell is deformed at constant volume, leading to minimal surfaces due to energy minimization. The restoring force F upon indentation with a conical indenter is given by:

$$F = 2\pi \left({R_1}^2 \left(\frac{R_1 \sin\phi + r_1 \sin\theta}{{R_1}^2 - {r_1}^2} \right) - R_1 \sin\phi \right) T(t) \tag{2.5}$$

with the radius R_1 of the spherical cell cap and the contact angle ϕ in response to deformation (Figure 2.7). r_1 is the contact radius with the indenter and $\theta = \pi/2 - \vartheta$ with the cone half angle ϑ. The cell geometries are adjusted depending on optical observation of the cells and corresponding AFM imaging data. Viscoelasticity is considered in the tension $T(t)$ via the time-dependent area compressibility modulus

$$K_A = {K_A}^0 (\frac{t}{t_0})^{-\beta}. \tag{2.6}$$

The power law exponent β gives the degree of fluidity and the energy dissipation during indentation.

Additionally, the membrane tension can be determined from AFM experiments by pulling membrane tethers during cantilever retraction.[15] A force plateau at the end of the retrace followed by a force jump indicates the formation and following rupture of a tether. From this tether force F_t, the apparent membrane tension T_t can be calculated:

$$T_t = \frac{F_t^2}{8\pi^2 \kappa} \tag{2.7}$$

with the bending modulus κ of 2.7 10^{-19} J, a typical value for fluid plasma membranes. Note, the apparent membrane tension is the sum of the in-plane tension of the membrane and the tension that arises from the attachment to the underlying cortex.

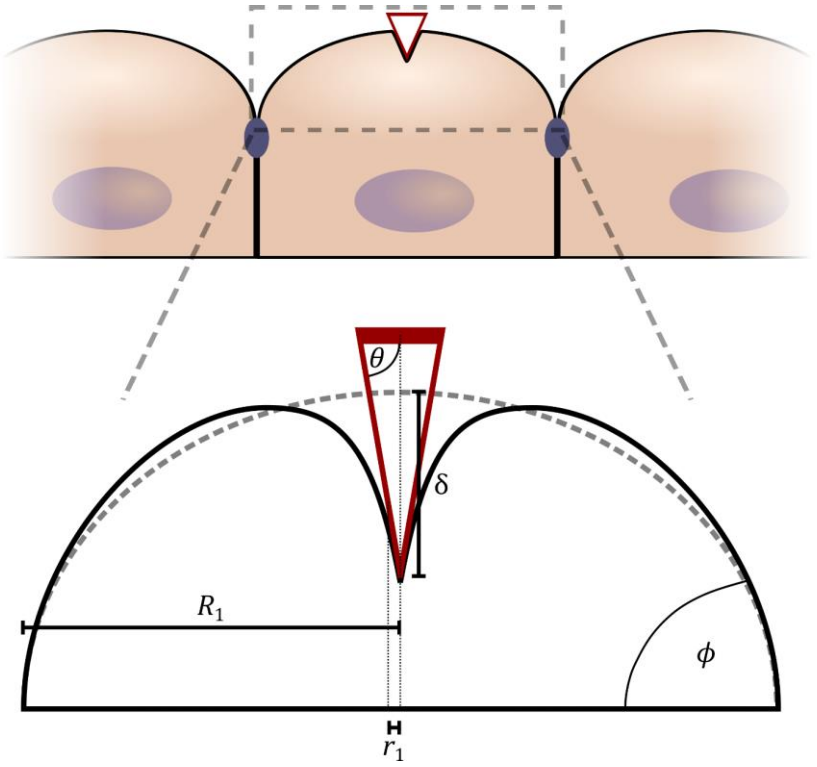

Figure 2.7: AFM force-indentation geometry. Upon indentation to a depth δ, the apical cap of individual cells in a layer is considered as a capped sphere. The base radius R_1 as well as the contact angle ϕ are adjusted depending on the geometries obtained from AFM imaging or confocal microscopy.

Cell-Cell Adhesion Measurements

AFM can also be used to measure the adhesion between two cells.[95] The experimental procedure for this is depicted in Figure 2.8.

A cell is attached to the cantilever (1.). This cell is then indented into another one which remains attached to the substrate. After indentation to a certain force, some time is allowed for the cells to establish adhesion bonds, e.g., through adherens or tight junction proteins (2.). Such bonds determine the force that pulls downwards on the cantilever during retraction (3.). The difference between the maximal negative force and the baseline can be used as a measure of the dynamic adhesion strength.

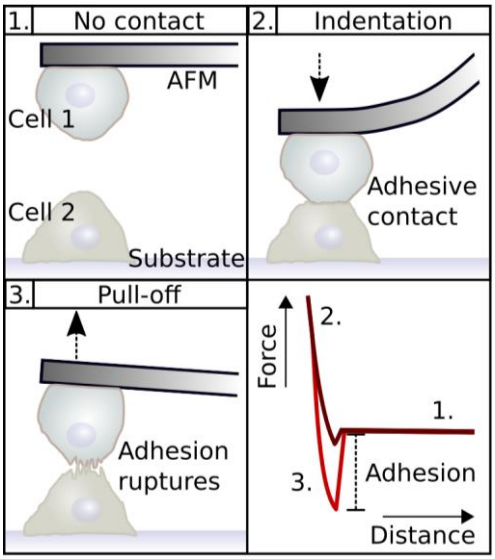

Figure 2.8: AFM-based cell-cell adhesion experiments. 1.) Before contact, a cell is attached to the cantilever while another cell remains on the substrate. 2.) Cells are brought into contact to reach a certain force, allowing the establishment of adhesive contact. 3.) Upon retraction, cells are pulled apart and the adhesion force is observed to act downwards on the cantilever. A schematic retraction force curve with low (dark red) and high adhesion (bright red) is shown in the lower right panel. Figure adapted from Figure 5.4 in Chapter 5.

2.2.5 Automated Cell Size, Geometry, and Motion Analysis Methods

Particle Image Velocimetry

A popular method to quantify local motion is particle image velocimetry (PIV), with openly available software optimized for migration assays with confluent cell sheets.[96] This technique is based on correlation analysis of consecutive frames of a video, e.g., from phase contrast microscopy. First, the original image is split into subwindows. Each subwindow is then cross-correlated with its counterpart from the next frame:

$$C(\vec{r}) = \langle I_t(\vec{R}) \times I_{t+\Delta t}(\vec{R} + \vec{r}) \rangle \tag{2.8}$$

with the function C correlating the subwindow I with position $\vec{R}$ at time point t and at t+Δt across the xy-space $\vec{r}$. The maximum of the cross-correlation gives the average displacement between the two time points. Normalizing by the time difference Δt between frames provides the velocity. This is iterated for all subwindows of the image and subsequently for all frames of a video, providing a velocity vector field and its evolution over time.

This vector field serves as the basis for further analyses. For instance, the spatial autocorrelation function AC gives information about the similarity of the vectors across the cell

layer, i.e., the degree to which the motion is coordinated. This function is the correlation of the vector field with itself:[97]

$$AC(\vec{r}, t) = \langle v(\vec{r}' + \vec{r}, t) \times v(\vec{r}', t) \rangle \tag{2.9}$$

with the velocity v at position $\vec{r}'$ and time t, iterated through space $\vec{r}$ by the distance between vectors. From this, a correlation length can be obtained as the integral over the weighted spatial correlation function:

$$\int_0^\infty \vec{r} \cdot AC(\vec{r})\, d\vec{r}. \tag{2.10}$$

The advantage that PIV gives mesoscopic, local dynamics that are independent of direct information about individual cells, is also a major limitation of this method. To overcome this and directly quantify the motion of single cells in a layer, tracking in combination with cell segmentation is used. Note that PIV and tracking yield comparable results.[53] However, the obtained information is highly complementary and was instrumental in Chapter 4.

Cell Segmentation, Tracking, and Neighbor Analysis

In this dissertation a particular task was to obtain information in an automated way about individual cells in a sheet, such as their size and geometric shape. In addition, the motion of each cell was tracked to enable direct correlation of all obtained parameters, answering questions in Chapter 4 such as: Is the motility of cells dependent on their size or shape? Or, are shape and size even interdependent parameters? Finally, in co-cultures of different cell types, this approach is the basis to automatically distinguish between them and to analyze their sorting behavior in Chapter 5.

Quite recently, several cell segmentation algorithms were newly developed.[98–101] More basic segmentation is often based on watershed, i.e., “filling up” the minima in an intensity image landscape. However, this approach is quite sensitive to local minima that frequently occur due to heterogenic cell structures. Therefore, in this thesis the deep learning-based, universal segmentation algorithm Cellpose was used.[98] With this, a segmented image is obtained which contains an outline and a mask for each cell as shown in Figure 2.9. Each pixel that was recognized to be part of a certain cell body or outline, respectively, is assigned the same index, while background pixels are zero.

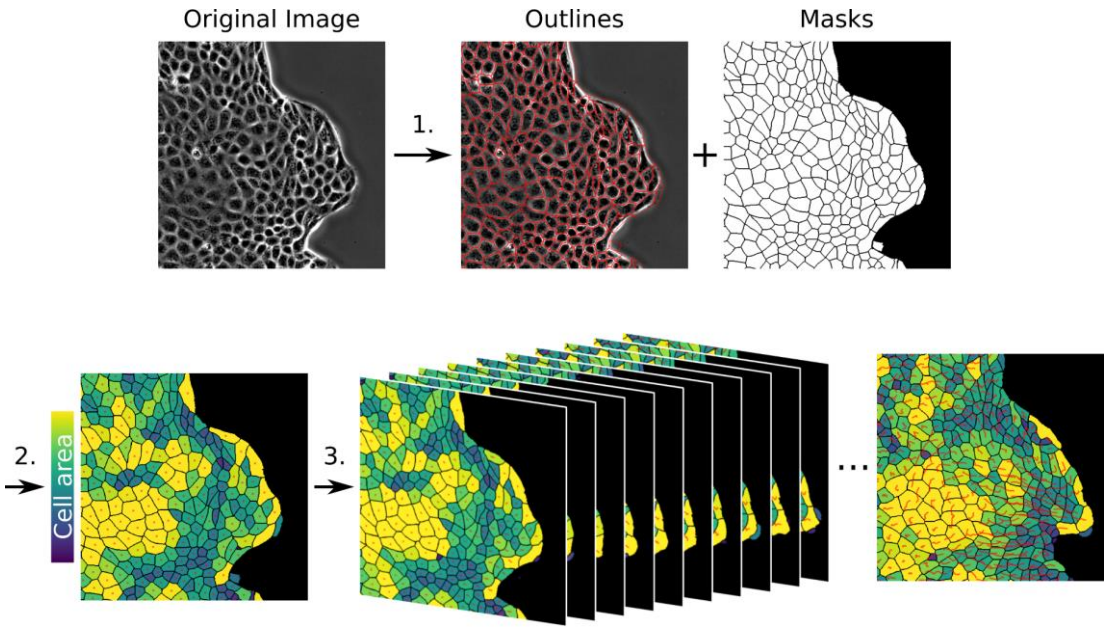

Figure 2.9: Automated cell segmentation and tracking. Phase contrast (or fluorescence, vide infra) images were first segmented using Cellpose (step 1), yielding an outline, shown as an overlay, and a mask for each cell in one image. Both contain the cell index as pixel values but are depicted here after binarization. In step 2, additional parameters, such as the projected area (color-coded), shape and position (red dots), are determined. Linking positions, i.e., tracking, is performed in step 3, yielding the final trajectories (red lines).

The projected area of a cell is the number of its pixels, normalized by a known conversion factor. This factor is calculated as the camera pixel size divided by the magnification of the microscope. The shape can be characterized as the lateral elongation or aspect ratio by dividing the length of the longest axis by the width. In this thesis, the aspect ratio was determined as the mean of two different approaches, an elliptical and a rectangular fit, to increase the robustness of the result. The position of each cell is determined as the center of its mask. Exemplary cell areas and positions are shown in Figure 2.9, step 2.

Once the positions are obtained, tracking is merely (but not easily) a matter of identifying the same cell from frame to frame, linking the positions (Figure 2.9, step 3). This is commonly done for Brownian particle diffusion but the same approach also works well for cells. Basically, a Gaussian probability distribution of the distance traveled around each position is assumed. The assignment of particle labels is then performed, so that the traveled distance maximizes the probability.[102] This essentially means that between two frames, the particles (cells) that are closest to each other are assigned the same index. Once the cells are properly assigned by tracking, velocity, persistence and other parameters can be calculated. The *x*- and *y*-velocity component is obtained for each cell as the discrete derivative of the *x*- and *y*-positions, respectively, divided by Δt. The Euclidean distance $\sqrt{\Delta x^2 + \Delta y^2}$ divided by Δt gives the absolute velocity. Additionally, the persistence parameter characterizes how directed a cell moves, with a value of 1 meaning direct,

straight-line movement. It is defined as the Euclidean distance between start- and end-position divided by the total distance traveled, i.e., the sum of all steps. Another trajectory analysis tool is the mean squared displacement *MSD* function. It is commonly used to examine Brownian diffusion, a concept that goes back to A. Einstein, but this approach can also be extended to cover active processes such as cell motion.[71,72,103] The *MSD* function

$$MSD(\tau) = \langle (x(t+\tau) - x(t))^2 \rangle \tag{2.11}$$

calculates the displacement between the position *x* of an object at time *t* and its position at $t + \tau$, iterating through all possible time differences τ. Brackets mark the averaging over time and all cells, giving the so-called ensemble *MSD*. For diffusion, the *MSD* scales linearly with τ as $MSD(\tau) = 2nD\tau$ depending on the dimensionality n and the diffusion constant D. In case diffusion is hindered or even accelerated, as in the case of active cells, this equation is modified: A power law $MSD(\tau) = a\,\tau^n$ is used with the exponent n and offset a. Similar to a diffusion coefficient, a characterizes the overall motion speed. The exponent distinguishes between passive diffusion-like motion at $n = 1$, hindered motion with $n < 1$, and active, directed motility at $n > 1$. Here, a maximum of $n = 2$ would indicate straight-line motion.

Having all geometry and motion parameters for each cell, another task was to distinguish between different cell types in a co-culture, and to calculate the degree to which the cell types mix. For this, only one cell type was fluorescently labeled and the fluorescence and phase contrast channels were compared. Essentially, the images of both channels are overlaid and subjected to a nearest neighbor analysis. Particularly, three main steps need to be performed. First, the phase contrast and fluorescence masks are compared: For each cell mask from phase contrast the pixel values at the same position in the fluorescence segmentation are examined. If the modal pixel value of the respective cell pixels in the fluorescence channel is zero (i.e., background) the cell is recognized as the unlabeled type. Otherwise, it is assigned as labeled. These cell type assignments were applied to the phase contrast channel, yielding a complete set of cells for each frame. Second, a nearest neighbor analysis recognizes the closest cells, for example, by applying a line scan between cell centers and evaluating the pixels it crosses. If only zeros and the two cell indices are crossed, the cells are considered to be direct neighbors. The result is typically noted in an adjacency matrix as one or zero. Finally, the sum in a column (or row, due to the symmetry of the matrix) corresponds to the number of neighbors of that particular cell. Filtering the columns/rows according to the cell type assignments before summation gives the number of homotypic or heterotypic neighbors.

To quantify the mixing degree by one parameter, a segregation index can be defined as the amount of homotypic divided by the amount of all neighbors.[104] Here, a value of 0.5 corresponds

to random mixing and larger values indicate segregation with homotypic neighbors clustering together. This method was central in Chapter 5.

2.3 REFERENCES

1. Purcell, E. M. Life at low Reynolds number. *Am. J. Phys.* **45**, 10 (1977).
2. Alberts, B., Johnson, A. & Lewis, J. *Molecular biology of the cell*. (Garland Publishing, 2008).
3. Pietuch, A., Brückner, B. R. & Janshoff, A. Membrane tension homeostasis of epithelial cells through surface area regulation in response to osmotic stress. *Biochim. Biophys. Acta BBA - Mol. Cell Res.* **1833**, 712–722 (2013).
4. Butor, C. & Davoust, J. Apical to basolateral surface area ratio and polarity of MDCK cells grown on different supports. *Exp. Cell Res.* **203**, 115–127 (1992).
5. Pietuch, A., Brückner, B. R., Fine, T., Mey, I. & Janshoff, A. Elastic properties of cells in the context of confluent cell monolayers: impact of tension and surface area regulation. *Soft Matter* **9**, 11490 (2013).
6. Cereijido, M. *et al.* New Diseases Derived or Associated with the Tight Junction. *Arch. Med. Res.* **38**, 465–478 (2007).
7. Dukes, J. D., Whitley, P. & Chalmers, A. D. The MDCK variety pack: choosing the right strain. *BMC Cell Biol.* **12**, 43 (2011).
8. Masters, J. R. HeLa cells 50 years on: the good, the bad and the ugly. *Nat. Rev. Cancer* **2**, 315–319 (2002).
9. Gey, G. Tissue culture studies of the proliferative capacity of cervical carcinoma and normal epithelium. *Cancer Res.* **12**, 264–265 (1952).
10. van Meer, G., Voelker, D. R. & Feigenson, G. W. Membrane lipids: where they are and how they behave. *Nat. Rev. Mol. Cell Biol.* **9**, 112–124 (2008).
11. Eggeling, C. *et al.* Direct observation of the nanoscale dynamics of membrane lipids in a living cell. *Nature* **457**, 1159–1162 (2009).
12. Honigmann, A. *et al.* Scanning STED-FCS reveals spatiotemporal heterogeneity of lipid interaction in the plasma membrane of living cells. *Nat. Commun.* **5**, 5412 (2014).
13. Morris, C. E. & Homann, U. Cell Surface Area Regulation and Membrane Tension. *J. Membr. Biol.* **179**, 79–102 (2001).
14. Fletcher, D. A. & Mullins, R. D. Cell mechanics and the cytoskeleton. *Nature* **463**, 485–492 (2010).
15. Sheetz, M. P. Cell control by membrane–cytoskeleton adhesion. *Nat. Rev. Mol. Cell Biol.* **2**, 392–396 (2001).
16. Goodson, H. V. & Jonasson, E. M. Microtubules and Microtubule-Associated Proteins. *Cold Spring Harb. Perspect. Biol.* **10**, a022608 (2018).
17. Block, J. *et al.* Nonlinear Loading-Rate-Dependent Force Response of Individual Vimentin Intermediate Filaments to Applied Strain. *Phys. Rev. Lett.* **118**, 048101 (2017).

18. Block, J., Schroeder, V., Pawelzyk, P., Willenbacher, N. & Köster, S. Physical properties of cytoplasmic intermediate filaments. *Biochim. Biophys. Acta BBA - Mol. Cell Res.* **1853**, 3053–3064 (2015).
19. Blanchoin, L., Boujemaa-Paterski, R., Sykes, C. & Plastino, J. Actin Dynamics, Architecture, and Mechanics in Cell Motility. *Physiol. Rev.* **94**, 235–263 (2014).
20. Carlsson, A. E. Actin Dynamics: From Nanoscale to Microscale. *Annu. Rev. Biophys.* **39**, 91–110 (2010).
21. Levayer, R. & Lecuit, T. Biomechanical regulation of contractility: spatial control and dynamics. *Trends Cell Biol.* **22**, 61–81 (2012).
22. Vicente-Manzanares, M., Ma, X., Adelstein, R. S. & Horwitz, A. R. Non-muscle myosin II takes centre stage in cell adhesion and migration. *Nat. Rev. Mol. Cell Biol.* **10**, 778–790 (2009).
23. Ladoux, B. & Mège, R.-M. Mechanobiology of collective cell behaviours. *Nat. Rev. Mol. Cell Biol.* **18**, 743–757 (2017).
24. Fritzsche, M., Erlenkämper, C., Moeendarbary, E., Charras, G. & Kruse, K. Actin kinetics shapes cortical network structure and mechanics. *Sci. Adv.* **2**, e1501337 (2016).
25. Salbreux, G., Charras, G. & Paluch, E. Actin cortex mechanics and cellular morphogenesis. *Trends Cell Biol.* **22**, 536–545 (2012).
26. Fritzsche, M., Lewalle, A., Duke, T., Kruse, K. & Charras, G. Analysis of turnover dynamics of the submembranous actin cortex. *Mol. Biol. Cell* **24**, 757–767 (2013).
27. Bovellan, M. *et al.* Cellular Control of Cortical Actin Nucleation. *Curr. Biol.* **24**, 1628–1635 (2014).
28. Tojkander, S., Gateva, G. & Lappalainen, P. Actin stress fibers - assembly, dynamics and biological roles. *J. Cell Sci.* **125**, 1855–1864 (2012).
29. Pellegrin, S. & Mellor, H. Actin stress fibres. *J. Cell Sci.* **120**, 3491–3499 (2007).
30. Parri, M. & Chiarugi, P. Rac and Rho GTPases in cancer cell motility control. *Cell Commun. Signal.* **8**, 23 (2010).
31. Chen, Y., Ju, L., Rushdi, M., Ge, C. & Zhu, C. Receptor-mediated cell mechanosensing. *Mol. Biol. Cell* **28**, 3134–3155 (2017).
32. Murthy, S. E., Dubin, A. E. & Patapoutian, A. Piezos thrive under pressure: mechanically activated ion channels in health and disease. *Nat. Rev. Mol. Cell Biol.* **18**, 771–783 (2017).
33. Gudipaty, S. A. *et al.* Mechanical stretch triggers rapid epithelial cell division through Piezo1. *Nature* **543**, 118–121 (2017).
34. Eisenhoffer, G. T. *et al.* Crowding induces live cell extrusion to maintain homeostatic cell numbers in epithelia. *Nature* **484**, 546–549 (2012).
35. Spadaro, D. *et al.* Tension-Dependent Stretching Activates ZO-1 to Control the Junctional Localization of Its Interactors. *Curr. Biol.* **27**, 3783-3795.e8 (2017).

36. Sun, Z., Costell, M. & Fässler, R. Integrin activation by talin, kindlin and mechanical forces. *Nat. Cell Biol.* **21**, 25–31 (2019).
37. Koirala, R. *et al.* Inside-out regulation of E-cadherin conformation and adhesion. *Proc. Natl. Acad. Sci.* **118**, e2104090118 (2021).
38. Buckley, C. D. *et al.* The minimal cadherin-catenin complex binds to actin filaments under force. *Science* **346**, 1254211 (2014).
39. Thomas, W. Catch Bonds in Adhesion. *Annu. Rev. Biomed. Eng.* **10**, 39–57 (2008).
40. Chang, Y.-C., Wu, J.-W., Wang, C.-W. & Jang, A. C.-C. Hippo Signaling-Mediated Mechanotransduction in Cell Movement and Cancer Metastasis. *Front. Mol. Biosci.* **6**, 157 (2020).
41. Engler, A. J., Sen, S., Sweeney, H. L. & Discher, D. E. Matrix Elasticity Directs Stem Cell Lineage Specification. *Cell* **126**, 677–689 (2006).
42. Godt, D. & Tepass, U. Drosophila oocyte localization is mediated by differential cadherin-based adhesion. *Nature* **395**, 387–391 (1998).
43. Harrison, O. J. *et al.* The Extracellular Architecture of Adherens Junctions Revealed by Crystal Structures of Type I Cadherins. *Structure* **19**, 244–256 (2011).
44. Strale, P.-O. *et al.* The formation of ordered nanoclusters controls cadherin anchoring to actin and cell–cell contact fluidity. *J. Cell Biol.* **210**, 333–346 (2015).
45. Wu, Y., Kanchanawong, P. & Zaidel-Bar, R. Actin-Delimited Adhesion-Independent Clustering of E-Cadherin Forms the Nanoscale Building Blocks of Adherens Junctions. *Dev. Cell* **32**, 139–154 (2015).
46. Yao, M. *et al.* Force-dependent conformational switch of α-catenin controls vinculin binding. *Nat. Commun.* **5**, 1–12 (2014).
47. Seddiki, R. *et al.* Force-dependent binding of vinculin to α-catenin regulates cell–cell contact stability and collective cell behavior. *Mol. Biol. Cell* **29**, 380–388 (2018).
48. Noethel, B. *et al.* Transition of responsive mechanosensitive elements from focal adhesions to adherens junctions on epithelial differentiation. *Mol. Biol. Cell* **29**, 2317–2325 (2018).
49. Borghi, N. *et al.* E-cadherin is under constitutive actomyosin-generated tension that is increased at cell–cell contacts upon externally applied stretch. *Proc. Natl. Acad. Sci.* **109**, 12568–12573 (2012).
50. Liu, Z. *et al.* Mechanical tugging force regulates the size of cell-cell junctions. *Proc. Natl. Acad. Sci.* **107**, 9944–9949 (2010).
51. Yonemura, S., Itoh, M., Nagafuchi, A. & Tsukita, S. Cell-to-cell adherens junction formation and actin filament organization: similarities and differences between non-polarized fibroblasts and polarized epithelial cells. *J. Cell Sci.* **108**, 127–142 (1995).
52. Gupta, S. & Yap, A. S. How adherens junctions move cells during collective migration. *Fac. Rev.* **10**, 56 (2021).

53. Bazellières, E. *et al.* Control of cell–cell forces and collective cell dynamics by the intercellular adhesome. *Nat. Cell Biol.* **17**, 409–420 (2015).
54. Vedula, S. R. K. *et al.* Quantifying Forces Mediated by Integral Tight Junction Proteins in Cell–Cell Adhesion. *Exp. Mech.* **49**, 3–9 (2009).
55. Martinez-Rico, C. *et al.* Separation Force Measurements Reveal Different Types of Modulation of E-cadherin-based Adhesion by Nectin-1 and -3. *J. Biol. Chem.* **280**, 4753–4760 (2005).
56. Fichtner, D. *et al.* Covalent and Density-Controlled Surface Immobilization of E-Cadherin for Adhesion Force Spectroscopy. *PLOS ONE* **9**, e93123 (2014).
57. Beutel, O., Maraspini, R., Pombo-García, K., Martin-Lemaitre, C. & Honigmann, A. Phase Separation of Zonula Occludens Proteins Drives Formation of Tight Junctions. *Cell* **179**, 923-936.e11 (2019).
58. Balda, M. S. & Matter, K. Tight junctions at a glance. *J. Cell Sci.* **121**, 3677–3682 (2008).
59. Citi, S. The mechanobiology of tight junctions. *Biophys. Rev.* (2019) doi:10.1007/s12551-019-00582-7.
60. Choi, W. *et al.* Remodeling the zonula adherens in response to tension and the role of afadin in this response. *J. Cell Biol.* **213**, 243–260 (2016).
61. Hatte, G., Prigent, C. & Tassan, J.-P. Tight junctions negatively regulate mechanical forces applied to adherens junctions in vertebrate epithelial tissue. *J. Cell Sci.* **131**, jcs208736 (2018).
62. Matsuzawa, K. *et al.* MAGIs regulate aPKC to enable balanced distribution of intercellular tension for epithelial sheet homeostasis. *Commun. Biol.* **4**, 1–11 (2021).
63. Fagotto, F. The cellular basis of tissue separation. *Development* **141**, 3303–3318 (2014).
64. Steinberg, M. S. Does differential adhesion govern self-assembly processes in histogenesis? Equilibrium configurations and the emergence of a hierarchy among populations of embryonic cells. *J. Exp. Zool.* **173**, 395–433 (1970).
65. Brodland, G. W. The Differential Interfacial Tension Hypothesis (DITH): A Comprehensive Theory for the Self-Rearrangement of Embryonic Cells and Tissues. *J. Biomech. Eng.* **124**, 188–197 (2002).
66. Harris, A. K. Is cell sorting caused by differences in the work of intercellular adhesion? A critique of the steinberg hypothesis. *J. Theor. Biol.* **61**, 267–285 (1976).
67. Dahmann, C., Oates, A. C. & Brand, M. Boundary formation and maintenance in tissue development. *Nat. Rev. Genet.* **12**, 43–55 (2011).
68. Landsberg, K. P. *et al.* Increased Cell Bond Tension Governs Cell Sorting at the Drosophila Anteroposterior Compartment Boundary. *Curr. Biol.* **19**, 1950–1955 (2009).
69. Sato, K. & Umetsu, D. A Novel Cell Vertex Model Formulation that Distinguishes the Strength of Contraction Forces and Adhesion at Cell Boundaries. *Front. Phys.* **9**, 406 (2021).

70. Alt, S., Ganguly, P. & Salbreux, G. Vertex models: from cell mechanics to tissue morphogenesis. *Philos. Trans. R. Soc. B Biol. Sci.* **372**, 20150520 (2017).
71. Bi, D., Yang, X., Marchetti, M. C. & Manning, M. L. Motility-Driven Glass and Jamming Transitions in Biological Tissues. *Phys. Rev. X* **6**, 021011 (2016).
72. Park, J.-A. *et al.* Unjamming and cell shape in the asthmatic airway epithelium. *Nat. Mater.* **14**, 1040–1048 (2015).
73. Kim, J. H. *et al.* Unjamming and collective migration in MCF10A breast cancer cell lines. *Biochem. Biophys. Res. Commun.* **521**, 706–715 (2020).
74. Ridley, A. J. *et al.* Cell Migration: Integrating Signals from Front to Back. *Science* **302**, 1704–1709 (2003).
75. Vicente-Manzanares, M., Webb, D. J. & Horwitz, A. R. Cell migration at a glance. *J. Cell Sci.* **118**, 4917–4919 (2005).
76. Vedula, S. R. K., Ravasio, A., Lim, C. T. & Ladoux, B. Collective Cell Migration: A Mechanistic Perspective. *Physiology* **28**, 370–379 (2013).
77. Trepat, X. & Fredberg, J. J. Plithotaxis and emergent dynamics in collective cellular migration. *Trends Cell Biol.* **21**, 638–646 (2011).
78. Reffay, M. *et al.* Interplay of RhoA and mechanical forces in collective cell migration driven by leader cells. *Nat. Cell Biol.* **16**, 217–223 (2014).
79. Trepat, X. *et al.* Physical forces during collective cell migration. *Nat. Phys.* **5**, 426–430 (2009).
80. Vishwakarma, M. *et al.* Mechanical interactions among followers determine the emergence of leaders in migrating epithelial cell collectives. *Nat. Commun.* **9**, 3469 (2018).
81. Tambe, D. T. *et al.* Collective cell guidance by cooperative intercellular forces. *Nat. Mater.* **10**, 469–475 (2011).
82. Serra-Picamal, X. *et al.* Mechanical waves during tissue expansion. *Nat. Phys.* **8**, 628–634 (2012).
83. Karsch, S., Kong, D., Großhans, J. & Janshoff, A. Single-Cell Defects Cause a Long-Range Mechanical Response in a Confluent Epithelial Cell Layer. *Biophys. J.* **113**, 2601–2608 (2017).
84. Zernike, F. & Stratton, F. J. M. Diffraction Theory of the Knife-Edge Test and its Improved Form, The Phase-Contrast Method. *Mon. Not. R. Astron. Soc.* **94**, 377–384 (1934).
85. Lichtman, J. W. & Conchello, J.-A. Fluorescence microscopy. *Nat. Methods* **2**, 910–919 (2005).
86. Nwaneshiudu, A. *et al.* Introduction to confocal microscopy. *J. Invest. Dermatol.* **132**, 1–5 (2012).

87. Fritzsche, M. & Charras, G. Dissecting protein reaction dynamics in living cells by fluorescence recovery after photobleaching. *Nat. Protoc.* **10**, 660–680 (2015).
88. Sprague, B. L., Pego, R. L., Stavreva, D. A. & McNally, J. G. Analysis of Binding Reactions by Fluorescence Recovery after Photobleaching. *Biophys. J.* **86**, 3473–3495 (2004).
89. Bulinski, J. C., Odde, D. J., Howell, B. J., Salmon, T. D. & Waterman-Storer, C. M. Rapid dynamics of the microtubule binding of ensconsin in vivo. *J. Cell Sci.* **114**, 3885–3897 (2001).
90. Roca-Cusachs, P., Conte, V. & Trepat, X. Quantifying forces in cell biology. *Nat. Cell Biol.* **19**, 742–751 (2017).
91. Liang, X., Michael, M. & Gomez, G. A. Measurement of Mechanical Tension at Cell-cell Junctions Using Two-photon Laser Ablation. *Bio-Protoc.* **6**, e2068 (2016).
92. Umetsu, D. *et al.* Local Increases in Mechanical Tension Shape Compartment Boundaries by Biasing Cell Intercalations. *Curr. Biol.* **24**, 1798–1805 (2014).
93. Hutter, J. L. & Bechhoefer, J. Calibration of atomic-force microscope tips. *Rev. Sci. Instrum.* **64**, 1868–1873 (1993).
94. Cordes, A. *et al.* Prestress and Area Compressibility of Actin Cortices Determine the Viscoelastic Response of Living Cells. *Phys. Rev. Lett.* **125**, 068101 (2020).
95. Puech, P.-H., Poole, K., Knebel, D. & Muller, D. J. A new technical approach to quantify cell–cell adhesion forces by AFM. *Ultramicroscopy* **106**, 637–644 (2006).
96. Deforet, M. *et al.* Automated velocity mapping of migrating cell populations (AVeMap). *Nat. Methods* **9**, 1081–1083 (2012).
97. Petitjean, L. *et al.* Velocity Fields in a Collectively Migrating Epithelium. *Biophys. J.* **98**, 1790–1800 (2010).
98. Stringer, C., Wang, T., Michaelos, M. & Pachitariu, M. Cellpose: a generalist algorithm for cellular segmentation. *Nat. Methods* 1–7 (2020) doi:10.1038/s41592-020-01018-x.
99. Javer, A., Rittscher, J. & Sailem, H. Z. DeepScratch: Single-cell based topological metrics of scratch wound assays. *Comput. Struct. Biotechnol. J.* **18**, 2501–2509 (2020).
100. Edlund, C. *et al.* LIVECell—A large-scale dataset for label-free live cell segmentation. *Nat. Methods* **18**, 1038–1045 (2021).
101. Greenwald, N. F. *et al.* Whole-cell segmentation of tissue images with human-level performance using large-scale data annotation and deep learning. *Nat. Biotechnol.* 1–11 (2021) doi:10.1038/s41587-021-01094-0.
102. Crocker, J. C. & Grier, D. G. Methods of Digital Video Microscopy for Colloidal Studies. *J. Colloid Interface Sci.* **179**, 298–310 (1996).
103. Saraswathibhatla, A. & Notbohm, J. Tractions and Stress Fibers Control Cell Shape and Rearrangements in Collective Cell Migration. *Phys. Rev. X* **10**, 011016 (2020).

104. Balasubramaniam, L. *et al.* Investigating the nature of active forces in tissues reveals how contractile cells can form extensile monolayers. *Nat. Mater.* 1–11 (2021) doi:10.1038/s41563-021-00919-2.

Chapter 3

Simultaneous Quantification of the Interplay Between Molecular Turnover and Cell Mechanics by AFM–FRAP

by Mark Skamrahl[a,b], Huw Colin-York[a], Liliana Barbieri[a], and Marco Fritzsche[a,c].

[a] University of Oxford, MRC Human Immunology Unit, Weatherall Institute of Molecular Medicine, Headley Way, Oxford, OX3 9DS, United Kingdom.

[b] University of Göttingen, Institute of Physical Chemistry, Tammannstr. 6, 37077 Göttingen, Germany.

[c] Kennedy Institute for Rheumatology, University of Oxford, Roosevelt Drive, Oxford, OX3 7LF, United Kingdom.

This Chapter was published in *Small*, Volume 15, Issue 40, Article Number 1902202, October 2019.
DOI: https://doi.org/10.1002/smll.201902202
Available under CC BY 4.0 open access license. Figure 3.3 (taken from the table of contents of *Small*) was added and the corresponding second paragraph of the discussion was adapted. Otherwise only minute and formatting-related changes were applied.

Author Contributions

The project was initiated and preliminary ideas were generated during my master's Erasmus internship. The genetically modified cells were generated before this project started. M.F. designed and supervised the research. I planned and executed the experiments and analyses. H.CY. and L.B. performed the bleaching calibration in polyacrylamide gels and helped with discussions. M.F. and I wrote the manuscript.

ABSTRACT

Quantifying the adaptive mechanical behavior of living cells is essential for the understanding of their inner working and function. Yet, despite the establishment of quantitative methodologies correlating independent measurements of cell mechanics and its underlying molecular kinetics, explicit evidence and knowledge of the sensitivity of the feedback mechanisms of cells controlling their adaptive mechanics behavior remain elusive. Here, we introduce a combination of atomic force microscopy and fluorescence recovery after photobleaching offering simultaneous quantification and direct correlation of molecule kinetics and mechanics in living cells. Systematic application of this optomechanical AFM-FRAP platform revealed changes in the actin turnover and filament lengths of ventral actin stress fibers in response to constant mechanical force at the apical actin cortex with a dynamic range from 0.1 nN to 10 nN, highlighting a direct relationship of active mechanosensation and adaptation of the cellular actin cytoskeleton. Simultaneous quantification of the relationship between molecule kinetics and cell mechanics may thus open-up unprecedented insights into adaptive mechanobiological mechanisms of cells.

3.1 INTRODUCTION

Living cells are biomechanical entities. Recent research indicates that they regulate their cell mechanics not exclusively downstream of signaling events triggered by for instance ligand–receptor binding, but that they employ a diversity of feedback mechanisms to dynamically adjust their mechanics in response to extrinsic conditions.[1–5] This remarkable attribute of cells to modulate their mechanics involve biochemical processes between a range of proteins, subcellular structures, and organelles, but is primarily related to the dynamic nature of their actin cytoskeleton.[5–9] Despite the significance for cell function,[10,11] our understanding of the interplay of cell mechanics and its underlying actin kinetics controlling the adaptive mechanical behavior of cells remains at best correlative from independent measurements.

Fluorescence recovery after photobleaching (FRAP) is perhaps the most successful quantification methodology of molecule kinetics and dynamics, owing to its versatility to measure reaction and diffusion dynamics at the right spatiotemporal scales.[12–14] In a typical FRAP experiment, a small region of interest (ROI) is bleached by a short exposure to high-power laser light, and subsequently the recovery of fluorescently-tagged molecules is monitored over time.[15-18] The shape of the FRAP recovery curve, the so-called mobile fraction, reflects all of the complexity of the reaction diffusion dynamics of the molecule of interest. Using a theoretical model or numerical simulations for the analysis of the molecular actions combined with knowledge of the recovery time(s) of the respective molecule, the reaction kinetics and diffusion dynamics can be calculated and interpreted.[19–21] Analysis of the experiments reveals whether a molecule undergoes reaction kinetics or diffusion dynamics or a combination of both

processes.[13,22] The presence of a substantial immobile fraction may be the result of the loss of fluorescence due to imaging as experienced by the fluorescent molecules during image acquisition, or it may signify that recovery has been followed over a duration that is short in comparison with the molecule's actual recovery time.[13] To this end, FRAP has been employed to identify and quantify the different types of filamentous actin (F-actin), their turnover dynamics, and lengths in the actin cortex, lamellipodium, and stress fibers.[22–26]

Atomic force microscopy (AFM) is the most broadly-used quantification methodology of cell mechanics. AFM allows the precise quantification and application of mechanical forces on the apical cell surface with piconewton resolution.[27–31] For the application of mechanical force over a micro-scaled subregion of a cell, the cantilever tip is typically functionalized with a micron-sized fluorescent bead, and then exerted against the apical cell surface. Using AFM electronic feedback loops allows the recording of nanoscale force indentations of the cell surface as a function of the applied constant mechanical force. For example, this type of approach has been applied to investigate the biological behavior and function of living cells in response to external mechanical force.[32,33]

Hence, efforts to understand the adaptive mechanical behavior of cells separately quantified cell mechanics by AFM and molecule dynamics by FRAP, and thus inferred a relationship through correlation upon different experimental conditions, precluding knowledge of the exact nature of cell mechanosensation and its feedback. Most attempts to understand the relationship between actin and cell mechanics, employed methodologies to study independently either the actin-assembly-pathways[34–36] (via classic cell-biological methods to identify a set of responsible pathways and proteins) or cellular mechanics[2,37,38] (via mechanical tools to measure mechanical properties and forces), allowing correlative predictions for example about the interwoven relationship of actin kinetics, respective F-actin lengths, and cellular mechanics.[38–41] However, in-depth understanding of the feedback mechanisms of the adaptive mechanical behavior of living cells profoundly necessitates simultaneous recordings and thus time-dependent correlation of actin kinetics and cell mechanics, which separate measurements do not allow due to the lack of temporally synchronized information. Such synchronous measurements also allow the quantification of the mechanical response time, the dynamic range of mechanical forces to which adaptation is possible, and mechanical propagation length scale at which living cells can sense and respond to external mechanical force.

Here, to overcome these challenges, we developed and applied an optomechanical platform combining AFM and FRAP, which offered the quantification of the adaptive mechanical behavior of living cells by simultaneous measurements of cell mechanics and the underlying actin kinetics. We found that cervical HeLa cells dynamically adjusted up to 2-fold the stress fiber F-actin turnover rates and nanoscale filament lengths within a dynamic range of 0.1 nN to 10 nN in response to constant mechanical force at the apical actin cortex applied through contact with a radius r = 5 μm bead connected to the AFM cantilever. Strikingly, the apical mechanical stress was

detected by the cells at their ventral interface resulting in adaptation of the nanoscale organization of F-actin stress fibers qualitatively comparable to those in the actin cortex, highlighting a mechanical propagation length scale equivalent of the entire cell volume. Consequently, such simultaneous experiments may thus become the methodology of choice to reveal the mechanobiological mechanisms underlying mechanoadaptation.

3.2 RESULTS

To quantify the effects of mechanoadaptation of the actin cytoskeleton in living cells, we combined simultaneous AFM and FRAP experiments (Figure 3.1a). This optomechanical AFM-FRAP platform consisted of a JPK AFM, Leica DMI8, and Rapp OptoElectronic FRAP modules (see methods, Chapter 3.4). The AFM module allowed the application of constant mechanical force by contact with a bead-functionalized AFM cantilever at the apical surface and proximity of the central cell plane away from the cell nucleus. Simultaneously, the FRAP module enabled measurements of the turnover dynamics of cellular structures directly underneath the cell surface-bead contact or any location within the cell volume.

To calibrate the AFM-FRAP experiments, we first optimized the FRAP protocol. To this end, we determined the diffraction-limited point spread function (PSF) of the FRAP laser (Figure 3.1b) and measured the volume of a FRAP photobleaching event in a region of interest (ROI) at two different axial locations within a 15-20 µm thick EGFP-functionalized polyacrylamide gel. We achieved laterally the best well-defined reduction in fluorescence of a 2 µm diameter-sized ROI with 50% laser power when adjusting between 25%-100% total laser power at both the glass-hydrogel interface and 4 µm deep into the fluorescent gel (Figure 3.1c), representing the ventral and central plane of HeLa cells, respectively.

To ensure that the laser settings of the FRAP photobleaching event were compatible with and not harmful to F-actin structures in cells, we next performed FRAP experiments on ventral actin stress fibers in fixed HeLa cells fluorescently labeled with the photostable dye phalloidin-Alexa488, which was kept present in the imaging medium of the fixed cells and thus allowed phalloidin turnover measurements. Notably, extended laser power of the photobleaching event could yield permanent damage to the F-actin architecture in addition to photobleaching the fluorescent dye. Consistent with our EGFP hydrogel calibration, we achieved a well-defined 2 µm-sized ROI, sufficient fluorescence reduction, and mobile fluorescence recovery. The recovery appeared continuous throughout the ROI volume with no indication of directed fluorescence growth from the geometric sides of the actin stress fibers as it could be expected from damaged and regrowing actin stress fibers (Figure 3.1d). Note, the FRAP calibration experiments were terminated after 600 s in the fixed cells because of sample drift, and partial 80% fluorescence mobile recovery of phalloidin was sufficient for the evaluation of the direction of fluorescence increase considering 10% loss of fluorescence due to photobleaching and immobile fraction.

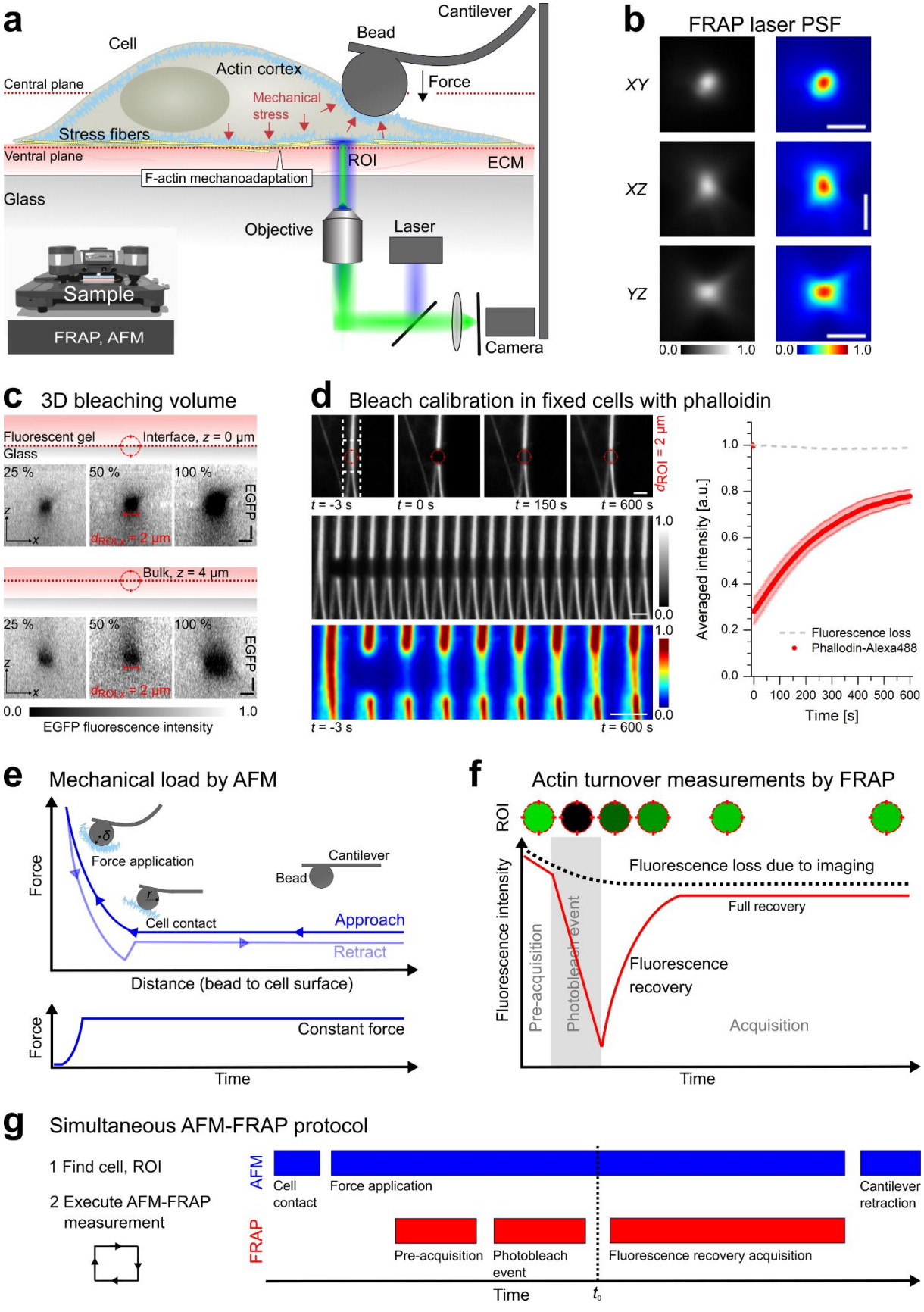

Figure 3.1: Establishment and calibration of the optomechanical AFM-FRAP platform. a) Schematic of the AFM-FRAP setup illustrating the experimental power of

simultaneous quantification of molecule kinetics and cell mechanics. b) Representative images of the diffraction-limited FRAP PSF in *xy*, *xz*, and *yz* orientation. Scale bars are 2 µm (*xy*) and 4 µm (*xz* and *yz*). c) Calibration of the FRAP ROI at both the glass-hydrogel interface and 4 µm deep into the fluorescent gel within a 15-20 µm thick EGFP-functionalized polyacrylamide gel for different laser powers. Scale bars are 2 µm (in *x*-direction) and 4 µm (in *y*-direction). d) Evaluation of FRAP photobleaching events on ventral actin stress fibers in fixed HeLa cells fluorescently labeled with phalloidin-Alexa488. Kymographs illustrate fluorescence recovery in the ROI (red). Scale bars: 2 µm. e,f) AFM and FRAP protocols for the application of mechanical force and measurements of the turnover kinetics in living HeLa cells. g) Workflow of a typical AFM-FRAP experiment.

Having optimized the FRAP protocol, we next established an experimental protocol for a full typical AFM-FRAP experiment (Figure 3.1e-g). We approached the cell with the bead-cantilever until initial contact (Figure 3.1e), then indented the cell surface by gradually further decreasing the distance and increasing the force until the maximal pre-defined force was reached, which was then maintained constant over the time of the AFM-FRAP experiment. Once constant force was established, we waited for 2 min post initial contact to equilibrate the bead-cantilever cell surface interaction, and subsequently executed the previous FRAP protocol simultaneously to the force application by AFM (Figure 3.1f), allowing turnover measurements under constant mechanical force. Finally, the cantilever would be retracted once full FRAP recovery was completed and the AFM-FRAP protocol was repeated in a different HeLa cell for statistical robustness (Figure 3.1g).

To gain a quantitative understanding of the length scale and sensitivity of mechanoadaptation in living cells, we first set out to characterize the actin cytoskeleton in control conditions in the absence of mechanical force. Because we reasoned to perform the AFM-FRAP experiment at a ROI representative for the global mechanical stiffness, we acquired a stiffness spectroscopy map of a HeLa cell applying the cantilever functionalized with a radius r = 5 µm bead (Figure 3.2a,b). We primarily aimed at quantifying the turnover dynamics in actin stress fibers and cortex without any contributions from the cytoplasmic actin network or cellular organelles such as the nucleus while applying a global mechanical stimulus. Hence, spectroscopic evaluation suggested a representative ROI location at the extended HeLa cell body away from the cell nucleus. (Figure 3.2b). We also avoided the cell edge to mitigate effects of the underlying stiffer glass and to probe a mechanically representative area, resulting in an optimal position in between the nucleus and the cell boundary (Figure 3.2b).

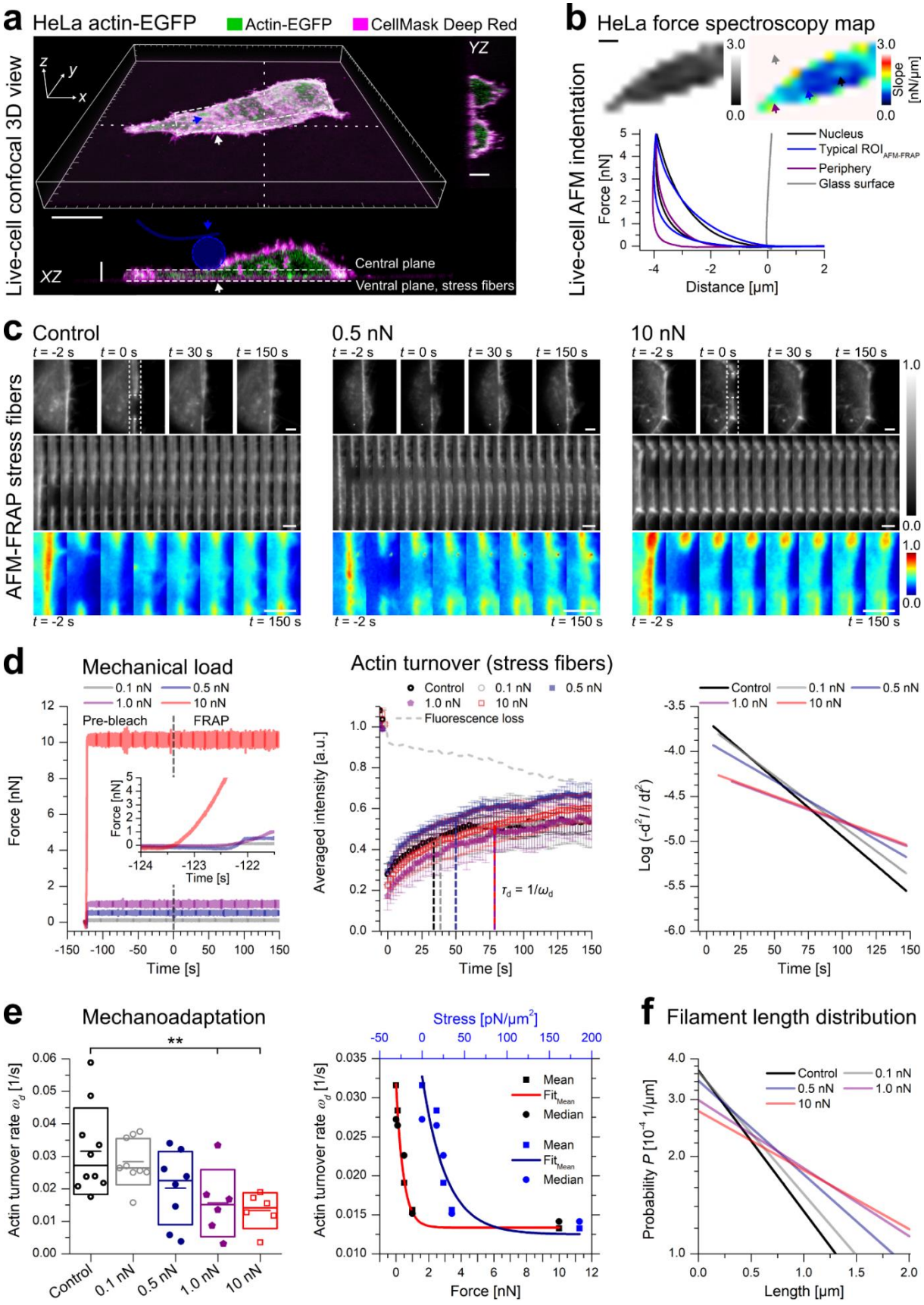

Figure 3.2: Application of AFM-FRAP experiments in ventral actin stress fibers.
a) Representative experimental AFM-FRAP live-cell setup showing the application of

mechanical force to the central plane at the apical surface of HeLa cells with a bead-functionalized cantilever (indicated in blue, blue arrow). Simultaneous FRAP experiments were acquired in ventral actin stress fibers (white arrow head). Scale bars are 10 µm (*x*/*y*-plane) and 4 µm (*z*-plane in horizontal views). b) Spectroscopic validation of the stiffness distribution and corresponding force-distance curves for a typical HeLa cell. Scale bar is 10 µm. c,d) AFM-FRAP experiments illustrated in kymographs, force-time plots, and FRAP recovery curves, and their corresponding Logarithmic acceleration plots showing the mechanoadaptation of ventral actin stress fibers in control conditions and in response to external mechanical force ranging from 0.1 nN to 10 nN. Scale bars are 2 µm. Corresponding mean and median turnover rates are presented in Table 3.1. e) Boxplot displaying the quantification of actin turnover kinetics in ventral actin stress fibers in control conditions and in response to external mechanical force ranging from 0.1 nN to 10 nN and turnover rate as a function of force and corresponding mechanical stress. Error bars show medians and standard deviations while means are indicated by a horizontal line inside the boxes. f) Quantification of the filament length distribution in control conditions and in response to external mechanical force ranging from 0.1 nN to 10 nN. Corresponding mean filament lengths are presented in Table 3.2. Two stars indicate a significance of $p < 0.01$.

Applying FRAP at the central actin cortex in live HeLa cells expressing fluorescently labeled actin-EGFP, we found two processes contributing to fluorescence recovery. Analysis of the FRAP experiments revealed an average turnover rate of $\omega_{\text{cortex, ARP2/3, Ctrl}} = 0.55 \pm 0.12$ (mean ± s.d.) 1/s for the ARP2/3-mediated F-actin and $\omega_{\text{cortex, formin, Ctrl}} = 0.040 \pm 0.009$ (mean ± s.d.) 1/s for the formin-mediated F-actin in control conditions consistent with our previous measurements (see methods, Chapter 3.4),[22,23] which were dominating fluorescence recovery on short time scales and long time scales, respectively. In contrast to cortical F-actin, actin stress fibers have been shown to be constituted by primarily formin-mediated F-actin. Consistent with this expectation, our FRAP experiments on ventral stress fibers displayed only one turnover process contributing to fluorescence recovery. Analysis of the FRAP experiments yielded one turnover rate $\omega_{\text{stress fibers, formin, Ctrl}} = 0.032 \pm 0.013$ (mean ± s.d.) 1/s statistically comparable to cortical formin-mediated turnover ($p = 0.22$ compared with second turnover kinetics in actin cortex), as reported by a full fluorescence recovery shown in kymographs, FRAP curves, and respective LogPlot functions (Figure 3.2c,d). Note, the LogPlot functions are logarithmic second order derivatives of the fluorescence recovery visualizing the number of turnover processes and relative abundance as described earlier.[13] The turnover dynamics for the corresponding cortical and stress fiber F-actins were identified previously in these HeLa cells.[22]

Having determined the turnover kinetics in live HeLa cells under control conditions, we next quantified these processes under mechanical force. Executing the full AFM-FRAP protocol at the ventral stress fibers in live HeLa cells in the presence of 1 nN constant mechanical force applied by the bead-cantilever at the central actin cortex revealed a statistically significant 2-fold change in the kinetics of the turnover rates of the F-actin structures from $\omega_{\text{stress fibers, formin, Ctrl}} = 0.032 \pm 0.013$ (mean ± s.d.) 1/s to $\omega_{\text{stress fibers, formin, 1 nN}} = 0.016 \pm 0.010$

(mean ± s.d.) 1/s ($p < 0.01$, Table 3.1 and Figure 3.2c,d), suggesting modulation of ventral actin turnover in stress fibers in response to apical mechanical force at the actin cortex.

To explore the sensitivity of such mechanoadaptation, we systematically measured the changes in the turnover kinetics in response to mechanical force ranging between 0.1 nN and 10 nN. Strikingly, we found that the mean and median turnover kinetics exponentially scaled as a function of the externally applied mechanical force and stress (Figure 3.2e) with the strongest response at the mean characteristic value of the exponential function at 1 nN and 35 pN/μm^2 (Figure 3.2e and Table 3.1), respectively, which corresponded to an apical indentation depth of 2 μm deflecting the cortical actin. Consistent with the exponential dependence, non-statistically different adjustments of turnover kinetics were detected at 0.1 nN ($\omega_{\text{stress fibers, formin, 0.1 nN}} = 0.028 \pm 0.007$ (mean ± s.d.) 1/s, $p = 0.84$) and 0.5 nN ($\omega_{\text{stress fibers, formin, 0.5 nN}} = 0.020 \pm 0.011$ (mean ± s.d.) 1/s, $p = 0.17$) but significant differences were found at 1 nN and 10 nN with $\omega_{\text{stress fibers, formin, 1 nN}} = 0.016 \pm 0.010$ (mean ± s.d.) 1/s, $p < 0.01$, which corresponded to a 0.4 μm (0.1 nN), a 1.4 μm (0.5 nN) and 2.0 μm (1 nN) indentation of apical cortical F-actin (Figure 3.2a,b). Together, the simultaneous AFM-FRAP revealed direct modulation of the F-actin kinetics in ventral stress fibers in response to apical mechanical force.

Table 3.1: Summary of FRAP fitting parameters in living HeLa cells. Single-component fitting of FRAP recovery curves revealed the turnover kinetics of the ventral actin stress fibers (mean ± s.d.). Fitting parameters of the turnover rate of F-actins in stress fibers is given by $\omega_{\textit{stress fibers, formin}}$. Two stars (**) indicate a significance level of $p < 0.01$.

Condition	Control	0.1 nN	0.5 nN	1.0 nN	10 nN
$\boldsymbol{\omega}_{\textbf{stress fibers, formin}}$ [1/s]	0.032 ± 0.013	0.028 ± 0.007	0.020 ± 0.011	0.016 ± 0.010	0.013 ± 0.005
p (compared with control)	-	$p = 0.84$	$p = 0.17$	$p < 0.01$**	$p < 0.01$**

Finally, we computed the filament length distributions and their mean filament lengths of the formin-mediated F-actin in the stress fibers from the FRAP quantification (see methods, Chapter 3.4). We found statistically significant differences with the nanoscale architecture adjusting a maximum of 2-fold $\langle L \rangle_{\text{stress fibers, formin, 1 nN}} = 2.1 \pm 0.9$ (mean ± s.d.) μm compared with control conditions $\langle L \rangle_{\text{stress fibers, formin, Ctrl}} = 1.0 \pm 0.45$ (mean ± s.d.) μm ($p < 0.01$, Table 3.2 and Figure 3.2f). For lower external forces, we found no or minor changes in the filament lengths of F-actins of $\langle L \rangle_{\text{stress fibers, formin, 0.1 nN}} = 1.15 \pm 0.5$ (mean ± s.d.) μm, $\langle L \rangle_{\text{stress fibers, formin, 0.5 nN}} = 1.5 \pm 0.75$ (mean ± s.d.) μm compared with control conditions ($p = 0.84$ for 0.1 nN and $p = 0.17$ for 0.5 nN).

No further statistical differences in the F-actin filament lengths were observed in response to 10 nN of external force $\langle L \rangle_{\text{stress fibers, formin, 10 nN}} = 2.4 \pm 1.2$ (mean ± s.d.) µm compared with 1 nN ($p = 0.94$, Table 3.2). These measurements highlighted nanoscale F-actin length remodeling of ventral stress fibers in direct response to apical mechanical stress.

Table 3.2: Summary of the filament lengths of ventral actin stress fibers in living HeLa cells. Computation of the mean filament length $\langle L \rangle$ (± s.d.) of formin-mediated F-actin in ventral actin stress fibers.

Condition	Control	0.1 nN	0.5 nN	1.0 nN	10 nN
$\langle L \rangle$ [µm]	1.0 ± 0.45	1.15 ± 0.5	1.5 ± 0.75	2.1 ± 0.9	2.4 ± 1.2

3.3 DISCUSSION

We introduced an optomechanical platform combining AFM and FRAP experiments offering simultaneous quantification and direct correlation of molecular kinetics and mechanics in living cells. We chose to quantify the effects of mechanoadaptation and their dynamic range by measuring the changes in the nanoscale turnover kinetics and filament lengths of F-actins under constant mechanical force in the ideal model system of ventral stress fibers, because they were predicted and experimentally-proven to function as mechanotransducers.[8,42,43] To this end, mechanoadaptation of the previously identified formin-mediated F-actins constituting stress fibers as well as ARP2/3- and formin-mediated F-actins in the cortical network were characterized.[22,23]

Together, our experimental and computational AFM-FRAP results paint the following picture of cytoskeletal mechanoadaptation (Figure 3.3). For actin filaments in ventral stress fibers, we measured a maximum of 2-fold change in the mean and median turnover kinetics and filament lengths at constant 1 nN force and 35 pN/µm² apical stress application, which corresponded to an indentation depth of 2 µm into the cortex. Interestingly, minor modulation of the turnover kinetics was detected in response to shallow indentation depths comparable to the thickness of the actin cortex. Similarly, F-actin turnover and lengths displayed effectively no further adjustment to critically high indentation of apical cortical F-actin comparable to over half of the height of a HeLa cell. Essentially, the actin turnover rate was modulated upon external force in an exponential fashion, with fast turnover and short filaments at small or no forces and slow turnover and longer filaments at large forces (Figure 3.3**,** bottom).

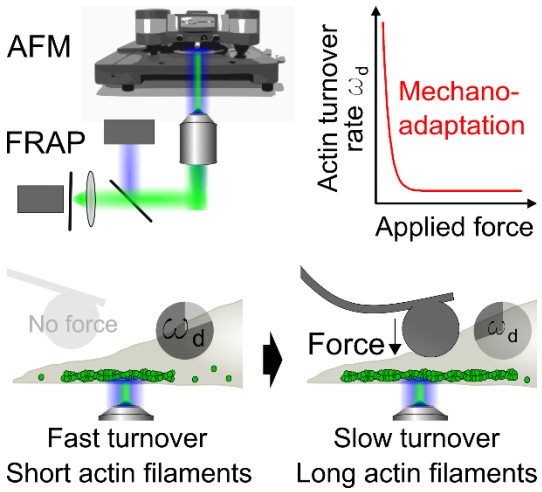

Figure 3.3: Overview of the AFM-FRAP platform and the results on actin stress fibers. AFM and FRAP were combined in a simultaneous fashion. Applying this platform revealed an adaptation of the actin turnover rate to external force in an exponential fashion. Accordingly, without (or upon small) force stimuli turnover is predominantly fast and filaments are short. Upon sufficient force, turnover is slowed down, yielding longer filaments. Figure taken from the journal's table of contents (vol. 15, issue 40).

On the basis of our work, we conclude that the simultaneous measurements and direct correlation of cell mechanics and its underlying actin kinetics is superior to independent quantification, because of the feedback mechanisms of the adaptive mechanical behavior of living cells and the additional accessible parameters such as mechanical response time, the mechanical propagation length scale, and the ability to determine the dynamic range of mechanoadaptation. We empirically found that the dynamic range of mechanoadaptation of the actin cytoskeleton is most effective at a length scale of 2 μm indentation allowing modulation of turnover kinetics and filament lengths on the length scale of the complete cytoplasm, possibly throughout all mechanically interlinked actin structures as a function of the externally applied stress as predicted by earlier studies.[44,45]

One might speculate that the dynamic range of mechanoadaptation is most effective at a length scale of a formin-mediated actin filament, which corresponded to ∼2 μm equivalent to the indentation depth at 1 nN, because formin-mediated F-actins are ten-times longer than ARP2/3-mediated F-actins and known to primarily determine cellular mechanical properties such as the elastic modulus and bending rigidity of the actin cytoskeleton.[23,46] Consequently, it is feasible to speculate that the typical length scale of a formin-mediated F-actin is critical for the sensitivity of mechanoadaptation. Consistent with this line of thought, high mechanical stress and large indentations on the length scale of the cell height resulted in poor mechanoadaptation, which is in contrast to favored cell adhesion on hard surfaces in the gigapascal range.[6] Similarly, indentations in the order of the cortex thickness,[47,48] but small compared with the average length of formin-mediated F-actin, yielded no significant mechanoadaptation. From the mechanical point of view, formins are well-known to contribute to mechanosensation.[49–51] To this end, the mechanical setting at the apical actin cortex in our experiments could translate into pulling or pushing forces on single formin molecules in cortical F-actin and the mechanically linked stress fibers, which have been demonstrated in vitro to accelerate or de-accelerate formin's polymerization activities.[52] In contrast to such passive mechanosensation by biophysical principles, active signaling-associated mechanosensation by dedicated molecules could be responsible for the actin mechanoadaptation. In light of this argument, we waited for 2 min post force application and prior execution of the FRAP experimentation for equilibration of the external forces applied to the living cells, allowing unaccounted time for signaling responses controlling actin and associated cross-linker turnover. In addition, stress propagation and transduction by mechanical tension release through the actin cytoskeleton could also contribute to the observed mechanosensation processes.[52]

One intriguing prediction of mechanosensation is hence that tuning the activity of actin kinetics to alter filament lengths may thus be a mechanism allowing cells to adjust their dynamic range and sensitivity of mechanoadaptation. The AFM-FRAP platform offers three major types of investigations, which are not possible in independent FRAP or AFM experiments: (1) Quantitative measurements of the dynamic range of cellular mechanosensation. (2) Mechanistic study of the

origin of cell mechanics: mechanical properties and mechanical force production by living cells can be dynamically interrogated in response to pharmacological and genetic treatments. (3) Mechanistic investigation of the implications of protein kinetics for cell mechanics: dissecting the molecular protein dynamics underlying cell mechanics by dynamically exerting mechanical load onto living cells. Consequently, AFM-FRAP will lay a foundation to address a plethora of open biological problems. Important examples include but are not restricted to T-cell activation, cancer cell mechanics, stem cell differentiation, cellular migration, and tissue functions. These time-dependent mechanoadaptive processes have thus far only been studied without the spatiotemporal synchronization as offered by AFM-FRAP. Simultaneous quantification of the relationship between molecule kinetics and cell mechanics may thus open up unprecedented insights into adaptive mechanobiological mechanisms of cells.

3.4 MATERIALS AND METHODS

3.4.1 CELL CULTURE

Cell culture was performed as described earlier.[24] HeLa cells (product 93021013, Sigma Aldrich, UK; mycoplasma tested) were cultured in sterile DMEM (Sigma Aldrich) supplemented with 10% FCS (Sigma Aldrich), 2 mM L-Glutamine (Sigma Aldrich) and 1% Penicillin-Streptomycin-Neomycin solution (Sigma Aldrich). Cells were maintained at 37 °C and 5% CO_2 during culturing, and handling was performed in HEPA-filtered microbiological safety cabinets. Cells were passaged every 48 h, kept subconfluent, and seeded to adhere overnight prior to experimentation.

3.4.2 GENERATION OF STABLE CELL LINES

HeLa lines stably expressing actin-EGFP were generated using a lentiviral transduction strategy. HEK-293T cells were plated in six-well plates at 3 10^5 cells/mL, 2 mL per well in DMEM (Sigma Aldrich) supplemented with 10% FCS. Cells were incubated at 37 °C and 5% CO_2 for 24 h before transfection with 0.5 mg per well each of the lentiviral packaging vectors p8.91 and pMD.G and the relevant pHR-SIN lentiviral expression vector using GeneJuice (Merck Millipore, UK) as per the manufacturer's instructions. 48 hours after transfection, the cell supernatant was harvested and filtered using a 0.45 mm Millex-GP syringe (Merck Millipore) filter unit to remove detached HEK-293T cells. In all wells, 3 mL of this virus-containing medium was added to 1.5 10^6 HeLa cells in 3 mL supplemented DMEM medium. After 48 h, cells were moved into 10 mL supplemented DMEM and passaged as described above.

3.4.3 CELL FIXATION AND STAINING

Cell fixation was effected as described previously.[54] HeLa cells were washed and immersed in cytoskeleton buffer [50 mM imidazole, 50 mM KCl, 0.5 mM $MgCl_2$, 0.1 mM EDTA, and 1 mM EGTA (pH 6.8)]. Petri dishes (FluoroDish, FD35-100; World Precision Instruments, UK) with adherent subconfluent HeLa cells were washed three times with 1 mL of cytoskeleton buffer. The cytoskeleton buffer was replaced with 1 mL of cytoskeleton buffer containing 0.25% glutaraldehyde and 0.5% Triton X-100, with care taken not to disturb the cells attached to the glass. Samples were fixed for 5 min at room temperature before they were washed twice with 1 mL of cytoskeleton buffer and covered with 1 mL cytoskeleton buffer containing 1:100 phalloidin-AlexaFluor488 (Life Technologies, UK). Before our FRAP calibration experiments, 20 µL of dye-containing buffer was removed and replaced by additional 20 µL of undiluted phalloidin-AlexaFluor488 in order to ensure sufficient amounts of the fluorophore in the medium.

3.4.4 AFM-FRAP EXPERIMENTS

The optomechanical AFM-FRAP platform allowed the simultaneous execution of AFM and FRAP experiments in living cells. FRAP was effected as described earlier[13,22] at 37°C using a 1.4 *NA* 100X oil immersion objective on a widefield fluorescence microscope (Leica DMI8, Leica Microsystems) and FRAP UGA-42-Firefly laser unit (Rapp OptoElectronic). In the FRAP experiments, a small circular ROI (diameter d = 2 μm) was centered on the basal stress fibers. The photobleaching event was executed by a single photobleaching spot of a 488 nm beam operating at 50% power of the 200 mW laser using a 1% transmission neutral-density filter to reduce the applied power finally to 0.5%. In our protocol, bleaching was realized with a single laser pulse of 2 s. The recovery of fluorescence was monitored at 10% fluorescence lamp intensity over 200 frames at 0.8 s to 2 s (live cells) or 3 s (fixed cells) intervals to minimize the loss of fluorescence due to imaging. For each recovery, two time-lapse image streams were recorded before the initial bleaching, which facilitated normalization of the fluorescence signal. To assess the loss in fluorescence during observation of the recovery (due to imaging), we selected the simultaneously recorded fluorescence signal from a non-bleached region. In all cases, the rate of fluorescence loss due to the imaging was significantly smaller than the rates of fluorescence recovery, with a characteristic time of ~1000 s, which was one order of magnitude larger than the slowest recovery time scale observed for actin. Hence, imaging-induced fluorescence loss did not significantly affect the turnover measurements.

AFM nanoindentation tests were performed with a JPK NanoWizard IV (JPK Instruments, Germany) interfaced with the Leica DMI8. For our measurements, we used tipless cantilevers with a nominal spring constant of 0.03 N/m (Arrow TL2, NanoWorld, Switzerland) functionalized with a polystyrene bead with 5 μm radius. Contact radii and respective mechanical stress were inferred following the Hertzian theory by numerically solving $\delta = 0.5a \ln((r+a)/(r-a))$ with the indentation depth δ, the bead radius r and the contact radius a for spherical indenters using Matlab (Mathworks, USA).

3.4.5 AFM ANALYSIS

Analysis of AFM force curves was performed using the JPK SPM Data Processing software and adapting the publicly available (GitHub) Python script Jpkfile. Actual spring constants of the cantilevers were determined using the thermal noise method implemented in the AFM software (JPK SPM). Before indentation tests, the sensitivity of the cantilever was set by measuring the slope of force-distance curves acquired on glass regions of the Petri dish. Note, the force spectroscopy map analyzed within the 1 nN dynamic range refers to linear fitting of 10% indentation depth from 1 nN force towards the contact point.

3.4.6 FRAP ANALYSIS

FRAP data analysis was effected as described by Fritzsche et al.[13,22] The total fluorescence intensity in stress fibers resulted from actin monomers bound to the actin architectures and monomers freely diffusing within these structures. Fluorescence recovery had thus contributions from (i) diffusive actin and (ii) from association/dissociation of actin monomers to the structures. Given the fast cytoplasmic actin diffusion coefficient ($D \sim 15$ μm^2/s of actin in our experimental geometry), diffusion of monomers took place with a characteristic time scale of $\tau_{\text{diffusion}} \sim r^2/4D < 1$ s (with $r = 1$ μm being the radius of the bleached zone), which was several-fold shorter than the characteristic times of the reactions examined in this study ($t \geq 10$ s). Hence, given the acquisition rate used in this study (1 to 2 s per frame), diffusive recovery was complete by the time we acquired the first post-bleach frame. Consequently, we could assume the fluorescence recovery to be solely reactive.

To determine how many first-order molecular processes contributed to turnover, we fitted recovery $I(t)$ with a combination of exponential functions I_i of the form $I_i(t) \sim [1-\exp(-t/\tau_{\text{d},i})]f_i F_0$, where F_0 is the initial fluorescence of the bleached region and i is the molecular process participating to recovery. Each function $I_i(t)$ represents the contribution of the molecular process i to the total recovery, with f_i being the portion of the total protein population undergoing turnover process i ($\Sigma_i f_i = 1$) and $\tau_{\text{d},i}$ being the characteristic dissociation time of process i. The characteristic dissociation time $\tau_{\text{d},i}$ is inverse to the turnover rate $\omega_{\text{d},i}$ and linked to the half-time reported in most FRAP experiments: $\tau_{1/2} = \ln(2)\ \tau_{\text{d}}$. If several molecular processes occur at similar time scales, they cannot be distinguished, and the apparent rate constant measured reflects an average over all of the molecular processes acting at that time scale. In practice, fluorescence recovery curves $I(t)$ were fitted with an increasing number of exponential functions until the following three conditions were met: the goodness of fit estimated through r^2 no longer increased, the total change in fluorescence associated with process i was less than 0.001%, and the sum of squared errors no longer decreased. Hence, this approach allowed determination of the number of molecular processes i that contribute to fluorescence recovery, their characteristic turnover times $\tau_{\text{d},i}$, and the portion f_i of the total protein population that recovered through process i. In this analysis, changes in the recovery half-time $t_{1/2}$ may have therefore resulted from changes in the number of processes i participating to recovery, changes in the characteristic times $\tau_{\text{d},i}$ of some or all of the processes, changes in the relative importance f_i of some or all of the turnover processes, or a combination of all of these factors.

Logarithmic acceleration plots that represent the logarithm of the second derivative of the fit function were used to compare the turnover rate constants across experimental conditions and to visualize the different possible processes participating in the fluorescence recovery of the FRAP data. In these plots, each piecewise linear segment corresponds to a different fluorescence recovery process. The slope of each segment is characteristic for the turnover rate $\omega_{\text{d},i}$. Notably,

we only found formin-mediated actin kinetics in the stress fibers while two main processes corresponding to ARP2/3- and formin-filaments dominate the actin cortex.[22-24] Furthermore, cells showing significant spatial motion during an experiment were excluded from the analysis to avoid possible artefacts in the results. Computation of the F-actin length distributions and their respective mean filament lengths were calculated from the actin turnover rates measured in the FRAP experiments as described previously.[23,53]

3.4.7 PHOTOBLEACHING OPTIMIZATION IN POLYACRYLAMIDE GELS

FRAP photobleaching volume calibration was performed using a 3D hydrogel substrate loaded with recombinant EGFP. Polyacrylamide hydrogels were prepared as previously described[54]. Acrylamide (Sigma Aldrich) and bis-acrylamide (Sigma Aldrich) were combined at concentrations of 10% (v/v) and 0.4% (v/v) respectively, including the addition of 1 µM EGFP (Sino Biological, China; Cat: 16118-S07E). Polymerization was initiated by the addition of TEMED (Sigma Aldrich) followed by APS (Sigma Aldrich). 3 µL of the gel solution was pipetted onto an 18 mm coverslip and the drop covered by a 12 mm coverslip to form a sandwich. After allowing 30 min for polymerization, the gel was imaged at the microscope. Photobleaching calibration was performed using the AFM-FRAP platform where a circular ROI was created at varying laser powers for 2 s and the resulting bleach volume imaged. Downstream analysis and visualization was performed using custom-written Matlab (Mathworks) scripts.

3.4.8 STATISTICAL ANALYSES

For each experimental condition, AFM-FRAP measurements were acquired from at least 12 individual cells over the course of at least three independent experiments. Statistical comparison of all conditions was carried out using a Kruskal-Wallis ANOVA test to detect a significant trend at the $p < 0.01$ level (**). Additionally, to test pair-wise significance Mann-Whitney U tests were performed and results were denoted as described in the legend of Figure 3.2 and Table 3.1. All statistical tests were applied using OriginPro 8.5.

3.5 REFERENCES

1. Rottner, K. & Kage, F. Actin Networks: Adapting to Load through Geometry. *Curr. Biol.* **27**, R1274–R1277 (2017).
2. Luo, T., Mohan, K., Iglesias, P. A. & Robinson, D. N. Molecular mechanisms of cellular mechanosensing. *Nat. Mater.* **12**, 1064–71 (2013).
3. Colin-York, H. *et al.* Cytoskeletal control of antigen dependent T-cell activation. *Cell Rep.* **26**, 3369-3379 (2019).
4. Harris, A. R., Jreij, P. & Fletcher, D. A. Mechanotransduction by the Actin Cytoskeleton: Converting Mechanical Stimuli into Biochemical Signals. *Annu. Rev. Biophys.* **47**, 617-631 (2018).
5. Ogneva, I. V. Cell mechanosensitivity: mechanical properties and interaction with gravitational field. *Biomed Res. Int.* **2013**, 598461 (2013).
6. Gupta, M. *et al.* Adaptive rheology and ordering of cell cytoskeleton govern matrix rigidity sensing. *Nat. Commun.* **6**, 7525 (2015).
7. Hayakawa, K., Tatsumi, H. & Sokabe, M. Mechano-sensing by actin filaments and focal adhesion proteins. *Commun. Integr. Biol.* **5**, 572–7 (2012).
8. Tojkander, S., Gateva, G., Husain, A., Krishnan, R. & Lappalainen, P. Generation of contractile actomyosin bundles depends on mechanosensitive actin filament assembly and disassembly. *Elife* **4**, e06126 (2015).
9. Oria, R. *et al.* Force loading explains spatial sensing of ligands by cells. *Nature* **552**, 219–224 (2017).
10. Chen, C. S. Forces as regulators of cell adhesions. *Nat. Rev. Mol. Cell Biol.* **18**, 715–715 (2017).
11. Schwarz, U. S. & Gardel, M. L. United we stand – integrating the actin cytoskeleton and cell–matrix adhesions in cellular mechanotransduction. *J. Cell Sci.* **125**, 3051–3060 (2012).
12. Axelrod, D., Koppel, D. E., Schlessinger, J., Elson, E. & Webb, W. W. Mobility measurement by analysis of fluorescence photobleaching recovery kinetics. *Biophys. J.* **16**, 1055–1069 (1976).
13. Fritzsche, M. & Charras, G. Dissecting protein reaction dynamics in living cells by fluorescence recovery after photobleaching. *Nat. Protoc.* **10**, 660–680 (2015).
14. Schneider, F. *et al.* Statistical Analysis of Scanning Fluorescence Correlation Spectroscopy Data Differentiates Free from Hindered Diffusion. *ACS Nano* **12**, 8540–8546 (2018).
15. Blumenthal, D., Goldstien, L., Edidin, M. & Gheber, L. A. Universal Approach to FRAP Analysis of Arbitrary Bleaching Patterns. *Sci. Rep.* **5**, 11655 (2015).
16. Mudumbi, K. C., Schirmer, E. C. & Yang, W. Single-point single-molecule FRAP distinguishes inner and outer nuclear membrane protein distribution. *Nat. Commun.* **7**, 12562 (2016).
17. Sprague, B. L., Pego, R. L., Stavreva, D. A. & McNally, J. G. Analysis of Binding Reactions by Fluorescence Recovery after Photobleaching. *Biophys. J.* **86**, 3473–3495 (2004).

18. Reits, E. A. J. & Neefjes, J. J. From fixed to FRAP: measuring protein mobility and activity in living cells. *Nat. Cell Biol.* **3**, E145–E147 (2001).
19. Bläßle, A. *et al.* Quantitative diffusion measurements using the open-source software PyFRAP. *Nat. Commun.* **9**, 1582 (2018).
20. Müller, P. *et al.* Differential diffusivity of Nodal and Lefty underlies a reaction-diffusion patterning system. *Science* **336**, 721–4 (2012).
21. Kang, M., Day, C. A., Kenworthy, A. K. & DiBenedetto, E. Simplified Equation to Extract Diffusion Coefficients from Confocal FRAP Data. *Traffic* **13**, 1589–1600 (2012).
22. Fritzsche, M., Lewalle, A., Duke, T., Kruse, K. & Charras, G. Analysis of turnover dynamics of the submembranous actin cortex. *Mol. Biol. Cell* **24**, 757–67 (2013).
23. Fritzsche, M., Erlenkämper, C., Moeendarbary, E., Charras, G. & Kruse, K. Actin kinetics shapes cortical network structure and mechanics. *Sci. Adv.* **2**, e1501337 (2016).
24. Fritzsche, M. *et al.* Self-organizing actin patterns shape membrane architecture but not cell mechanics. *Nat. Commun.* **8**, 1-14 (2017).
25. Smith, M. B., Kiuchi, T., Watanabe, N. & Vavylonis, D. Distributed actin turnover in the lamellipodium and FRAP kinetics. *Biophys. J.* **104**, 247–57 (2013).
26. Dimchev, G. *et al.* Efficiency of lamellipodia protrusion is determined by the extent of cytosolic actin assembly. *Mol. Biol. Cell* **28**, 1311–1325 (2017).
27. Moeendarbary, E. & Harris, A. R. Cell mechanics: principles, practices, and prospects. *Wiley Interdiscip. Rev. Syst. Biol. Med.* **6**, 371–388 (2014).
28. Sen, S., Subramanian, S. & Discher, D. E. Indentation and Adhesive Probing of a Cell Membrane with AFM: Theoretical Model and Experiments. *Biophys. J.* **89**, 3203–3213 (2005).
29. Eghiaian, F., Rico, F., Colom, A., Casuso, I. & Scheuring, S. High-speed atomic force microscopy: Imaging and force spectroscopy. *FEBS Lett.* **588**, 3631–3638 (2014).
30. Katan, A. J. & Dekker, C. High-speed AFM reveals the dynamics of single biomolecules at the nanometer scale. *Cell* **147**, 979–82 (2011).
31. Ando, T. Directly watching biomolecules in action by high-speed atomic force microscopy. *Biophys. Rev.* **9**, 421–429 (2017).
32. Charras, G. T. & Horton, M. A. Single Cell Mechanotransduction and Its Modulation Analyzed by Atomic Force Microscope Indentation. *Biophys. J.* **82**, 2970–2981 (2002).
33. Mollaeian, K. *et al.* Nonlinear Cellular Mechanical Behavior Adaptation to Substrate Mechanics Identified by Atomic Force Microscope. *Int. J. Mol. Sci.* **19**, 3461 (2018).
34. Wyckoff, J. B. *et al.* Direct Visualization of Macrophage-Assisted Tumor Cell Intravasation in Mammary Tumors. *Cancer Res.* **67**, 2649–2656 (2007).
35. Köster, D. V. *et al.* Actomyosin dynamics drive local membrane component organization in an in vitro active composite layer. *Proc. Natl. Acad. Sci.* **113**, E1645–E1654 (2016).
36. Blanchoin, L., Boujemaa-Paterski, R., Sykes, C. & Plastino, J. Actin Dynamics, Architecture, and Mechanics in Cell Motility. *Physiol. Rev.* **94**, 235–263 (2014).

37. Fletcher, D. A. & Mullins, R. D. Cell mechanics and the cytoskeleton. *Nature* **463**, 485–492 (2010).
38. Chugh, P. *et al.* Actin cortex architecture regulates cell surface tension. *Nat. Cell Biol.* **19**, 689–697 (2017).
39. Stachowiak, M. R. *et al.* A mechanical-biochemical feedback loop regulates remodeling in the actin cytoskeleton. *Proc. Natl. Acad. Sci.* **111**, 17528–17533 (2014).
40. De La Cruz, E. M. & Gardel, M. L. Actin Mechanics and Fragmentation. *J. Biol. Chem.* **290**, 17137–44 (2015).
41. Elson, E. L. & Genin, G. M. The role of mechanics in actin stress fiber kinetics. *Exp. Cell Res.* **319**, 2490–2500 (2013).
42. Stricker, J., Falzone, T. & Gardel, M. L. Mechanics of the F-actin cytoskeleton. *J. Biomech.* **43**, 9–14 (2010).
43. Burridge, K. & Wittchen, E. S. The tension mounts: stress fibers as force-generating mechanotransducers. *J. Cell Biol.* **200**, 9–19 (2013).
44. Walcott, S. & Sun, S. X. A mechanical model of actin stress fiber formation and substrate elasticity sensing in adherent cells. *Proc. Natl. Acad. Sci.* **107**, 7757-7762 (2010).
45. McFadden, W. M., McCall, P. M., Gardel, M. L. & Munro, E. M. Filament turnover tunes both force generation and dissipation to control long-range flows in a model actomyosin cortex. *PLOS Comput. Biol.* **13**, e1005811 (2017).
46. Fritzsche, M. *et al.* Cytoskeletal actin dynamics shape a ramifying actin network underpinning immunological synapse formation. *Sci. Adv.* **3**, e1603032 (2017).
47. Clausen, M. P., Colin-York, H., Schneider, F., Eggeling, C. & Fritzsche, M. Dissecting the actin cortex density and membrane-cortex distance in living cells by super-resolution microscopy. *J. Phys. D. Appl. Phys.* **50**, 064002 (2017).
48. Koenderink, G. H. & Paluch, E. K. Architecture shapes contractility in actomyosin networks. *Curr. Opin. Cell Biol.* **50**, 79–85 (2018).
49. Romero, S. *et al.* Formin is a processive motor that requires profilin to accelerate actin assembly and associated ATP hydrolysis. *Cell* **119**, 419–29 (2004).
50. Kubota, H. *et al.* Biphasic Effect of Profilin Impacts the Formin mDia1 Force-Sensing Mechanism in Actin Polymerization. *Biophys. J.* **113**, 461–471 (2017).
51. Higashida, C. *et al.* F- and G-actin homeostasis regulates mechanosensitive actin nucleation by formins. *Nat. Cell Biol.* **15**, 395–405 (2013).
52. Jégou, A., Carl*ier, M.*-F. & Romet-Lemonne, G. Formin mDia1 senses and generates mechanical forces on actin filaments. *Nat. Commun.* **4**, 1883 (2013).
53. Brückner, B. R. *et al.* Mechanical and morphological response of confluent epithelial cell layers to reinforcement and dissolution of the F-actin cytoskeleton. *Prog. Biophys. Mol. Biol.* **144**, 77-90 (2018).

54. Colin-York, H. *et al.* Dissection of mechanical force in living cells by super-resolved traction force microscopy. *Nat. Protoc.* **12**, 783-796 (2017).

Chapter 4

TIGHT JUNCTION ZO PROTEINS MAINTAIN TISSUE FLUIDITY, ENSURING EFFICIENT COLLECTIVE CELL MIGRATION

by Mark Skamrahl[a], Hongtao Pang[a], Maximilian Ferle[a], Jannis Gottwald[a], Angela Rübeling[b], Riccardo Maraspini[c], Alf Honigmann[c], Tabea A. Oswald[b], and Andreas Janshoff[a].

[a] University of Göttingen, Institute of Physical Chemistry, Tammannstr. 6, 37077 Göttingen, Germany.

[b] University of Göttingen, Institute of Organic and Biomolecular Chemistry, Tammannstr. 2, 37077 Göttingen, Germany.

[c] Max Planck Institute of Molecular Cell Biology and Genetics, Pfotenhauerstr. 108, 01307 Dresden, Germany.

This Chapter was published in *Advanced Science*, Volume 8, Issue 19, Article Number 2100478, August 2021.
DOI: https://doi.org/10.1002/advs.202100478
Available under CC BY 4.0 open access license. Only minute and formatting-related changes were applied.

AUTHOR CONTRIBUTIONS

I performed the migration experiments and fluorescence microscopy measurements with help from H.P. and A.R. I performed the AFM imaging. Except for the force curve analysis, I performed all analyses. M.F. developed parts of the cell segmentation-based analyses and carried out initial analyses. J.G. and I performed the force spectroscopy, and A.J. and J.G. did the corresponding analysis. I designed and planned the experiments. R.M. and A.H. carried out the genetic modifications. T.A.O., A.H., and A.J. designed and supervised the research. A.J. and I wrote the manuscript. All authors helped with discussions and proofreading.

ABSTRACT

Tight junctions (TJs) are essential components of epithelial tissues connecting neighboring cells to provide protective barriers. While their general function to seal compartments is well understood, their role in collective cell migration is largely unexplored. Here, the importance of the TJ zonula occludens (ZO) proteins ZO1 and ZO2 for epithelial migration is investigated employing video microscopy in conjunction with velocimetry, segmentation, cell tracking, and atomic force microscopy/spectroscopy. The results indicate that ZO proteins are necessary for fast and coherent migration. In particular, ZO1/2 double knockdown (dKD) induces actomyosin remodeling away from the central cortex towards the periphery of individual cells, resulting in altered viscoelastic properties. A tug-of-war emerges between two subpopulations of cells with distinct morphological and mechanical properties: 1) smaller and highly contractile cells with an outward-bulging apical membrane, and 2) larger, flattened cells, which, due to tensile stress, display a higher proliferation rate. In response, the cell density increases, leading to crowding-induced jamming and more small cells over time. Co-cultures comprising wildtype (WT) and dKD cells migrate inefficiently due to phase separation based on differences in contractility with dKD cells being particularly immobile. This study shows that ZO proteins are necessary for efficient collective cell migration by maintaining tissue fluidity and controlling proliferation.

4.1 INTRODUCTION

Cellular junctions endow epithelial tissues with their barrier functions by physically connecting neighboring cells. Junction integrity is critical to prevent many diseases. While, among the various junction types, adherens junctions are typically considered as mechanical couplers between cells in epithelia, recent evidence also suggests an important mechanical role for tight junctions (TJs).[1–7] It is conceived that TJs provide a mechanical feedback system regulating the contractility of individual cells via the actomyosin cytoskeleton and their adhesion strength to neighboring cells.[1,4,8–11] Specifically, it was shown that TJs provide a negative mechanical feedback to individual cells in a layer, so that they contract less, lowering the forces on the adherens junctions.[1,4] Once TJ formation is inhibited, cells respond by building thick actomyosin rings at the cell periphery, which, upon contraction, lead to severe heterogeneity of the cell morphology, particularly visible at the apical side.[8,4,12,11] Since this mechanical TJ-based mechanism was established only recently, explicit knowledge of its implications for crucial biological processes such as collective migration remains limited. Collective cell migration depends on an intricate interplay of the mechanical interaction in a cell layer ranging from single cells, e.g., leader cells at the advancing migration front, to the collective behavior of the cell sheet on a mesoscopic level.[13–19] This interplay depends on the fine tuning of cell motility, density, contractility, and cell-cell adhesion.[20–32]

Important advances have been achieved in understanding how collective cell migration is generally influenced by the adhesion-mediating junction proteins.[28] However, there is controversial evidence on the influence of different TJ components on collective migration. While knockout of the transmembrane protein occludin has been shown to severely compromise migration dynamics,[33] interference with the scaffolding zonula occludens (ZO) proteins was associated with both migration acceleration (ZO2; Raya-Sandino et al.[34], ZO1; Bazellières et al.[28]) as well as deceleration (ZO1; Tornavaca et al.[5], ZO3; Bazellières et al.[28]) in different epithelial cell lines. This discrepancy in evidence might be explained by the fact that such studies focused on the modification of only one single TJ component at a time. More recently, there were in-depth efforts to understand the impact of interfering with multiple ZO proteins on cell- and mechanobiology in general.[1,2,4] However, the consequences for collective cell migration remain elusive.

To close this gap in knowledge, we performed migration experiments with ZO1 KO (single knockout) and ZO1/2 dKD (double knockdown) MDCKII cell lines as well as co-cultures comprising dKD and WT (wildtype) cells in a 1:1 ratio accompanied by mechanical measurements and various imaging techniques. We observed that loss of ZO proteins substantially diminishes migration speed and coherence. This was induced by a liquid-to-solid-like transition leading to cellular jamming upon progressing migration. We found that collective cell migration is impaired by jamming through a mechanical tug-of-war that occurred in response to the enhanced contractility of MDCKII cells in the absence of ZO1 and ZO2. In the adherent state, dKD cells try to keep the balance between maximization of area occupied by the cells (adhesion) and assuming a highly contractile state induced by the enhanced perijunctional actomyosin ring. This leads to the coexistence of two subpopulations reflecting the interplay between cell-matrix and cell-cell adhesion. One subpopulation (‘winner’ cells) consists of small contractile cells that exert enormous stretching forces on their neighboring cells. As a result, a second population (‘loser’ cells) emerges displaying a larger, elongated footprint and increased apical tension. The increase in tension fosters cell division preferentially among the large ‘loser’ cells, which in turn feeds the subpopulation of small condensed ‘winner’ cells. In the final analysis, this fosters cellular jamming and thus renders the entire monolayer less mobile. Stalling cellular division in the later stage of confluence reestablishes faster migration as jamming is scaled down.

ZO1 KO cells showed similar but less pronounced proliferational, mechanical, and cytoskeletal adaptations. Albeit they also exhibited signs of jamming at late migration stages, no distinct small and large cell phenotypes arose as found for dKD cells. This finding emphasizes that the coexistence of large cells, which proliferate more and induce crowding, and small cells, which migrate less actively, is an important feature of jamming in TJ-deficient cells.

4.2 RESULTS

4.2.1 ZO PROTEINS ENSURE FAST AND COHERENT EPITHELIAL MIGRATION

To investigate the role of TJs in collective cell migration, we first performed migration experiments using phase contrast microscopy combined with particle image velocimetry (PIV)-based analyses (Figure 4.1A/B).[35] Strikingly, video microscopy revealed that migration velocity of dKD cells was substantially lower than that of WT and even ZO1 KO cells. We first summarized data from the overall migration dynamics of the whole cell layers by averaging over all time points and all vectors (Figure 4.1C). While ZO1 KO cells did not display significant changes in migration dynamics (16 ± 2 μm h^{-1} (mean ± s.d.)) compared with WT MDCKII (18 ± 2 μm h^{-1} (mean ± s.d.), $p = 0.13$), ZO1/2 dKD cells migrated significantly slower (8 ± 1 μm h^{-1} (mean ± s.d.), $p < 0.001$). Additionally, we calculated the order parameter, which quantifies how directed the local motion is towards the migration edge (Figure 4.1C). We found that dKD cells migrated less directed (order parameter of 0.12 ± 0.04) than WT (0.29 ± 0.09) and ZO1 KO (0.31 ± 0.08) cells ($p < 0.001$), respectively.

To characterize the velocity transmission from the migration edge into the bulk of the monolayer, time-averaged velocity and order profiles were computed (Figure 4.1C). Here, we observed a subtle velocity decay in the range of the standard deviation with increasing distance from the migration edge for the WT and the ZO1 KO cells from about 20 μm h^{-1} at the edge to 17 μm h^{-1} (15% decrease), 400 μm away from the edge, while the dKD cells showed a sharper velocity drop from approximately 12 μm h^{-1} to 8 μm h^{-1} (33% decrease), approaching a plateau at about 400 μm, indicating an impaired velocity transmission from the edge into the layer. The order parameter also decreased with increasing distance from the edge into the bulk layer for all three cell lines. Interestingly, for dKD cells the order parameter was not only lower at every distance from the edge but even approached zero at approximately 600 μm (indicating zero net movement towards the edge). This highlights that the cell collectivity was diminished, which goes hand in hand with the increased number of leader cells emerging from the dKD layers (Figure 4.1B). Almost twice as many leader cells were observed in the dKD (11 ± 2 mm^{-1} (mean ± s.d.)) as in the WT monolayers (6 ± 2 mm^{-1} (mean ± s.d.), $p < 0.001$). The ZO1 KO cells also showed an elevated number of leader cells (8 ± 2 mm^{-1} (mean ± s.d.), $p < 0.01$) compared with the WT, albeit less leader cells than the dKD variant.

To further study the reach of force transmission into the monolayer, we also computed the spatial velocity correlation of the migrating cells (Figure 4.1D). While the spatial velocity correlation of ZO1 KO cells decayed slightly slower than that of WT cells, yielding longer correlations lengths of 63 ± 9 μm (mean ± s.d.) for the KO than 57 ± 6 μm (mean ± s.d.) for the WT ($p = 0.08$), dKD cells showed considerably shorter correlation lengths of 35 ± 2 μm (mean ± s.d.) than both WT and ZO1 KO cells ($p < 0.001$, respectively).

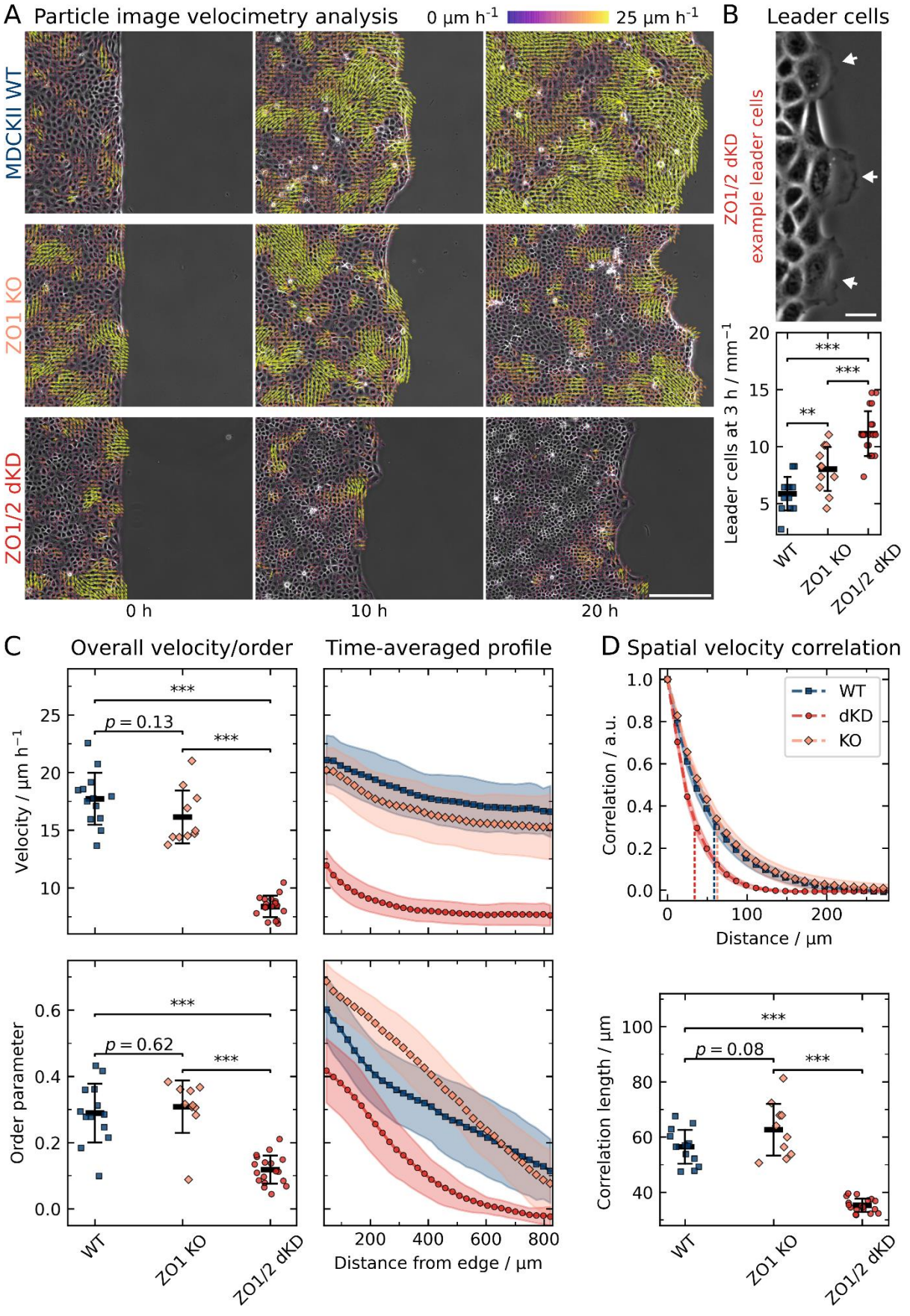
A Particle image velocimetry analysis
0 µm h-1
25 µm h-1
MDCKII WT
ZO1 KO
ZO1/2 dKD
0 h
10 h
20 h
B Leader cells
ZO1/2 dKD
example leader cells
Leader cells at 3 h / mm-1
WT
ZO1 KO
ZO1/2 dKD
C Overall velocity/order
Time-averaged profile
Velocity / µm h-1
p = 0.13
Order parameter
p = 0.62
Distance from edge / µm
D Spatial velocity correlation
Correlation / a.u.
Distance / µm
WT
dKD
KO
Correlation length / µm
p = 0.08

Figure 4.1: Collective cell migration dynamics of wildtype (WT), ZO1 knockout (KO) and ZO1/2 double knockdown (dKD) MDCKII cells. A) Migrating cell monolayers with the corresponding velocity vectors obtained from particle image velocimetry (PIV). To enhance the figure's visibility, cropped images are shown (about a fourth of the original field of view). Scale bar: 200 μm. B) Quantification of leader cell emergence and a corresponding dKD example. The amount of leader cells was normalized by the image width for better comparison. Scale bar: 25 μm. C) The overall velocity and order are defined as the average over all vectors and time points, velocity and order were additionally averaged over time along the distance from the edge of the cell layer. D) Spatial velocity function. Vertical dashed lines indicate the corresponding characteristic correlation lengths below. All data are shown as means and standard deviations. Sample sizes (independent experiments): 13 (WT), 10 (KO), 18 (dKD).

Taken together, these findings suggest that ZO1/2 dKD cells migrate slower, less correlated, and less directed than the WT, thereby showing a significant loss of the hallmark parameters of cell collectivity. This behavior could be induced by a variety of mechanisms, from biochemical signaling to cell mechanical adaptations and possibly cellular jamming, in which the last two ones will be investigated further (vide infra).

4.2.2 ZO Proteins Prevent Jamming and Cell Crowding

The following question remains to be answered: To what extent is the reduced migration speed an intrinsic property of ZO1/2-depleted cells or a consequence of compromised cell-cell contacts and therefore a collective effect? Figure 4.2A shows the analysis of both single cell migration and migration of individual cells within a confluent monolayer. Interestingly, the velocity of single dKD cells in the absence of cell-cell-contacts is even larger than the velocity of single WT cells (21.5 μm h^{-1} compared with 15.3 μm h^{-1} (median, $p < 0.01$)), which is in sharp contrast to their collective behavior when being part of a confluent monolayer. To scrutinize this collective effect, we expanded our time-averaged PIV analysis from before (Chapter 4.2.1) to cell tracking in monolayers during very early (first 0.5-2.5 h) and late (19-21 h) migration. At an early confluent stage, the difference between WT cells and dKD is moderate (16.3 μm h^{-1} compared with 11.0 μm h^{-1}, $p < 0.001$), while the drop in migration speed becomes more pronounced at a later stage when jamming sets in (vide infra). We rationalize the increased single-cell motility of dKD cells by their elevated contractility and actomyosin activity due to upregulation of ROCK.[36,37] We can therefore safely rule out that dKD cells are intrinsically less motile, rather the opposite. In the early stage (Figure 4.2A), where proliferation is largely absent, likely the enhanced contractility of dKD cells as described below and by previous studies already slows down collective migration compared with WT cells.[1,2,4]

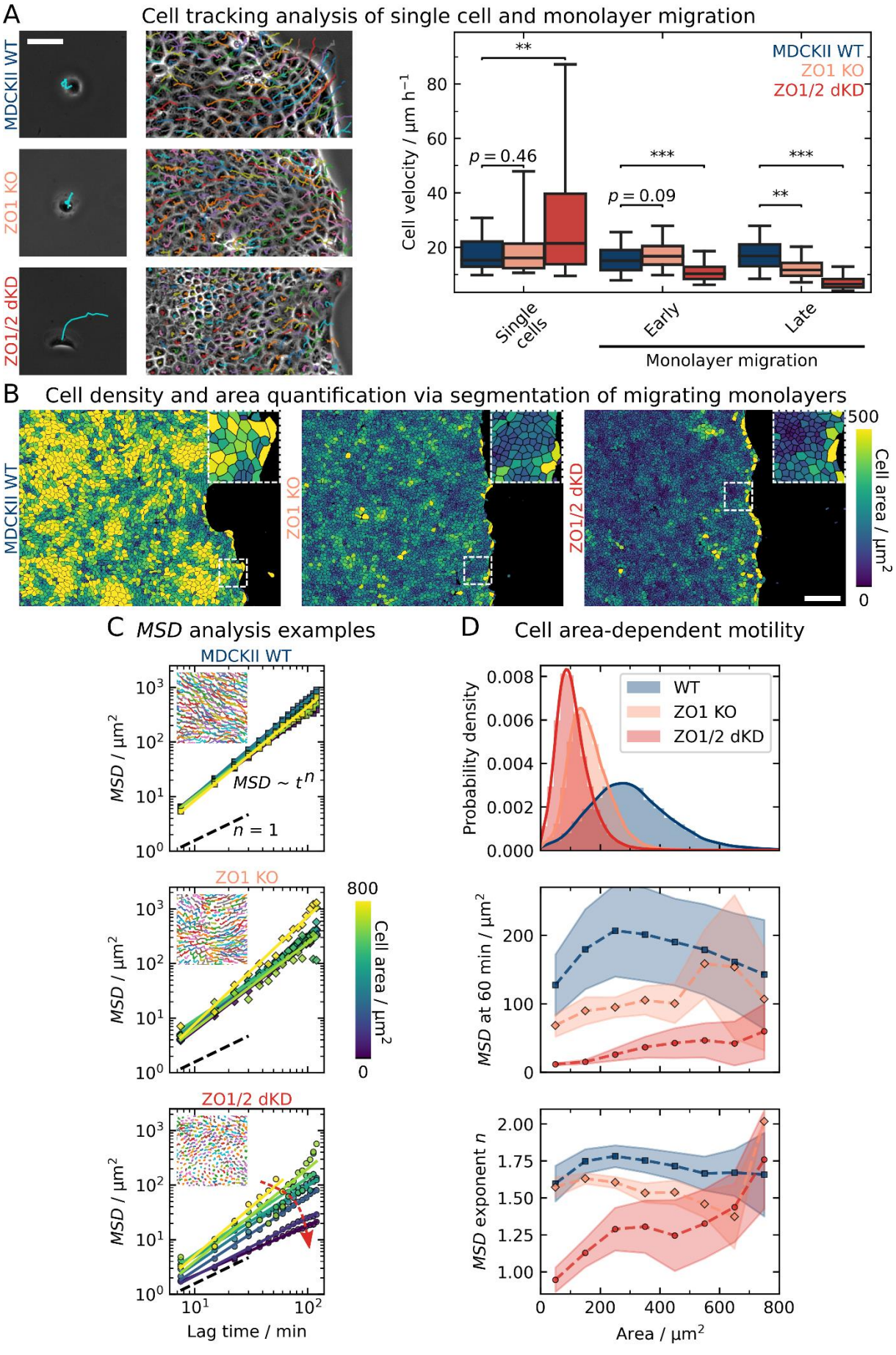
A
Cell tracking analysis of single cell and monolayer migration
MDCKII WT
ZO1 KO
ZO1/2 dKD
Cell velocity / µm h⁻¹
p = 0.46
p = 0.09
**
***
Single cells
Early
Late
Monolayer migration
B
Cell density and area quantification via segmentation of migrating monolayers
Cell area / µm²
500
0
C
MSD analysis examples
MSD / µm²
MSD ~ t^n
n = 1
800
Lag time / min
D
Cell area-dependent motility
Probability density
WT
ZO1 KO
ZO1/2 dKD
MSD at 60 min / µm²
MSD exponent n
Area / µm²

Figure 4.2: Quantifying individual cell velocities of early and late monolayer as well as single cell migration using tracking and segmentation-based cell area-dependent motility analysis. A) Migration tracks of single cells and individual cells in a confluent cell monolayer colored randomly and quantification of the average velocity of individual cells during single cell migration and during early (0.5-2.5 h) and late (19-21 h) monolayer migration. Scale bar: 50 µm. B) Segmented cells in migrating monolayers at 20 h of migration, colored by the respective individual projected area in 2D. Scale bar: 200 µm. C) Tracking and mean squared displacement (*MSD*) analysis. *MSD*s and corresponding power law regressions for a time window between 19 h and 21 h are shown for ensembles of cells in 100 µm^2 area bins of an exemplary movie per cell line. The insets show exemplary tracks colored randomly. The red arrow indicates a decrease of the *MSD* with decreasing area, only prominent for the dKD cells. D) Cell area-dependent *MSD* parameters from C. The area distribution of all cells at 20 h of migration is shown at the top. ZO protein interference induced a shift to smaller areas with a pronounced skewness of 1.23 for the KO and 2.25 for the dKD as compared with the WT cells (0.94). Below, the *MSD* at 60 min and the power law exponent *n* are plotted vs the cell area. Points correspond to bins of 100 µm^2 (around the point location), starting from 0 µm^2. Sample sizes: 13 WT, 9 KO, 18 dKD independent monolayers, and 53 WT, 54 KO, 141 dKD cells (distributed over 2 independent experiments each). The boxes in A show the median and upper and lower quartiles. Whiskers indicate the 5th and 95th percentile. The boxplot comprises individual cell velocities. For more accurate statistical testing, cell velocities were averaged over separate monolayers. Means and standard deviations are shown in D.

Already from visual inspection of the epithelia, it was obvious that the KO and particularly the dKD monolayers showed decreased contact inhibition, becoming increasingly dense over time during migration due to continuous proliferation, whereas the WT layers showed no obvious change in density. Therefore, we quantified this peculiarity and also examined the impact of crowding on collective migration. While PIV is a well-established technique for the quantification of migration dynamics of cell collectives, it lacks information about the behavior of individual cells in the layer. To overcome this limitation, we applied the automated cell segmentation algorithm Cellpose (Stringer et al.) outlining the area occupied by each individual cell in 2D as shown in Figure 4.2B.[38]

Indeed, we found a substantial lack of contact inhibition of proliferation for the dKD cells as indicated by a strong increase of the cell density over time during migration (Figure S 4.1A). While the density of the WT cells remained approximately constant, the KO cells displayed a cellular density increase similar to dKD cells but less pronounced. Yet, this density increase could also come from a lack of edge displacement combined with additional cells moving into the field of view. To confirm that mainly proliferation induced the density increase, we quantified cell density without a migration edge in a separate experiment (Figure S 4.1E). Indeed, the dKD cell density increased stronger within the first 60 h and then reached a higher steady-state density than either WT or KO cells.

Two prominent parameters serve to characterize jamming transitions of cell layers: cell density and cell shape. Particle-based models attribute jamming to an increased cell density,[39]

whereas vertex models predict the shape of cells, as quantified by the shape index or the projected aspect ratio in 2D, to be the main determinant for jamming.[24] However, along with the density increase with elapsed time, we did not observe a clear change in the projected cell aspect ratio in 2D (length divided by width) as shown in Figure S 4.1A. Except for a short increase to a median aspect ratio of 1.60 around 5 h for the WT, all cell lines had a similar and only very subtly decreasing aspect ratio at around 1.45. However, the WT cells exhibited a slightly higher aspect ratio at all times, with a slightly broader distribution shifted to larger values (Figure S 4.1B). Note that the observed aspect ratio values here are above the jamming threshold of 1.18,[21] as calculated from the shape index of 3.81 as previously proposed by Bi et al.[24] Notably, there was no correlated variation between cell area and aspect ratio of individual cells (Figure S 4.1C), rendering these parameters largely independent of each other for each cell.

The decrease of migration velocity over time of dKD cells together with their increased proliferation rate suggests that jamming of the monolayer slows down migration speed. It is, however, important to distinguish earlier stages, in which cell division is still absent, from later stages, in which jamming increases due to increased proliferation. In the early stage, less immobile clusters of small contractile cells coexist with larger, highly strained cells in response to a competition between contractility and extensibility of cells to cover the matrix. The small contractile cells barely move and thereby slow down the monolayer. In later stages, the larger cells generate excess cells through cell division and thereby trigger jamming (vide infra).

A marked difference in the averaged PIV data of WT and ZO1 KO became apparent only after 15 h (Figure S 4.1A), when the KO also slowed down and showed uncontrolled proliferation and slightly decreasing aspect ratios, similar to the behavior of dKD cells. However, the dKD cells display the slowest dynamics of all three cell lines, which could not be attributed solely to a change in the cell density, as this was also altered in ZO1 KO cells. The elevated contractility of dKD cells, which emerges in response to lack of ZO1/2 proteins, fostering remodeling and strengthening of the perijunctional actomyosin belt, is the key difference (vide infra).

Importantly, our individual cell segmentation-based approach revealed a morphological heterogeneity (small and large cells) particularly for dKD cells at later time points (Figure 4.2B). This brought up the question, whether these morphological differences could be responsible for the impaired cellular dynamics. Therefore, we utilized single cell tracking to investigate the dynamics of individual cells in a layer during late-stage migration (19-21 h after insert removal), depending on the cell density and the projected cell area in 2D. We found that the motility, as quantified by the *MSD* (mean squared displacement), of WT and KO cells generally did not depend on the cell area. In contrast, the *MSDs* of individual dKD cells showed a clear dependency on cell area (Figure 4.2C). Specifically, we observed that the movement amplitude (*MSD* at 60 min) as well as the exponent *n* of the *MSD*s as a function of lag time rises with increasing cell area for the dKD. The small and most abundant bulk cells with an area around the distribution peak of about 120 μm^2 showed passive diffusion-like movement with $n \sim 1$ and small amplitudes of about

10 μm². In contrast, the larger cells exhibited active motion with up to n = 1.75, which is similar to the WT cells and close to straight-line motion at n = 1.75, and five-fold increased amplitudes of 50 μm² (Figure 4.2D). The KO cells had a similarly skewed cell area distribution with small bulk cell of about 180 μm² showing movement amplitudes of about 80 μm² while the sparse large cells moved about 110-200 μm². However, neither WT nor KO cells showed any clear dependence of n on the cell area. Interestingly, the WT showed a more symmetrical cell area distribution around 280 μm² (skewness of 0.94 as compared with 1.23 for the KO and 2.25 for the dKD cells) with averaged-sized cells showing the largest movements (*MSD* around 200 μm²) and cells at the extreme ends of the distribution moving less (*MSD* of about 130 μm²). Importantly, we did not find any clear dependence of the individual cell motility on the aspect ratio (Figure S 4.1B).

Together, these results show that contractility and cell density, the latter being the result of the former, are the determining factors explaining the observed jamming of dKD cells due to an abundance of slow-moving small cells coexisting with faster-moving large and actively dividing cells.

As we have identified an important connection between jamming, proliferation, and migration speed in cells lacking ZO proteins, we investigated the distribution of the Yes-associated protein (YAP), a Hippo mechanotransduction signaling effector localizing to both the cytoplasm and the nucleus, where it is in its active state. YAP is known to influence cell proliferation as an important effector of the Hippo pathway, playing important roles in regulating cell migration. Mechanical signals that regulate YAP nuclear import comprise pulling, compressing, and shearing detected through cell-substrate as well as cell-cell junctions but also cytoskeletal remodeling.[40,41]

Therefore, we determined the ratio of YAP found in the nucleus to YAP in the cytoplasm for WT and dKD MDCKII cells (Figure 4.3A). We found indeed that in dKD cells a higher relative amount of YAP (0.8 ± 0.2 (median ± s.d.)) transits into the nucleus than in WT cells (0.5 ± 0.2 (median ± s.d.), $p < 0.001$), suggesting an increased propensity for proliferation in ZO1/2 depleted cells. As discussed above and elaborated further in the following, uncontrolled contractility eventually leads to jamming and consequently slows down collective cell migration. Additionally, the interplay of contractility and proliferation generates jamming through a positive feedback loop in which the small contractile cells stretch their neighbors to trigger cell division that in turn increases the number density of small, contractile cells (see below and Figure S 4.7). Eventually, the monolayer assumes a frustrated state and slows down like a glassy material.

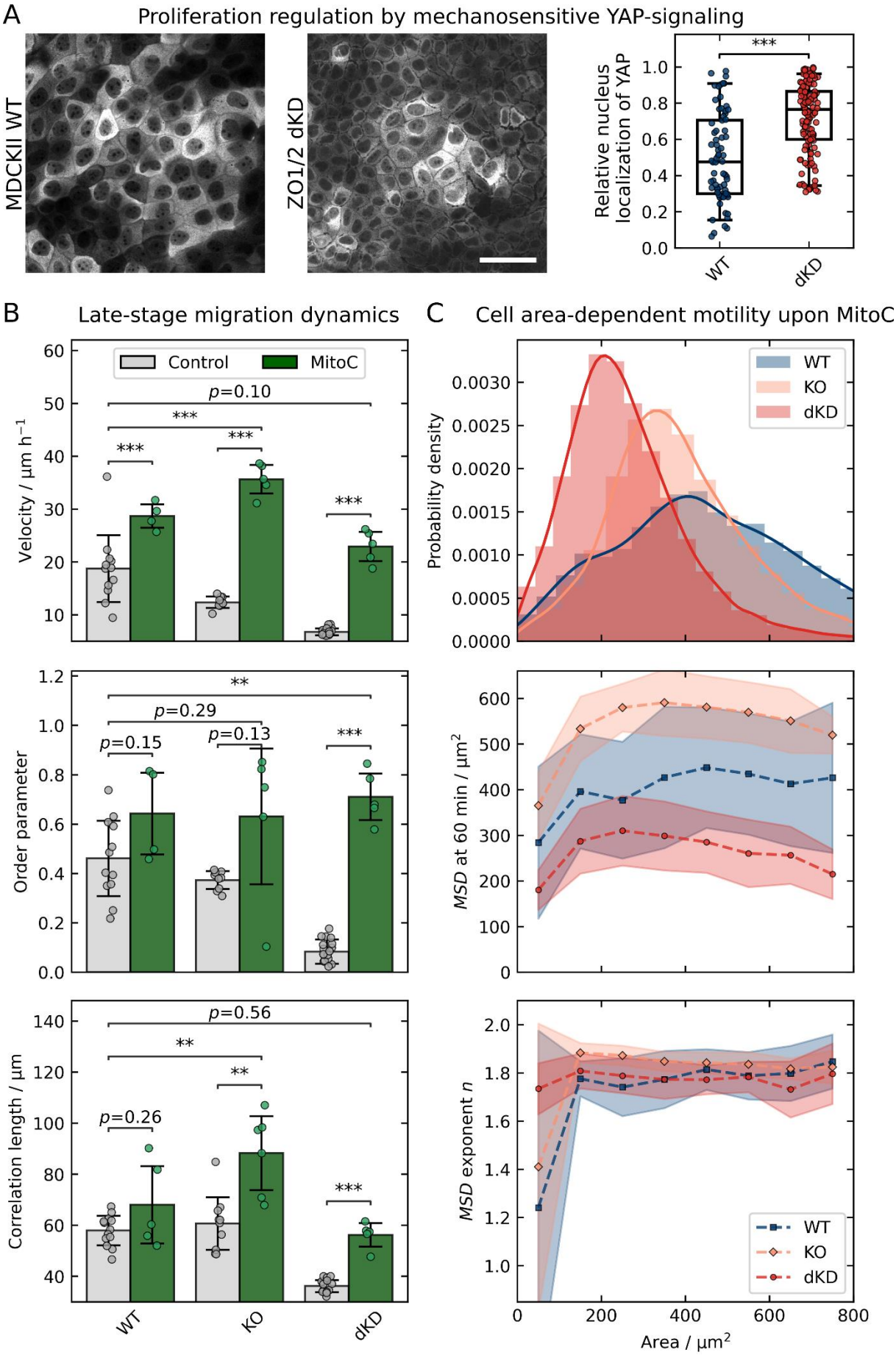
A
Proliferation regulation by mechanosensitive YAP-signaling
MDCKII WT
ZO1/2 dKD
Relative nucleus localization of YAP
***
WT
dKD
B
Late-stage migration dynamics
Control
MitoC
Velocity / µm h⁻¹
p=0.10
***
***
***
Order parameter
p=0.15
p=0.29
p=0.13
**
***
Correlation length / µm
p=0.26
p=0.56
**
**
***
WT
KO
dKD
C
Cell area-dependent motility upon MitoC
Probability density
WT
KO
dKD
MSD at 60 min / µm²
MSD exponent n
Area / µm²

Figure 4.3: Late-stage jamming is induced via Yes-associated protein (YAP)-based upregulation of proliferation and can be largely prevented by proliferation inhibition with Mitomycin C. A) Confocal images and corresponding relative localization of YAP in the cytoplasm and nucleus of WT and dKD cells, respectively. Scale bar: 50 µm. B) Migration dynamics later than 19 h with (control) and without proliferation (MitoC). Overall velocity, order and correlation were calculated as in Figure 4.1. C) Cell area-dependent *MSD* parameters upon proliferation inhibition (MitoC treatment). The area distribution of all MitoC-treated cells at 20 h of migration is shown at the top. Larger cell areas and skewness parameters of 1.01 (WT), 1.36 (KO), and 1.83 (dKD) were observed. Below, the *MSD* at 60 min and the power law exponent *n* are plotted vs the cell area. *MSD*s and corresponding power law fits were calculated for a time window between 19 h and 21 h, in accordance with Figure 4.2. Points correspond to bins of 100 µm^2 (around the point location), starting from 0 µm^2. Boxes in A show the median and upper and lower quartiles. Whiskers indicate the 5th and 95th percentile. Data in A correspond to 72 WT and 124 dKD cells. Means and standard deviations are shown in B and C.

We therefore aimed to stall or even reverse the cellular crowding and jamming by the inhibition of proliferation using the well-established drug Mitomycin C (MitoC).[20,22,42–44]. As expected, upon MitoC treatment, the density of all three cell lines did not increase but instead even slightly decreased over time, confirming a successful inhibition of proliferation (Figure S 4.2A). Concomitantly, the migration velocity increased while the overall aspect ratio slightly decreased over time. To quantify the impact of proliferation inhibition, we now focused again on the late-stage migration dynamics, after 19 h onward (Figure 4.3B). The drug increased the migration speed of WT MDCKII cells from 19 ± 6 µm h^{-1} to 29 ± 2 µm h^{-1} (mean ± s.d., $p < 0.001$), whereas the order parameter and correlation length did not change significantly ($p = 0.15$ and $p = 0.26$, respectively).

In comparison, we observed a significant increase of all migration parameters for the dKD cells (Figure 4.3B). Specifically, the dKD velocity increased from 7 ± 1 µm h^{-1} to 23 ± 3 µm h^{-1} (mean ± s.d., $p < 0.001$), which is similar to the velocity of untreated WT cells ($p = 0.10$), the order increased from 0.08 ± 0.05 to 0.7 ± 0.1 (mean ± s.d., $p < 0.001$), which is significantly higher than that of untreated WT cells (0.5 ± 0.2 (mean ± s.d., $p < 0.01$)), and the correlation length increased from 36 ± 2 µm to 56 ± 5 µm (mean ± s.d., $p < 0.001$), which is similar to the correlation length of untreated WT cells, being 58 ± 6 µm (mean ± s.d., $p = 0.56$).

The ZO 1 KO cells showed a similar behavior as the dKD cells upon proliferation inhibition, but with a less pronounced increase in all parameters. The velocity of KO cells increased in the presence of MitoC from 12 ± 1 µm h^{-1} to 35 ± 3 µm h^{-1} (mean ± s.d., $p < 0.001$), which is also significantly higher than the velocity of untreated WT cells ($p < 0.001$), the order parameter increased from 0.37 ± 0.04 to 0.6 ± 0.3 (mean ± s.d., $p = 0.13$), which is slightly higher than the order parameter of untreated WT cells ($p = 0.29$), and the correlation length increased from 61 ± 10 µm to 88 ± 14 µm (mean ± s.d., $p < 0.01$), which is also higher than the correlation length of untreated WT cells ($p < 0.01$).

Taken together, the velocimetry data showed that inhibition of proliferation largely prevented the very late jamming process of dKD, and, less pronounced, that of ZO1 KO cells, by preventing an uncontrolled density increase.

Interestingly, the area-dependence of the *MSD* of dKD cells during late migration (19-21 h, vide supra) also vanished upon inhibition of proliferation (Figure 4.3C). In general, the individual cell area was larger in the presence of MitoC for all three cell lines as expected for proliferation inhibition. This was most pronounced for dKD cells, where the cell area increased from 120 μm^2 to about 220 μm^2 (see area distribution in Figure 4.3C). Importantly, less separation into small and large cells occurred as indicated by the decreased area distribution skewness (Figure 4.3C) and confocal side views (Figure S 4.2C). The *MSD* also showed a higher amplitude (*MSD* at 60 min) as well as exponent *n* for all treated cell lines than for untreated cells. Specifically, the dKD *MSD* amplitude was between 200 μm^2 and 300 μm^2 upon proliferation inhibition, which is slightly higher than for the untreated WT cells (150-200 μm^2). The treated WT cells showed slightly larger amplitudes of 300-400 μm^2 and the KO cells surpassed both other cell lines at about 300-550 μm^2. Interestingly, the *MSD* exponent is equalized upon proliferation inhibition for all cell lines at about 1.8, which indicates completely restored directionality. This is in good accordance with the higher order parameter upon proliferation inhibition as shown in Figure 4.3B (vide supra).

Notably, upon proliferation inhibition we did not observe a clear trend in the movement amplitude and the *MSD* exponent with decreasing cell area as before anymore (Figure 4.3C). In contrast to untreated KO and dKD cells, upon inhibited proliferation the KO and dKD bulk cells of about 380 μm^2 and 220 μm^2, respectively, even showed a peak in the movement amplitude, while larger and smaller cells both moved slightly less. The *MSD* exponent remained constant with varying area.

Together, these results indicate that the strong crowding-induced jamming during late migration can be largely prevented by proliferation inhibition. However, it is important to note that, besides proliferation, MitoC might also influence other cellular functions, which could potentially contribute to the observed migration dynamics. It is conceivable that since the propensity of large cells to divide is abolished, less excess volume is generated by the 'loser' cells and thereby the pulling of the small cells is stalled. Along the same line, small cells might produce more cell volume during the prolonged interphase and thus contract less. This leads to cells almost equal in height as shown in Figure S 4.2C.

4.2.3 SUCCESSFUL ZO KNOCKDOWN INDUCES ACTOMYOSIN REMODELING

Given such severe phenotypical changes in the migration dynamics and proliferation rates of the ZO1 KO and dKD cells, we sought to investigate the phenomena also on the molecular level.

First, to ensure successful genetic interference, we performed confocal immunofluorescence microscopy. Indeed, ZO1 and ZO2 proteins were no longer visible upon double knockdown (Figure S 4.3). Corresponding western blot analyses can be found in Beutel et al.[45]

ZO1 knockout was also successful as shown in Figure S 4.3A. Importantly, ZO2 was only slightly upregulated indicating a possible compensation for ZO1. Notably, adherens junctions are not obviously affected (Figure S 4.6) highlighting that the observations described here mainly reflect the ZO protein loss.

Since the transmembrane proteins in TJs are connected to the actin cytoskeleton via ZO proteins, we next investigated changes in the actomyosin architecture of the cells (Figure 4.4). Indeed, the actin cytoskeleton of the dKD cells was changed in a distinct way as shown in Figure 4.4C. Actin was accumulated at the periphery of individual cells, organized in thick rings, which were slightly separated at the apical plane of neighboring cells. ZO1 KO cells on the other hand showed an intermediate phenotype with a less marked actin accumulation at cell-cell borders with a slight separation into two thinner cables. In comparison, the WT cells displayed the typical actin structure of MDCKII cells with a continuous mesh between cells and without any separation between neighboring cells or any obvious actin accumulation.

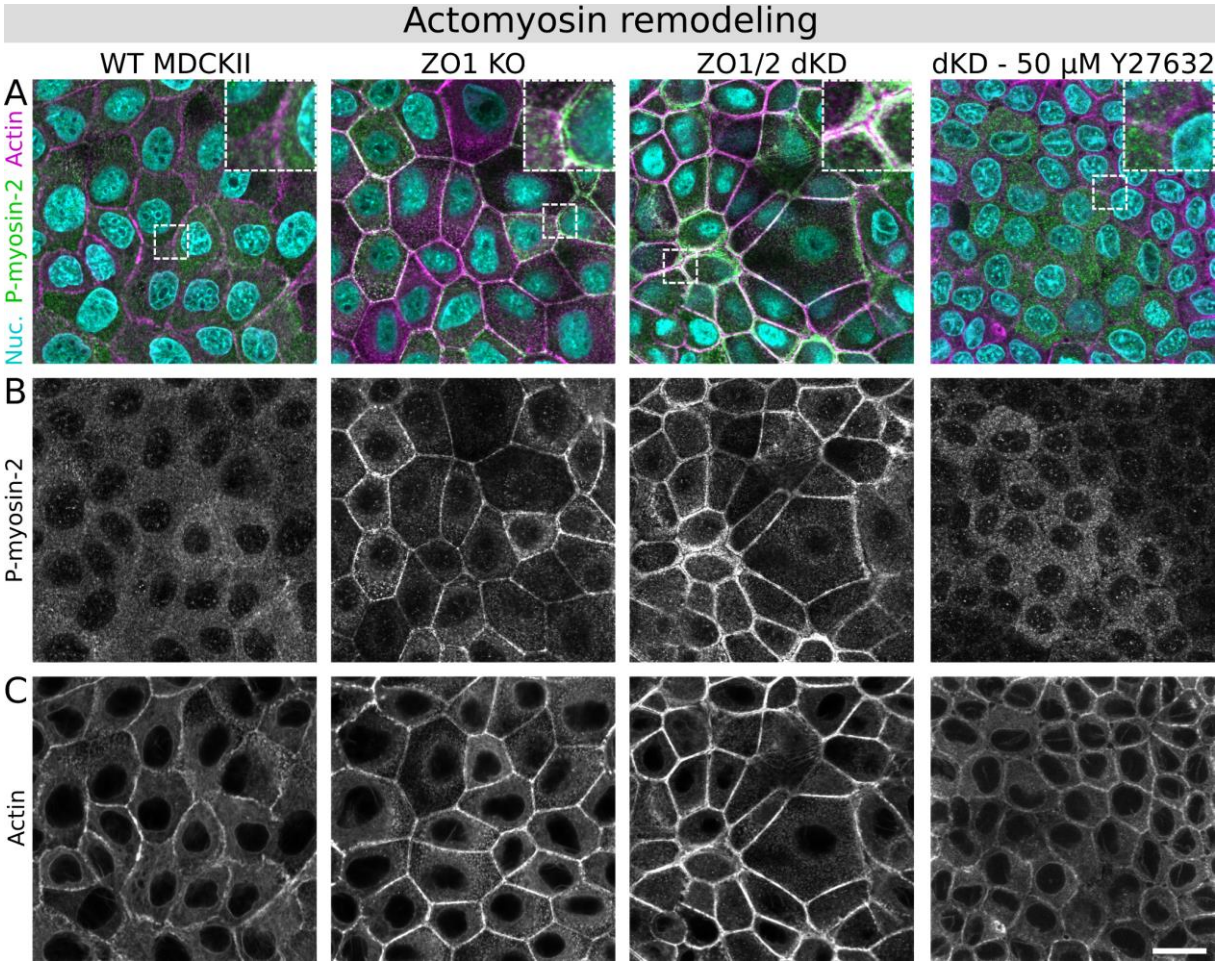

Figure 4.4: Actomyosin architecture remodeling upon ZO protein interference. A) Phosphorylated myosin-2 (P-myosin-2; green), actin (magenta) and nuclei co-staining of all three MDCKII cell lines and 50 µM Y27632 treated dKD cells (22.5 h incubation upon late migration). B) Corresponding gray-scale images of P-myosin-2. C) Corresponding gray-scale images of actin. Shown representative examples far from the edge of migrating monolayers. Scale bar: 20 µm.

In addition, activated (phospho-) myosin-2 upregulation was particularly prominent at the cell-cell border in conjunction with the actin accumulation in dKD cells (Figure 4.4B), indicating upregulated actomyosin contractility. Interestingly, it seems that smaller dKD cells accumulated more peripheral actomyosin than their larger neighbors. On the other hand, ZO1 KO also showed accumulation of activated myosin at the cell periphery, albeit not as severe as in the dKD. In contrast, the WT cells showed little activated myosin without any prominent pattern or structure. Additionally, the occurrence of many small and some large dKD cells (as described above) was observed. In contrast, the WT and KO cell area appeared much more homogeneous.

If contractility is the key feature for the observed emergence of two subpopulations of cells balancing their shape through a tug-of-war in keeping the balance between pulling forces and cell-matrix interactions we would expect to relax this highly tensed state when impairing actomyosin contractility by blocking Rho-associated, coiled-coil containing protein kinase (ROCK) signaling.

To this end, we used Y27632, a cell-permeable and highly selective inhibitor of ROCK, to reinstall tension homeostasis in dKD cells. Figure 4.4 exemplarily shows that P-myosin-2 upregulation and actin remodeling is reversed in dKD cells upon addition of the inhibitor. Additionally, the two subpopulations of dKD cells disappear upon actomyosin relaxation, supporting our hypothesis that mechanical imbalance is responsible for the emergence of two cell populations. Upon Y27632 administration, the cells clearly adopt a homogenous size in the monolayer, rendering it almost indistinguishable from the morphology of the WT. Figure S 4.5 provides further experiments also at lower Y27632 concentrations and an additional quenching experiment in which we supply Y27632 to a cell layer during late stage migration of a confluent monolayer.

Taken together, these findings show that interfering with ZO proteins induces actin remodeling accompanied by myosin activation and accumulation, which is reversible by ROCK inhibition. This suggests that lack of ZO proteins is directly responsible for formation of contractile cells eventually entering jamming through a mechanical imbalance that generates condensed clusters of immobile cells.

4.2.4 The Cell Topography Reflects Actomyosin Remodeling upon ZO Loss and Shows a Heterogeneous Apical Cell Height Distribution

Because severe actomyosin remodeling and accumulation at the apical cell periphery was observed, we also expected changes in the cellular topography (Figure 4.5). Consistent with the changes in the actomyosin structures, using atomic force microscopy (AFM) imaging we found prominently elevated ring-like structures at the periphery of individual dKD cells, slightly separated from each other (zoom-in in Figure 4.5A). In contrast, WT cells exhibit a less pronounced but continuous cell border. ZO1 KO cells showed only a slight change of the cell border topography.

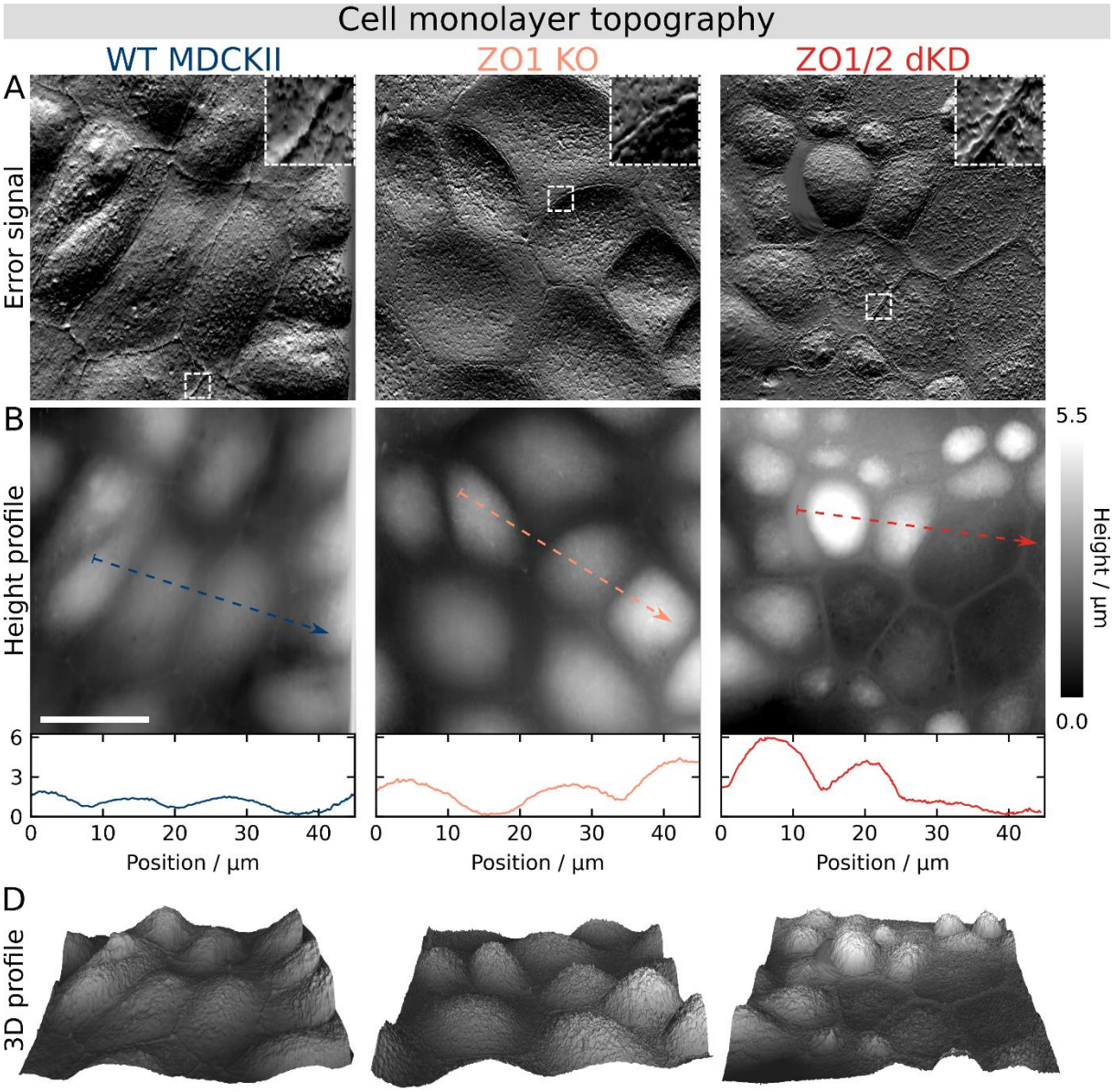

Figure 4.5: Cell monolayer topography adaptations reflect the actomyosin remodeling upon ZO protein interference as shown by AFM imaging. A) Error signal (deflection images). B) Height profile and cross-sections. D) Corresponding 3D topography maps, slightly up-scaled vertically, with the *z*-axis length being 20% of the *x*/*y*-axis (13.3% corresponds to an aspect ratio of 1). Scale bar: 20 µm.

Furthermore, AFM imaging confirmed the data from confocal fluorescence microscopy and segmentation indicating a pronounced height and area heterogeneity in dKD cells. While the apical cap of cells with a small area of about 100 µm² (compare with Chapter 4.2.2) was several micrometers high (> 3 µm), other cells were larger in area but did not exhibit any distinct apical cap rising above the peripheral ring. In comparison, the apical cap of WT cells was typically 1-1.5 µm high and homogenously distributed across the monolayer. The ZO1 KO cells displayed an intermediate phenotype with a homogenous cap height distribution, which are typically slightly higher than WT cells, at about 2-3 µm.

In conjunction with the actomyosin results, these data show that ZO1/2 dKD consistently induces distinct molecular and topographical changes, most notably, severe actomyosin accumulation underneath the membrane at the cell-cell borders in the small cell population being responsible for altered mechanical properties, which are scrutinized next.

4.2.5 ZO Proteins are Necessary for Mechanical Integrity and Tissue Fluidity by Preventing an Uneven Tug-of-War-Like Imbalance

In light of the prominent cell topography adaptations and concomitant actomyosin remodeling, and because contact inhibition of proliferation and jamming are typically tightly coupled with cellular mechanics, the consequences of ZO depletion for cell mechanics were investigated. To this end, we performed AFM measurements with an emphasis on force relaxation experiments that also permit to assess the rheological properties of the cells. First, force volume imaging showed that stiffness was increased considerably at the cell periphery of ZO1 KO and dKD compared with WT cells (AFM maps in Figure 4.6A), whereas the center appeared to be softer compared with WT cells.

This is consistent with the observed accumulation of actin into a contractile actomyosin ring and the altered topography at the cell periphery of ZO depleted cells. Apart from stiffness maps, we also used site-specific indentation experiments followed by force relaxation to study the mechanical and rheological cortex properties in greater detail. The model we applied was introduced recently by Cordes et al.[46] Briefly, it considers stress relaxation of the cortex according to a power law providing us with a prestress corresponding to the isotropic cortical tension T_0 plus membrane tension T_t, the area compressibility modulus K_A of the cortex and the fluidity β, which classifies the flowing propensity of the network. A β value of 1 corresponds to a Newtonian fluid whereas a value of 0 describes a solid. Since we observed a prominent heterogeneity of the dKD cell morphology with a flat surface observed for large cells and a high apical cap seen for smaller cells, we considered the resulting geometrical differences in the model and distinguished between large (about 200 μm²) and small dKD cells (80 μm²).

Notably, we observed statistically significant changes in all mechanical parameters upon ZO protein loss (Figure 4.6B).

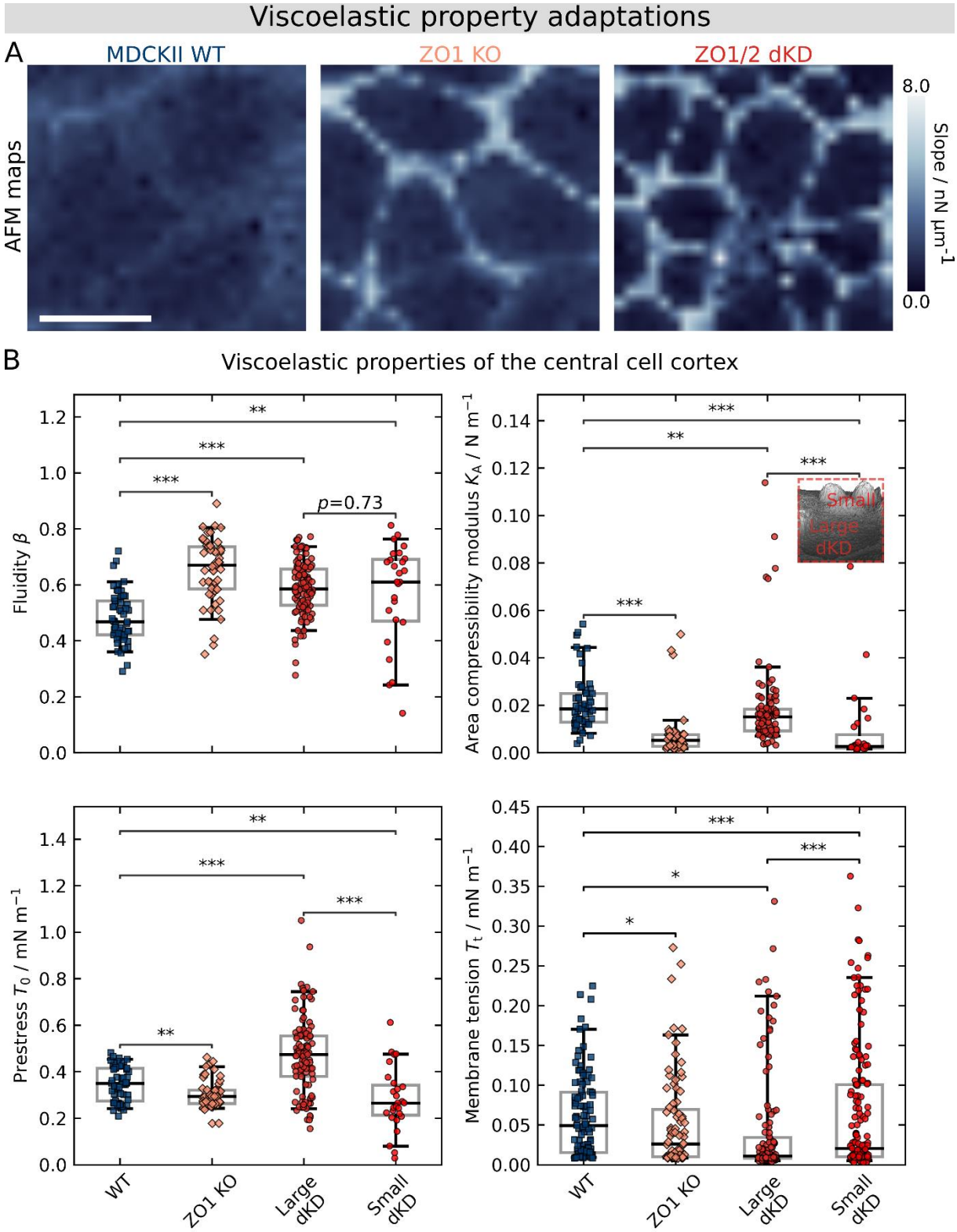

Figure 4.6: ZO proteins ensure viscoelastic integrity of cells as shown by atomic force microscopy (AFM). A) Exemplary AFM maps of migrating WT, ZO1 KO and ZO1/2 dKD cells showing the slope of the force during contact, mirroring the apparent stiffness of cells. Scale bar: 20 µm. B) Site-specific viscoelastic properties of the central cell cortex. Fluidity β, area compressibility modulus K_A, prestress T_0, and membrane tension T_t are shown. Five curves were immediately recorded on the same position at

the center of one cell. Individual data points represent the average of the respective fitting parameter for an individual cell. The boxes show the median and the upper and lower quartiles. Whiskers indicate the 5th and 95th percentile.

Cortex-dominated prestress T_0 was significantly lower in the center of KO (0.30 ± 0.06 (median ± s.d.) mN m^{-1}, $p < 0.01$) and small dKD cells (0.27 ± 0.13 (median ± s.d.) mN m^{-1}, $p < 0.01$) than in the center of WT cells (0.35 ± 0.07 (median ± s.d.) mN m^{-1}), indicating a downregulation of the actin cortex in both populations due to remodeling of the actin cytoskeleton. In contrast, the large dKD cells showed an increased prestress (0.47 ± 0.16 (median ± s.d.) mN m^{-1}, $p < 0.001$ compared with WT as well as with small dKD cells). This goes hand in hand with a flatter morphology indicative of area expansion, leading to higher tension. A similar behavior was found recently by us, in which the elastic modules of confluent MDCKII cells increase with increasing projected apical cell area in a nonlinear fashion. Generally, the prestress T_0 contains contributions from i) membrane tension that originates from adhesion of the plasma membrane to the underlying cytoskeleton, ii) area expansion of the apical shell and iii) active contraction by myosin-2 motors. To tell apart the contribution of the actin cortex from that of the plasma membrane-cytoskeleton attachment to the prestress T_0 we additionally pulled out membrane tethers upon retraction to measure the membrane tension T_t. We observed that T_t decreased upon ZO protein KO for all cell lines. It dropped from 0.05 ± 0.05 (median ± s.d.) mN m^{-1} (WT) to 0.03 ± 0.06 (median ± s.d.) mN m^{-1} (KO, $p < 0.05$), 0.01 ± 0.09 (median ± s.d.) mN m^{-1} (large dKD, $p < 0.001$), and to 0.02 ± 0.08 (median ± s.d.) mN m^{-1} (small dKD, $p < 0.05$). This shows that the prestress changes were only partly explainable by a decrease in membrane tension. However, the membrane tension of large dKD cells decreased, supporting the idea that prestress of the larger and flatter dKD cells stems from area expansion rather than a reinforced attachment of the cortex to the membrane.

Along with smaller prestress, we also observed a fluidization of the cortex represented by an increase of β from 0.5 ± 0.1 (median ± s.d.) to β = 0.7 ± 0.1 (median ± s.d., $p < 0.001$) for KO cells, and to β = 0.6 ± 0.2 (median ± s.d., $p < 0.01$) for the small dKD cells, respectively. Also, for large dKD cells an increase in fluidity was found (β = 0.6 ± 0.1 (median ± s.d.), $p < 0.001$). Recently we showed that fluidity and area compressibility modulus of the cortex are not necessarily independent parameters. Accordingly, the area compressibility modulus K_A decreased from 0.02 ± 0.01 (median ± s.d.) mN m^{-1} for WT to 0.005 ± 0.001 (median ± s.d.) mN m^{-1} for KO ($p < 0.001$) and to even 0.003 ± 0.002 (median ± s.d.) mN m^{-1} for small dKD cells ($p < 0.001$), respectively. For the large dKD cells, K_A fell by only 50% to 0.01 ± 0.01 (median ± s.d.) mN m^{-1} ($p < 0.01$) albeit the fluidity was rather high (β = 0.6 ± 0.1). Notably, the large dKD cells showed a significantly higher K_A than the small dKD cells. This might indicate the presence of a prestressed cortex with less membrane reservoir to compensate for the external deformation. This view is backed up by the finding that the geometrical apical membrane of the large dKD cells is also larger

than that of the small dKD cells despite the apical bulging (as inferred from geometrical considerations based on the topography measurements in Figure 4.5). Interestingly, the large and prestressed dKD cells were observed to proliferate over twice as much as the small dKD cells (Figure S 4.7), indicating a possible connection between the mechanical phenotype of the large dKD cells and proliferation.

The drop in area compressibility modulus in the small dKD and KO cells could be either due to a higher cortical elasticity or a larger apical excess area, giving rise to apparent area compressibility modules. Considering the substantial morphological changes of the apical membrane/cortex in response to ZO1/2 loss, such as bulging of the cortex and the reported occurrence of membrane reservoirs (small dKD cells), it is conceivable that both effects contribute to the observed softening.

Taken together, these findings show a loss of mechanical homeostasis upon ZO protein depletion: Actomyosin is recruited from the cortex to the periphery of individual cells building up a stiff and contractile actomyosin ring while leaving the apical cortex weakened. On one hand, this leads to bulging of the central cell cortex, formation of excess area, and fluidization of the cortex in small dKD cells, making these cells into 'winner' cells in this cellular tug-of-war. On the other hand, large 'loser' dKD cells are prestressed by the contractile small cells and thereby seem to start proliferating upon mechanical activation of the Hippo pathway through YAP signaling (Figure 4.3) and possibly Piezo1-signaling. In fact, a statistical analysis by visual inspection (Figure S 4.7) confirms this hypothesis and shows that larger cells proliferate more frequently, while smaller ones divide less. As a consequence, a larger amount of the small 'winner' dKD cells, which exhibit jamming, are generated by the uncontrolled proliferation and gradually impair collective migration more and more.

4.2.6 The Tug-of-War Outcome is Unequivocally Determined in Co-Cultures of DKD and WT Cells as a Phase Separation into Two Mechanically Distinct Subpopulations

Our working hypothesis proposes that two subpopulations emerge in ZO1/2 depleted cells due to enhanced contractility as a result of cytoskeletal remodeling of the actomyosin belt. A way to ultimately verify this hypothesis is accomplished by substituting the larger 'loser' cells in the dKD layer by WT cells with intrinsically lower contractility. If our assumption was correct, we would expect a separation into small, highly contractile cells, exclusively consisting of dKD cells, coexisting with outstretched WT cells, replacing the former 'loser' cells. This shifts the tug-of-war to more dKD cells assuming a compact morphology due to higher contractility. As a consequence, jamming is introduced into the co-culture by the over-contractile 'all-winning' dKD cells and migration speed diminishes accordingly.

Figure 4.7 shows the results of a co-culture analysis of a 1:1 mixture of WT and dKD cells at early and late-stage migration, respectively. WT cells that synthesize an intrinsic fluorophore (myosin-2 marked with GFP, green) were chosen to readily identify them in the co-culture. Figure 4.7A clearly shows that, after 20 h of migration, indeed two subpopulations emerge that can be unequivocally assigned to dKD cells (phase contrast with false color, magenta) and WT cells (green). After 20 h of migration, cells were allowed to migrate for another 6 h before the ROCK inhibitor Y27632 was added and incubated for 5 h (31 h overall migration, the last 5 h with 50 µM Y27632). This caused a dramatic relaxation and expansion of the dKD cells (Figure 4.7A) reducing the appearance of the two populations dramatically. During non-inhibited mix migration, the dKD cells are extremely small compared with the WT cells (see histogram, Figure 4.7B) and immobile rendering the whole layer less motile (boxplot in Figure 4.7B). Indeed, our working hypothesis that over-contractile small cells are immobile and thereby slow down the whole layer, while larger extensile cells are still rather mobile, was confirmed.

Specifically, co-cultures moved significantly slower than pure WT cells (12.0 ± 1.2 µm h^{-1} compared with 18.3 ± 2.9 µm h^{-1} (median ± s.d.), $p < 0.01$), which was indeed slowed down by the contracted dKD cells. The generally higher motility of the WT cells maintained an overall larger migration velocity within the co-cultures compared with a cell layer solely consisting of dKD cells (12.0 ± 1.2 µm h^{-1} compared with 7.1 ± 0.6 µm h^{-1} (median ± s.d.), $p < 0.01$). However, WT cells in the co-culture were also slowed down due to the low-motility dKD cells (15.3 ± 0.8 µm h^{-1} (WT in mixed layer), 18.3 ± 2.9 µm h^{-1} (pure WT) (median ± s.d.), $p < 0.05$). Lastly, the WT cells in the co-culture mix were still faster than the overall mix (15.3 ± 0.8 µm h^{-1} compared with 12.0 ± 1.2 µm h^{-1} (median ± s.d.), $p < 0.05$). Accordingly, in the tug-of-war the 'winners' (dKD) slow down and induce jamming while the 'loser' (here WT) cells maintain a certain amount of fluidity and motility.

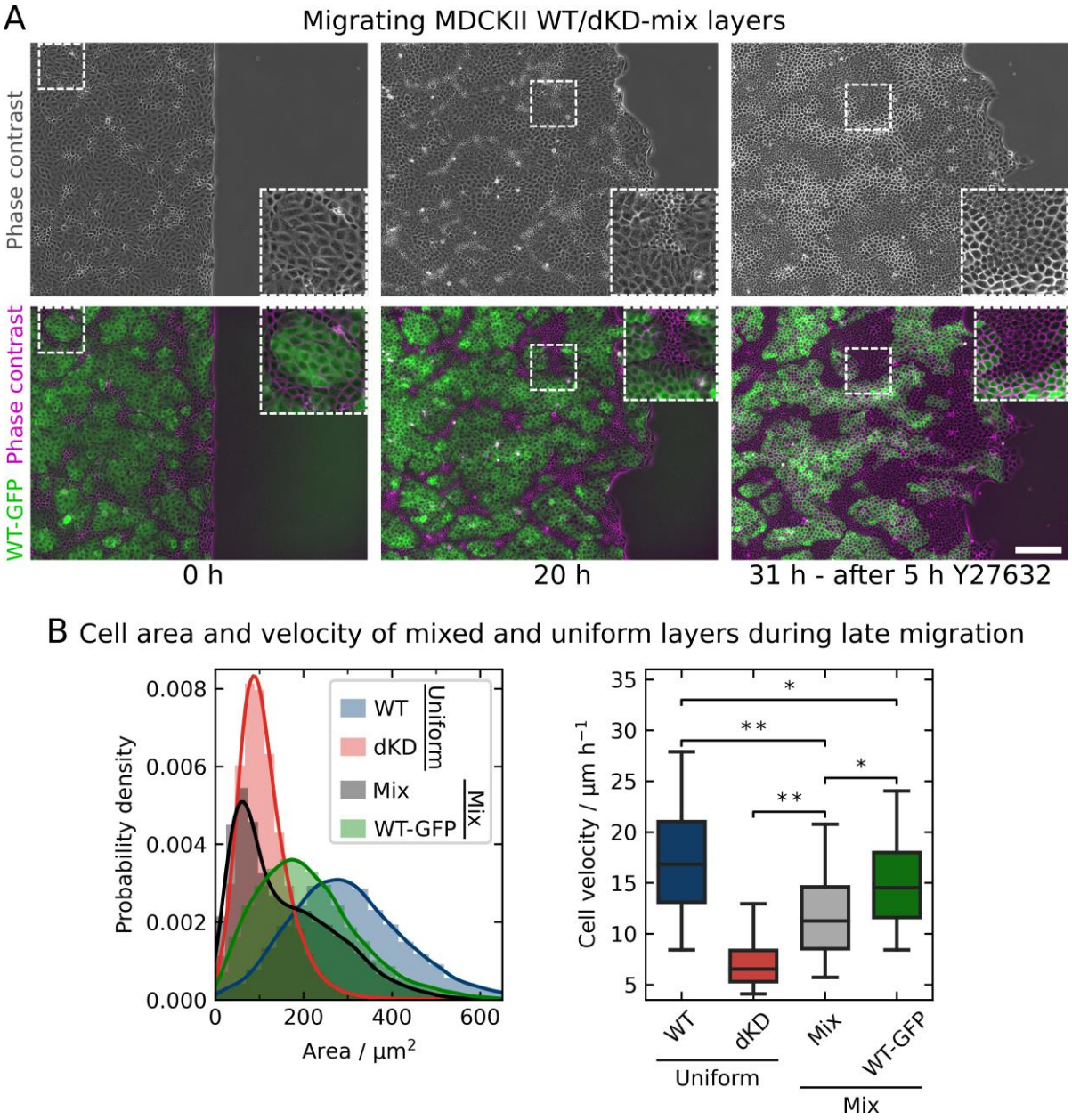

Figure 4.7: Co-cultures comprising WT and dKD cells in a 1:1 ratio migrate inefficiently due to phase separation based on differential contractility. A) Migrating cell monolayer examples of WT and dKD co-cultures at the start of migration, after 20 h of migration and after additional 11 h of migration, the latest 5 h of which with 50 µM Y27632. WT cells (stably transfected with GFP-myosin-2-A, called WT-GFP) are shown in green, WT-GFP and dKD cells (phase contrast with false-color) are shown in magenta. Cropped areas shown for better visibility. Scale bar: 200 µm. B) Quantification of the cell area and velocities in pure WT and dKD and a co-culture of both cell types in monolayers during late-stage migration (area at 20 h and velocities between 19 h and 21 h). The left hand shows the area distribution of uniform WT and dKD cultures, as well as the 1:1 mix co-culture of both and the WT-GFP cells contained in the co-culture migration. Cell velocities on the right hand side of the same cell (sub-) populations have been calculated as in Figure 4.2. Samples sizes (independent monolayers): WT: 13, dKD: 18, Mix: 4. The histogram and boxplot comprise individual cells. For more accurate statistical testing, cell velocities were first averaged over separate monolayers.

In summary, we found that addition of WT cells substituted the 'loser' cell population otherwise recruited from the dKD population, which is enforced in a tug-of-war between cell-cell and cell-matrix adhesion. This is distinct from phase separation based on differential adhesion between two cell types and has first been reported by Balasubramaniam et al. using WT MDCKII cells mixed with more contractile E-cadherin KO cells.[47] The majority of dKD cells within this mixture is now capable of adopting the preferred, condensed and highly contractile phenotype, while the WT cells maintain their extensile behavior. The presence of this jammed phase eventually slows down collective migration of the whole layer and the WT. This series of experiments clearly supports our mechanistic view of the role of ZO proteins not only as intracellular linkers that directly connect the actomyosin cytoskeleton with transmembrane adhesion proteins but also as regulators of apical tension. Once this delicate balance is perturbed by depletion of ZO proteins, a reorganization of the perijunctional actomyosin cytoskeleton into large thick cables of actomyosin occurs. Highly contractile and jammed cells emerge, which eventually lead to a partial jamming of the whole cell layer, exhibiting reduced migration speed.

4.3 DISCUSSION

In this study, we were able to show that efficient collective cell migration depends on the ZO proteins of TJs. We show that ZO protein loss leads to severe cellular crowding and eventually jamming, which is fostered by morphological, mechanical, and cytoskeletal integrity loss.

Essentially, we found that ZO protein loss leads to formation of thick and contractile perijunctional actomyosin cables. This is in line with previous characterizations of cells lacking ZO proteins.[1,4,8,11] Particularly, recent evidence suggests that TJs provide a negative mechanical feedback to the actomyosin cytoskeleton of individual cells in a layer, so that they do not contract and pull excessively.[1] Because this feedback loop is missing in our cell lines, it is expected that most individual cells contract in an uncontrolled manner.

Indeed, many cells contract excessively via the perijunctional actomyosin ring. The constriction of this ring leads to laterally smaller cells with a projected area in 2D of about 80 μm^2 that bulge out apically, presumably in order to maintain constant volume. Since actin is remodeled and potentially recruited from the cortex into these rings, the cortex is softened.

These observations are in line with recent studies showing similar actomyosin remodeling in conjunction with such morphological changes, particularly of the cell cap.[1,4,8,11] In general, actomyosin remodeling is known to determine cell mechanical as well as morphological adaptations.[48–50] Together, the dome-like apical membrane and the weakened cortex result in excess membrane area accompanied by lower prestress and higher fluidity while the actomyosin ring itself becomes extremely stiff as visible in our force maps.

In contrast to our observations of softening and fluidization of the cell body, former work by Cartagena-Rivera and coworkers report an overall tension and viscosity increase in ZO1/2 knockout cells.[2] However, experiments in this study either targeted cell junctions directly or were carried out with much larger probes (> 20 μm) than our conical indenters of only a few tens of nanometers. Therefore, their measurements are integrated over a larger area capturing the mechanical response from both the extremely stiff cell borders and the soft cell body, which might explain the controversial findings.[2] Another reason could be the fact that the authors used much longer cell growth times than us of over one week. Coupled with the uncontrolled proliferation, this might explain the discrepancies in the observed mechanical behavior: Upon long culturing times, the cell layer becomes increasingly dense and more small ‘winner’ cells, meaning more contractile cells and thereby actin rings per area which, in turn, will dominate the mechanical readout in those studies.

The balance between adhesion to the substrate or matrix and the intercellular tension leads to the coexistence of two subpopulations. Besides the small and contractile ‘winner’ cells a second population formed by large and outstretched ‘loser’ cells emerges displaying increased apical tension. This second cell phenotype occurs in ZO1/2 depleted dKD cells. It is generally characterized by: 1) a larger projected area of 150-250 μm^2, i.e., larger than most dKD cells but

smaller than average WT cells, 2) thinner perijunctional actomyosin rings, 3) a flattening of the apical cortex, and 4) much higher prestress T_0 and less excess membrane area than the small dKD cells. Hence, two mechanically and morphologically distinct but coexisting dKD cell phenotypes emerge with time. For clarity, we distinguish between these two phenotypes and refer to them as *small ('winner')* and *large ('loser')* dKD cells.

The perijunctional actin contraction of the small cells is presumably responsible for the flattening and stretching of neighboring cells, which become larger. In response, the large cells need to sacrifice some of the excess area stored in the apical cell membrane, explaining the smaller decrease in K_A in contrast to the smaller dKD cells. Similarly, the pulling force from the contractile small cells is reflected in the increase in T_0 in the large cells. Larger cells typically display larger tension due to lateral strain imposed from adjacent cells.[51] In essence, the small cells contract and thereby pull on the large cells and stretch them, balancing the forces across the cell layer.

However, the large cells are unable to escape from the tensile stress into the third dimension (which is further exemplified in 3D dKD cultures, where we do not observe a separation into small and large cells (data not shown)). As a consequence, the cells become laterally stressed and respond by proliferation (possibly by activation of the Hippo pathway through YAP signaling and/or though Piezo1)[40,41,52], which relaxes the lateral stress. In turn, the increased proliferation leads to higher cell densities and eventually to partial jamming, impairing cell migration.

We were able to further confirm this view by virtually substituting the larger 'loser' cells with WT cells monitoring the dynamics of co-cultures comprising dKD and WT cells in a ratio of 1:1 (Figure 4.7). The co-culture with WT cells allowed all highly contractile dKD cells to adopt a condensed and contracted shape with an almost circular perimeter, while the WT cells took the place of the 'loser' cells being stretched and forming the liquid-like phase, which still displays higher motility. The dKD cells assume a jammed, solid-like phase, which slows collective cell migration of both cell populations substantially. This tug-of-war mechanism, where phase separation happens and 'winner' cells stretch out 'loser' cells is in line with quite similar co-culture experiments of contractile and non-contractile cells by Ladoux and co-workers.[47] Essentially, we observe a similar contractility-driven phase separation as a consequence of activity differences rather than differential adhesion between the two cell types.

The observations of uncontrolled proliferation and mechanical imbalances are in line with the idea that TJs are both biological signaling hubs[53,54] and mechanical sensors.[1,3] Cell mechanics could be rescued by ROCK inhibition, identifying a crucial mechanosensitive pathway at play in ZO-depleted cells, which is in line with previous work.[4,55] Notably, Matsuzawa et al. similarly observed distinct subpopulations in ZO1/2-depleted epithelial cells as well as WT/ZO-dKD mixes, which could be resolved by ROCK inhibition.[55] Regarding proliferation, ZO proteins have been shown to directly control proliferation through cell cycle arrest.[56,57] On the other hand, Rosenblatt and coworkers recently showed that mechanically stretched MDCKII cells divide more frequently than unstressed cells.[52] Mechanical stretch itself rapidly stimulates cell proliferation through activation

of the Piezo1 ion channel.[52] We propose that the contractile smaller cells provide exactly this kind of mechanical stimulus leading to cell divisions primarily of the larger, flat cells, which are stretched considerably.

This proliferation and cell density increase coupled with the mechanical changes of individual cells leads to migration disruption and jamming. Strikingly, evidence accumulates that particularly smaller cells are responsible for the onset of jamming in dKD cells.

Specifically, the differences in the jamming expansion of KO and dKD cells, respectively, can only be explained by the area-dependence of active migration on the individual cell area. While the KO and WT cells display the same fast and active dynamics regardless of their cell area, dKD cells become increasingly less dynamic with decreasing cell areas. Particularly, the small dKD cells, which constitute the majority, show passive diffusion-like behavior with a power law exponent of about 1, whereas the larger cells display active motion with a similar exponent to the WT cells of about 1.8. Accordingly, the small cells are particularly immobile and thereby impair the migration of the whole dKD layer.

Together, these results draw the following picture (Figure 4.8): dKD cells respond to lack of TJ proteins by remodeling of the perijunctional actomyosin into thick sarcomeric ring-like structure that contract excessively. The contraction leads to two coexisting subpopulations of cells: Small contractile cells pull on their neighbors, thereby generating so-called 'loser cells' that exhibit a large elongated footprint to maintain a maximized adhesion area. In response to external pulling they show an increased apical tension since they are not able to escape into the third dimension (the two subpopulations are not observed in 3D cell culture). The large cells respond to the lateral stress by proliferation leading to even more small cells and eventually to crowding because a higher cell density allows the cells to transfer more and more cells into the subpopulation of small and immobile cells.

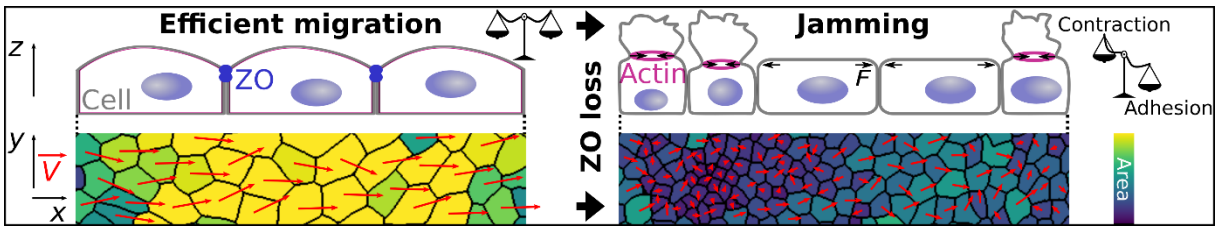

Figure 4.8: Proposed model of the delicate force balance necessary for cell layer fluidity. WT cells display a balance equilibrium between contraction and adhesion, and, thus, display a homogenous morphology and can migrate efficiently (left). In contrast, cells lacking ZO proteins develop a new and perturbed force balance leading to heterogeneous cell morphology and jamming (right). Two cell populations emerge: small, highly contractile cells with apically bulged-out excess membrane and large, stretched cells. The small cell population is particularly immobile and additional crowding amplifies this jamming.

On a mesoscopic scale, both migration velocity and order are diminished in ZO1/2 dKD cells and, upon progressing migration and proliferation, also in ZO1 KO cells. This is in line with recent work showing the deceleration of migration in cells lacking ZO proteins.[5,58] For instance, endothelial cells lacking ZO1 were shown to migrate slower.[5] For MDCKII cells, Fedele et al. found that the migration dynamics of monolayers with already inhibited adherens junctions are diminished upon ZO1/2 double knockout.[58] In addition, ZO protein loss significantly shortens the spatial velocity correlation length. Along the same line, the KO and particularly the dKD monolayers develop more individual leader cells. Both velocity correlation and leader cell emergence were implicated as hallmarks of collective cell behavior and mechanical coupling.[15,27,32,59,60] Accordingly, cells lacking ZO proteins behave less collectively and exhibit perturbed mechanical coupling.

Yet, since cell mechanics and proliferation are tightly coupled, the relative impact of each on the stalled migration remains to be elucidated. Therefore, we investigated the peculiar relationship between cell mechanics and cell density by inhibiting proliferation. In line with recent studies, proliferation inhibition slightly increases migration speed in WT MDCK cells.[20,22] Strikingly, inhibiting the proliferation of dKD cells succeeds in almost complete recovery of the migration velocity, order, and correlation length observed for WT cells. This underlines the importance of the mechanically induced proliferation and cell crowding as a decisive control parameter for collective migration. However, it is conceivable that upon inhibited proliferation, the 'loser' cells cannot be stretched as easily anymore due to missing mitotic rounding forces and increased interphase growth of small dKDs, which might partly restore the mechanical balance.[61]

The observation that MDCK cells at low densities show such a high, and at higher densities a significantly lower power law exponent is shared by recent experimental evidence.[62,63] This general effect of cell density on collective migration dynamics is also in line with physical particle-based models of tissue dynamics.[39] These models predict cell density to be the main determinant parameter for collective motility with motion arrest at high densities. However, to our knowledge, the direct dependence of cell motility of individual cells in a monolayer on their projected area has not been observed experimentally before.

Interestingly, the cell shape (projected aspect ratio in 2D), as predicted by vertex-based models, does not seem to be the decisive parameter in contrast to the cell area itself. Particularly, while we do see a slight shift towards lower overall aspect ratios, we do not observe a clear dependency of the motility of individual cells on the aspect ratio as on the area. It is important to note that instead of addressing the aspect ratio of individual cells, current models focus on the properties of monolayers as a bulk. However, as Devany et al. showed in simulations and experiments that absolute changes of the cell shape can vary greatly and could thus be inconclusive, depending on the experimental situation.[63] Importantly, Saraswathibhatla and Notbohm found a correlation between cell density, shape, and motility.[62] While we only observe small changes in cell shape, we do observe a similar impact of cell density.

In addition, most studies identifying the cell shape as the predictive parameter for cell motility worked with other cell types and on longer times scales. Typically, fully polarized cells, such as airways smooth muscle cells cultivated for several days and up to weeks, were used, whereas our MDCKII cells only had about 28 h to grow to full (over-)confluence.[21,26,64] Studies working with (ZO protein-inhibited) MDCK or MCF10A lines also cultivated the cells much longer,[2,65] which in conjunction with the observed uncontrolled proliferation could explain the density-related discrepancies. Furthermore, related studies investigated the motion of confluent cell layers, whereas we focused on freely migrating epithelia.[21,26,31,62,64,65]

4.4 CONCLUSION

We showed that ZO proteins are not only crucial for barrier function but also required for efficient collective cell migration of epithelial monolayers. Our results draw the following picture of the impact of ZO1 and 2 protein loss: Due to missing mechanical feedback from ZO1/2, a thick actomyosin ring builds at the cell periphery that leads to strong contraction of individual cells, constricting the apical cell cortex and leading to in- or outward bulging. In order to keep the adhesion to the substrate not all cells can adopt this morphology and competition between contractility and adhesion emerges. As a consequence, two subpopulations of cell phenotypes arise in ZO1 and 2 depleted cells after a few hours of migration: 1) Small contractile cells ('winners') with an apically bulged-out and softened cortex and 2) large, flat cells ('losers') with an elevated prestress. The larger cells respond to the mechanical stimulus from the highly contractile neighbors by increased proliferation, leading to more immobile 'winner' cells and eventually to crowding that slows down migration of the cell sheet. We conclude that functioning tight junctions are necessary for tension homeostasis to maintain fluidity of epithelial monolayers and thereby guarantee for fast and coherent cell migration.

4.5 MATERIALS AND METHODS

4.5.1 CELL CULTURE

Madin-Darby Canine Kidney cells (strain II, MDCKII; European Collection of Authenticated Cell Cultures, Salisbury, UK) were cultured in minimum essential medium (MEM; Life Technologies, Paisley, UK) containing Earle's salts, 2 mM GlutaMAX™ (ThermoFisher Scientific, Waltham, Massachusetts, USA), 2.2 g/L $NaHCO_3$, and 10% fetal bovine serum (FCS; BioWest, Nuaillé, France), called $M10F^-$ in the following, at 37°C and 5% CO_2 in a humidified incubator. The cells were passaged before reaching confluence two to three times per week using phosphate buffered saline pH 7.4 (PBS^-; Biochrom, Berlin, Germany) containing trypsin/EDTA (0.25%/0.02% w/v; BioWest/Biochrom).

4.5.2 GENETIC MODIFICATION OF ZO PROTEINS

ZO knockdowns were effected as described in Beutel et al.[45] To knockdown ZO1 and ZO2 in MDCKII cells, frame-shift mutations were introduced at the N-termini by CRISPR/Cas9. The following RNA guides (gRNA) were used for ZO1: ACACACAGTGACGCTTCACA and ZO2: GTACACTGTGACCCTACAAA. Selected DNA oligos and their trans-encoded RNA (TRCR) were purchased from Integrated DNA Technologies. Each gRNA was annealed for 1h at room temperature with its TRCR. To finally generate the riboprotein complex, the gRNA/TRCR complex was incubated with homemade purified Cas9. Electroporation of each complex was performed in 300,000 cells (Invitrogen NEON electroporation machine and kit, 2 pulses, 20 ns, 1200 V). Single cells were sorted after 48 h by FACS (fluorescence activated cell sorting) and grown clonally. The genomic sequence of the genes of interests were sequenced and only clones carrying homozygous frame-shifts leading to an early stop codon were kept. To generate a combined ZO1/ZO2 knockdown KD line, we first created a ZO1 knockout and then we targeted ZO2. The ZO1 KO clone was mutant for two alleles, both alleles have a 1 bp insertion in the guide region (ACACACAGTGACGCTTC-1 bp insertion-ACAGGG) leading to an early stop of translation. The ZO2 KD has 5 bp deletion at the end of the guide region (GTACACTGTGACCCTACA-5 bp deletion-GG) leading to an early stop. Immunostaining and western-blot analysis showed that ZO1 and ZO2 presented a residual expression level of the full-length protein equal to 2-3% of the WT line expression level (Fig. S5 in Beutel et al.).

4.5.3 GENERATION OF MDCKII WT-GFP CELLS

Clones of MDCKII expressing GFP-myosin-2-A were created by transfecting cells with pTRA-GFP-NMCH II-A plasmid (Addgene plasmid # 10844). Stable expressing clones were selected via

Neomycin resistance (G418). After selection, the cell pool was sorted by FACS to enrich for cells expressing GFP at a moderate level.

4.5.4 CELL MIGRATION EXPERIMENTS

For migration experiments Petri dishes with a culture-insert (Culture-Insert 2 Well in µ-Dish 35 mm, ibiTreat #1.5 polymer cover slip; ibidi, Martinsried, Germany) were used. Cells were seeded at 4 10^5 cells in 1 mL M10F$^-$ on the outside of the insert and grown to (over-) confluence for 28 h (± 1.5 h). WT-GFP/dKD co-cultures were trypsinized and mixed well before being seeded simultaneously at 2 10^5 each (1:1 ratio) and grown as described above. Upon visual inspection, the insert was removed, the cells were rinsed with M10F$^-$, supplied with sufficient M10F$^-$ (2-3 mL), and placed into the incubation system of an inverted optical microscope (BZ-X810; Keyence, Neu-Isenburg, Germany) equipped with a 10X phase contrast objective (Nikon CFI60 Series; Keyence). The temperature was calibrated to be 37°C at the cell sample using a local temperature measurement instrument (Testo 735; Testo, Lenzkirch, Germany), a partial CO_2 pressure of 5% was chosen, and sufficient humidity was ensured by injecting distilled water into the incubator appliance. Phase contrast frames were recorded at 1 frame/2.5 min, 14 bit, 25% illumination power, typical exposure times of about 1/25 s, and without zoom, gain, or binning. Focus tracking was applied and three vertical slices were chosen in a range of 5 µm to avoid drift effects. The cell edge was carefully aligned vertically and set to be at a similar position for all experiments. Typically, migration was observed overnight for 20-30 h.

4.5.5 MITOMYCIN C TREATMENT

Mitomycin C (MitoC; Sigma-Aldrich, Steinheim, Germany) was dissolved in water to reach 500 µg mL^{-1} and stored in aliquots of 150 µL.

Cell seeding was performed as described above. The samples were rinsed once and then incubated with M10F$^-$ containing 10 µg mL^{-1} of MitoC at 37°C and 5% CO2 for 1 h. Then, the insert was removed after about 28 h growth time (± 1.5 h). To remove any extruded cells and, most importantly, to prevent the cytotoxic effects of Mytomycin C occurring after 12 h of exposure,[18] samples were rinsed with 1 mL M10F$^-$ three times, before the dishes were filled with 2-3 mL M10F$^-$ and then imaged as described above.

4.5.6 ROCK INHIBITION BY Y27632 TREATMENT

Y27632 (”InSolution” Y27632; Sigma-Aldrich) was diluted in M10F$^-$ to the desired concentration, cells were rinsed once and then incubated in the Y27632-containing medium. In the case of continuous treatments, 30 min of incubation was allowed before insert removal, cells were rinsed again and 2-3 mL Y27632-containing medium was added.

4.5.7 EXPERIMENTS WITH NON-MIGRATING MONOLAYERS

5 10^5 cells were seeded in 4 mL M10F$^-$ and placed on the same microscope as above and the same conditions as for the migration experiments were used but without an insert. Four areas per sample were imaged every hour with the same settings as above. Two WT samples, one KO and one dKD sample were recorded. Analysis was performed as described below.

4.5.8 MIGRATION DATA ANALYSIS

First, migration phase contrast movies were down-sampled to 1 frame/7.5 min to ensure good PIV (particle image velocimetry) quality. Velocity vector maps were obtained using the Matlab (MathWorks, Natick, USA) -based PIV tool AVeMap from Deforet et al.[35] A window size of 32 x 32 pixels corresponding to 24.16 µm x 24.16 µm with an overlap of 0.5 was used, yielding a vector mesh size of 16 pixels (12.08 µm). The first row width was set to 12.08 µm and typical mask parameters were 0.60-0.75. The default filters of 1.1 signal-to-noise ratio, 0.3 peak height, and 4 global filtering were used. A PIV quality of > 0.8 was achieved for all data and exemplarily checked by visual inspection. The order parameter was defined as $\cos\alpha$, where α is the angle between the local velocity vector and the normal to the average migration direction, according to Deforet et al. The add-on AVeMap+ was used to analyze the data with respect to the distance from the migration edge. Note, the first two to three data points are not shown due to a known edge-induced artefact.[66]

Vector fields were further analyzed using home-written Python scripts. Before correlation functions were calculated, the leader cell fingers were cut from the vector fields to yield rectangular input data for the spatial correlation and to avoid edge-induced artefacts.

The correlation function was calculated for each time point individually: The 2D spatial autocorrelation AC of the velocity vector field was calculated based on Petitjean et al. using the Scipy function signal.correlate2d:[32,67]

$$AC(\vec{r},t) = \langle v(\vec{r}'+\vec{r},t) \times v(\vec{r}',t)\rangle \tag{4.1}$$

With the deviation of the y-component (perpendicular to the migration direction) $v = v_i - \langle v\rangle$, which is corrected by the offset $\langle v\rangle$, of the vector $\vec{r}$ at time point t. The brackets denote averaging over all vectors. Additionally, the AC is normalized by its maximum, so that it starts from one. To gain a one-dimensional function, the 2D correlation function was then radially averaged in space. The correlation function was finally averaged for each migration movie over time.

The correlation length was defined as the integral over the weighted spatial correlation function $AC(r)$:

$$\int_0^\infty \vec{r} \cdot AC(\vec{r})\, d\vec{r} \tag{4.2}$$

To exclude any anti-correlation artefacts ($AC < 0$) at large distances, the curves were integrated only up to the first *x*-intercept for all analyses.

The amount of leader cells was determined from the phase contrast movies manually. Leader cells were defined by their position at a protrusion in the front of the leading edge, an increased cell size compared with bulk cells, and a lamellipodium towards the empty space.

4.5.9 Automated Cell Segmentation

The deep learning-based cell segmentation algorithm Cellpose (Stringer et al.[38]) was used to extract a mask and an outline for each individual cell body in an image. The model type was set to *cyto* and the grayscale phase contrast images were used as input. Before segmentation, the image contrast was auto-corrected using Fiji to facilitate optimal cell recognition.[68] In order to accurately capture all cells in the layer, the flow and cell probability thresholds were set to 1 and -6, respectively, for the phase contrast monolayer images. The parameters for other analyses were set as follows: Single cell phase contrast: 0.7 and -2. Mixed monolayer GFP-fluorescence-channel: 0.95 and -5. Confocal YAP- and corresponding DAPI-images: 0.4 and 0 (Cellpose default values). Confocal actin-images: 0.7 and -2. Diameters were detected automatically, except for confocal images, where they were pre-adjusted by visual inspection.

We found these parameters to be optimal for our images, because smaller (or larger, respectively) values resulted in missed cells. No novel model training was necessary. The input diameter was estimated automatically for every image individually by the software.

4.5.10 Cell Area, Position, and Aspect Ratio Calculation and Processing

For every segmented image, the masks array and the outlines array were extracted from the returned segmentation dictionary. The arrays were normalized, so that ones specified cell bodies (or cell outlines) and zeros empty space, respectively. The outlines were subtracted from the masks to prevent overlap of cells. The resulting array was converted into the data type uint8 and scaled up to a value of 255. The array was then subjected to a threshold at a value of 127 and binarized using the image processing library OpenCV.[69] The arrays were then transposed into vectors of coordinates specifying the outer contour of each cell using the function *findContours* of OpenCV.[69] Only outer contours were extracted and the Teh-Chin chain approximation algorithm was applied to save memory.[70] On the basis of the extracted vectors, the area of each cell was computed using the function contourArea of OpenCV. The moments function was used to determine the center of each cell, yielding the positions later used by Trackpy. Cell density was

calculated dividing the number of segmented cells by the area occupied by the monolayer (either the mask obtained from AVeMap or the whole field of view).

To determine cell aspect ratios (length/width), two approaches were utilized to define the front-rear (anterior-posterior) axis for each individual cell. First, the fitEllipse function of OpenCV was used for every given set of coordinates to compute and fit an ellipse to the 2D points. Since this function works by fitting the coordinates in a least-squares approach, it was found that the algorithm seemed to be biased towards high aspect ratios for some cell shapes. Therefore, the function minAreaRect was used to verify the results by calculating a rotated minimum-area rectangle enclosing the respective set of coordinates. This procedure, however, seemed to be biased towards low aspect ratios for the aforementioned cell shapes. Accordingly, we computed the aspect ratio with both algorithms independently and then used the mean for every cell in each image individually. The validity of this approach was verified by visual inspection of overlaid input and output images.

4.5.11 Cell Tracking and Analysis

Single cell tracking was performed with the cell positions calculated before by the OpenCV moments function (vide supra). Trackpy was used to link the cell positions, yielding individual tracks.[71,72] The link function was used with a memory of 4 frames and 4.6 or 5.7 μm² (8 or 10 pixels) as maximal displacement (10 frames and 20 pixels for single cell migration). The resulting trajectories were filtered, so that only the ones that persisted for at least 5 frames were kept, to avoid spurious trajectories. No drift correction was necessary. The temporal resolution was 1/7.5 min for all monolayer data and 1/2.5 min for the single cells. Cell velocities were calculated for each cell by averaging over all time steps, which automatically normalizes for the different frame rates.

Mean squared displacements (*MSD*s) were calculated using the ensemble *MSD* function of Trackpy as:

$$MSD(\tau) = \langle (x(t+\tau) - x(t))^2 \rangle \tag{4.3}$$

The brackets denote averaging over time and over all cells. Before calculation and fitting of the *MSD*s, the trajectories were filtered by discrete bins of 100 μm² cell area (see Figure 4.2 and Figure 4.3) or 0.25 aspect ratio (see Figure S 4.1 and Figure S 4.2). *MSD*s were fitted by a power law of the form $MSD(\tau) = a\,\tau^n$ with a power law exponent *n* and an offset *a* using a linear regression in logarithmic space implemented in Trackpy.

4.5.12 AFM-Based Force Spectroscopy

Force spectroscopic indentation measurements were carried out with a NanoWizard 4 (JPK Instruments, Berlin, Germany) mounted on an inverted microscope (IX 81; Olympus, Tokyo, Japan) using silicon nitride cantilevers with a nominal spring constant of 0.01 N m^{-1} (MLCT C; Bruker AFM Probes, Camarillo, USA). Before an experiment, cantilevers were rinsed with isopropanol and PBS^- as well as incubated with fluorescein isothiocyanate-conjugated Concanavalin A solution (2.5 mg mL^{-1} in PBS^-; Sigma-Aldrich) for 1 h.

The sensitivity of the AFM was determined by recording force curves in the empty space without cells and the exact spring constant of each cantilever was determined by the thermal noise method.[73] Approximately 20 h after removing the insert (vide supra), cells were rinsed three times with $M10F^-$ containing 0.2 mg mL^{-1} Penicillin (Biochrom), 0.2 mg mL^{-1} Streptomycin (Biochrom), and 15 mM HEPES ($M10F^+$; BioWest).

For the measurements, samples were mounted on the AFM stage, 2.5 mL $M10F^+$ was supplied, and the heater (JPK Instruments) was set to 37°C. The cells were indented at a constant speed of 2 µm s^{-1} to maximum force of 1 nN. After a dwell time of 0.5 s at constant height the indenter was retracted at the same speed. Force maps of 25 pixels x 25 pixels in an area of 50 µm x 50 µm were recorded by lateral scanning across the sample recording one force indentation cycle at each pixel. Additionally, five consecutive force curves in the center of individual cells in the monolayer were acquired using the same parameters.

4.5.13 Force Curve Analysis and Mechanical Model

Generally, force-relaxation curves were recorded as detailed previously.[46] After indentation of the center of the cell with a velocity of 2 µm s^{-1} to avoid artefacts from hydrodynamic drag acting on the cantilever, we switched off the constant force feedback loop and kept the system at constant height. During this time the decrease of cantilever deflection is monitored as a function of time (for 0.5 s). We used the same MLCT C cantilevers as for imaging (vide infra). The curves were modeled using a theory introduced recently.[46,74] Briefly, the surfaces of the confluent MDCKII cells are described as capped cylinders. The average geometry as derived from AFM imaging was employed to describe the apical cap of the deformed cells in terms of contact angle and radius of the basis. Generally, we consider the cell as a liquid-filled object surrounded by an isotropic viscoelastic shell deformed at constant volume. The force *F* acting on the apex of the cell is given by:

$$F = 2\pi \left({R_1}^2 \left(\frac{R_1 \sin\phi + r_1 \sin\theta}{{R_1}^2 - {r_1}^2} \right) - R_1 \sin\phi \right) T(t) \tag{4.4}$$

with R_1, the radius at the base of the spherical cap and ϕ the contact angle in response to deformation. r_1 is the contact radius with the conical indenter, $\theta = \pi/2 - \vartheta$ with ϑ, the cone half angle. The following apical cap geometries were used. WT: R_1 = 10 µm, ϕ = 10°. KO: R_1 = 8 µm, ϕ = 20°. Small dKD: R_1 = 5 µm, ϕ = 31°. Large dKD: R_1 = 8 µm, ϕ = 2°.

Viscoelasticity of the shell enters the tension term $T(t)$ through a time dependent area compressibility modulus $K_\mathrm{A} = {K_\mathrm{A}}^0 (t/t_0)^{-\beta}$. Now we need to solve a set of nonlinear equations for the shape of the deformed cell to fulfill force balances and the constant volume boundary condition. The resulting shapes are minimal surfaces to minimize the stretching energy. Membrane tension T_t was calculated from the tether rupture force F_t at the end of the retraction curve with the bending modulus $\kappa = 2.7 \cdot 10^{-19}$ J via [75–77]

$$T_\mathrm{t} = \frac{F_\mathrm{t}^2}{8\pi^2 \kappa}. \tag{4.5}$$

Analysis was performed using self-written Python and Matlab scripts in combination with the JPK SPM Data Processing (JPK Instruments / Bruker) software. The baseline was corrected by a linear fit before contact. The contact point was determined individually using the JPK SPM Data Processing. Tether forces were acquired with the same software.

4.5.14 AFM Imaging

Approximately 20 h after removing the insert (vide supra), cells were rinsed three times with PBS containing 0.1 g L^{-1} Mg^{2+} and 0.133 g L^{-1} Ca^{2+} (PBS^{++}; Sigma-Aldrich) and incubated with glutaraldehyde solution (2.5% (v/v) in PBS^{++}) for 20 min. PBS^{++} was used instead of PBS without magnesium and calcium ions, because live dKD and KO cells were more prone to dissolution of ion-dependent adhesions upon rinsing due to the missing diffusion barrier function. Before imaging, the samples were rinsed again three times to remove residual glutaraldehyde. Cell imaging was performed using a NanoWizard III (JPK Instruments) mounted on an inverted optical microscope (IX 81; Olympus) to enable additional visual inspection via phase contrast. Imaging was carried out as described in Brückner et al.[49] in contact mode using MLCT C cantilevers (Bruker AFM Probes) in PBS^{++} with typical line scan rates of about 0.3 Hz and typical forces of 0.1 nN. Height and error images were obtained using the JPK SPM Data Processing software provided by the manufacturer.

4.5.15 Cell Labeling and Fluorescence Microscopy

Prior to cell labeling, cells were fixed by incubation with paraformaldehyde/glutaraldehyde solution (4% (w/v)/0.1% (w/v) in PBS^-; Science Services, Munich, Germany/Sigma-Aldrich) for 20 min. To permeabilize the cellular plasma membrane, samples were incubated with 0.1% (v/v)

Triton X-100 in PBS^- for 5 min. After three rinsing steps with 1 mL PBS^- each, to block unspecific binding sites, cells were incubated with blocking/dilution buffer (PBS^- containing 2% (w/v) bovine serum albumin and 0.1% (v/v) Tween20) for 30 min.

For ZO1 staining, a fluorophore-conjugated primary antibody (mouse ZO1-1A12 IgG1 AlexaFluor488; Invitrogen, ThermoFisher Scientific, Waltham, Massachusetts, USA) was diluted with blocking/dilution buffer to a concentration of 5 μg mL^{-1} and cells were incubated for 1 h. For all other proteins, the following primary antibodies were diluted in blocking/dilution buffer.

ZO2: 1 μg mL^{-1} Clone 3E8D9 mouse IgG1; Invitrogen. *Phospho-myosin*: 1:200 light chain 2 (Ser 19) rabbit IgG1; Cell Signaling Technology, Danvers, Massachusetts, USA. *E-cadherin*: 1:50 Clone 36 mouse IgG1; BD Biosciences, Heidelberg, Germany. *ß-catenin*: 5 μg mL^{-1} mouse IgG1; BD Biosciences. *Occludin*: 6.5 μg mL^{-1} EPR20992 rabbit IgG; Abcam, Cambridge, UK. *Claudin 1*: 11.6 μg mL^{-1} rabbit IgG; Abcam. *YAP*: 1:100 (5-10 μg mL^{-1}) Anti-YAP1 rabbit, SAB2108066; Sigma-Aldrich.

After the primary antibody, cells were rinsed briefly with PBS^-, and then washed with PBS^-, with 0.1% (v/v) Triton X-100 in PBS^- and again with PBS^- for 5 min each on a shaker plate (75 rpm). The secondary antibody (AlexaFluor488- or AlexaFluor546-conjugated goat anti-mouse or anti-rabbit IgG; Life Technologies, Carlsbad, USA) was diluted with blocking/dilution buffer to a concentration of 5 μg mL^{-1}. The cells were incubated for 1 h. Actin labeling was performed using AlexaFluor488- or AlexaFluor546-phalloidin (Invitrogen), diluted together with the secondary antibody in blocking/dilution buffer to a concentration of 165 nM. Incubation time: 45 min. Following the secondary antibody, samples were washed with PBS^- for 5 min each on a shaker plate (75 rpm). Nucleus staining was performed by incubation with Hoechst 33342 (Invitrogen), diluted to 1 μg mL^{-1}, for 15 min. For imaging, samples were rinsed three times with PBS^- and kept in PBS^-. All labeling steps were performed at room temperature.

A confocal laser scanning microscope (FluoView1200; Olympus), equipped with a 60X oil immersion objective (*NA* = 1.25), was used for fluorescence imaging. Image processing, brightness adjustment, and analysis was performed using Fiji.[68]

4.5.16 Nucleus/Cytoplasm-Localization Quantification of YAP

As described above, Cellpose was used to segment the cytoplasm and nucleus for each cell in a confocal image of the central plane. Segments were used as masks to extract the respective intensities (YAP in the cytoplasm and nucleus) from the original image. For each cell, the mean intensity in the nucleus was divided by the mean intensity in the whole cell, yielding a ratio between nucleus and cytoplasm, i.e., the relative nucleus localization of YAP. Values above 1, which resulted from false segmentation, were excluded from the results.

4.5.17 Cell Volume Analysis

The base cell area was determined using Cellpose and OpenCV at the basal side of the cell from confocal actin-images. The cell height was determined visually from side views in Fiji. Cell volume was calculated by multiplying area and height. Lastly, the theoretical isotropic expansion was calculated for a cylinder, considering proportionally even changes in radius and height.

4.5.18 Statistical Analyses

The data were tested for normality using the Shapiro-Wilk test. Because for none of the PIV-based data (Figure 4.1, and Figure 4.3B) the null hypothesis of a normal distribution was rejected (at the $p < 0.05$ level), significance was tested using Welch's t-test. The Mann-Whitney U test was applied to the rest of the data to accommodate non-normality. All statistical analyses were performed in Python.

A p-value of < 0.05 was considered significant and denoted by one asterisk (*), $p < 0.01$ and $p < 0.001$ we indicated by two (**) and three (***) asterisks, respectively.

4.6 REFERENCES

1. Hatte, G., Prigent, C. & Tassan, J.-P. Tight junctions negatively regulate mechanical forces applied to adherens junctions in vertebrate epithelial tissue. *J. Cell Sci.* **131**, jcs208736 (2018).
2. Cartagena-Rivera, A. X., Itallie, C. M. V., Anderson, J. M. & Chadwick, R. S. Apical surface supracellular mechanical properties in polarized epithelium using noninvasive acoustic force spectroscopy. *Nat. Commun.* **8**, 1–12 (2017).
3. Spadaro, D. *et al.* Tension-Dependent Stretching Activates ZO-1 to Control the Junctional Localization of Its Interactors. *Curr. Biol.* **27**, 3783-3795.e8 (2017).
4. Choi, W. *et al.* Remodeling the zonula adherens in response to tension and the role of afadin in this response. *J. Cell Biol.* **213**, 243–260 (2016).
5. Tornavaca, O. *et al.* ZO-1 controls endothelial adherens junctions, cell–cell tension, angiogenesis, and barrier formation. *J. Cell Biol.* **208**, 821–838 (2015).
6. Citi, S. The mechanobiology of tight junctions. *Biophys. Rev.* (2019) doi:10.1007/s12551-019-00582-7.
7. Brückner, B. R. & Janshoff, A. Importance of integrity of cell-cell junctions for the mechanics of confluent MDCK II cells. *Sci. Rep.* **8**, 14117 (2018).
8. Odenwald, M. A. *et al.* The scaffolding protein ZO-1 coordinates actomyosin and epithelial apical specializations *in vitro* and *in vivo*. *J. Biol. Chem.* **293**, 17317–17335 (2018).
9. Odenwald, M. A. *et al.* ZO-1 interactions with F-actin and occludin direct epithelial polarization and single lumen specification in 3D culture. *J. Cell Sci.* **130**, 243–259 (2017).
10. Fanning, A. S., Jameson, B. J., Jesaitis, L. A. & Anderson, J. M. The tight junction protein ZO-1 establishes a link between the transmembrane protein occludin and the actin cytoskeleton. *J. Biol. Chem.* **273**, 29745–29753 (1998).
11. Fanning, A. S., Van Itallie, C. M. & Anderson, J. M. Zonula occludens-1 and -2 regulate apical cell structure and the zonula adherens cytoskeleton in polarized epithelia. *Mol. Biol. Cell* **23**, 577–590 (2011).
12. Tokuda, S., Higashi, T. & Furuse, M. ZO-1 knockout by TALEN-mediated gene targeting in MDCK cells: involvement of ZO-1 in the regulation of cytoskeleton and cell shape. *PLOS One* **9**, e104994 (2014).
13. Jain, S. *et al.* The role of single-cell mechanical behaviour and polarity in driving collective cell migration. *Nat. Phys.* (2020) doi:10.1038/s41567-020-0875-z.
14. Sunyer, R. *et al.* Collective cell durotaxis emerges from long-range intercellular force transmission. *Science* **353**, 1157–1161 (2016).
15. Reffay, M. *et al.* Interplay of RhoA and mechanical forces in collective cell migration driven by leader cells. *Nat. Cell Biol.* **16**, 217–223 (2014).

16. Anon, E. *et al.* Cell crawling mediates collective cell migration to close undamaged epithelial gaps. *Proc. Natl. Acad. Sci.* **109**, 10891–10896 (2012).
17. Trepat, X. *et al.* Physical forces during collective cell migration. *Nat. Phys.* **5**, 426–430 (2009).
18. Poujade, M. *et al.* Collective migration of an epithelial monolayer in response to a model wound. *Proc. Natl. Acad. Sci.* **104**, 15988–15993 (2007).
19. Karsch, S., Kong, D., Großhans, J. & Janshoff, A. Single-Cell Defects Cause a Long-Range Mechanical Response in a Confluent Epithelial Cell Layer. *Biophys. J.* **113**, 2601–2608 (2017).
20. Gauquelin, E. *et al.* Influence of proliferation on the motions of epithelial monolayers invading adherent strips. *Soft Matter* **15**, 2798–2810 (2019).
21. Atia, L. *et al.* Geometric constraints during epithelial jamming. *Nat. Phys.* **14**, 613–620 (2018).
22. Tlili, S. *et al.* Collective cell migration without proliferation: density determines cell velocity and wave velocity. *R. Soc. Open Sci.* **5**, 172421 (2018).
23. Malinverno, C. *et al.* Endocytic reawakening of motility in jammed epithelia. *Nat. Mater.* **16**, 587–596 (2017).
24. Bi, D., Yang, X., Marchetti, M. C. & Manning, M. L. Motility-Driven Glass and Jamming Transitions in Biological Tissues. *Phys. Rev. X* **6**, 021011 (2016).
25. Notbohm, J. *et al.* Cellular Contraction and Polarization Drive Collective Cellular Motion. *Biophys. J.* **110**, 2729–2738 (2016).
26. Park, J.-A. *et al.* Unjamming and cell shape in the asthmatic airway epithelium. *Nat. Mater.* **14**, 1040–1048 (2015).
27. Garcia, S. *et al.* Physics of active jamming during collective cellular motion in a monolayer. *Proc. Natl. Acad. Sci.* **112**, 15314–15319 (2015).
28. Bazellières, E. *et al.* Control of cell–cell forces and collective cell dynamics by the intercellular adhesome. *Nat. Cell Biol.* **17**, 409–420 (2015).
29. Sadati, M., Taheri Qazvini, N., Krishnan, R., Park, C. Y. & Fredberg, J. J. Collective migration and cell jamming. *Differentiation* **86**, 121–125 (2013).
30. Tambe, D. T. *et al.* Collective cell guidance by cooperative intercellular forces. *Nat. Mater.* **10**, 469–475 (2011).
31. Angelini, T. E. *et al.* Glass-like dynamics of collective cell migration. *Proc. Natl. Acad. Sci.* **108**, 4714–4719 (2011).
32. Petitjean, L. *et al.* Velocity Fields in a Collectively Migrating Epithelium. *Biophys. J.* **98**, 1790–1800 (2010).
33. Du, D. *et al.* The Tight Junction Protein, Occludin, Regulates the Directional Migration of Epithelial Cells. *Dev. Cell* **18**, 52–63 (2010).
34. Raya-Sandino, A. *et al.* Zonula occludens-2 regulates Rho proteins activity and the development of epithelial cytoarchitecture and barrier function. *Biochim. Biophys. Acta BBA - Mol. Cell Res.* **1864**, 1714–1733 (2017).

35. Deforet, M. *et al.* Automated velocity mapping of migrating cell populations (AVeMap). *Nat. Methods* **9**, 1081–1083 (2012).
36. Terry, S. J. *et al.* Stimulation of Cortical Myosin Phosphorylation by p114RhoGEF Drives Cell Migration and Tumor Cell Invasion. *PLOS ONE* **7**, e50188 (2012).
37. Shiu, Y.-T. *et al.* Rho Mediates the Shear-Enhancement of Endothelial Cell Migration and Traction Force Generation. *Biophys. J.* **86**, 2558–2565 (2004).
38. Stringer, C., Wang, T., Michaelos, M. & Pachitariu, M. Cellpose: a generalist algorithm for cellular segmentation. *Nat. Methods* 1–7 (2020) doi:10.1038/s41592-020-01018-x.
39. Henkes, S., Fily, Y. & Marchetti, M. C. Active jamming: Self-propelled soft particles at high density. *Phys. Rev. E* **84**, 040301(R) (2011).
40. Zou, R. *et al.* YAP nuclear-cytoplasmic translocation is regulated by mechanical signaling, protein modification, and metabolism. *Cell Biol. Int.* **44**, 1416–1425 (2020).
41. Dupont, S. *et al.* Role of YAP/TAZ in mechanotransduction. *Nature* **474**, 179–183 (2011).
42. Heuzé, M. L. *et al.* Myosin II isoforms play distinct roles in adherens junction biogenesis. *eLife* **8**, e46599 (2019).
43. Xi, W., Sonam, S., Beng Saw, T., Ladoux, B. & Teck Lim, C. Emergent patterns of collective cell migration under tubular confinement. *Nat. Commun.* **8**, 1517 (2017).
44. Iyer, V. N. & Szybalski, W. A MOLECULAR MECHANISM OF MITOMYCIN ACTION: LINKING OF COMPLEMENTARY DNA STRANDS*†. *Proc. Natl. Acad. Sci.* **50**, 355–362 (1963).
45. Beutel, O., Maraspini, R., Pombo-García, K., Martin-Lemaitre, C. & Honigmann, A. Phase Separation of Zonula Occludens Proteins Drives Formation of Tight Junctions. *Cell* **179**, 923-936.e11 (2019).
46. Cordes, A. *et al.* Prestress and Area Compressibility of Actin Cortices Determine the Viscoelastic Response of Living Cells. *Phys. Rev. Lett.* **125**, 068101 (2020).
47. Balasubramaniam, L. *et al.* Investigating the nature of active forces in tissues reveals how contractile cells can form extensile monolayers. *Nat. Mater.* 1–11 (2021) doi:10.1038/s41563-021-00919-2.
48. Guillot, C. & Lecuit, T. Mechanics of Epithelial Tissue Homeostasis and Morphogenesis. *Science* **340**, 1185–1189 (2013).
49. Brückner, B. R., Nöding, H., Skamrahl, M. & Janshoff, A. Mechanical and morphological response of confluent epithelial cell layers to reinforcement and dissolution of the F-actin cytoskeleton. *Prog. Biophys. Mol. Biol.* **144**, 77–90 (2019).
50. Skamrahl, M., Colin-York, H., Barbieri, L. & Fritzsche, M. Simultaneous Quantification of the Interplay Between Molecular Turnover and Cell Mechanics by AFM–FRAP. *Small* **15**, 1902202 (2019).
51. Nehls, S., Nöding, H., Karsch, S., Ries, F. & Janshoff, A. Stiffness of MDCK II Cells Depends on Confluency and Cell Size. *Biophys. J.* **116**, 2204–2211 (2019).

52. Gudipaty, S. *et al.* Mechanical stretch triggers rapid epithelial cell division through Piezo1. *Nature* **543**, 118–121 (2017).
53. Zihni, C., Balda, M. S. & Matter, K. Signalling at tight junctions during epithelial differentiation and microbial pathogenesis. *J. Cell Sci.* **127**, 3401–3413 (2014).
54. González-Mariscal, L., Tapia, R. & Chamorro, D. Crosstalk of tight junction components with signaling pathways. *Biochim. Biophys. Acta BBA - Biomembr.* **1778**, 729–756 (2008).
55. Matsuzawa, K. *et al.* MAGIs regulate aPKC to enable balanced distribution of intercellular tension for epithelial sheet homeostasis. *Commun. Biol.* **4**, 1–11 (2021).
56. Sourisseau, T. *et al.* Regulation of PCNA and Cyclin D1 Expression and Epithelial Morphogenesis by the ZO-1-Regulated Transcription Factor ZONAB/DbpA. *Mol. Cell. Biol.* **26**, 2387–2398 (2006).
57. Capaldo, C. T. *et al.* Tight function zonula occludens-3 regulates cyclin D1–dependent cell proliferation. *Mol. Biol. Cell* **22**, 1677–1685 (2011).
58. Fedele, C. *et al.* Azobenzene-based sinusoidal surface topography drives focal adhesion confinement and guides collective migration of epithelial cells. *Sci. Rep.* **10**, 15329 (2020).
59. Vishwakarma, M. *et al.* Mechanical interactions among followers determine the emergence of leaders in migrating epithelial cell collectives. *Nat. Commun.* **9**, 3469 (2018).
60. Rausch, S. *et al.* Polarizing cytoskeletal tension to induce leader cell formation during collective cell migration. *Biointerphases* **8**, 32 (2013).
61. Sorce, B. *et al.* Mitotic cells contract actomyosin cortex and generate pressure to round against or escape epithelial confinement. *Nat. Commun.* **6**, 8872 (2015).
62. Saraswathibhatla, A. & Notbohm, J. Tractions and Stress Fibers Control Cell Shape and Rearrangements in Collective Cell Migration. *Phys. Rev. X* **10**, 011016 (2020).
63. Devany, J., Sussman, D. M., Yamamoto, T., Manning, M. L. & Gardel, M. L. Cell cycle–dependent active stress drives epithelia remodeling. *Proc. Natl. Acad. Sci.* **118**, e1917853118 (2021).
64. Mitchel, J. A. *et al.* In primary airway epithelial cells, the unjamming transition is distinct from the epithelial-to-mesenchymal transition. *Nat. Commun.* **11**, 5053 (2020).
65. Kim, J. H. *et al.* Unjamming and collective migration in MCF10A breast cancer cell lines. *Biochem. Biophys. Res. Commun.* **521**, 706–715 (2020).
66. Serra-Picamal, X. *et al.* Mechanical waves during tissue expansion. *Nat. Phys.* **8**, 628–634 (2012).
67. Virtanen, P. *et al.* SciPy 1.0: fundamental algorithms for scientific computing in Python. *Nat. Methods* **17**, 261–272 (2020).
68. Schindelin, J. *et al.* Fiji: an open-source platform for biological-image analysis. *Nat. Methods* **9**, 676–682 (2012).
69. BRADSKI, G. The OpenCV library. *Dr Dobbs J Softw. Tools* **25**, 120–125 (2000).
70. Teh, C.- & Chin, R. T. On the detection of dominant points on digital curves. *IEEE Trans. Pattern Anal. Mach. Intell.* **11**, 859–872 (1989).

71. Dan Allan *et al. soft-matter/trackpy: Trackpy v0.4.2*. (Zenodo, 2019). doi:10.5281/zenodo.3492186.
72. Crocker, J. C. & Grier, D. G. Methods of Digital Video Microscopy for Colloidal Studies. *J. Colloid Interface Sci.* **179**, 298–310 (1996).
73. Hutter, J. L. & Bechhoefer, J. Calibration of atomic-force microscope tips. *Rev. Sci. Instrum.* **64**, 1868–1873 (1993).
74. Hubrich, H. *et al.* Viscoelasticity of Native and Artificial Actin Cortices Assessed by Nanoindentation Experiments. *Nano Lett.* (2020) doi:10.1021/acs.nanolett.0c01769.
75. Dai, J. & Sheetz, M. P. Membrane Tether Formation from Blebbing Cells. *Biophys. J.* **77**, 3363–3370 (1999).
76. Brochard-Wyart, F., Borghi, N., Cuvelier, D. & Nassoy, P. Hydrodynamic narrowing of tubes extruded from cells. *Proc. Natl. Acad. Sci.* **103**, 7660–7663 (2006).
77. Pietuch, A., Brückner, B. R., Fine, T., Mey, I. & Janshoff, A. Elastic properties of cells in the context of confluent cell monolayers: impact of tension and surface area regulation. *Soft Matter* **9**, 11490 (2013).

4.7 Supporting Information

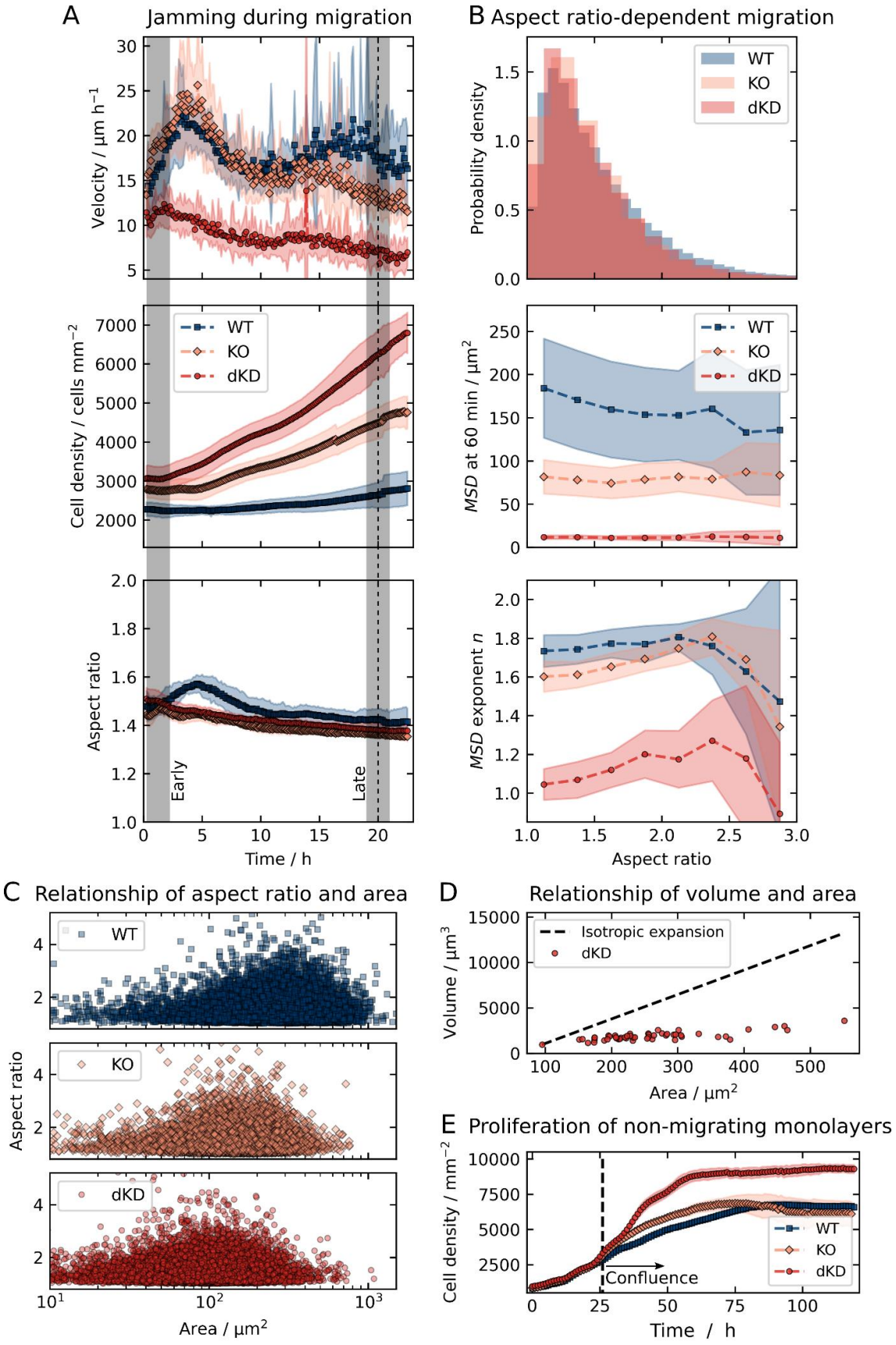

Figure S 4.1: Temporal evolution of cell density, velocity, and aspect ratio as well as aspect ratio-dependent motility of all three untreated MDCKII cell lines. A) Cell crowding and jamming during migration as quantified by the velocity, cell density, and aspect ratio over time. The gray shades at 0.5-2.5 h ('early') and 19-21 h ('late') correspond to the time windows of the cell velocity and *MSD* analyses. B) Aspect ratio distribution and aspect ratio-dependent *MSD* parameters. C) The aspect ratio showed a high variance but no co-variation with the area. D) Relationship between the increase in cell volume with respect to the cell area in dKD cells determined from 3D-confocal actin stacks. For comparison, theoretical isotropic expansion is shown as a dashed line. E) Additional proliferation experiment immediately after seeding of cells without insert. The dashed line indicates reaching of confluence, corresponding to the beginning of our typical migration experiments (0 h in all other figures). Means and standard deviations are shown. The aspect ratio in A is the median for each experiment and then averaged over all experiments.

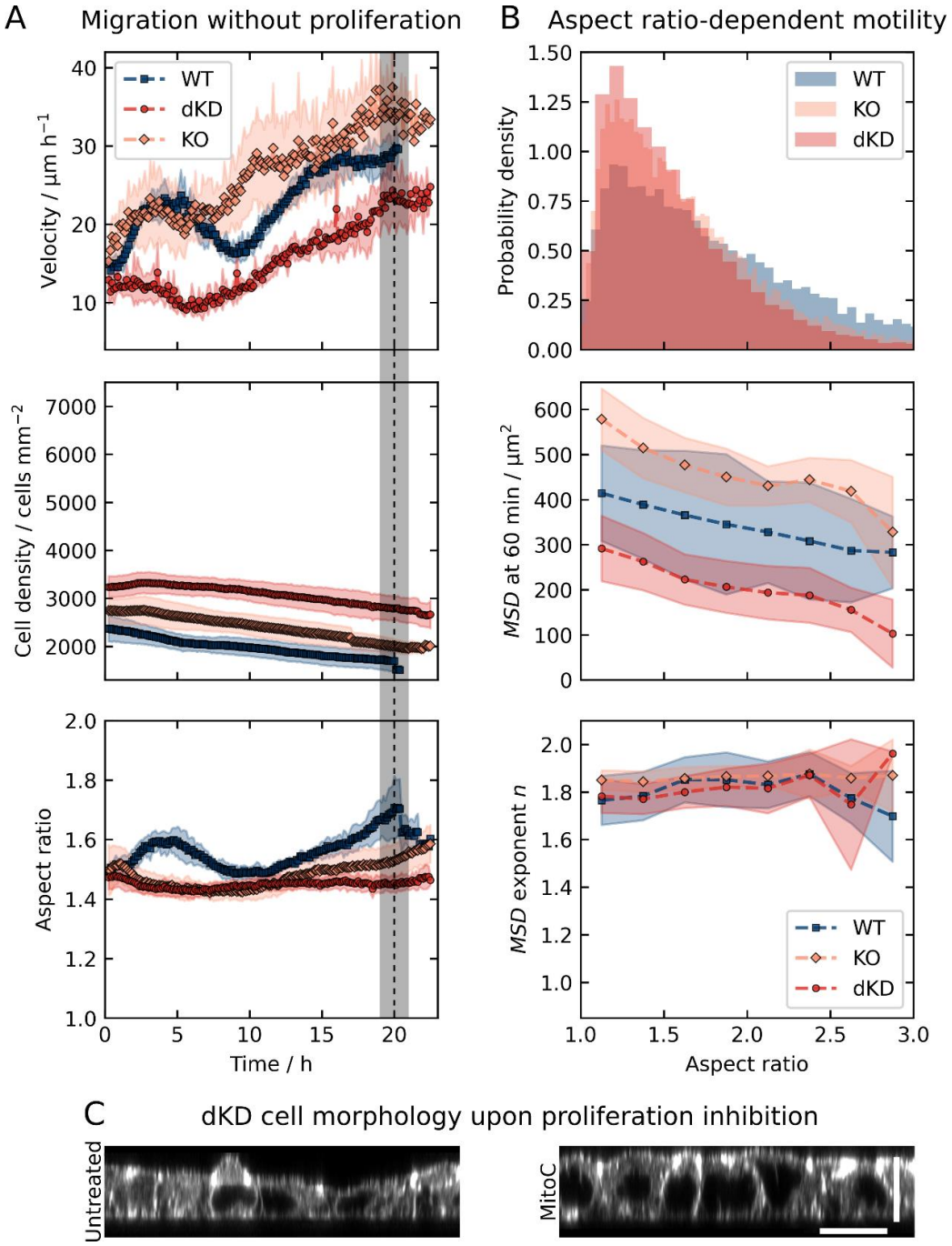

Figure S 4.2: Temporal evolution of cell density, velocity, and aspect ratio as well as aspect ratio-dependent motility of all three MDCKII cell lines upon proliferation inhibition by Mitomycin C. A) Cell crowding and jamming were prevented by proliferation inhibition via MitoC during migration as quantified by the velocity, cell density, and aspect ratio over time. The gray shade at 19-21 h corresponds to the time window of the *MSD* analyses. B) Aspect ratio distribution and aspect ratio-dependent *MSD* parameters. Means and standard deviations are shown. The aspect ratio in A is the median for each experiment and then averaged over all experiments. C) Side-view of untreated and MitoC-treated dKD cells from 3D confocal actin stacks. Scale bars: 10 µm (z), 20 µm (x).

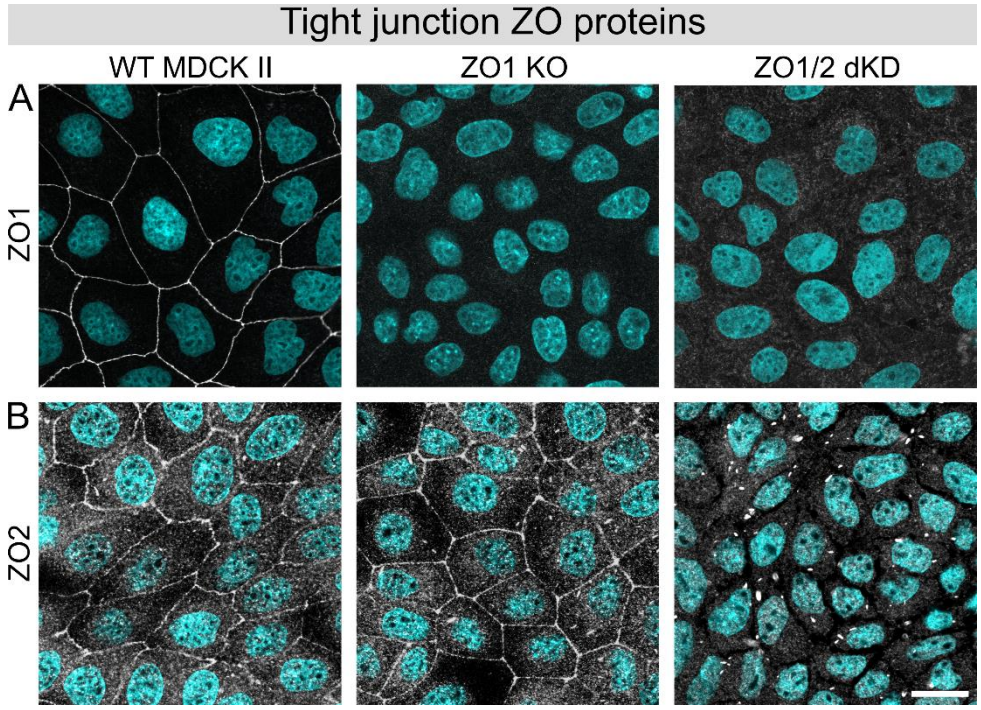

Figure S 4.3: Immunofluorescence measurements confirming successful ZO protein knockout/-down. A) ZO1 antibody-based staining of all three MDCKII cell lines. B) ZO2 antibody-based staining of all three MDCKII lines. Nuclei are shown in cyan. Scale bar: 20 µm.

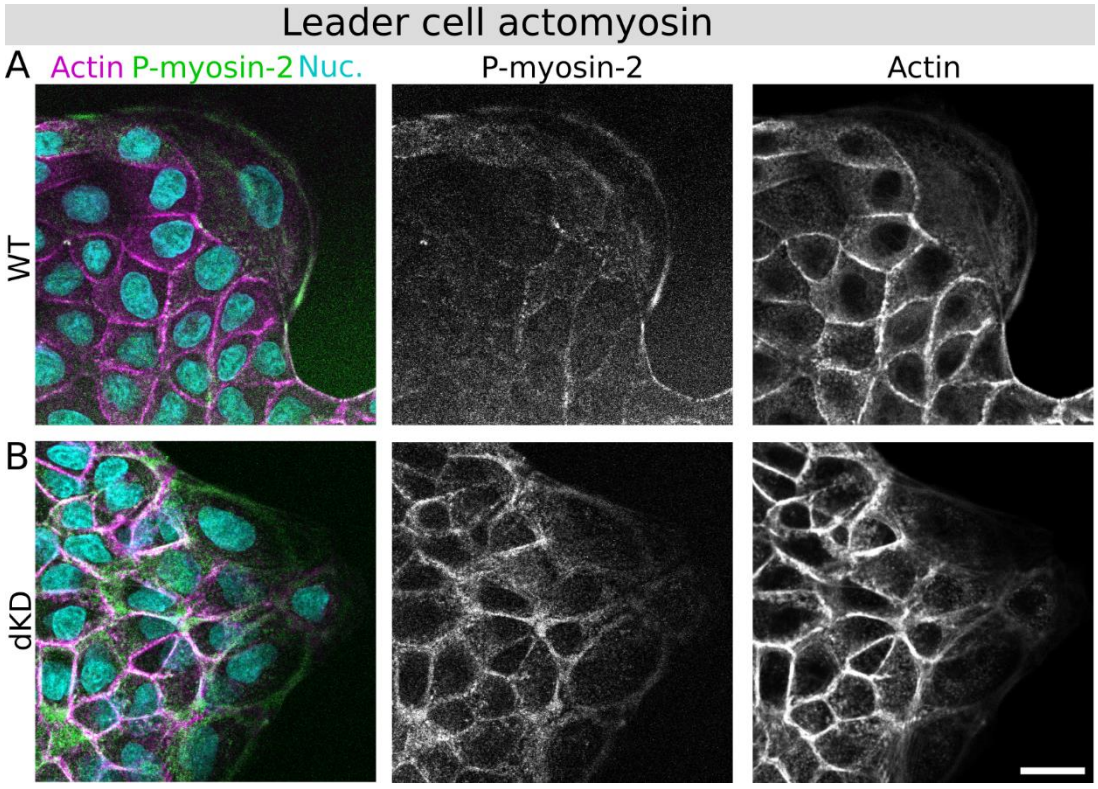

Figure S 4.4: Actomyosin architecture remodeling for leader cells at the migration front of migrating WT and dKD cell layers. Phosphorylated myosin-2 (P-myosin-2;

green), actin (magenta) and nuclei co-staining of MDCKII WT (A) and dKD (B) cell lines with corresponding gray-scale images of P-myosin-2 and actin. Scale bar: 20 μm.

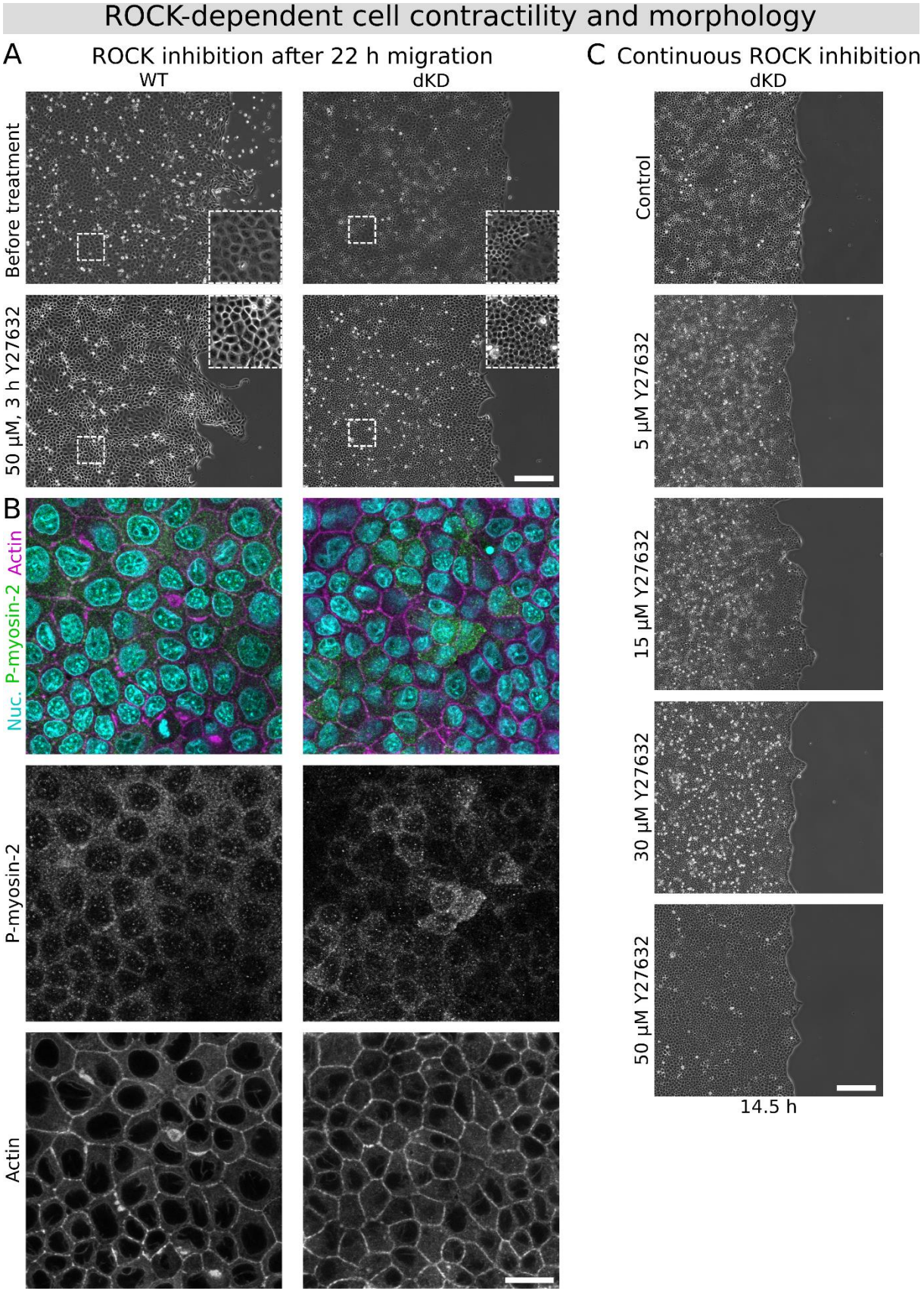

Figure S 4.5: MDCKII WT and dKD cell lines show altered migration and actomyosin architecture remodeling upon inhibition of ROCK with Y27632. A) Inhibition of ROCK by Y27632 after 22 h of migration in WT and dKD cells. Top shows

cell monolayers before treatment and bottom the same layers after 3 h of migration in the presence of 50 µM Y27632. Scale bar: 200 µm B) Confocal actomyosin images of the same MDCKII WT and dKD layers from A after Y27632 treatment after 22 h of migration with corresponding gray-scale images of P-myosin-2 and actin. Scale bar: 20 µm. C) Migration of dKD cells for 14.5 h in the presence of increasing concentrations of Y27632 (starting continuously from 30 min before insert removal). Scale bar: 200 µm.

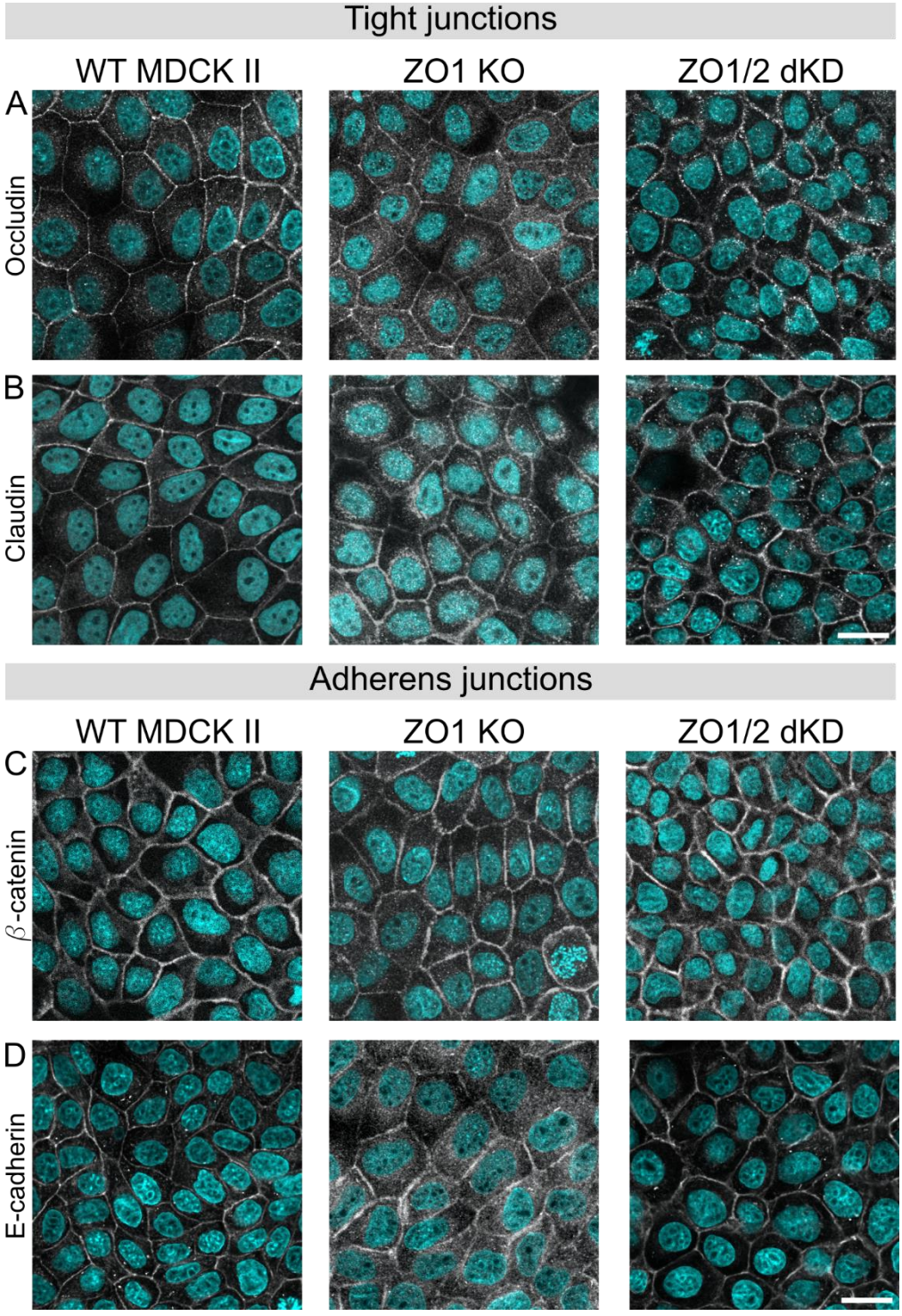

Figure S 4.6: Immunofluorescence of tight junction transmembrane proteins and adherens junction proteins. A) Occludin. B) Claudin 1. C) β-catenin. D) E-cadherin. Nuclei are shown in cyan. Scale bars: 20 µm.

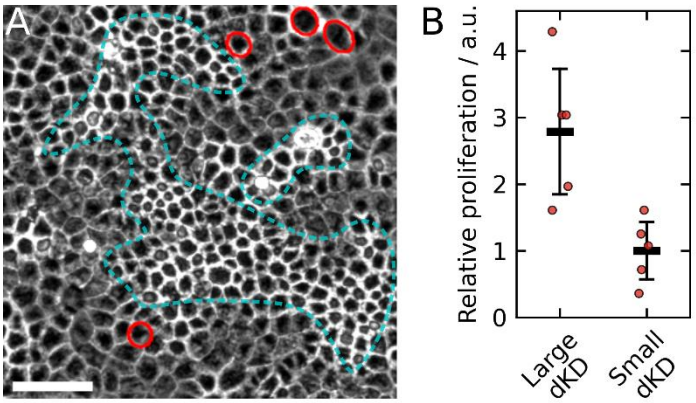

Figure S 4.7: In the dKD monolayers, more of the large and stretched cells were observed to proliferate than the small and contractile cells. A) Example of dKD cells during migration with proliferation events indicated by red circles and patches of small cells highlighted in cyan. Scale bar: 50 µm. B) Relative proliferation of five example regions from A, normalized by the average number of small cell proliferation events. Proliferation events were counted and attributed by hand and the examples were chosen, so that approximately the same amount of large and small cells was present. These data were collected in the same time window as the *MSD* analysis, i.e., between 19 h and 21 h.

Chapter 5

Cellular Segregation in Co-Cultures Driven by Differential Adhesion and Contractility on Distinct Time Scales

by Mark Skamrahl[a], Justus Schünemann[a], Markus Mukenhirn[c], Jannis Gottwald[a], Maximilian Ferle[a], Angela Rübeling[b], Alf Honigmann[c], and Andreas Janshoff[a].

[a] University of Göttingen, Institute of Physical Chemistry, Tammannstr. 6, 37077 Göttingen, Germany.

[b] University of Göttingen, Institute of Organic and Biomolecular Chemistry, Tammannstr. 2, 37077 Göttingen, Germany.

[c] Max Planck Institute of Molecular Cell Biology and Genetics, Pfotenhauerstr. 108, 01307 Dresden, Germany.

This Chapter was published as a preprint on *bioRxiv*, Version 1, May 2022.
DOI: https://doi.org/10.1101/2022.05.23.492966
Available under CC BY-NC 4.0 open access license. Only minute and formatting-related changes were applied.

Author Contributions

The research was initiated in the bachelor's thesis of J.S. J.S. and I performed initial mixing experiments and confocal microscopy. Together with A.R. I performed additional mixing experiments (called "second approach" in this Chapter) and I carried out the AFM imaging. M.M. performed the laser ablation experiments and analyzed the data with A.H. After a few experiments together with me, J.G. carried out the indentation experiments. J.G. also performed the adhesion measurements. J.G. did most of the AFM analyses. M.F. and I developed the segmentation-based analyses and I performed all analyses. A.H. and A.J. initiated and supervised the research. I wrote the manuscript with the help of A.J. All authors helped with discussions and careful proofreading.

ABSTRACT

Cellular sorting and pattern formation is crucial for many biological processes such as development, tissue regeneration, and cancer progression. Prominent physical driving forces for cellular sorting are differential adhesion and contractility. Here, we studied the segregation of epithelial co-cultures containing highly contractile, ZO1/2-depleted MDCKII cells (dKD) and their wildtype (WT) counterparts using multiple quantitative, high-throughput methods to monitor their dynamical and mechanical properties. We observe a time-dependent segregation process, governed mainly by differential contractility on short (< 5 h) and differential adhesion on long (> 5 h) time scales, respectively. The overly contractile dKD cells exert strong lateral forces on their WT neighbors, thereby apically depleting their surface area. This is reflected in a six-fold difference in excess surface area between both cell types. The lateral forces lead to a four- to six-fold increase in tension at all junctions that are in contact with the contractile cells including the interface between heterotypic cell-cell contacts. Concomitantly, the tight junction-depleted, contractile cells exhibit weaker cell-cell adhesion. Drug-induced contractility reduction delays the initial segregation but ceases to change the final demixed state, rendering differential adhesion the dominant segregation force at longer time scales.

This well-controlled model system shows how cell sorting is accomplished through a complex interplay between differential adhesion and contractility and can be explained largely by generic physical driving forces.

5.1 INTRODUCTION

Cellular sorting and tissue separation are essential processes in embryogenesis and tissue development, studied across multiple species.[1,2] Early work has shown that cells taken from different embryonic tissues and remixed together eventually segregate, or demix, again.[3,4] Sorting of cells in tissues can be governed by different biological and physical factors. Owing to our accumulated knowledge about cell-cell junctions and the cytoskeleton, a hypothesis for cellular demixing based on differential adhesion was proposed.[5,6] To accommodate different biological scenarios, this first hypothesis was complemented by incorporating differential cell contractility.[7,8] Adhesion- and contractility-induced tensions basically act antagonistically: Contractility induces cell rounding to minimize the contact zone, whereas adhesion enlarges the cell-cell contact region. The resulting surface tension of the tissue is the ratio of adhesion and contractility.[9] This view has been extended more recently by the addition of local contractile cues, for example in the anteroposterior compartment boundary in Drosophila flies.[10–12] Alternatively, active cell forces have been proposed to also play a role in regulating cellular demixing in co-cultures.[13] However, it remains difficult to differentiate between the various factors that govern cell sorting. In recent years, many simulation-based studies characterized different physical

driving forces of demixing, identifying many possible pathways to cellular segregation via differential physical cell properties.[9,14–22] Such simulations have the idea in common that the overall free energy in a cell layer, as determined by parameters such as contractility and adhesion, needs to be minimized. However, fundamental experimental evidence remains scarce, only applicable in certain scenarios, and often correlative.

Recently, it has been shown that in tight junction-depleted epithelial cells (ZO1 and 2 knockdown; abbreviated as dKD) two distinct cell populations emerge: some cells contract and by that adopt a roundish shape; pulling on their neighbors eventually results in laterally elongated cells that coexist with the contracted cells.[23,24] In initial experiments, the stretched cell population was successfully replaced by less contractile wildtype (WT) cells, substantially increasing the mismatch in mechanical properties. In this co-culture, overly contractile dKD cells inhibited layer fluidity and migration by means of jamming. However, the driving forces for segregation in such a co-culture remain to be elucidated.

Here, we now address this question by studying co-cultures of dKD and WT cells using high-throughput/content (de-) mixing experiments in combination with quantitative mechanical measurements. We focus on the quantification of cellular viscoelasticity, contractility, and cell-cell as well as cell-substrate adhesion to shine light on the emergence and persistence of segregated cell monolayers. We found that a time-dependent demixing process in these co-cultured monolayers is governed by differential contractility on short time scales (within the first five hours), while on longer time scales (> 5 h) differential adhesion prevails. Such separation of demixing time scales has not been observed before. In addition, we show that the overly contractile dKD cells stretch out their WT neighbors and apically deplete their excess surface area, with a six-fold difference between the cell types. The dKD contractility leads to an about four- to six-fold increase in tension at all junctions in contact with these cells including the interface between heterotypic cell contacts. Additionally, the tight junction-compromised, contractile dKD cells exhibit weaker cell-cell adhesion. Taken together, our experimental results indicate that differential interfacial tension prevails in the beginning to segregate the cell types, while with elapsed time differential adhesion becomes more and more important for demixing.

5.2 RESULTS

5.2.1 DEMIXING OF HIGHLY CONTRACTILE DKD AND COMPLIANT WT CELL CO-CULTURES

First, live cell (de-) mixing experiments were recorded directly after thorough mixing and seeding using phase contrast and fluorescence microscopy (Figure 5.1A). We used WT cells with a GFP tag, (named WT-GFP from here on, see methods, Chapter 5.4) to distinguish them from dKD cells. Cell segmentation and neighbor analysis using both the fluorescence signal and phase contrast images allowed for automatic assignment of cells as WT or dKD. This enabled us to quantify how much the cells mixed randomly or demixed into clusters, also called segregation. Therefore, we defined a segregation index *SI* as the number of homotypic neighbors divided by the number of all neighbors.

In the case of a completely random cell distribution, an average segregation index of 0.5 would be expected. However, this parameter is also impacted by natural, local processes such as cell division. To account for these deviations from randomness, we performed control experiments using a pseudo co-culture consisting of WT-GFP cells and unmodified WT cells.

After detaching the cells and mixing the suspensions thoroughly prior to seeding, initially, both the WT/WT control as well as the WT/dKD mixture showed a segregation index close to 0.5 (Figure 5.1B1). The slight shift to higher values was likely already introduced upon initial seeding when most cells were still sedimenting, while others were already attached. Within the first hour, both co-cultures initially demixed from about 0.52 to 0.57 (Figure 5.1B1). However, after this time only the WT/dKD mixture segregated further, as expected. The *SI* increased to about 0.63 within the first 5 h, whereas the control remained at 0.57. After this fast initial demixing, both co-cultures segregated further at a similar rate to reach values close to 0.7 for the WT/dKD and 0.6 for the WT/WT cells.

In co-culture with dKD, WT cells sorted into large, preferentially round clusters (Figure 5.1A) with a higher average *SI* than their dKD counterparts (Figure 5.1B1, on the right). The dKD cells, with a lower *SI*, were arranged in elongated, string-like clusters around the WT domains. In contrast, the WT/WT control showed an inconspicuous and less defined layer morphology. The *SI* of the labeled WT cells was generally higher than that of the unlabeled ones. However, this *SI*-difference vanished over time in the WT/WT co-culture, whereas in the WT/dKD mixture it even increased. Accordingly, WT/dKD co-cultures exhibited a sorting behavior into distinct clusters, different from homotypic monolayers.

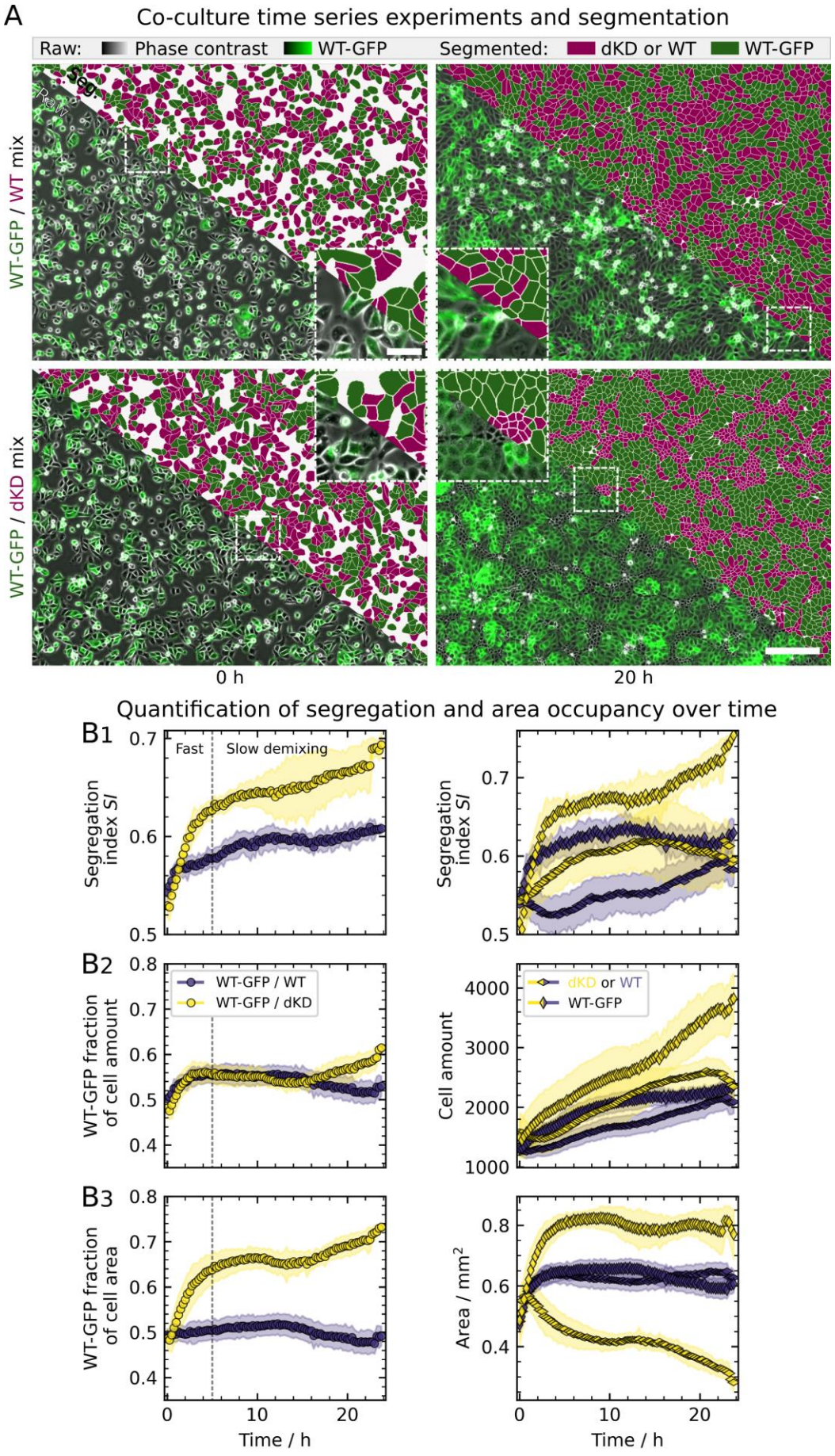
A
Co-culture time series experiments and segmentation
Raw: Phase contrast WT-GFP
Segmented: dKD or WT WT-GFP
WT-GFP / WT mix
WT-GFP / dKD mix
0 h
20 h
Quantification of segregation and area occupancy over time
B1
Segregation index SI
Fast
Slow demixing
B2
WT-GFP fraction of cell amount
WT-GFP / WT
WT-GFP / dKD
Cell amount
dKD or WT
WT-GFP
B3
WT-GFP fraction of cell area
Area / mm²
Time / h
Time / h

Figure 5.1: Demixing behavior of dKD and WT cell co-cultures at an initial mixing ratio of 50:50. A) Example overlay of phase contrast (grayscale) and fluorescence (green: WT-GFP cells) channels with corresponding segmentations (green: WT-GFP, magenta: dKD cells in WT-GFP/dKD mix or WT in WT-GFP/WT control, respectively). Samples were imaged immediately after seeding and mounting on the microscope (0 h). Scale bars: 200 µm and 50 µm (zoom-in). B) Demixing, cell amount, and area occupancy quantification. The vertical dashed line at 5 h indicates two distinct demixing time scales. B1) The segregation index *SI*, defined as the average ratio of homotypic and all cell neighbors, quantifies the demixing degree. The *SI* is shown averaged over both cell types (left) as well as separately for each cell type (right). B2) Left: Relative cell amount, calculated as the ratio of the amount of WT-GFP cells and the total cell amount. Right: Total cell amounts of each cell type. B3) Left: WT-GFP fraction of the overall cell area, calculated as the ratio of the WT-GFP area and the total cell area, indicating contractility discrepancies between the cell types. Right: Total covered area of each cell type. Corresponding distributions of the individual cell areas are depicted in Figure S 5.1. Means and standard deviations are shown. 12 separate regions from 6 culture dishes, acquired on three separate days (two regions per dish, two dishes per day), were measured and are shown per co-culture mix.

As a control/normalization parameter for the *SI*, we next examined the cell amount of both cell types in each co-culture, because a difference in the relative cell amount could influence the *SI* as well. However, we observed no difference in the relative cell amount (WT-GFP fraction of the cell amount in Figure 5.1B2) between the WT/WT control and the WT/dKD cells. Interestingly, the total cell amount differed, with overall higher proliferation rates and larger cell amounts in the WT/dKD mixture. After a short delay in dKD cell proliferation, the dKD increased at a similar rate as the WT-GFP amount until about 15 h after seeding. Importantly, the resulting small difference in the cell amount between the cell types was present in both the WT/dKD co-culture and WT/WT control, slightly biasing the *SI* of both to larger values. After 15 h, dKD cells started to extrude apically out of the layer, offsetting proliferation and thereby stalling the cell amount. In the WT/WT mixture, the WT-GFP also showed slightly more proliferation until 15 h after seeding, which then leveled off.

Next, to examine the cell contractility discrepancy of these cell lines, which was described previously[23,24], we first quantified the labeled WT fraction of the cell area (Figure 5.1B3). If there were no discrepancies in contractility in the co-culture, this parameter would be expected to be 0.5 because each cell type would occupy 50% of the covered area. Indeed, this was the case for the WT/WT control. In contrast, however, the WT/dKD co-cultures showed a strong increase of the WT area fraction within the first 5 h, nicely correlating with the *SI* increase. This highlights a great differential contractility with highly contractile dKD cells occupying smaller areas and stretched WT cells covering more space on the culture dish. At the same time, as described before, the cell number ratio stayed constant, confirming that the larger area coverage of WT cells is due to lateral extension provoked by contractile dKD cells and not a consequence of an increased amount of WT cells. Notably, this effect only develops over time due to collective cell-cell interactions because the WT/dKD mixture also starts out at *SI* = 0.5. However, the contractile discrepancy is generally

underestimated here. This is because the phase contrast channel was used for analysis (the fluorescence was only used to assign the cell type, see methods, Chapter 5.4) but the lateral stretching of bordering WT cells by dKD neighbors can be best observed in the WT-GFP specific fluorescence channel (white arrows in Figure 5.2B). This is because the WT cell body extension, even overlapping above dKD cells, is specifically seen in the GFP channel (Figure 5.2B) while in phase contrast, the overlapping WT and dKD cell bodies cannot be distinguished well (Figure 5.1A).

5.2.2 Differential Actomyosin Contractility and 3D Cell Morphology of WT/DKD Co-Cultures

To further study the differential contractility of WT/dKD co-cultures on a molecular and cell morphological level, we applied confocal fluorescence microscopy and AFM imaging (Figure 5.2).

In accordance with previous work[23], we observed a strong actomyosin upregulation at the apical-lateral cell periphery of dKD cells (Figure 5.2A). Particularly, activated (phosphorylated) myosin accumulated at the apical cell-cell junctions. A thick perijunctional actomyosin ring was formed, constricting the cells apically. Conversely, the WT cells did not show any upregulation of phosphorylated myosin or of the actin cytoskeleton. To conserve the cellular volume, dKD cells were forced to bulge out apically. Since all dKD cells were still connected to their neighbors, adjacent WT cells were stretched out and flattened by the apical pull of the dKD cells. Strikingly, WT cells at the WT/dKD interface were partially pulled across their direct dKD neighbors towards the center of the dKD cluster (Figure 5.2B, white arrows). Note that this lateral pulling translocates certain cell components, such as ZO1 or myosin in Figure 5.2A and B, relative to the nucleus.

The lateral elongation of WT and apical contraction of dKD cells was confirmed by AFM imaging (Figure 5.2C). Interestingly, the bordering junctions at the interface between a WT and dKD cluster are particularly pronounced on the apical side (Figure 5.2C). This was mirrored by an increased myosin accumulation in this region (Figure 5.2B), which, taken together, highlights the mechanical discrepancy between the cell types.

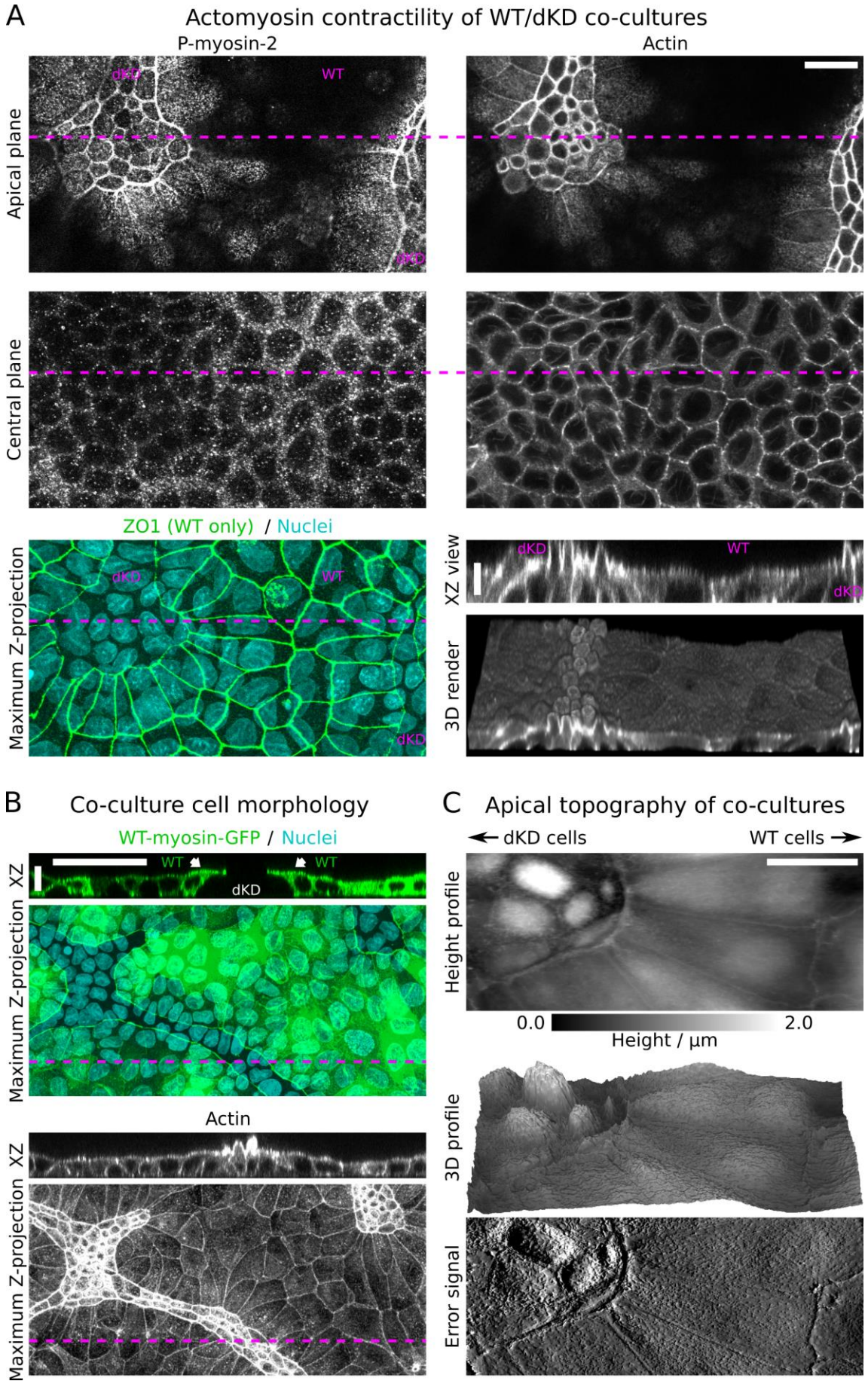
A
Actomyosin contractility of WT/dKD co-cultures
P-myosin-2
Actin
Apical plane
Central plane
dKD
WT
ZO1 (WT only) / Nuclei
Maximum Z-projection
XZ view
3D render
B
Co-culture cell morphology
WT-myosin-GFP / Nuclei
XZ
Maximum Z-projection
Actin
C
Apical topography of co-cultures
dKD cells
WT cells
Height profile
0.0
2.0
Height / µm
3D profile
Error signal

Figure 5.2: Differential actomyosin contractility of WT/dKD co-cultures. A) Representative WT/dKD co-cultures co-stained for phosphorylated myosin (P-myosin-2 antibody), actin (phalloidin), nuclei (DAPI, cyan), and ZO1 (ZO1 antibody, green). ZO1 was used to distinguish ZO1/2 dKD from WT cells. Magenta lines indicate the location of the *xz* view. *xy* scale bar: 20 µm, *z*: 5 µm. B) WT-GFP/dKD co-culture co-stained for actin (phalloidin) and nuclei (DAPI, cyan). The green channel was used to identify the WT-GFP cells and to examine their morphology in 3D. *xy* scale bar: 50 µm, *z*: 10 µm. C) Apical topography of WT-GFP/dKD co-cultures obtained by AFM imaging. Height profile, the corresponding 3D topography map which was up-scaled vertically by 50%, and error signal (deflection image). Scale bar: 20 µm. Cells in A were fixed after 28 h, and in B and C after about 48 h of growth.

5.2.3 Differential Mechanics of dKD and WT Cells in Co-Culture

To directly quantify the mechanical consequences of the described contractile, molecular, and morphological disparities in WT/dKD co-cultures, we examined their mechanical phenotypes by AFM indentation-relaxation as well as laser ablation (Figure 5.3).

First, we acquired AFM indentation maps (Figure 5.3A) and examined the apparent local stiffness, which is reflected in the slope of the force-distance curve. Here, we observed a similar picture as in pure dKD monolayers,[23] dKD cells were softer at the central cortex and extremely stiff at the perijunctional actomyosin ring (vide supra). In contrast, neighboring WT cells showed only slightly pronounced cell boundaries but an increased stiffness at the center in comparison with dKD neighbors.

To further characterize this stiffness difference at the center of the two cell types, we performed site-specific indentation experiments followed by force relaxation and applied a tailor-made viscoelastic fitting model as described in several recent studies.[23,25,26] In brief, this model fits the stress relaxation of the composite viscoelastic shell upon indentation according to a power law of the area compressibility modulus. Importantly, the cell geometry (area and angle of the apical cap), which differs tremendously between both cell lines (vide supra), can be adjusted in this model (Figure 5.3B). Three parameters are obtained: the prestress T_0 corresponding to the actomyosin cortex tension, the apparent area compressibility modulus K_A, which mirrors the excess cell surface area, and the fluidity β representing the viscous behavior (energy dissipation) of the cortex. A β value of 1 corresponds to a Newtonian fluid, whereas $\beta = 0$ refers to an elastic solid.

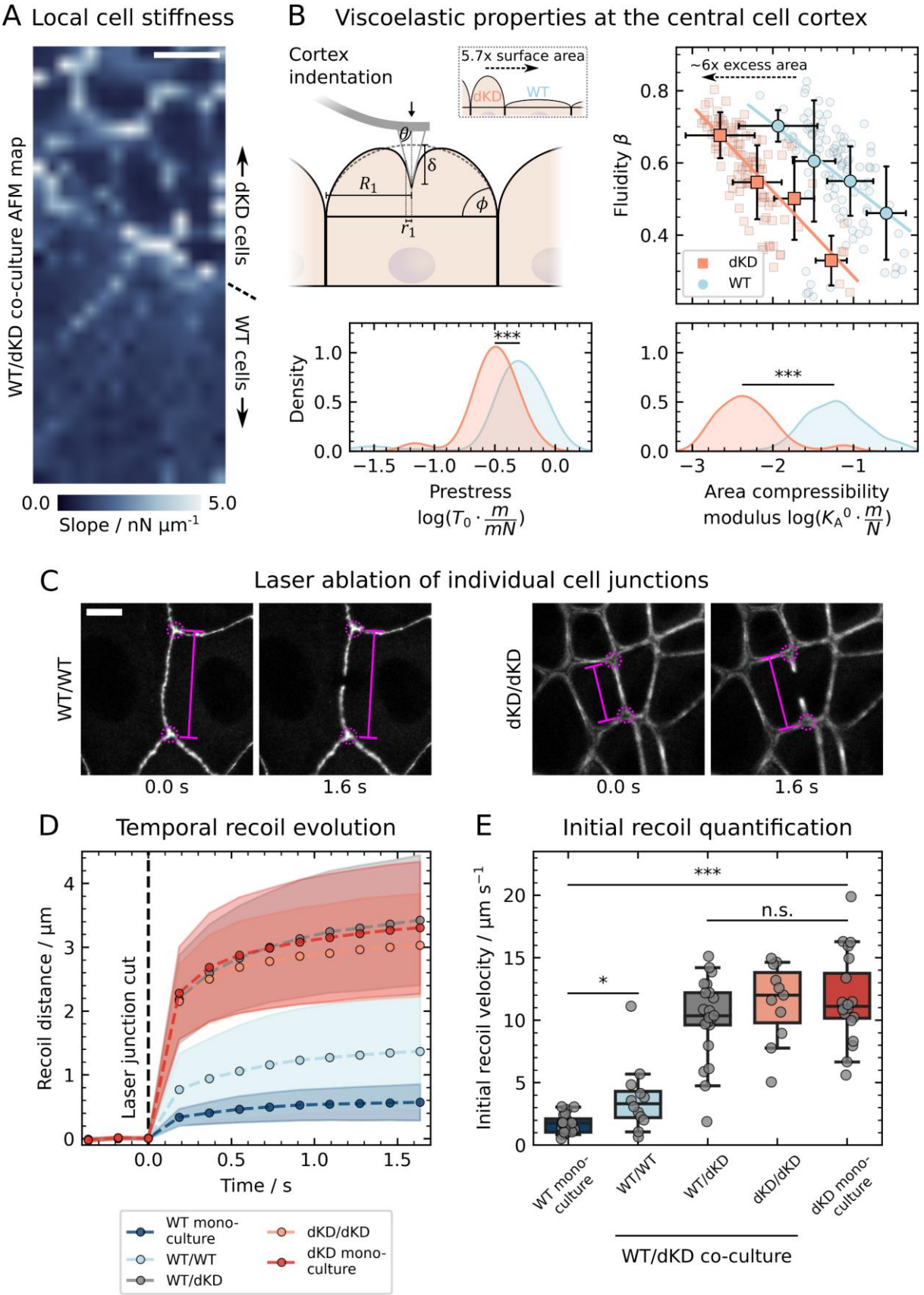

Figure 5.3: Differential mechanical properties of dKD and WT cells in co-culture.
A) AFM map showing the slope of the force curve during contact, which locally reflects

the apparent mechanical stiffness. Scale bar: 10 µm. B) Site-specific viscoelastic properties of the central cell cortex in proximity to the WT/dKD interface. The cortex indentation geometry considered in the Evans model includes the contact angle ϕ and base radius R_1 of the spherical cell cap, the indentation depth δ and the contact radius r_1. Importantly, dKD cells had a pronounced cap with larger ϕ and smaller R_1 than WT cells (vide supra), yielding a 5.7-fold surface area difference. Upon fitting, the fluidity β was plotted against the decade logarithm of the area compressibility modulus $K_A{}^0$, and histograms for the latter and the prestress T_0 are shown. Small transparent data points represent individual indentations. Large symbols and error bars are binned means and standard deviations. Lines indicate linear fits (in log space) of the binned means. C) Laser ablation examples of individual cell junctions. In WT cells, ZO1 in the tight junctions was stained, and in dKD cells, myosin was stained. D) Tensile junction properties were obtained by tracking the distance (magenta lines) between two opposing junction vertices (magenta circles) upon recoil. Temporal means and standard deviations are shown. E) The initial recoil velocity was calculated between the last point before (0.00 s) and the first one after ablation (0.18 s). The boxes show the median and the upper and lower quartiles. Whiskers indicate the 5th and 95th percentile, while data points represent a single cut of one junction. Scale bar: 10 µm. All measurements were repeated in at least three independent experiments and performed on multiple WT/dKD clusters.

Because $K_A{}^0$ was previously found not to be independent of but scale with the fluidity β,[26] we plotted β against $K_A{}^0$ (Figure 5.3B). Interestingly, we found that the fluidity was not significantly different between WT and dKD cells (p = 0.53, with the same median of 0.6). However, we found a shift to larger $K_A{}^0$ values for WT cells compared with their dKD neighbors in co-culture. This increase can be attributed to the removal of excess surface area A_{ex} compared with the geometrical surface area A_0 of the cells via $K_A{}^0 = \tilde{K}_A{}^0 (A_0 + A_{ex})/A_0$.[27]

The picture which therefore emerges suggests that surface area is sacrificed to mitigate the external stress from adjacent dKD cells. This occurs at the expense of stiffening but preservation of fluidity. On one hand, we observed an unchanged fluidity and only a relatively small difference in prestress within the range of the standard deviation (0.49 ± 0.22 mN m^{-1} for WT cells compared with 0.31 ± 0.14 mN m^{-1} for dKD (median ± s.d.)). On the other hand, WT cells exhibited a substantially larger scaling factor $K_A{}^0$, with an increase of more than one order of magnitude (0.061 ± 0.084 mN m^{-1} for WT compared with 0.004 ± 0.016 N m^{-1} for neighboring dKD cells (median ± s.d.)). From $K_A{}^0$ we were able to estimate that about six-fold as much excess area was stored in dKD as in WT cells. This fits to the theoretical 5.7-fold surface area difference between the different cap geometries, indicating that the apical surface material is conserved upon stretching, i.e., dKD cells contract laterally and store the membrane/cortex apically, while WT cells sacrifice apical excess area. Although a tremendous amount of excess surface material is sacrificed by WT cells, the mechanics of the cortex is largely unaffected, with small differences in prestress. In agreement, we also did not observe an obvious change in the actin signal at the central cortex in Figure 5.2A (vide supra). In consequence, the observed lateral contraction of the dKD cells did

not stem directly from their cortex but most likely from their perijunctional actomyosin ring (Figure 5.2A).

To test this and to characterize how the differential contractility translates into interfacial tension in the layer, we specifically examined the junctional tension using laser ablation, severing the cell junctions (Figure 5.3C-E). Particularly, we addressed the tensile properties of the cell junction between a WT and another WT cell, dKD/dKD junctions as well as the WT/dKD interface. In addition, we compared the new mechanical equilibrium in co-cultures with the junction tension in WT and dKD mono-cultures. To this end, we analyzed the recoil dynamics of the opposing vertex knots of the ablated junction over time (Figure 5.3D) and plotted the initial recoil velocity (Figure 5.3E).

We found a significant, four- to six-fold increase in recoil velocity for all junctions bordering a contractile dKD cell (10-12 µm s^{-1}, compared with 2-3 µm s^{-1} without any direct contact to a dKD cell). dKD/dKD junctions in co-culture were comparable with dKD mono-cultures ($p = 0.83$). Interestingly, the WT/dKD interface had slightly smaller recoil velocities than dKD/dKD junctions ($p = 0.29$), while WT/WT junctions displayed slightly but significantly higher velocities than WT mono-cultures. This highlights the establishment of a new mechanical equilibrium in co-cultures based on a tug-of-war between highly contractile dKD cells and compliant WT neighbors; in co-cultures, tension from dKD cells is accommodated by WT cells, while in dKD mono-cultures all cells exhibit increased tension. Overall, the data shows that the increased contractility of dKD cells indeed translates into increased junctional tension of all direct neighbors in the layer.

A further indication that the observed segregation in our study is based on interfacial tension, was another set of experiments in which we varied the mixing ratio between dKD and WT cells prior to seeding (Figure S 5.2). We observed that the pattern of elongated dKD cell stripes which surrounded the predominately round WT clusters remained the same, independent of the mixing ratio. This is indicative of interfacial energy minimization according to the tension-based sorting hypothesis and in contrast to, e.g., demixing driven by active forces as reported recently.[13] It also supports the notion that the roundness of WT clusters was the consequence of the minimization of the interfacial contact region (and thereby interfacial tension) between WT cells and their dKD counterparts.

5.2.4 Differential Cell-Cell Adhesion of WT and DKD Cells

While the increased contractility of dKD cells is well documented and could induce segregation via energy minimization, changes in intercellular adhesion might also be expected due to the loss of the adhesion-mediating junctional ZO proteins.

To quantify cell-cell adhesion, we performed AFM experiments with one cell attached to the AFM cantilever serving as the probe and the other one adhered onto the Petri dish. The two cells were brought into conformal contact and separated after a short dwell in contact (Figure 5.4A).

The separation forces between the two cells are not obtained under equilibrium conditions and are therefore referred to as the dynamic adhesion strength.

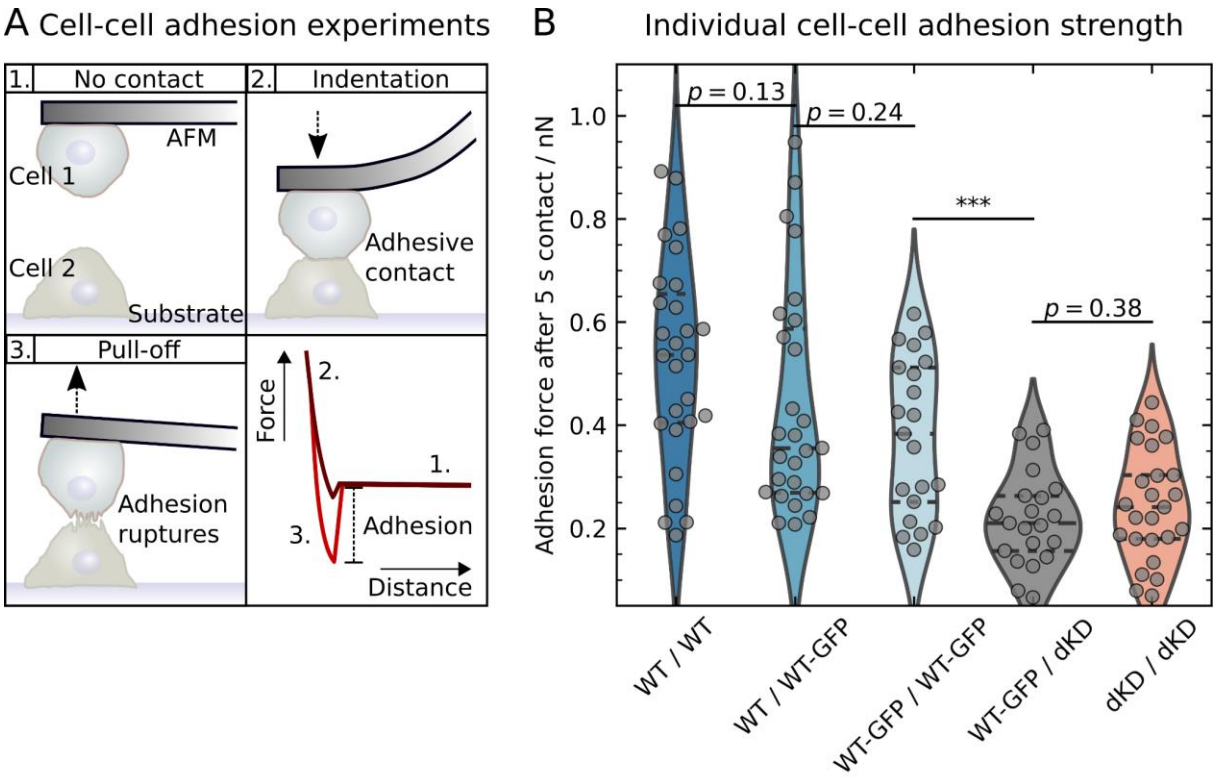

Figure 5.4: Differential intercellular adhesion of WT and dKD cells. A) AFM-based adhesion measurements: 1. Before and after an experiment, one cell is connected to the cantilever and one adheres to the culture dish substrate, without contact to each other. 2. Adhesive contact between cells is established at 2 nN for 5 s. 3. As the cantilever is retracted, the cells are pulled apart und bonds rupture. Schematic retraction curves depict small (dark red) and large (light red) adhesion forces. B) These adhesion forces are compared between different important cell combinations. Violins represent a kernel density estimation with horizontal, dashed lines showing the quartiles and median. Violins are scaled to have the same area. Single data points represent individual adhesion peak forces. Three consecutive indentation/retraction cycles were performed for each cell pair. For each combination, at least 4 individual cell-cantilever probes, and at least 8 cells on the substrate were measured, with experiments repeated on at least 4 days.

We found decreased adhesion forces for all dKD cells (two dKD cells as well as a dKD adhering to a WT-GFP cell) as shown in Figure 5.4B. As a control we also compared WT cells and GFP-tagged WT cells. While the WT-GFP cells displayed slightly lower adhesion forces than pure WT cells, they are still consistently more adhesive than dKD cells ($p < 0.001$ compared with WT-GFP/dKD and $p < 0.01$ with dKD/dKD). Interestingly, the adhesion between two cells was always dominated by the respective weaker binding partner, i.e., the dKD cells, indicative of largely immobile receptor-

ligand pairs. Accordingly, in WT/dKD co-cultures differential adhesion and contractility together determined the differential interfacial tension during cell segregation.

5.2.5 Time Scale Dependency: Contractility Drives Early, Adhesion Final Sorting

While we established that there is differential contractility and differential adhesion in WT/dKD co-cultures, it remains unclear, which one dominates over the other. Therefore, we performed the demixing experiments shown in Figure 5.1 again, however, this time in the presence of the Rho kinase (ROCK) inhibitor Y27632, in order to reduce cell contractility, switching off one of the contributions to demixing (Figure 5.5). This drug mainly affects the actomyosin contractility of cells, while the difference in cell-cell adhesion should remain the same.

Upon first visual inspection after ROCK inhibition (Figure 5.5A), at early time stages no difference was discernible between the WT/dKD mixture and the WT/WT control. Only at later times, stronger demixing was observed in the WT/dKD co-culture as mirrored in the segregation index (Figure 5.5B1). Here, we plotted the untreated WT/dKD mixture from Figure 5.1, as a control, together with contractility-inhibited WT/dKD and WT/WT co-cultures. While the WT/WT control did not change its segregation behavior upon Y27632 administration, the very fast, early segregation of WT/dKD co-cultures (< 5 h) was prevented. Instead of this fast initial behavior, segregation of the WT/dKD mixture was slowed down. Nevertheless, after about 15 h the contractility-inhibited WT/dKD mixture reached approximately the same *SI* of about 0.7 as the untreated counterpart. Accordingly, the upregulated contractility of dKD cells was critical for early segregation, while the adhesion differential was still able to induce cellular demixing upon longer time scales.

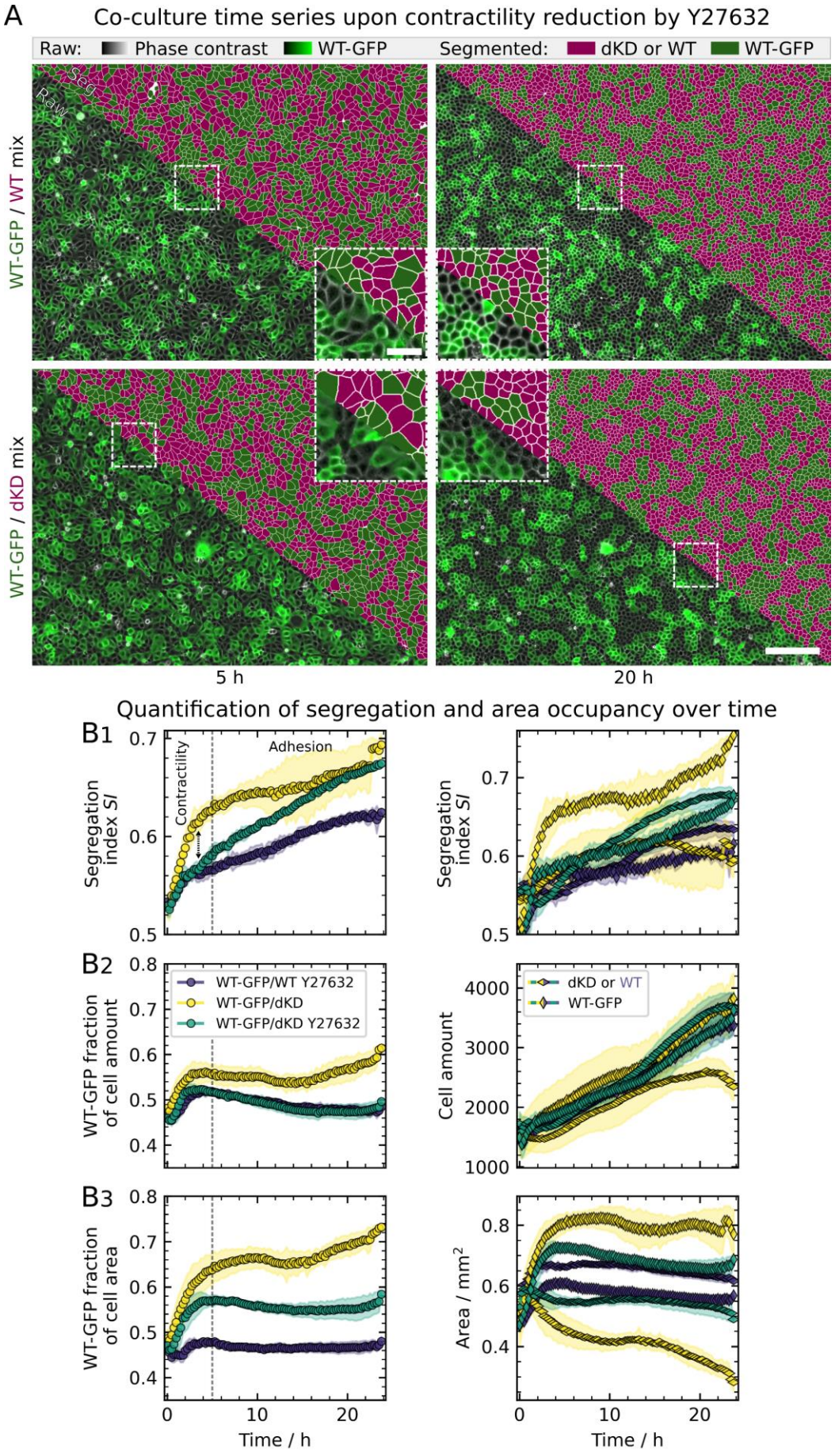
A
Co-culture time series upon contractility reduction by Y27632
Raw: Phase contrast WT-GFP
Segmented: dKD or WT WT-GFP
Seg
Raw
WT-GFP / WT mix
WT-GFP / dKD mix
5 h
20 h
Quantification of segregation and area occupancy over time
B1
Segregation index SI
Contractility
Adhesion
B2
WT-GFP fraction of cell amount
WT-GFP/WT Y27632
WT-GFP/dKD
WT-GFP/dKD Y27632
Cell amount
dKD or WT
WT-GFP
B3
WT-GFP fraction of cell area
Area / mm²
Time / h
Time / h

Figure 5.5: Contractility drives early, adhesion final sorting. Demixing behavior of highly contractile dKD and WT cell co-cultures at an initial mixing ratio of 50:50, treated with 50 µM Y27632. Experiments and Figure panels are set up analogously to Figure 5.1, and, for comparison, untreated WT/dKD from Figure 5.1 was included. A) Example overlay of phase contrast (grayscale) and fluorescence (green: WT-GFP cells) channels with corresponding segmentations (green: WT-GFP, magenta: dKD cells in WT-GFP/dKD mix or WT in WT-GFP/WT control, respectively). Samples were imaged immediately after seeding and mounting on the microscope (0 h). Scale bars: 200 µm and 50 µm (zoom-in). B) Demixing, cell amount, and area occupancy quantification. The vertical dashed line at 5 h indicates two distinct demixing time scales, thought to be determined by contractility and adhesion. B1) The segregation index *SI*, defined as the average ratio of homotypic and all cell neighbors, quantifies the demixing degree. The *SI* is shown averaged over both cell types (left) as well as separately for each cell type (right). B2) Left: Relative cell amount, calculated as the ratio of the amount of WT-GFP cells and the total cell amount. Right: Total cell amounts of each cell type. B3) Left: WT-GFP fraction of the overall cell area, calculated as the ratio of the WT-GFP area and the total cell area, indicating contractility discrepancies between the cell types. Right: Total covered area of each cell type. Additional analyses can be found in Figure S 5.3. Means and standard deviations are shown. 6 separate regions from 3 culture dishes (two per dish), acquired on separate days, were measured and are shown per co-culture mix.

As a control parameter, we also inspected the ratios of cell area and amount (Figure 5.5B2-3) as in Figure 5.1. The WT fraction of the cell amount (Figure 5.5B2) again served to provide context for the *SI* values and relative area coverage. While the untreated WT/dKD cell amount ratio was slightly shifted towards more WT cells, both drug-treated co-cultures remained at a 0.5 ratio (Figure 5.5B2). Interestingly, the proliferation in the WT/WT control was increased by Y27632 to the same level present in treated and untreated WT/dKD (except for the dKD extrusion after 15 h) as shown in Figure 5.5B2 and Figure S 5.3A, while the *SI* remained much lower.

To further rule out that local clustering due to proliferation dominates the segregation, we investigated the relationship between the *SI* and the cell amount (Figure S 5.3A). The *SI* generally increased with increasing cell amounts but with a lower slope at higher cell amounts. However, while for both treated cultures and the WT/dKD mixture the proliferation rate was approximately constant over time, the scaling of the *SI* with the total cell amount was much different. At the same cell amount, the *SI* remained lower in the treated WT/WT control than in the untreated WT/dKD mixture. In addition, the difference in proliferation between the treated and untreated WT/WT samples did not translate into an increase in segregation. Note that the cell amount is essentially equivalent to cell density in our experiments because the size of the field of view was always the same. Together, while we cannot completely rule out an impact of proliferation, adhesion and contractility seemed to dominate the segregation.

To assess the cell contractility, the area ratio once again served as a broad-scale readout (Figure 5.5B3). Here, we did observe the expected drop upon contractility inhibition for the WT/dKD mixture, while the WT/WT control was unaffected. Importantly, this drop in

contractility remained over the whole duration of the experiments, confirming that the effect of the drug did not wear off over time.

To rule out that the drug acts on cell motility (e.g., due to effects on the focal adhesions on the substrate) influencing demixing, we quantified the velocity and persistence via cell tracking (Figure S 5.3B). We investigated this particularly for the first 5 h, where the impact of the drug on segregation is the strongest. If higher motility actually was a driving factor for random mixing, we would expect an increase in the motility parameters particularly of the WT/dKD mixture upon drug treatment. However, this was not the case, but, to the contrary, the motility parameters even decreased slightly or remained the same (Figure S 5.3B). The WT/WT control showed a slight drop in both parameters, while its (de-) mixing behavior was largely unaffected. Accordingly, the drug provoked the delay in WT/dKD sorting not by affecting motility but indeed via inhibiting cellular contractility.

Together, data of this experiment showed that co-cultures can display an intricate interplay of contractility and adhesion driving cell segregation on distinct time scales.

5.3 DISCUSSION

Our goal was to scrutinize the driving force for demixing of co-cultures consisting of WT and dKD MDCKII cells displaying both different adhesion due to knock down of ZO1/2 and differential contractility due to actomyosin upregulation. We found that the main driving forces for creating clusters of dKD cells coexisting with WT clusters are time scale separated. On short time scales (within the first five hours) differential contractility prevails, while on longer time scales (>5 h) cell sorting is driven predominately by differential adhesion. To our knowledge, this is the first time that a separation of time scales in cellular segregation is described and attributed to distinct mechanical properties. Our data suggest that if differential contractility is abolished, differential adhesion alone is sufficient for cell demixing, but less efficient.

The envisioned mechanism comprising adhesion- and contractility-based cell segregation is summarized in Figure 5.6: while in randomly mixed WT cultures adhesion between all cells is the same and they display similar contractility, in WT/dKD co-cultures the adhesion and contractility between the cell types are considerably different, inducing segregation into clusters. In response to the contraction of adjacent dKD neighbors, WT cells are stretched and sacrifice excess surface area. If contractility is balanced again by pharmacological intervention, segregation based on differential contractility is strongly delayed. However, upon longer time scales the remaining adhesion differential still induces the same amount of segregation as in untreated layers, highlighting a redundant but time-dependent role of contractility and adhesion. Considering that adhesion complexes mature progressively over time,[28] whereas contractility is a property of individual cells, it makes sense that differential contractility promotes sorting immediately while adhesion acts on longer time scales.

It is well established that tight junction-depleted cells show increased contractility.[29–34] However, the implications of increased contractility of dKD cells for the behavior of the monolayer was only studied with emphasis on impaired migration dynamics and signaling.[23,24] Here, we showed that epithelial cells which are stretched by their contractile neighbors respond primarily by apical area dilatation, instead of by cortex mechanics adaptation. We were able to quantify a six-fold excess area difference between the stretched WT and the constricted dKD cells, equivalent to the change in geometric surface area, indicating the conservation of excess material instead of its recycling. This seems reasonable for co-cultures as well as dKD mono-cultures, which were described previously, where two populations emerged in a tug-of-war: a contractile population that stretches out the neighboring cell population.[23] However, in that work it remained unclear if excess membrane area dilatation indeed dominates the stretch response.

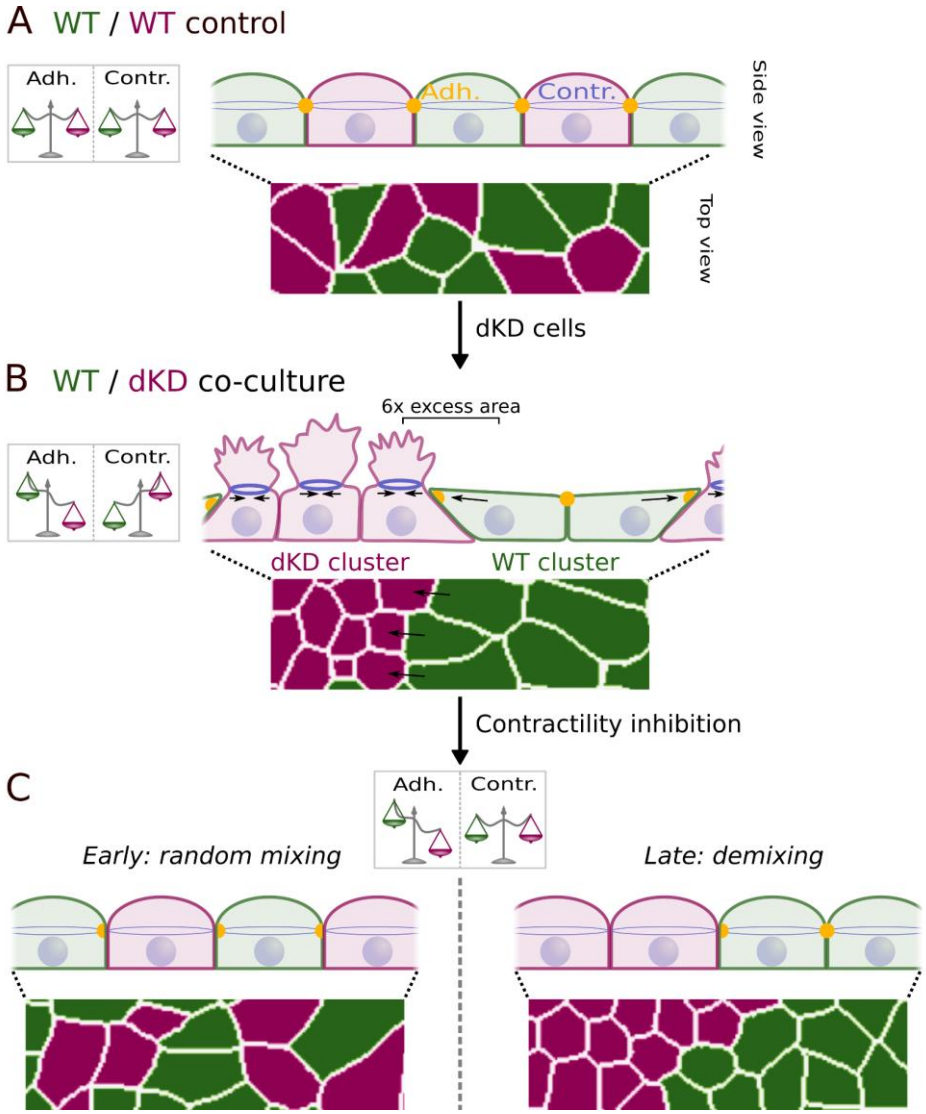

Figure 5.6: Proposed model of the interplay between adhesion and contractility in WT/dKD cell layers. A) In WT/WT control layers, adhesion is the same between all cells and they are equally contractile, hence, random mixing takes place. B) Adding dKD cells induces differences in both adhesion and contractility between the cell types. dKD cells lose some adhesive contact and contract excessively, yielding tremendous apical excess surface area. As a consequence, neighboring WT cells are stretched out and respond by surface area dilatation. C) To test the relative impact of adhesion and contractility, the latter was balanced again by drug addition, revealing a temporal dependency: balanced contractility restores random mixing at early stages but differential adhesion is still able to promote cell sorting into clusters on long time scales.

During development a generation of two mechanical cell populations among the same cell type was in fact identified as an emergent property upon collective cell interactions.[35] A recent study implicated asymmetric ROCK signaling in inducing these two populations interacting in confluent dKD mono-cultures.[24] This tug-of-war might intuitively favor a segregation into clusters in order to decrease the number of WT cells that is stretched by adjacent dKD neighbors.

Our study confirms that segregation can be fostered by differential interfacial tension, however, we identified a stronger contribution from differential adhesion than contractility. On the one hand, adhesion-based sorting was shown before to emerge in cell cultures, e.g., upon different expression levels of cadherins.[6,36–38] Similarly, sorting based on cadherin levels was demonstrated in follicle and retina cells of Drosophila oocytes.[39,40] Signaling-controlled cadherin turnover has also been implicated in cell segregation.[41,42] Note, in our study, adhesion differences were induced by tight junction disruption, which was also shown by previous work to decrease adhesion strength, in agreement with our data.[43] Purely adhesion-based sorting was recently confirmed via simulations and experiments in direct relation to constant contractility.[18] On the other hand, differential contractility was found to aid sorting in an embryo and possibly dominate over adhesion.[44,45] In co-cultures of zebrafish germ layer cells, differential contractility alone was found to be sufficient for sorting.[44] However, while sorting also took place on two time scales, a fast, early (< 0.5 h) and a slower, later time scale, the authors did not investigate the temporal evolution further. An interplay between adhesion and contractility was confirmed in recent studies using vertex/Voronoi models.[9,15,16] In particular, interfacial tension was shown to be determined by the ratio of cell adhesion and contractility, governing the tissue-scale tension.[9] Accordingly, the increased contractility paired with the lower adhesion of dKD cells translates well into the high tension values measured by laser ablation.

However, a demixing mechanism of locally increased contractility at the boundary between two cell types, as reported in Drosophila wing discs, can be ruled out in our work.[10–12] While we measured tremendous differences in line tension between the different cell types, the WT/dKD interface did not exhibit the highest tension but rather values equal or slightly below that of dKD/dKD junctions.

Another mechanism in contrast to our data was proposed by a recent study examining the demixing of E-cadherin-depleted and WT MDCK cells. The authors identified active cell forces as the governing factor of sorting.[13] While the demixing behavior in that study appears very similar to our data, the initial segregation was slower. Furthermore, they observed a pattern reversal at uneven mixing ratios which was absent in our co-cultures. This stability of the sorting pattern is indicative of interfacial energy minimization by minimizing the contact region between heterotypic cell types upon sorting, based on adhesion and/or contractility.[13] E-cadherin-depleted and WT keratinocytes were recently shown to sort mainly based on shape disparities and this was thoroughly explained in vertex simulations as well as observed earlier in zebrafish embryos.[14,46] While in our cell lines shape differences seem to be small, we cannot rule out their contribution.[23] Although, similarly to the area disparities, both parameters are probably only a consequence of the tremendous tension differential with stretched WT and laterally constricted and therefore rounded dKD cells.

One limitation of our study, similar to most fundamental demixing experiments, is the possible crosstalk of contractility and adhesion.[47] For instance, actomyosin contractility has been shown

to enhance adherens junction-based adhesion.[48–50] Accordingly, our Y27632 experiments might not only have reduced contractility but also adhesion. However, there would still be the disruption of the tight junctions in dKD cells. In addition, if the adhesion difference had been just as abolished as the differential contractility, we would not have observed the prevailing demixing at longer time scales. Actomyosin contractility has also been shown to modulate focal adhesions and thereby cell motility.[51–53] However, we observed no influence of motility on sorting, possibly due to the high cell density in our experiments (with confluence reached after only a few hours).

In addition, cell sorting could be influenced by proliferation creating local clusters. However, upon Y27632 treatment the WT/WT control increased its proliferation to the same level present in treated and untreated WT/dKD mixtures, yet, its *SI* remained much lower. At the same cell amount, the *SI* remained lower in the treated WT/WT control than in the untreated WT/dKD mixture. In addition, the large difference in proliferation between the treated and untreated WT/WT samples did not translate into an increase in segregation. The cell amount ratio of the cell types was also consistent among the WT/dKD mixture and its respective WT/WT counterpart, both treated and untreated, whereas their *SI* differed. Together, while we cannot completely rule out an impact of proliferation, contractility and adhesion seem to dominate the segregation.

Another caveat to note is that due to technical limitations, our cell adhesion measurements are on much shorter timescales than the observed mixing dynamics and the relevant cell-cell interactions in general.[54] Nevertheless, in agreement with other work, it is reasonable to assume that the loss of tight junction integrity reduces intercellular adhesion on all relevant timescales.[43]

In general, the presented model system has the advantage of great experimental accessibility compared with in vivo experiments but lacks some physiological conditions, e.g., properties of the substrate. While the cell-substrate adhesion might be different, it is well suited to capture the general physics of cell-cell interactions that also governs sorting in vivo. Along this line, previous work successfully compared consistent in vivo and in vitro tension-based cell sorting experiments.[44,45]

Ultimately, our data suggest that adhesion alone is sufficient, but less efficient in driving cell sorting without differential contractility. This could yet be another example of how biology employs functional redundancy to ensure fundamental processes such as sorting of different cell types.

5.4 MATERIALS AND METHODS

5.4.1 CELL CULTURE HANDLING

Madin-Darby Canine Kidney cells (strain II, MDCKII; European Collection of Authenticated Cell Cultures, Salisbury, UK) were cultured at 37°C and 5% CO_2, under humid conditions, and in minimum essential medium (Life Technologies, Paisley, UK) containing Earle's salts, 2 mM GlutaMAX (ThermoFisher Scientific, Waltham, Massachusetts, USA), 2.2 g L^{-1} $NaHCO_3$, and 10% fetal bovine serum (BioWest, Nuaillé, France), here termed M10F$^-$. The cells were passaged two to three times per week before reaching confluence with phosphate buffered saline pH 7.4 (PBS; Biochrom, Berlin, Germany) containing trypsin/EDTA (0.25%/0.02% w/v; BioWest/Biochrom).

5.4.2 GENETIC GENERATION OF CELL LINES

ZO1/2 knockdown was effected by Beutel et al. using Crispr/Cas.[55] WT-GFP cells were created as described in Skamrahl et al.[23] Clones of MDCKII cells expressing GFP-myosin-2-A were generated by transfecting cells with pTRA-GFP-NMCH II-A plasmid (Addgene plasmid # 10844). Clones expressing the GFP tag in a stable manner were selected via Neomycin resistance (G418). Upon selection, the cell pool was sorted using FACS to enrich cells with GFP at a moderate level. For N-terminal endogenous labeling of myosin with mNeon in dKD cells, the myosin-2-A exon was targeted using Crispr/Cas. MDCKII WT-ZO1-mNeonGreen cells were generated by Beutel et al. targeting the initial ZO1 exon with Crispr/Cas.[55]

5.4.3 CELL SEEDING AND DEMIXING EXPERIMENTS

Petri dishes (35 mm, ibiTreat 1.5 polymer cover slip; ibidi, Martinsried, Germany) were used. Cells were trypsinized and mixed well before being seeded to ensure an initially random distribution.

Two sets of seeding conditions were used: In *seeding approach one*, cells were seeded at 6 10^5 cells in 1 mL M10F$^-$, rinsed after about 5 h with M10F$^-$, supplied with sufficient M10F$^-$ (2-3 mL), and then imaged over time or fixed/measured after 28 h or 48 h. These conditions were used for experiments in Figure 5.2 and Figure 5.3. Because in the first experimental approach the initial demixing dynamics were missed and the cells were still subconfluent for a long time (while the image quality was slightly better due to the rinsing step and the lower cell density), we changed the experiment: Cells were seeded at 1.2 10^6 cells in 1 mL M10F$^-$ and imaged immediately. This *second seeding approach* was used for the main demixing experiments in Figure 5.1, Figure 5.5 and Figure S 5.1-3. To reduce cellular contractility, the same second set of experiments was performed with Y27632 ("InSolution" Y27632; Sigma-Aldrich, Steinheim, Germany) added to the mixed cell solution, to reach the desired final concentration, immediately before seeding.

Importantly, the cell behavior (*SI*, cell area ratio, number ratio as well as morphology) was comparable between both seeding conditions.

For imaging, cells were placed into the incubation system of a fully automated inverted light microscope (BZ-X810; Keyence, Neu-Isenburg, Germany) equipped with a 10X phase contrast objective (Nikon CFI60 Series; Keyence). The temperature was calibrated to be 37°C at the cells using a local temperature probe (Testo 735; Testo, Lenzkirch, Germany), 5% partial CO_2 pressure was set, and sufficient humidity was ensured with distilled water in the appliance of the incubation system as described before.[23] Phase contrast images were recorded at 1 frame per 7.5 min, 14 bit, 25% illumination power, exposure times of 1/25 s, and without binning, zoom, or gain, yielding a field of view of 1920 x 1440 pixels (1449.6 µm x 1087.2 µm). Corresponding fluorescence images for each frame were recorded at low light exposure to prevent phototoxicity. For this, we used 40% illumination power, 3.5 s exposure and 4X gain, without binning to allow direct overlay of both channels. In between frames, all light exposure was turned off. Focus tracking was applied and three vertical slices were chosen in a range of 10 µm (5 µm pitch) to avoid drift effects. For the manuscript Figures, images were brightness-adjusted in Fiji to improve visibility,[56] particularly in relation to the phase contrast. The fluorescence brightness was typically increased (images were relatively dark due to the low-exposure settings).

5.4.4 Automated Cellular Segmentation

Cell segmentation was performed as described in Skamrahl et al.[23] using Cellpose 1.0[57] in conjunction with Python-based parallel processing. Raw phase contrast or fluorescence images were directly used as input. To optimize cell recognition, the following parameters were used: For the phase contrast channel, the flow and cell probability thresholds were set to 1 and -6, respectively. For the fluorescence channel, the flow and cell probability thresholds were set to 0.9 and -5, respectively.

5.4.5 Further Automated Analysis of Cell Parameters

To calculate cell parameters such as the *x*- and *y*-position, area, and aspect ratio, OpenCV was used as described in Skamrahl et al.[23,58,59] Note that OpenCV might omit a small amount of cells present in the Cellpose data, for example due to a failed aspect ratio calculation (e.g., due to a falsely recognized particle which is only a few pixels in size). Therefore, to ensure correct cell indexing between Cellpose and OpenCV in all functions, we used the contours (and masks) from OpenCV for all following operations. For cell tracking, Trackpy[60] was used to link the cell positions from OpenCV. The link function was used with a memory of 3 frames and 6.04 µm (8 pixels) as the maximal displacement. Trajectories shorter than 5 frames were discarded. Drift correction was not necessary.

5.4.6 Automated Cell Type Recognition, Neighbor Analysis, and Segregation Index Calculation

Using the masks generated by Cellpose, three main steps were performed in Python. To identify the cell type (WT-GFP or unlabeled WT in WT-GFP/WT, WT-GFP or unlabeled dKD in WT-GFP/dKD mixes), the mask returned by Cellpose for the fluorescence and phase contrast channel were compared. In the masks, all pixel values belonging to one cell body correspond to the respective cell index with the background being zero. We iterated over the masks in the phase contrast channel and evaluated the modal value of the respective cell pixels in the fluorescence channel. If the modal value of the respective cell pixels corresponded to zero in the fluorescence channel (i.e., background without a cell), the cell was assigned as unlabeled. If the modal value was greater than zero, it was assigned as WT-GFP. The cell types were assigned in the phase contrast masks to finally yield a complete set of all cells for each image.

Next, nearest neighbor analysis was performed to find direct neighbors. For each cell, an OpenCV line scan was performed between the center of this cell and each surrounding cell. All zeros, the own cell index, and the index of the respective neighbor were removed from the line. Only if no values remained in the line, i.e., no other cell index was crossed, the two cells were assigned as neighbors. This was restricted to a window of 50 pixels x 50 pixels (37.75 µm x 37.75 µm) around each cell to prevent extremely high computation times and also false neighbor assignment of cells that are separated by empty space in the early, not fully confluent state. Neighbor assignments were noted as ones in a so-called adjacency matrix, in which the column (or row) number corresponds to the cell index, the rest of this symmetric matrix was filled with zeros. Lastly, the number of neighbors of each cell in the image was the sum of all ones in the respective column (or row) in the matrix. We distinguished the number of homotypic neighbors by only summing over the positions in the matrix given by the cell assignments. Per definition, the segregation index *SI* was the ratio of the homotypic and all neighbors for each cell. Finally, to generate the plots, the *SI* was averaged over all cells or separately over all cells of each cell type.

5.4.7 Cell Labeling and Confocal Fluorescence Microscopy

For the depicted confocal images, 6 10^5 cells in 1 mL were seeded (first seeding approach, vide supra) and fixed after 28 h or 48 h. Before labeling, samples were incubated for 20 min with a paraformaldehyde/glutaraldehyde solution (4% (w/v) / 0.1% (w/v) in PBS; Science Services, Munich, Germany / Sigma-Aldrich). Cells were incubated for 5 min in Triton X-100 (0.1% (v/v) in PBS) to permeabilize the plasma membrane. After rinsing three times with PBS, samples were incubated in blocking/dilution buffer (PBS containing 2% (w/v) bovine serum albumin and 0.1% (v/v) Tween20) for 30 min to block unspecific binding sites.

Samples were incubated in primary antibody diluted in blocking/dilution buffer for 1 h using the following reagents. Phospho-myosin: 2 µg mL^{-1} (1:200) light chain 2 (Ser 19) rabbit IgG1 (Cell Signaling Technology, Danvers, Massachusetts, USA), ZO1: 5 µg mL^{-1} (1:100) mouse ZO1-1A12 IgG1 AlexaFluor 488 (Invitrogen, ThermoFisher Scientific, Waltham, Massachusetts, USA). After incubation with the primary antibody, samples were briefly rinsed with PBS. Next, they were washed with PBS, with 0.1% (v/v) Triton X-100 in PBS, and again with PBS, each for 5 min on a shaking plate (75 rpm).

The secondary antibody (AlexaFluor 546-conjugated goat anti-rabbit IgG; Life Technologies, Carlsbad, USA) was diluted with blocking/dilution buffer to a concentration of 5 µg mL^{-1}. Actin labeling was performed using 165 nM AlexaFluor 647-phalloidin (Invitrogen), incubated and diluted together with the secondary antibody. The incubation time was 1 h. Following the secondary antibody, samples were washed three times with PBS for 5 min each on a shaker (75 rpm).

Nucleus staining was performed by a 15 min-incubation with DAPI (Sigma-Aldrich), diluted to 50 ng mL^{-1}. Before imaging, the cells were rinsed with PBS three times and then kept in PBS. Labeling and microscopy were performed at room temperature.

For fluorescence imaging experiments a confocal laser scanning microscope (FluoView1200; Olympus, Tokyo, Japan) was used with a 60X objective (oil immersion, *NA* = 1.25). Image processing (3D representations, *z*-projections, color choice, and overlay) and brightness adjustment were performed in Fiji.[56] For the Figures, brightness usually had to be slightly increased due to low-bleaching acquisition settings.

5.4.8 AFM IMAGING

Two days after seeding at 6 10^5 cells in 1 mL (first seeding approach), cells were rinsed once with PBS containing 0.1 g L^{-1} Mg^{2+} and 0.133 g L^{-1} Ca^{2+} (PBS^{++}; Sigma-Aldrich) and incubated with glutaraldehyde solution (2.5% (v/v) in PBS^{++}) for 20 min. PBS^{++} was used instead of PBS without magnesium and calcium ions, because the dKD cell layers were more susceptible to dissolution of ion-dependent adhesion sites due to the impaired diffusion barrier function. Prior to AFM imaging, samples were rinsed three times to remove residual glutaraldehyde. A NanoWizard 4XP AFM (Bruker Nano, JPK, Berlin, Germany) was used for imaging. The AFM was mounted on an inverted light microscope (IX 83; Olympus) to allow visual inspection via phase contrast and cell recognition via fluorescence. Imaging was carried out in contact mode with MSCT C cantilevers (Bruker AFM Probes, Camarillo, USA) in PBS with a line scan rate of 0.18 Hz translating to a velocity of 40 µm s^{-1}, a force of 0.14 nN, and a pixel size of 50 nm. The IGain was set to 20 Hz and the PGain was 0.002. The AFM was calibrated as described below, in a small area at the edge of the dish where a few cells were scratched off. Height and error images were obtained from the

manufacturer's SPM Data Processing software (JPK, Berlin, Germany) upon standard linear plane correction (to correct for a slight tilt of the Petri dish surface) without further processing.

5.4.9 AFM Indentation and Force Relaxation Measurements

Force indentation-relaxation experiments were performed using a NanoWizard 4XP AFM (Bruker Nano) with a 37°C-heated stage (JPK) mounted on an inverted microscope (IX 83; Olympus) using silicon nitride cantilevers with a nominal spring constant of 0.01 N m^{-1} (MLCT C; Bruker AFM Probes). Prior to experimentation, cantilevers were rinsed with isopropanol and PBS and functionalized by incubation for 1 h with fluorescein isothiocyanate-conjugated Concanavalin A (2.5 mg mL^{-1} in PBS; Sigma-Aldrich).

The sensitivity of the AFM was determined by recording force curves on bare substrate and the spring constant of each cantilever was determined by the thermal noise method.[61] To allow the co-culture system to fully establish its differential collective mechanics, we allowed 2 days before measuring (with the first seeding approach). Cells were rinsed three times with $M10F^-$ containing 0.2 mg mL^{-1} Penicillin (Biochrom), 0.2 mg mL^{-1} Streptomycin (Biochrom), and 15 mM HEPES ($M10F^+$; BioWest).

Before the experiments, 2.5 mL $M10F^+$ was supplied to the cells and the temperature was set to 37°C. The cells were indented at a constant speed of 2 µm s^{-1} to a maximum force of 1 nN. After a dwell time of 1 s at constant height the indenter was retracted at the same speed. Maps were recorded at a lateral scan resolution of 2 µm per pixel with one indentation-relaxation cycle each. Furthermore, five consecutive force curves at the center of individual cells in the monolayer were measured with the same parameters. For the data in Figure 5.3B the individual curves at the cell center were pooled with curves at the cell center from maps.

5.4.10 Force Curve Fitting and Viscoelastic Model

Indentation-relaxation curves of the cell center were analyzed as described recently[23] using the viscoelastic theory introduced by Cordes et al.[26] Briefly, the cell surface was described as a spherical cap. In this model the cell is considered as a liquid-filled object surrounded by a thin isotropic viscoelastic shell, which is deformed at constant volume. The force *F* acting on the apical cortex is given by:

$$F = 2\pi \left({R_1}^2 \left(\frac{R_1 \sin\phi + r_1 \sin\theta}{{R_1}^2 - {r_1}^2} \right) - R_1 \sin\phi \right) T(t) \qquad (5.1)$$

with the radius R_1 at the base of the spherical cap and the contact angle ϕ upon deformation. r_1 is the contact radius with the conical indenter, $\theta = \pi/2 - \vartheta$ with ϑ, the cone half angle.

Viscoelasticity of the shell is included in the tension term $T(t)$ through a time t dependent area compressibility modulus $K_A = K_A{}^0(t/t_0)^{-\beta}$ with the scaling parameter $K_A{}^0$ and $t_0 = 1$ s (set arbitrarily). Now, a set of nonlinear equations for the shape of the deformed cell is solved to fulfill force balance and the boundary condition of constant volume. The resulting shapes are minimal surfaces to minimize the stretching energy. The average geometry was derived via AFM imaging, confocal microscopy, and AFM-combined phase contrast and fluorescence: for WT cells a radius of 12 µm and an initial cap angle of 15° were used, while in case of dKDs R_1 = 5 µm and an angle of 25° was used. Cells were chosen close to the WT/dKD interface to most closely compare the mechanical differential. The difference in excess area A_{ex} between cell types was calculated via the correction factor $K_A{}^0\ (A_0 + A_{ex})/A_0$ with the surface area A_0 of the cell cap as first described in a study comparing isolated membranes and epithelial cells.[27]

Self-written Python scripts in conjunction with the JPK SPM Data Processing software were used for the analysis. A linear fit prior to the contact point was applied to correct the baseline. JPK SPM Data Processing was used to determine the contact point. Poorly fitted curves, e.g., yielding non-physical (negative) parameters, were discarded.

5.4.11 Laser Ablation

Laser ablation was performed on a Zeiss LSM 780 NLO system driven by Zen Black software version 11.00. Image pixel size was 0.268 µm x 0.268 µm. The objective used was a Zeiss C-Apochromat 40X/1.2 W. Ablation was performed with an 800 nm Titanium/Saphire femtosecond pulsed laser Chameleon from Coherent (Santa Clara, USA) with a power of 3.2 W at the laser head, 60% laser output set in Zen Black, reflected by MBS 760+, with pixel dwell time for photomanipulation of 7.2 µs, single iteration, ablation area was line scan, 10 pixels. For measuring the recoil velocity, the lateral membrane of MDCKII WT and MDCKII ZO1/2 dKD cells was highlighted by ZO1-mNeonGreen and myosin-2-A-mNeon, respectively, with the following settings: mNeonGreen was excited with 488 nm (Argon Laser) with MBS 488/561/633, emission filter used was 490-570 nm, pixel dwell time 2.83 µs, approximately 7.7 fps with GaAsP detector. Allowing the cell layer to fully establish its mechanics, laser ablation was performed after 2 days of growth (first seeding approach).

5.4.12 Cell-Cell Adhesion Measurements

All cell-cell adhesion measurements were carried out using a Cellhesion 200 AFM (JPK). The AFM was mounted on an optical IX 83 microscope (Olympus) to allow identification of GFP-tagged and unlabeled cells. Experiments were performed immediately after seeding in M10F+. Prior, tip-less cantilevers (MLCT-O10 B; Bruker AFM Probes) were rinsed several times with distilled water and isopropanol and then treated with poly-D-lysine hydrobromide (0.1 mg mL^{-1} in water, Sigma-Aldrich) for about two days. A cell was picked and centered as well as possible above a cell on the

substrate. Indentation was performed to a force of 2 nN, and a dwell of 5 s at constant height was chosen. The approach and retract velocity was set to 0.5 µm s^{-1}. The experiments were restricted to 2 h per day to avoid proliferation and advancing adhesion, which could interfere with the measurements. The adhesion peak force was determined using the JPK Data Processing software after linear baseline correction and contact point detection.

5.4.13 Statistical Analyses and Reproducibility

The cell behavior was very reproducible between different samples as well as among seeding conditions. Significance of the AFM indentation data in Figure 5.3 was tested using the Mann-Whitney U test. The laser ablation data in Figure 5.3 and the cell-cell adhesion forces in Figure 5.4 were tested using Welch's t-test. All statistical analyses were performed in Python.

A p value of < 0.05 was considered significant and denoted by one asterisk (*). $p < 0.01$ and $p < 0.001$ were indicated by two (**) and three (***) asterisks, respectively.

5.5 REFERENCES

1. Fagotto, F. The cellular basis of tissue separation. *Development* **141**, 3303–3318 (2014).
2. Heisenberg, C.-P. & Bellaïche, Y. Forces in Tissue Morphogenesis and Patterning. *Cell* **153**, 948–962 (2013).
3. Moscona, A. & Moscona, H. The dissociation and aggregation of cells from organ rudiments of the early chick embryo. *J. Anat.* **86**, 287–301 (1952).
4. Townes, P. L. & Holtfreter, J. Directed movements and selective adhesion of embryonic amphibian cells. *J. Exp. Zool.* **128**, 53–120 (1955).
5. Steinberg, M. S. Does differential adhesion govern self-assembly processes in histogenesis? Equilibrium configurations and the emergence of a hierarchy among populations of embryonic cells. *J. Exp. Zool.* **173**, 395–433 (1970).
6. Foty, R. A. & Steinberg, M. S. The differential adhesion hypothesis: a direct evaluation. *Dev. Biol.* **278**, 255–263 (2005).
7. Harris, A. K. Is cell sorting caused by differences in the work of intercellular adhesion? A critique of the steinberg hypothesis. *J. Theor. Biol.* **61**, 267–285 (1976).
8. Brodland, G. W. The Differential Interfacial Tension Hypothesis (DITH): A Comprehensive Theory for the Self-Rearrangement of Embryonic Cells and Tissues. *J. Biomech. Eng.* **124**, 188–197 (2002).
9. Manning, M. L., Foty, R. A., Steinberg, M. S. & Schoetz, E.-M. Coaction of intercellular adhesion and cortical tension specifies tissue surface tension. *Proc. Natl. Acad. Sci.* **107**, 12517–12522 (2010).
10. Dahmann, C., Oates, A. C. & Brand, M. Boundary formation and maintenance in tissue development. *Nat. Rev. Genet.* **12**, 43–55 (2011).
11. Landsberg, K. P. *et al.* Increased Cell Bond Tension Governs Cell Sorting at the Drosophila Anteroposterior Compartment Boundary. *Curr. Biol.* **19**, 1950–1955 (2009).
12. Umetsu, D. *et al.* Local Increases in Mechanical Tension Shape Compartment Boundaries by Biasing Cell Intercalations. *Curr. Biol.* **24**, 1798–1805 (2014).
13. Balasubramaniam, L. *et al.* Investigating the nature of active forces in tissues reveals how contractile cells can form extensile monolayers. *Nat. Mater.* 1–11 (2021) doi:10.1038/s41563-021-00919-2.
14. Sahu, P. *et al.* Small-scale demixing in confluent biological tissues. *Soft Matter* **16**, 3325–3337 (2020).
15. Sussman, D. M., Schwarz, J. M., Marchetti, M. C. & Manning, M. L. Soft yet Sharp Interfaces in a Vertex Model of Confluent Tissue. *Phys. Rev. Lett.* **120**, 058001 (2018).
16. Krajnc, M. Solid–fluid transition and cell sorting in epithelia with junctional tension fluctuations. *Soft Matter* **16**, 3209–3215 (2020).

17. Gradeci, D. *et al.* Cell-scale biophysical determinants of cell competition in epithelia. *eLife* **10**, e61011 (2021).
18. Sato, K. & Umetsu, D. A Novel Cell Vertex Model Formulation that Distinguishes the Strength of Contraction Forces and Adhesion at Cell Boundaries. *Front. Phys.* **9**, 406 (2021).
19. Glazier, J. A. & Graner, F. Simulation of the differential adhesion driven rearrangement of biological cells. *Phys. Rev. E* **47**, 2128–2154 (1993).
20. Hirashima, T., Rens, E. G. & Merks, R. M. H. Cellular Potts modeling of complex multicellular behaviors in tissue morphogenesis. *Dev. Growth Differ.* **59**, 329–339 (2017).
21. Zhang, Y., Thomas, G. L., Swat, M., Shirinifard, A. & Glazier, J. A. Computer Simulations of Cell Sorting Due to Differential Adhesion. *PLOS ONE* **6**, e24999 (2011).
22. Fletcher, A. G., Osterfield, M., Baker, R. E. & Shvartsman, S. Y. Vertex Models of Epithelial Morphogenesis. *Biophys. J.* **106**, 2291–2304 (2014).
23. Skamrahl, M. *et al.* Tight Junction ZO Proteins Maintain Tissue Fluidity, Ensuring Efficient Collective Cell Migration. *Adv. Sci.* **8**, 2100478 (2021).
24. Matsuzawa, K. *et al.* MAGIs regulate aPKC to enable balanced distribution of intercellular tension for epithelial sheet homeostasis. *Commun. Biol.* **4**, 1–11 (2021).
25. Janshoff, A. Viscoelastic properties of epithelial cells. *Biochem. Soc. Trans.* **49**, 2687–2695 (2021).
26. Cordes, A. *et al.* Prestress and Area Compressibility of Actin Cortices Determine the Viscoelastic Response of Living Cells. *Phys. Rev. Lett.* **125**, 068101 (2020).
27. Janshoff, A. Viscoelasticity of basal plasma membranes and cortices derived from MDCK II cells. *Biophys. Rep.* **1**, 100024 (2021).
28. Baum, B. & Georgiou, M. Dynamics of adherens junctions in epithelial establishment, maintenance, and remodeling. *J. Cell Biol.* **192**, 907–917 (2011).
29. Hatte, G., Prigent, C. & Tassan, J.-P. Tight junctions negatively regulate mechanical forces applied to adherens junctions in vertebrate epithelial tissue. *J. Cell Sci.* **131**, jcs208736 (2018).
30. Choi, W. *et al.* Remodeling the zonula adherens in response to tension and the role of afadin in this response. *J. Cell Biol.* **213**, 243–260 (2016).
31. Cartagena-Rivera, A. X., Van Itallie, C. M., Anderson, J. M. & Chadwick, R. S. Apical surface supracellular mechanical properties in polarized epithelium using noninvasive acoustic force spectroscopy. *Nat. Commun.* **8**, 1-12 (2017).
32. Odenwald, M. A. *et al.* The scaffolding protein ZO-1 coordinates actomyosin and epithelial apical specializations *in vitro* and *in vivo*. *J. Biol. Chem.* **293**, 17317–17335 (2018).
33. Odenwald, M. A. *et al.* ZO-1 interactions with F-actin and occludin direct epithelial polarization and single lumen specification in 3D culture. *J. Cell Sci.* **130**, 243–259 (2017).

34. Fanning, A. S., Van Itallie, C. M. & Anderson, J. M. Zonula occludens-1 and -2 regulate apical cell structure and the zonula adherens cytoskeleton in polarized epithelia. *Mol. Biol. Cell* **23**, 577–590 (2011).
35. Bhide, S. *et al.* Mechanical competition alters the cellular interpretation of an endogenous genetic program. *J. Cell Biol.* **220**, e202104107 (2021).
36. Duguay, D., Foty, R. A. & Steinberg, M. S. Cadherin-mediated cell adhesion and tissue segregation: qualitative and quantitative determinants. *Dev. Biol.* **253**, 309–323 (2003).
37. Foty, R. A. & Steinberg, M. S. Cadherin-mediated cell-cell adhesion and tissue segregation in relation to malignancy. *Int. J. Dev. Biol.* **48**, 397–409 (2004).
38. Schötz, E.-M. *et al.* Quantitative differences in tissue surface tension influence zebrafish germ layer positioning. *HFSP J.* **2**, 42–56 (2008).
39. Godt, D. & Tepass, U. Drosophila oocyte localization is mediated by differential cadherin-based adhesion. *Nature* **395**, 387–391 (1998).
40. Hayashi, T. & Carthew, R. W. Surface mechanics mediate pattern formation in the developing retina. *Nature* **431**, 647–652 (2004).
41. Ulrich, F. *et al.* Wnt11 Functions in Gastrulation by Controlling Cell Cohesion through Rab5c and E-Cadherin. *Dev. Cell* **9**, 555–564 (2005).
42. Kraft, B., Berger, C. D., Wallkamm, V., Steinbeisser, H. & Wedlich, D. Wnt-11 and Fz7 reduce cell adhesion in convergent extension by sequestration of PAPC and C-cadherin. *J. Cell Biol.* **198**, 695–709 (2012).
43. Vedula, S. R. K. *et al.* Quantifying Forces Mediated by Integral Tight Junction Proteins in Cell–Cell Adhesion. *Exp. Mech.* **49**, 3–9 (2009).
44. Krieg, M. *et al.* Tensile forces govern germ-layer organization in zebrafish. *Nat. Cell Biol.* **10**, 429–436 (2008).
45. Maitre, J.-L. *et al.* Adhesion Functions in Cell Sorting by Mechanically Coupling the Cortices of Adhering Cells. *Science* **338**, 253–256 (2012).
46. Wang, G., Manning, M. L. & Amack, J. D. Regional cell shape changes control form and function of Kupffer's vesicle in the zebrafish embryo. *Dev. Biol.* **370**, 52–62 (2012).
47. Amack, J. D. & Manning, M. L. Knowing the Boundaries: Extending the Differential Adhesion Hypothesis in Embryonic Cell Sorting. *Science* (2012) doi:10.1126/science.1223953.
48. Liu, Z. *et al.* Mechanical tugging force regulates the size of cell-cell junctions. *Proc. Natl. Acad. Sci.* **107**, 9944–9949 (2010).
49. Koirala, R. *et al.* Inside-out regulation of E-cadherin conformation and adhesion. *Proc. Natl. Acad. Sci.* **118**, e2104090118 (2021).
50. Seddiki, R. *et al.* Force-dependent binding of vinculin to α-catenin regulates cell–cell contact stability and collective cell behavior. *Mol. Biol. Cell* **29**, 380–388 (2018).
51. Reffay, M. *et al.* Interplay of RhoA and mechanical forces in collective cell migration driven by leader cells. *Nat. Cell Biol.* **16**, 217–223 (2014).

52. Ren, X.-D. *et al.* FAK suppresses Rho activity to promote focal adhesion turnover. *J. Cell Sci.* **113**, 3673–3678 (2000).
53. Yin, J. & Yu, F.-S. X. Rho kinases regulate corneal epithelial wound healing. *Am. J. Physiol.-Cell Physiol.* **295**, C378–C387 (2008).
54. Wyatt, T., Baum, B. & Charras, G. A question of time: tissue adaptation to mechanical forces. *Curr. Opin. Cell Biol.* **38**, 68–73 (2016).
55. Beutel, O., Maraspini, R., Pombo-García, K., Martin-Lemaitre, C. & Honigmann, A. Phase Separation of Zonula Occludens Proteins Drives Formation of Tight Junctions. *Cell* **179**, 923-936.e11 (2019).
56. Schindelin, J. *et al.* Fiji: an open-source platform for biological-image analysis. *Nat. Methods* **9**, 676–682 (2012).
57. Stringer, C., Wang, T., Michaelos, M. & Pachitariu, M. Cellpose: a generalist algorithm for cellular segmentation. *Nat. Methods* 1–7 (2020) doi:10.1038/s41592-020-01018-x.
58. Bradski, G. The OpenCV library. *Dr Dobbs J. Softw. Tools* **25**, 120–125 (2000).
59. Teh, C.- & Chin, R. T. On the detection of dominant points on digital curves. *IEEE Trans. Pattern Anal. Mach. Intell.* **11**, 859–872 (1989).
60. Crocker, J. C. & Grier, D. G. Methods of Digital Video Microscopy for Colloidal Studies. *J. Colloid Interface Sci.* **179**, 298–310 (1996).
61. Hutter, J. L. & Bechhoefer, J. Calibration of atomic-force microscope tips. *Rev. Sci. Instrum.* **64**, 1868–1873 (1993).

5.6 SUPPORTING INFORMATION

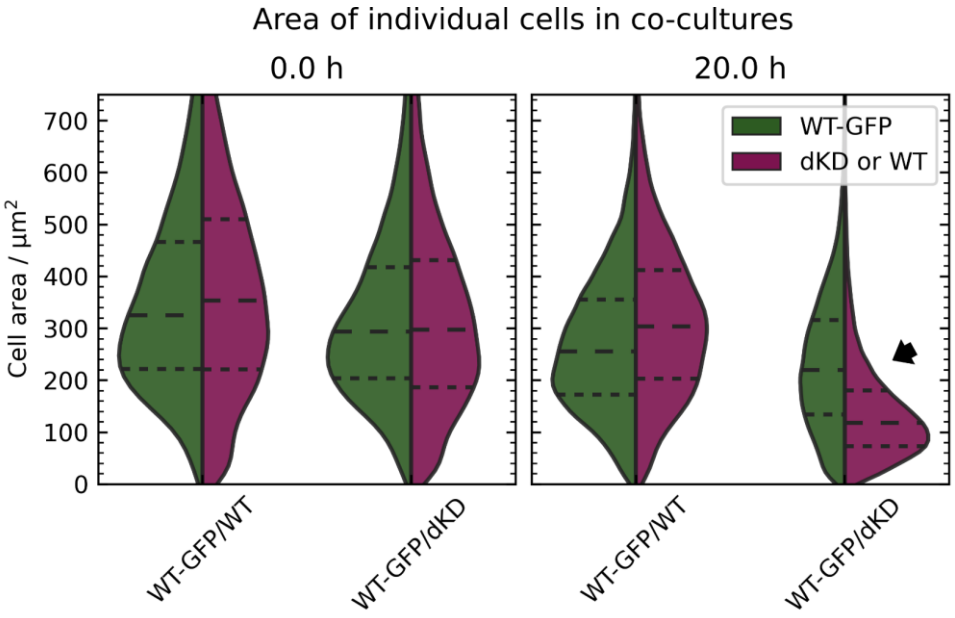

Figure S 5.1: Area of individual cells in the co-cultures from Figure 5.1. Violin plots are shown, depicting the kernel density estimation with horizontal, dashed lines showing the quartiles and median. Violins are scaled to have the same area. The arrow indicates the unique area offset in WT/dKD co-cultures due to differential contractility.

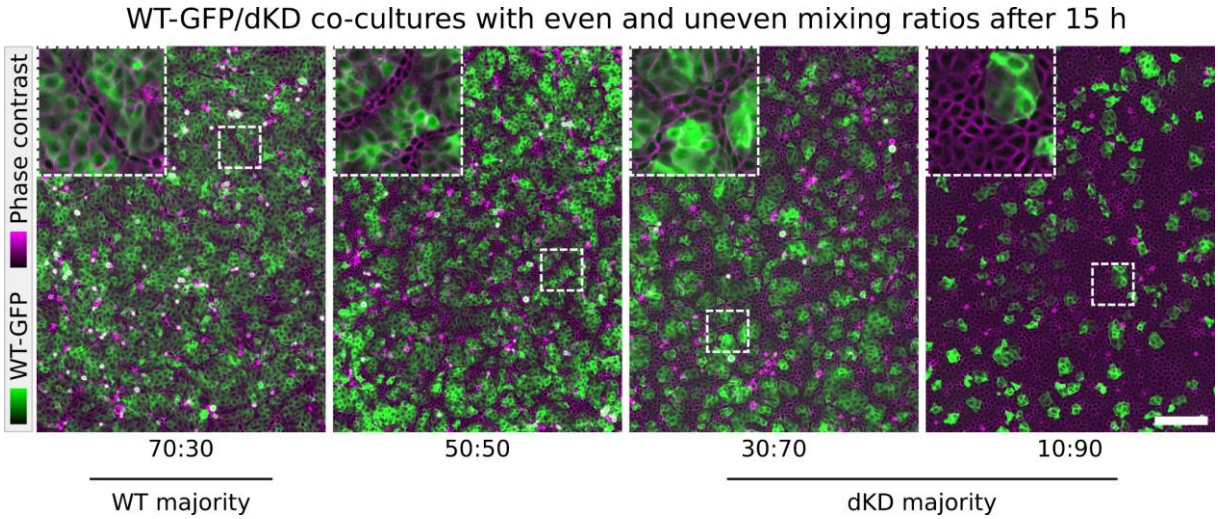

Figure S 5.2: Demixing WT/dKD co-culture experiments performed as in Figure 5.1 after 15 h of incubation, seeded at even and uneven mixing ratios. Scale bar: 200 µm.

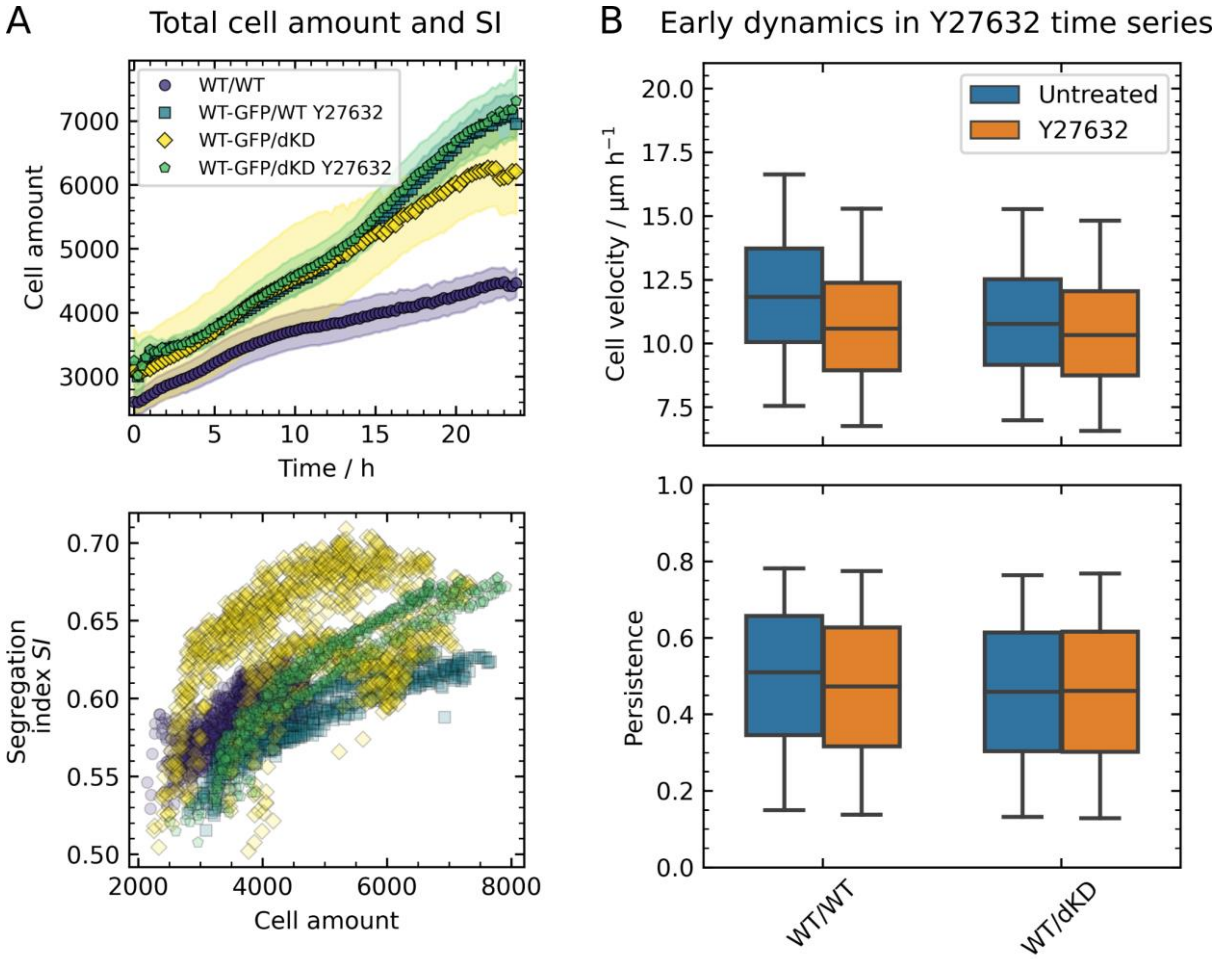

Figure S 5.3: Additional analyses of the co-culture (de-) mixing experiments from Figure 5.1 and 5.5. A) Total cell amount over time and the *SI* plotted against the total cell amount. B) Velocity and persistence within the first 5 h after seeding. Both parameters were calculated from individual cell tracks. Velocity was averaged over all frames. Persistence was defined as the ratio of the direct distance between the start- and endpoint and the sum of the distances traveled in each step.

Chapter 6
DISCUSSION AND CONCLUSIONS

While the discussion sections of the experimental Chapter 3 through Chapter 5 detailed the main points of each specific topic, here I will discuss new findings that were published after the manuscript of the respective Chapter and summarize the main results. I will also try to relate the findings and highlight key elements common among the projects, such as the impact of the actin cytoskeleton and the observed collective phenomena.

6.1 SINGLE CELL MECHANOADAPTATION BASED ON THE ACTIN CYTOSKELETON

In Chapter 3, a novel combination of AFM and FRAP was established to study mechanical sensing and adaptation of single cells to external force. Mechanical sensing and adaptation are vital in nature, even determining the fate of stem cells to specify different tissues.[1,2] Cells not only regulate their mechanics downstream of signaling events such as ligand-receptor binding but employ a diversity of feedback systems. As described in a recent review by De Belly et al.,[2] the interplay of mechanosensing, cell surface mechanics, and intracellular signaling is critical in regulating cell fate. While a plethora of molecules can contribute to this mechanical regulation, it is largely related to the actin cytoskeleton, the main target in Chapter 3. We identified the regulation of actin molecule turnover as a response to withstand external stress. Actin turnover was decreased up to two-fold in an exponential fashion with increasing stress, yielding longer filaments. Interestingly, this was the case in stress fibers while the force was applied via AFM at the top of the cell. This long-range signal transmission could on one hand be accomplished by signaling, such as Piezo channel activation and calcium flow, but direct force transmission could also be at play. While at the time of the publication of the data the process of force transmission from the apical cortex to the stress fibers was elusive, more recent studies may provide additional insights and hint at an impact of direct force transmission.

In particular, new publications showed stress fibers to be generated from, embedded in, and tightly connected to the actin cortex.[3,4] As the cortex lines the membrane of the entire cell and the persistence length of actin is in the whole-cell range of several micrometers (about 15 μm for actin), one may speculate that the mechanical signal is transmitted directly through the cortex. In addition, AFM indentation probably stretched the membrane and cortex significantly at indentation depths of roughly 2 μm in our experiments. In confluent cells in Chapter 5, we were able to quantify a buffering of membrane strain by excess area dilatation, with a six-fold difference in excess area between cells. However, single cells spread on a substrate generally have less

membrane reservoirs than confluent epithelial layers to respond to the indentation.[5,6] Accordingly, in the experiments on single cells in Chapter 3, owing to the smaller buffering reservoir, direct mechanical transduction across the cortex may be more efficient. At the stress fibers, this could translate into forces on individual formin molecules, which have been shown to increase their actin polymerization activity upon force.[7,8]

Interestingly, a study published simultaneously with our work identified stress relaxation in response to external force to follow the same actomyosin-based mechanism both in tissues and single cells.[9] The authors indeed identified a central role of formins in actin modulation upon stress response. Stress relaxation and actin remodeling occurred on similar time scales of about 15 s, consistent with the actin turnover time in the present thesis upon forces of 1 nN and 10 nN. However, note that while we focused on adherent cells, that study examined how rounded cells before spreading respond to force application.

In addition to responding to external force, cells use the actin cytoskeleton to precisely exert forces on their environment. In particular, the stress fibers play an important role in exerting contractile forces on the substrate to facilitate forward motion during cell migration.

6.2 From Single Cell Mechanics and Motility to Collective Migration

During the migration of single cells, stress fibers, which terminate in focal adhesions at the cell-substrate interface, dynamically remodel. Thereby, an optimal interplay between adhesion, contraction, cell body extension, and detachment is accomplished. The corresponding force profile needs to be asymmetric between the leading and the trailing edge and the process must be tightly regulated. While Rac-mediated signaling induces actin polymerization extending the leading lamellipodium, Rho promotes contraction of the trailing edge. In the present dissertation, such a Rho-controlled increase of contractility upon ZO protein depletion (in dKD cells) led to increased motility of single cells. Strikingly, when the same cells were interconnected in a monolayer, migration was severely stalled.

This jamming of confluent cell layers caused by an extreme actomyosin contractility upon TJ integrity loss was the main result of Chapter 4. While initially more leader cells emerged, overly contracting bulk cells became increasingly immobile over time, jamming the whole dKD MDCKII sheet. Accordingly, increased contractility upon junction disruption can lead to both migration deceleration in collectives and acceleration in single cells. This is in good agreement with related work published after our study, which also found MDCKII cells lacking TJ components to migrate faster as single cells but slower in an interconnected monolayer.[10] Specifically, the authors attributed deceleration of monolayers upon depletion of junctional adhesion molecule-A mainly to the disruption of cryptic lamellipodia dynamics. This indicates a role of cell-substrate dynamics

that would also be interesting to investigate upon ZO knockdown and the resulting actomyosin upregulation.

These findings highlight not only the mechanical importance of the actomyosin cytoskeleton but also the occurrence of emergent properties when multiple cells act in a collective manner. The results underline the essence of so-called emergent or collective phenomena in biophysics, i.e., that the behavior of a collective cannot be predicted by the behavior of its constituents such as single cells. Collective phenomena are critical to the understanding of a diverse range of processes: not only on the mesoscopic scale of cell collectives but also on smaller scales of the collective interplay of molecules as well as on larger scales such as of the coordination in bird flocks, fish swarms, or even human crowds.[11–15]

Another striking behavior that emerged from the contractility overshoot upon impaired TJs was the occurrence of clusters constituted by two mechanically distinct cell populations: As all cells in a tissue attempt to contract, some cells indeed constrict laterally while others are stretched out by the pull from adjacent neighbors, in order to still cover the space without gaps. This uniquely collective behavior was also crucial in Chapter 4 as the constricted cell clusters were particularly immobile. While clearly detrimental to migration dynamics, it was not clear how these clusters of two populations emerged. In an attempt to shine light on this behavior, we introduced a co-culture in which the stretched dKD population was essentially replaced by WT cells. The co-culture additionally confirmed our view that the constricted dKD cell population stalls the migration of a layer and it exhibited even more pronounced clustering. Upon further experiments specifically targeting the segregation into clusters, the causes of the segregation as well as the mechanics in the layer became clearer.

6.3 The Interplay of Cell-Cell Adhesion and Contractility, Governing Collective Sorting Behavior

In a WT/dKD co-culture layer, the dKD cells constricted laterally, pulling on their WT neighbors. In turn, the WT cells were stretched laterally and particularly accommodated this stimulus by sacrificing excess membrane area as shown in Chapter 5. Overall, the difference in excess surface area between both cell types in co-culture was quantified as a factor of six, fitting to the difference in geometric surface area of the cell cap. Accordingly, the same amount of excess area released by WT cells was stored in dKD neighbors, indicating the conservation of surface material instead of its recycling. Excess membrane reservoirs are critical in diverse processes and commonly enable cells to withstand stress.[5,16–18] However, the present stretching response via area dilatation in a tug-of-war like mechanism inside an epithelial layer, to my knowledge, has not been reported previously. This mechanism seems reasonable for co-cultures as well as for the two mechanically distinct cell populations in dKD mono-cultures. Recent work identified asymmetric Rho signaling to induce these two populations upon mechanical interaction in interconnected dKD

layers.[19] The generation of two mechanical cell populations among the same cell type was indeed recently identified as an emergent phenomenon due to collective cell-cell interactions during development.[20] Both in mono- and co-cultures, another observation underlined the emergent nature of this collective behavior, simply via the cell morphology: In the subconfluent state all cells had the same area, and only due to cell-cell interactions upon confluence, smaller (constricted dKD) cells and larger (stretched dKD or WT) cells emerged. Accordingly, similar as during migration, actomyosin can have distinct impacts depending on the connectivity between cells via the junctions.

Finally, we scrutinized the clustering tendencies of dKD and WT cells in co-culture in Chapter 5. We identified both differential contractility and adhesion to promote segregation into clusters in a novel time-dependent manner. Together, these generic physical forces determine differential interfacial tensions between different cell types. However, while clustering was faster with a difference in both contractility and adhesion, differential adhesion dominated on longer time scales and determined the final segregation into clusters. This might be reasonable because differences in contractility seem to take effect immediately, even in single cells, whereas adhesion sites mature over time. This is another example of how biology employs collective behavior and, via functional redundancy, might ensure the robustness of fundamental sorting processes.

While in Chapter 4 and Chapter 5 method development was not the focus, automating the cell segmentation-based analyses did enable quantitative, high-throughput approaches examining thousands of cells in parallel, absent in many other studies. For instance, the cell area-dependent motility analysis was critical in Chapter 4 and the computation underlying the segregation quantification was fundamental in Chapter 5. These approaches are well complimented by lower throughput yet very specific methods such as AFM in conjunction with tailor-made models and fluorescence microscopy.

In conclusion, using a combination of biophysical tools the importance of cell mechanics and motility was highlighted across a selection of biological settings. From single cell mechanoadaptation and motility to collective interaction, sorting and migration, wide-ranging insights into mechanobiology of epithelial cells were provided.

6.4 REFERENCES

1. Engler, A. J., Sen, S., Sweeney, H. L. & Discher, D. E. Matrix Elasticity Directs Stem Cell Lineage Specification. *Cell* **126**, 677–689 (2006).
2. De Belly, H., Paluch, E. K. & Chalut, K. J. Interplay between mechanics and signalling in regulating cell fate. *Nat. Rev. Mol. Cell Biol.* 1–16 (2022) doi:10.1038/s41580-022-00472-z.
3. Lehtimäki, J. I., Rajakylä, E. K., Tojkander, S. & Lappalainen, P. Generation of stress fibers through myosin-driven reorganization of the actin cortex. *eLife* **10**, e60710 (2021).
4. Vignaud, T. *et al.* Stress fibres are embedded in a contractile cortical network. *Nat. Mater.* **20**, 410–420 (2021).
5. Pietuch, A. & Janshoff, A. Mechanics of spreading cells probed by atomic force microscopy. *Open Biol.* **3**, 130084 (2013).
6. Erickson, C. A. & Trinkaus, J. P. Microvilli and blebs as sources of reserve surface membrane during cell spreading. *Exp. Cell Res.* **99**, 375–384 (1976).
7. Jégou, A., Carlier, M.-F. & Romet-Lemonne, G. Formin mDia1 senses and generates mechanical forces on actin filaments. *Nat. Commun.* **4**, 1883 (2013).
8. Zimmermann, D. & Kovar, D. R. Feeling the force: formin's role in mechanotransduction. *Curr. Opin. Cell Biol.* **56**, 130–140 (2019).
9. Khalilgharibi, N. *et al.* Stress relaxation in epithelial monolayers is controlled by the actomyosin cortex. *Nat. Phys.* **15**, 839–847 (2019).
10. Thölmann, S. *et al.* JAM-A interacts with α3β1 integrin and tetraspanins CD151 and CD9 to regulate collective cell migration of polarized epithelial cells. *Cell. Mol. Life Sci.* **79**, 88 (2022).
11. Anderson, P. W. More Is Different. *Science* **177**, 4 (1972).
12. Witt, H. Using Force Spectroscopy to Study Collective Behavior in Biological Model Systems. (University of Göttingen, 2017).
13. Trepat, X. & Fredberg, J. J. Plithotaxis and emergent dynamics in collective cellular migration. *Trends Cell Biol.* **21**, 638–646 (2011).
14. Trepat, X. & Sahai, E. Mesoscale physical principles of collective cell organization. *Nat. Phys.* **14**, 671–682 (2018).
15. Silverberg, J. L., Bierbaum, M., Sethna, J. P. & Cohen, I. Collective Motion of Humans in Mosh and Circle Pits at Heavy Metal Concerts. *Phys. Rev. Lett.* **110**, 228701 (2013).
16. Pietuch, A., Brückner, B. R. & Janshoff, A. Membrane tension homeostasis of epithelial cells through surface area regulation in response to osmotic stress. *Biochim. Biophys. Acta BBA - Mol. Cell Res.* **1833**, 712–722 (2013).
17. Pietuch, A., Brückner, B. R., Fine, T., Mey, I. & Janshoff, A. Elastic properties of cells in the context of confluent cell monolayers: impact of tension and surface area regulation. *Soft Matter* **9**, 11490 (2013).

18. Gauthier, N. C., Masters, T. A. & Sheetz, M. P. Mechanical feedback between membrane tension and dynamics. *Trends Cell Biol.* **22**, 527–535 (2012).
19. Matsuzawa, K. *et al.* MAGIs regulate aPKC to enable balanced distribution of intercellular tension for epithelial sheet homeostasis. *Commun. Biol.* **4**, 1–11 (2021).
20. Bhide, S. *et al.* Mechanical competition alters the cellular interpretation of an endogenous genetic program. *J. Cell Biol.* **220**, e202104107 (2021).

APPENDIX

LIST OF FIGURES

LIST OF ABBREVIATIONS

AC	autocorrelation
AFM	atomic force microscopy/microscope
ARP2/3	actin-related protein 2/3-complex
ATP/ADP	adenosine triphosphate/diphosphate
β	fluidity
D	diffusion constant
dKD	double knockdown
DMEM	Dulbecco's Modified Eagle Medium
F-/G-actin	filamentous / globular actin
FCS	fetal bovine serum
FRAP	fluorescence recovery after photobleaching
GFP	green fluorescent protein
HEPES	4-(2-hydroxyethyl)-1-piperazineethanesulfonic acid
K_A	area compressibility modulus
KO	knockout
M10F	MEM with Earle's salts, 2 mM GlutaMAX, 2.2 g/L $NaHCO_3$, and 10% FCS
MDCK	Madin-Darby canine kidney
MEM	minimum essential medium
MitoC	Mitomycin C
MSD	mean squared displacement
n	*MSD* power law exponent
NA	numerical aperture
p	*p*-value in statistical significance testing
P	phosphate/phospho-
PBS	phosphate buffered saline
PIV	particle image velocimetry
PSF	point spread function
ROCK	Rho-associated, coiled-coil containing protein kinase
ROI	region of interest
s.d.	standard deviation
SI	segregation index
t	time
τ	characteristic time scale (inverse of rate constant) / time difference
T_0	prestess
TJ	tight junction
v	volume

w	weight
ω_d	actin turnover rate / dissociation rate constant
WT	wildtype
YAP	Yes-associated protein
ZO	zonula occludens

DANKSAGUNG

Wissenschaft ist außerordentlich von Kollaboration geprägt und so ist auch diese Arbeit mit der Hilfe vieler Leute entstanden. Daher möchte ich mich abschließend bei allen Beteiligten herzlich bedanken.

Mein besonderer Dank gilt Prof. Dr. Andreas Janshoff für die Möglichkeit an solch spannenden Themen zu arbeiten und diese Doktorarbeit in seiner Gruppe anzufertigen. Die wissenschaftliche Freiheit und das entgegengebrachte Vertrauen, sowohl bei meinem Hauptprojekt als auch bei dem Seitenprojekt in Oxford, weiß ich sehr zu schätzen. Ich hoffe ich habe bei unseren außerordentlich hilfreichen Diskussionen die Nerven nicht überstrapaziert.

Prof. Dr. Sarah Köster danke ich ausdrücklich für die bereitwillige Übernahme des Zweitgutachtens und die tolle Betreuung in den Treffen des Thesis-Komitees, besonders zum Einstieg am Anfang. Auch Prof. Dr. Jörg Großhans danke ich für die tollen Ratschläge und die angenehme Atmosphäre während dieser Treffen, insbesondere vielen Dank für den letzten, virtuellen Termin. Unsere gemeinsamen Diskussionen haben mich immer in eine gute Richtung gewiesen. Zudem möchte ich mich bei den weiteren Mitgliedern der Prüfungskommission, Prof. Dr. Silvio Rizzoli, Prof. Dr. Holger Bastians und Prof. Dr. Timo Betz, bedanken.

Für die nette und geduldige Hilfe danke ich auch dem GGNB und IMPRS-PBCS.

Dr. Tabea Oswald danke ich ausdrücklich für die tolle Betreuung, stets offene Tür und hilfreiche Unterstützung. Dein frischer Wind und die neue Strukturiertheit in der Arbeit sowie unsere Planungstreffen haben wirklich sehr geholfen.

Prof. Dr. Alf Honigmann, Dr. Markus Mukenhirn und Dr. Riccardo Maraspini danke ich für die tolle Zusammenarbeit, die hilfreichen Diskussionen und die interessanten Zelllinien. Die dKD Zellen waren wirklich fundamental für diese Arbeit.

Ich danke Prof. Dr. Marco Fritzsche für den tollen Kontakt über die Jahre, die hilfreichen Ratschläge und das Vertrauen in unserem AFM-FRAP-Projekt. Den Fritzsche- und Eggeling-Gruppen danke ich für das warme Willkommen in Oxford und die tolle, intensive Zeit. Insbesondere Dr. Huw Colin-York und Dr. Liliana Barbieri danke ich für die Hilfe bei den Experimenten.

Dr. Jonathan Bodenschatz danke ich für das Korrekturlesen der Dissertation, die Hilfe beim Programmieren, die guten Diskussionen und generell die tolle Zeit, auch wenn unsere Projekte dann doch nicht fusionierten. Außerdem vielen Dank für die coole Zeit bei der ersten Konferenz seit der Pandemie in Wien und deine Geduld mit Yasmin und mir.

Dr. Susanne Karsch danke ich für die tolle Einarbeitung und die nette Einführung in das SPP. Auch Dr. Bastian R. Brückner danke ich für das Bereiten eines angenehmen Starts in der Gruppe. Dr. Alexey Chizhik, danke für deine Geduld bei unseren MIET Experimenten, ganz am Anfang meiner Doktorarbeit, sowie für dein schickes Cover-Bild.

Prof. Dr. Burkhard Geil danke ich für die hilfreichen Diskussionen und die Hilfe beim Programmieren. Mein Dank gilt auch Dr. Ingo Mey für die spaßigen „Auseinandersetzungen“ und die tollen Planungstreffen, die mir wirklich die richtige Richtung gewiesen und mich auf Kurs gehalten haben.

Ich danke allen Studierenden und Praktikanten, mit denen ich zusammenarbeiten durfte, in chronologischer Reihenfolge: Hongtao Pang, Jannis Gottwald, Maximilian Ferle, Marcel Jipp und Justus Schünemann. Ihr habt wirklich sehr viel zu den jeweiligen Projekten beigetragen und es war eine außergewöhnlich gute Zusammenarbeit. Es hat echt Spaß gemacht und euer Einsatz war wirklich beeindruckend.

Angela Rübeling danke ich dafür, dass du im Zelllabor alles am Laufen hältst, sogar meist für alle mitdenkst und man immer auf dich zählen kann. Insbesondere deine Hilfe während der Pandemie war extrem viel wert.

Außerdem danke ich der gesamten Arbeitsgruppe Janshoff, inklusive aktueller wie vorheriger Mitglieder für die tolle Atmosphäre, die Abwechslung in den Kaffeepausen, u.ä., sowie die angeregten Diskussionen in den Seminaren und Kleingruppen. Auch wenn die Pandemie die Interaktion in der Gruppe erschwert hat, haben wir das Beste aus der Zeit gemacht. Ich danke Dr. Marian Vache für die ausführliche Einarbeitung in die Rolle des Sicherheitsbeauftragten sowie in die Betreuung der Biophysikalischen Chemie-Vorlesung. Tanmaya Sethi, vielen Dank für die tolle Nachfolge im „Pillar-Projekt“ und sorry, dass du das „abbekommen“ hast. Auch Danke für die Entlastung bei der Betreuung der Übungen der Biophysikalischen Chemie-Vorlesung während der Paper-Revision im Sommer 2021. Der Arbeitsgruppe Kruss danke ich für die Zusammenarbeit im Labor und insbesondere Gabriele Selvaggio für das „Brückenbauen“ zwischen den Gruppen. Außerdem vielen Dank an alle Hilfskräfte, die über die Jahre bei den Übungen der Biophysikalischen Chemie-Vorlesung mitgeholfen haben.

Bei Petra Lappe möchte ich mich dafür bedanken, dass sie hier alles am Laufen gehalten hat und wünsche einen schönen, wohlverdienten Ruhestand.

All meinen Freunden danke ich dafür, dass obwohl man sich leider nicht so häufig sieht, wir immer wieder eine tolle Zeit zusammen haben. Nach der Doktorarbeit wird es hoffentlich wieder öfter klappen.

Insbesondere danke ich meiner ganzen Familie für die Unterstützung und die vielen positiven Worte während der Doktorarbeit. Auch wenn es oft schwierig ist, alle „unter einen Hut“ zu bekommen, genieße ich immer die gemeinsame Zeit. Zudem möchte ich mich für die tolle Unterstützung während des gesamten Studiums bedanken.

Maya, du hast die Zeit des „Zusammenschreibens“ zwar etwas anstrengend, aber vor Allem auch unendlich aufregend und schön gemacht. Yasmin, ich denke es ist kaum möglich sich für deinen riesigen Rückhalt hier ausreichend zu bedanken. Vielen Dank für alles.